Imperial College London

Department of Electrical and Electronic Engineering

Optical and Semiconductor Devices Group

Metamaterial MRI-based Sensor for the Post-operative Monitoring of Colorectal Anastomosis

By

Hanan Kamel

Supervised by

Prof. Richard Syms

A thesis submitted in fulfilment for the degree of

Doctor of Philosophy

March 2018

Declaration of Originality

I certify that all material in this dissertation entitled, ‘Metamaterial MRI-based Sensor for the Post-operative Monitoring of Colorectal Anastomosis’, and the work in it is my own. Other work that is not my own has been appropriately referenced and acknowledged.

Hanan Kamel

Copyright Declaration

Abstract

Anastomotic leakage (AL) is the leading cause of morbidity and mortality after bowel anastomosis, a surgical procedure used to restore luminal continuity after bowel tumour resection. Even after years of research, its occurrence has not decreased, and new methods of monitoring the wound and predicting anastomotic failure are therefore urgently required.

Here we propose the use of an internal coil to increase the signal-to-noise ratio (SNR) during Magnetic Resonance Imaging (MRI) and/or Spectroscopy (MRS). Both methods may be used to identify ischemia and oedema, considered to be clinical indications of AL. The annular nature of the anastomotic surgical wound suggests the use of a coil with an annular field-of view, mounted on a Biodegradable Anastomosis Ring (BAR), a surgical device commonly used as a temporary mechanical support that is fragmented and excreted from the body after wound healing.

The proposed solution is a Magneto-Inductive (MI) ring resonator, based on a set of magnetically coupled L-C resonators. Its advantages are that its separate elements fit comfortably inside the BAR, are not mechanically connected, and consequently may be fragmented and excreted with the BAR itself. A coupled pair of 8-element MI ring resonators is proposed, operating on an anti-symmetric spatial mode to avoid coupling to the B_1 field during the excitation phase of MRI. However, the electrical response of an early prototype shows that insufficient rejection of uniform fields is achieved using the most obvious arrangement. Therefore, a search of the effect of design parameters on the spectra of resonant modes supported by the electrical system is carried out to identify an arrangement offering improved decoupling. A suitable design is developed, based on physical overlap between adjacent elements in the same ring, which alters the sign and magnitude of a key magnetic coupling coefficient.

MRI fields-of-view are theoretically estimated for several different arrangements for signal extraction, including devices that are mutually coupled to an external read coil and directly coupled devices. Difficulties with combining mutual coupling and B_1 field rejection are identified, and wired connections are proposed as a solution. It is found that a device with a single such connection gives a sensitivity pattern with partial symmetry, whereas a quadrature tap restores full symmetry.

In vitro ^{1}H MRI is then carried out at 1.5 T and 3.0 T using agar gel immersion phantoms, both for mutually coupled systems and for directly coupled systems. As expected, mutual coupling is found to be an unsuitable readout method for a device operating on its anti-symmetric mode, but does allow analysis of the effectiveness of B_1 field decoupling. Directly coupled devices operate essentially as expected, providing up to 15-fold local enhancement in SNR, compared to the system body coil.

Acknowledgements

I'd like to start by thanking my supervisor, Prof. Richard Syms, for supporting and guiding me throughout the PhD. He always went above and beyond and I am forever grateful to him. I count myself lucky to have worked with him and learned from his knowledge.

I am very grateful to Imperial College London for providing me with a PhD studentship and for a wonderful undergraduate and postgraduate experience. I also really appreciate the help of everyone from the EEE department, including Dr. Munir Ahmad, Phil Jones, Victor Boddy, Amine Halimi, May.Tang. and Dr. Evi Kardoulaki. Thank you all for your helpful discussion and advice.

Thank you also to Tabassum Zabwala from the Barts Health NHS Trust, and Dr. Marc Rae and Dr. Rebecca Quest from the Imperial NHS Trust – thank you very much for your time and advice regarding MRI scanning.

Last but not least, thank you to my family and friends for being interested in my research and providing help whenever needed. I am especially indebted to my parents, Hussein and Hanan, for being my rock, and supporting me in everything I do; to my husband, Yazan, for his encouragement and support; and of course to my son, Abdulrahman, without whom my PhD time would have probably been shorter but not nearly as enjoyable!

Table of Contents

List of Figures

List of Tables

1 Introduction

Colorectal anastomosis is a common surgical procedure used to treat many types of bowel diseases, including cancer, polyps and Crohn's disease. Unfortunately, one of the leading complications of the procedure is anastomotic leak which has a mortality rate of up to 33% [1] Even with clinical monitoring and radiological examination, it has not been possible to reduce the incidence of anastomotic leak [2], [3] Therefore, the aim of this thesis is to develop an internal sensor, used in conjunction of Magnetic Resonance Imaging and Spectroscopy (MRI and MRS) to increase their SNR and allow for the accurate monitoring of post-operative colorectal anastomosis, potentially predicting the occurrence of anastomotic leak.

This Chapter starts by outlining the methods of performing colorectal anastomosis. The use of compression rings, specifically the Biodegradable Anastomosis Ring (BAR), is highlighted. It is found to be as safe as sutures and staples, with the addition of offering more standardization and time efficiency. The risk factors associated with anastomotic leak are then explained, and we focus on the precursor of ischemia (blood constriction) as an indication for leakage. Current methods of diagnosis are also presented, and it is clear that they have low positive and negative predictive values, with radiological evaluation becoming accurate only after the 5^{th} post-operative day. By then it might be too late for any salvage operation. Therefore, we present the solution of MRI and MRS, along with an internal coil to increase their SNR. The former is used to check for oedema, while the latter is used to measure ischemia. The working principles of MRI are explained, with a comparison between imaging and spectroscopy. Finally, the research objective is clearly stated and a brief plan of the remaining thesis Chapters is presented.

1.1 Colorectal Anastomosis

The human bowel is composed of the small intestines, the large intestines, also called the colon, and the rectum. Figure 1.1 shows a diagram of the bowel, where we see the last part of the small intestines (the ileum) connecting to the first part of the colon (the cecum). We also see the colon itself, which is approximately 1.5 m long and 6-7 cm in diameter. It is made up of four main parts. In order of travel through the body, they are: the ascending the colon, the transverse colon, the descending colon, and finally the sigmoid which connects to the rectum. The function of the small intestines is to absorb water and important nutrients into the body. The leftover waste is then passed onto the colon and squeezed along by its muscles, eventually being expelled from the body through the rectum.

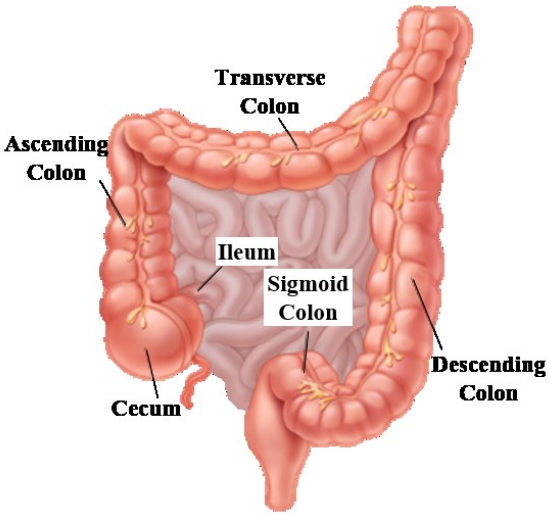

Figure 1.1 Anatomy of the lower digestive system [4]

There are many diseases of the colon varying in severity and treatment. Some are managed by a simple change of diet; others require medicines or even surgery. The surgery performed also depends on the disease, and can be minimally invasive, such as a colonoscopy, or life-changing such as a total proctocolectomy (used to remove the entire colon and rectum). A surgical procedure in the middle of this scale is an anastomosis. Used to bring together two separate hollow tubes, a colorectal anastomosis usually occurs after a resection where a diseased section of the colon and/or rectum is removed, then an anastomosis is used to establish communication between the remaining parts of the bowel.

Here we mention some of the colorectal diseases that may require an anastomosis. Firstly, and arguably the most dangerous, is colorectal cancer, with over 42 thousand diagnoses made annually in the UK, it is the third most common cancer for both men and women, tragically taking the lives of over 16 thousand people annually [5]. Therefore, the cancerous tumour has to be removed by means of a resection and anastomosis as shown in Figure 1.2. From the early to the late stages of cancer, this surgery is the most recommended treatment; accompanied in late stages by chemotherapy and/or radiotherapy [6]. Colonic polyps are also abnormal growths that start in the inner lining of the colon. They are mostly benign, but can potentially become cancerous. They affect 30% of Americans [7] and also need to be removed by resection and anastomosis. There are also some inflammatory bowel diseases which require surgical intervention, such as Crohn's disease and diverticulitis. In the former, the lining of the colon becomes inflamed and in 60-70% of cases surgery in the only treatment option [8]. In the latter, small abnormal pouches in the colon or small intestines become inflamed or start bleeding, and again the affected part has to be removed using resection and anastomosis.

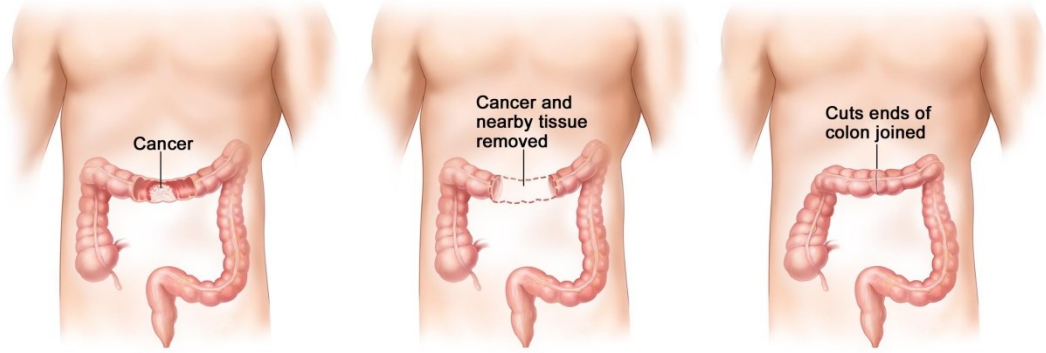

Figure 1.2 Resection of the colon with anastomosis [9]

Apart from colorectal diseases, there are also colorectal structural defects which require surgical intervention [10]. Some of these defects are Intussusception, Fistulas and Volvulus. Intussusception is when one part of the intestine folds in on itself like a telescope. Fistulas is the occurrence of an abnormal connection between two organs or between an organ and the outside body; and volvulus is when a part of the intestine twists around itself and around the artery that supports it, creating an obstruction. These conditions are usually treated with minimally invasive surgery, but some cases do require a resection and anastomosis. It is therefore apparent that a colorectal anastomosis is an important and common surgical procedure in both the emergency and elective settings [11], used often and required for the treatment of many conditions.

To perform a colorectal anastomosis in open surgery, a midline incision is firstly made to allow adequate access to the bowel, and usually either sutures or staples are used to complete the anastomosis. Although stapling was introduced much later than suturing (in the 1970s), both are now equally successful and are used interchangeably depending on the surgeon's preference [12]. There are a few other variables when considering how to conduct an anastomosis, some of which are: the suture material, the size of the suture bites, the distance between bites, interrupted or continuous sutures, using single or double layer sutures, the type of stapler used and conducting an end-to-end or a side-to-side (or a combination thereof) anastomosis. These options are usually constricted by the reason for the anastomosis and its position along the bowel. However, there have been many studies comparing these techniques to establish the best surgical method, and these are summarised by Sliecker et. al in [12]. Figure 1.3 shows an end-to-end anastomosis with double layered sutures, here the outer layers use interrupted sutures and the inner layers use two different continuous sutures. Figure 1.4 shows an example of a stapled anastomosis made with a non-cutting stapler.

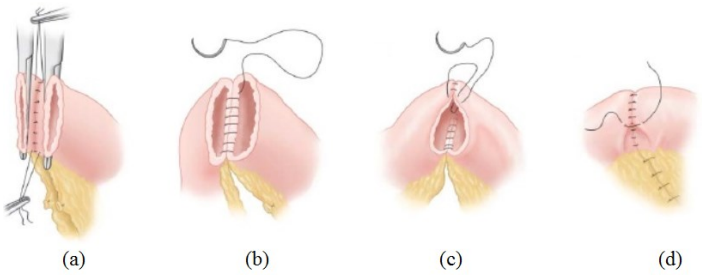

Figure 1.3 A Double layer End-to-End Anastomosis. (a) Interrupted Lembert stiches are used to form the posterior outer layer. (b) A full thickness continuous over-and-over stich is used to form the posterior inner layer. (c) A Connell stich is used to form the anterior inner layer. (d) Interrupted Lembert stiches are used to form the anterior outer layer [13]**.**

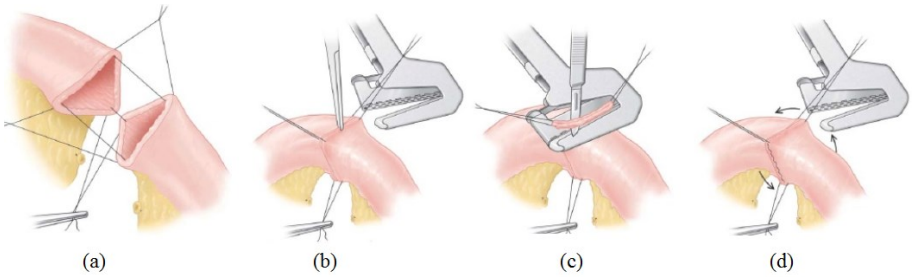

Figure 1.4 End-to-End stapled Anatomosis. (a) The bowel ends are triangulated with three traction sutures. (b) A non-cutting stapler (TA) is placed between two of the sutures. (c) The stapler is closed and the excess tissue in excised. (d) The bowel is rotated, and steps b and c are repeated twice more to close the remaining two sides of the triangle [13]**.**

Other anastomosis methods include compression rings, laser welding, glue and RF fusion. The latter three methods aim to introduce a sutureless anastomosis without a foreign body at the wound site. In the case of laser tissue welding [14], an optical laser beam with specific characteristics, most important of which being the wavelength, is targeted at the tissue to be welded. The laser wavelength determines the amount of tissue penetration, with longer waves (near infra-red) having deeper penetration and shorter waves (near UV) exhibiting more scattering. However, the final wavelength value is chosen depending on the absorption properties of the tissue in question; with actual tissue welding occurring at temperatures between 70 and 80^{o}C [15]. Although medical applications of laser have been successful in dentistry and ophthalmology, more research is still needed before it can be used in hospitals for colorectal anastomosis. The first experimental study for large bowel anastomosis using laser tissue welding was performed on 14 rabbits in 1992 by Kawahara et. al [16] and showed that sutured anastomosis was still superior, having higher burst pressure. Seven years later, similar trials were carried out on porcine small bowel describing higher burst pressure for lased over sutured anastomosis [17]. However, here the control group only had 5 samples, while the lased group contained 15 samples. Thus more development is needed before this method can be used in hospitals on human patients.

RF fusion is an even newer method for resection and anastomosis, involving sealing the tissue between two electrodes delivering RF current. The LigaSure device, by ValleyLab, is currently used

for haemostasis sealing of blood vessels and arteries up to 7mm in diameter [18]. It contains a closed-loop feedback control RF generator and uses both high frequency current and controlled pressure for tissue sealing. The LigaSure patent describes vessel sealing as "the process of liquefying the collagen, elastin and ground substances in the tissue so that it reforms into a fused mass with significantly reduced demarcation between the opposing tissue structures" [19]. Although, it has proved to be a time-saving method for vessel sealing [20], [21], more research is still being carried out to use it for bowel anastomosis [22], [23]. It has mostly been non in-vivo studies, but they do show that the LigaSure method for intestinal anastomosis could withstand the intraluminal pressure of the bowel [24], [25] (although it did perform worse than staples in both studies referenced). It is worth noting that there are other thermal tissue fusion devices such as the Altrus from Conmed [26], currently available on the market and also offering vessel sealing up to 7mm in diameter.

Finally, for glued anastomosis, animal trials are still being conducted to either establish the possibility of using glue on its own to perform the anastomosis [27], or using it to reinforce a sutured anastomosis [28], [29] to increase the allowed intraluminal pressure before rupture and therefore decreasing the occurrence of anastomotic failure. And so none of the three methods mentioned above is currently suitable for bowel anastomosis.

1.2 The Compression Ring Method

Now we come to compression rings, which – unlike the three previous methods – are as successful as sutures and staples [30], offering benefits such as cost-effectiveness, procedural standardization and ease of use, and saving time [31]. The first such compression ring is Murphy's button, shown in Figure 1.5 [3]. Invented in 1892 it is even considered to be the father of the current end-to-end surgical stapler. The button is made from two steel parts; each inserted into each part of the resected bowel and when brought together form the anastomosis.

Figure 1.5 Murphy's button [3]

The advantage of using the ring is that necrosis (tissue death) occurs at the bowel stumps leaving only healthy tissue behind to form the anastomosis. This is demonstrated in the diagram of Figure 1.6 and is the principle behind many of the compression devices currently available.

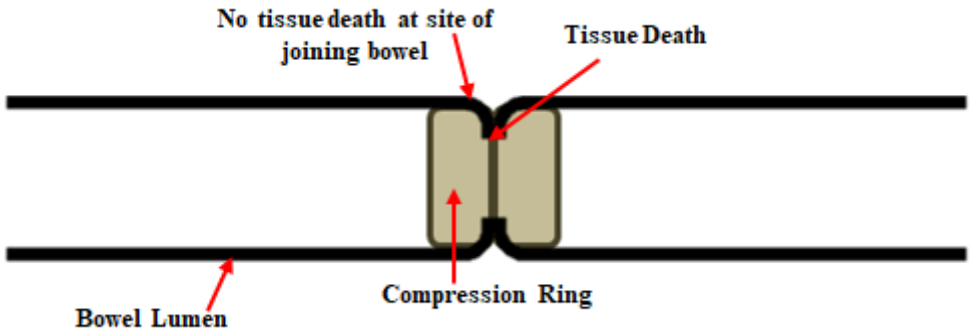

Figure 1.6 Principle of operation of compression rings.

Murphy's button was the method of choice for intestinal anastomosis for approximately 30 years, being used by the Mayo Clinic in the USA and in the country's other hospitals [32]. However, its disadvantages were that it was a permanent foreign body in the bowel causing narrowing of the intestinal lumen. The button was revisited in 1985 by Hardy et. al who introduced the Valtrac™ Biofragmentable Anastomosis Ring (BAR), shown in Figure 1.7. Correcting the drawbacks of Murphy's button, the BAR is made from polyglycolic acid with 12% barium sulphate [33], it therefore biofragments and is excreted from the body after approximately 2 weeks.

Figure 1.7 Hardy's Biofragmentable Anastomosis Ring (a) with applicator, (b) close-up [34], [35]

The first part of the BAR is inserted into one part of the bowel, already having a purse-string suture, then the suture is closed. Similarly, the second part is then inserted into the second part of the bowel having its own purse-string suture and then the suture is closed. Finally, the two parts of the BAR are clicked shut. This process is shown in Figure 1.8, while Figure 1.9 shows the fragmented BAR (having been excreted from the body) from early animal studies by Hardy et. al.

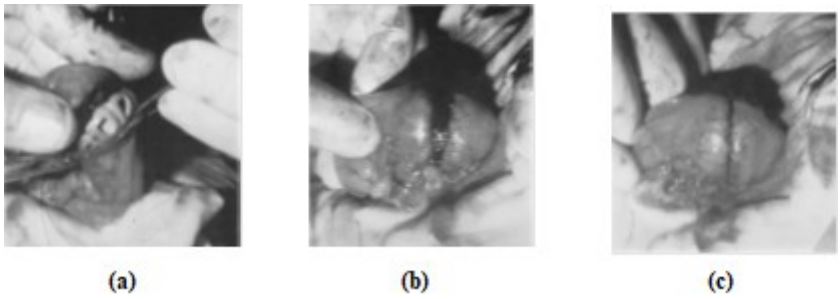

Figure 1.8 Procedure for inserting BAR into bowel (a) the first part of the BAR is inserted into one part of the bowel, (b) the second part of the BAR is inserted into the other part of the bowel, (c) the two parts are clicked shut. [33]

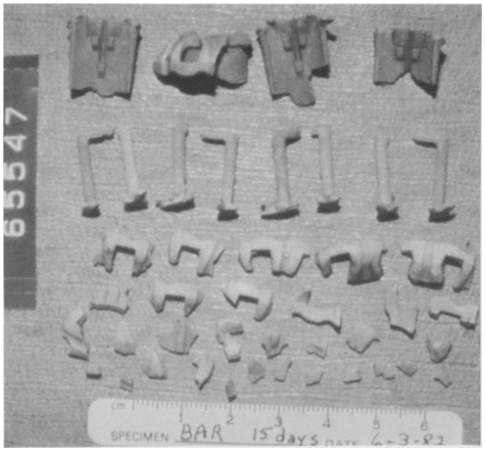

Figure 1.9 Fragmented BAR from early animal testing [33]

There have been many studies over the years evaluating the performance of the BAR for bowel anastomosis [36]–[44] in terms of the burst pressure, anastomotic leakage, the operation time, ease of use, patient discharge time, possible advantages in irradiated bowel, etc. with all confirming that it is equal to – if not better than – sutures and staples. One of the earliest clinical trials was on 438 patients in 1989 [45], where it was confirmed that the BAR shows no difference in morbidity or mortality of the patients compared with sutures or staples. It is, however, mentioned that the BAR's advantage lies in its speed of application and it uniformity of use over the whole GI tract (except the lower rectum). The first European study of the BAR was conducted in the same year and with similar results [46]. This time it is also confirmed that the BAR is easy to use and is a safe alternative to sutures and staples. Similarly, in one of the most recent studies, published in late 2016 [47], the authors study bowel anastomoses conducted on 203 patients using the BAR, their findings show that 6 patients develop anastomotic leakage (3%) and 2 develop intestinal obstruction. Other complications requiring re-surgery (8.4%) were not related to the use of the BAR. They conclude that the use of the BAR for upper and lower GI tract anastomoses is safe, simple and fast, and they recommend its use for various clinical scenarios. There are even new methods being developed for using the BAR, such as with an intra-bypass tube – as shown in Figure 1.10 [43], [48] – as an alternative to an ileostomy with stoma.

Here the authors from both studies confirm that this new method avoids the need for re-surgery, shortens the operation time, shortens the hospital stay significantly and is in fact more cost effective.

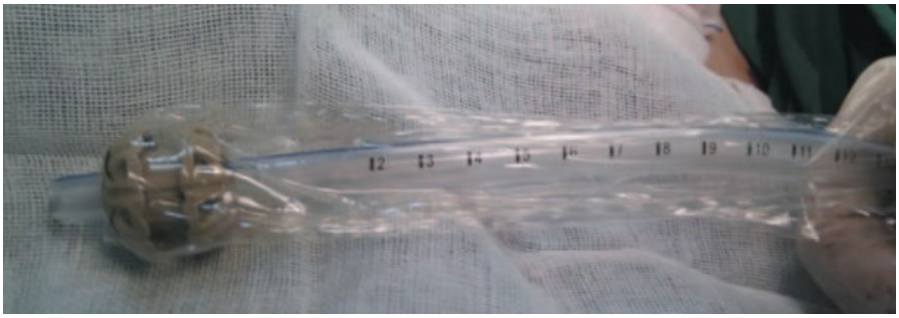

Figure 1.10 Inter-bypass tube for use with the BAR [48]

It is therefore evident that the safety, reliability and advantages of the BAR have been confirmed throughout the years, and that it is indeed the most used compression ring nowadays [30]. There are, however, other compression rings available – and currently in use – and it is worth mentioning some of them here. Firstly is the AKA-2 (and later AKA-4) device developed at the same time as the BAR, in Russia. It is used more in Russia and Germany, and most of the articles evaluating its performance are indeed non-English. The AKA-2 device is again composed of two parts as seen in Figure 1.11, but this time, the device is non-biofragmentable and is meant to be expelled from the intestines after approximately 2 weeks. One part of the device is plastic and the other is metal with pins all round. The AKA-4 device includes a transanal applicator for operations in the lower rectum. The first published use of the device is in 1984 with 225 operations [49], showing good initial results and recommendation for future use. Further clinical trials – along the whole of the GI tract – confirm this [50]–[57].

Figure 1.11 (a) AKA-2 compression anastomosis. Metal pins with metal ring springs are attached on the base ring (grey). When performing the anastmosis the pins penetrate through the inverted resection margins in the proximal plastic ring (white). (b) The AKA-4 transanal applicator. [58]

Now we come to the newest compression ring currently in use, the ColonRing or CAR [59], made from the alloy nickel titanium (NiTi or Nitinol) which exhibits shape memory and super elasticity. Nitinol is made from equal parts of nickel and titanium. Below a certain temperature, it is in what is called a 'weak state'. It can be easily deformed, by up to 6% of its original form; and when re-heated again, it gradually goes back to its original shape and 'strong state'. Similarly, under mechanical strain,

Nitinol goes into its weak state, allowing deformation with small changes in stress. When the strain is removed it goes back to its original shape [60]. The Colon Ring, shown in Figure 1.12, makes use of this second property.

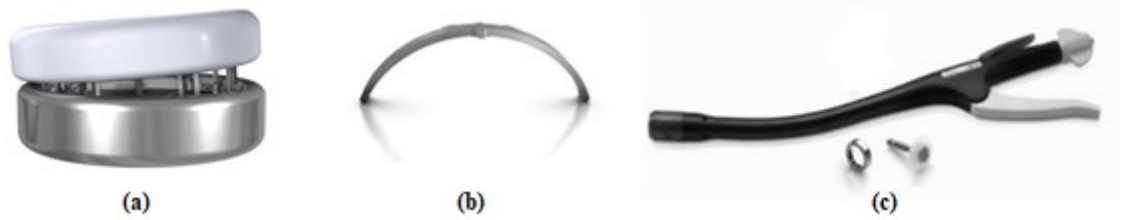

Figure 1.12 (a) the ColonRing device (b) the spring 'leaf' in its original position. This is located inside the metal part of the ColonRing, connected to the pins. When mounted on the applicator, strain is applied to make the leaf flat. It gradually returns to its original shape when released and the ColonRing is gradually closed, compressing the colon tissue. (c) Applicator, anvil and metal part of ColonRing. [61]

The device is again made of two separate parts, the top made of plastic, and the bottom, made of metal, containing the NiTi 'leaf'. The first animal testing results were published in 2007 [62], [63] showing significantly higher burst pressure than staples at day 0. Several clinical trials then confirm its safety and efficacy in colorectal anastomosis [64]–[69], at least matching those of stapled and sutured anastomoses. It is worth noting that the ColonRing is the sister device of the CAR (Colon Anastomotic Clip) which was developed first for side-to-side colorectal anastomosis. It is also now available for clinical use with comparable results to sutures and staples [70]–[74], however, it is not relevant to this research.

1.3 Anastomotic Leak

It must now be obvious that there has been much research and development into choosing and creating the most successful method for colorectal anastomosis. The reason for this is that in approximately 3-6% [75], [76] of anastomoses, dehiscence occurs (rupturing of the wound along the incision), leading to leakage and anastomotic failure. In some studies, this figure can even go up to 30% (In [75], [76] a summary of the different leak rates for recent studies is presented). Anastomotic Leak (AL) is indeed considered to be the most devastating post-operative complication and is associated with higher morbidity and mortality. In fact, the mortality rate after AL varies from 15 to 33% in literature [1]. Factors associated with AL include inflammation of the anastomotic wound and neighbouring bowels, an abscess formation and even peritonitis, which is inflammation of the tissue that lines the inner wall of the abdomen and supports most of our organs [77]. These complications are, in turn, associated with 30% higher hospital readmission rate and up to 90% increased risk of infection [78]. Additionally it was also shown that after an anastomotic leak, cancer patients have a 26% increased risk of systemic cancer recurrence and a 19% increased risk of mortality than patients without an anastomotic leak after curative resection [79]–[81]. There are also economic factors

associated with AL, which are an increased hospital length of stay by 7.3 days, associated with a cost of $24,129 per patient. And so for every 1000 patients undergoing colorectal anastomosis, the economic burden of AL alone adds up to 9,500 days of hospital stay and an extra $28.6million [78].

The reason that anastomotic leak occurs is unclear, but there are some risk factors that have been studied. These include some patient factors such as malnutrition, high white blood cell count, male gender (due to different pelvic anatomy), obesity, steroid use, non-steroidal anti-inflammatory drug use [82], tobacco and alcohol use, cardiovascular disease, and an ASA score of 3 or more [75], [76], [83]. The ASA score is the American Society of Anaesthesiologists' way of grading patients before an operation, with 1 being healthy and 5 not likely to survive the next 24 hours. Some operative risk factors of AL are an operation time longer than 2 hours, an emergency surgery, having a gynaecological or urological operation at the same operative time, preoperative blood transfusion, intra-operative blood loss of more than 200mL and an anastomosis closer to the anal verge. A history of radio- and chemotherapy also increase the AL rate, as well as a histologic specimen margin involvement in patients with inflammatory bowel disease [75], [76], [83]–[86].

In many years of research, it has not been possible to reduce the AL rate [2], [3] and so early diagnosis and detection of anastomotic leak are key to the success of any salvage operation. However, the clinical symptoms associated with early AL are subtle and so postoperative observation is essential. Clinicians must look for signs of cardiac complications, higher inflammatory indices and failure of the patient to thrive [87]. This non-specificity of clinical signs is the reason for the importance of radiological diagnosis, and the most recognised imaging method is by CT (Computed Tomography) and contrast radiography. CT is non-invasive, painless and fast. During a CT scan, cross-sectional images of the body are produced by utilizing the fact that different parts of our body absorb x-rays in different amounts. The patient lies on a bed that is gradually inserted in a doughnut-shaped structure, shown in Figure 1.13. This is called a gantry, and it has an x-ray beam transmitter and receiver inside it.

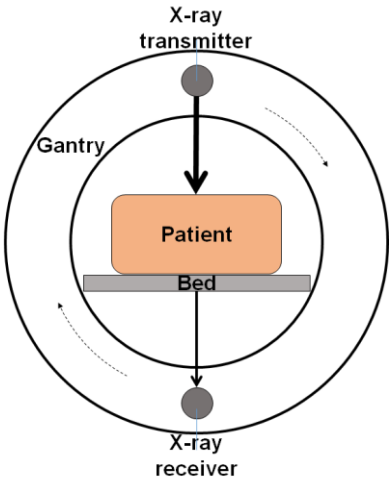

Figure 1.13 Simplified diagram of a CT scanner

The transmitter emits beams that pass through the body and are then picked up by the receiver. The transmitter and receiver rotate around the patient bed, and once a full rotation is complete, the data is sent to the computer which converts it to a 2D image. The patient bed is incrementally moved further inside the gantry until the full number of images is obtained. The clinician can then use these images to determine exactly where a disease or complication is (in this case the existence, location and severity of an anastomotic leak); or the images can all be used together to form a 3D image of the patient, allowing a different view and possible extra information to be discovered [88]. Sometimes, soft tissue is not very clear on a CT scan due to its relative inability to absorb enough x-rays. In this case, an intravenous contrast agent is needed, which is a highly visible substance in a CT scan. Contrast agents for imaging different tissue vary; and for the GI tract, barium-based compounds are used and are administered orally. The image in Figure 1.14 shows a CT scan with contrast of a patient who underwent a left hemicolectomy – a procedure to remove the left half of the colon (i.e. the descending colon) and anastomose the remaining colon to the rectum. Here the contrast agent was administered via the rectum and we see that there is some fluid collection near the anastomosis, but no contrast outside the intestinal lumen, indicating no AL. However, this turned out to be a false negative, as AL was indeed found the same day during re-operation and it was due to ischemia (blood congestion) [89].

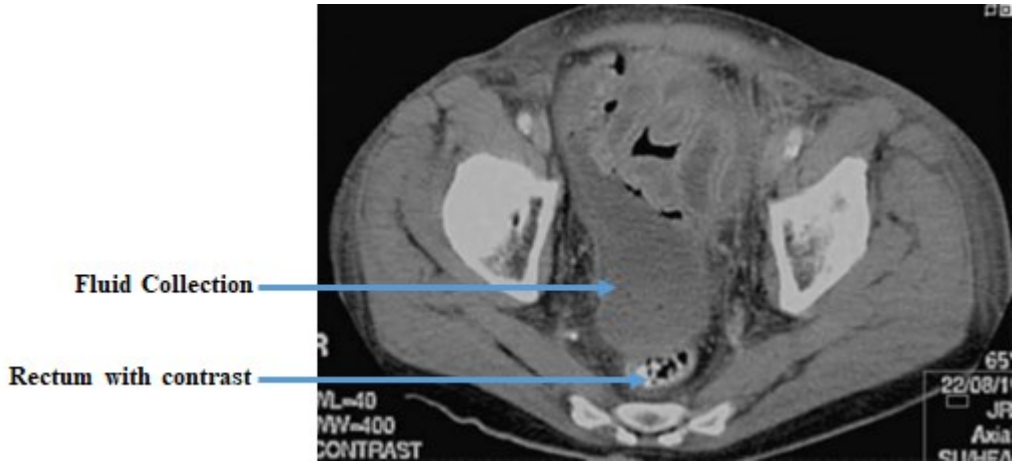

Figure 1.14 CT scan with rectally administered contrast. [89]

The scenario shows the limitations of radiography. It has a false positive and false negative occurrences of 22% and 12% respectively [1]. As well as an interobserver variability rate of 10% [89], meaning that in 10% of cases two clinicians would interpret the same result differently. Moreover, it has been shown that a false negative increases the diagnosis time by up to 4 days [90], [91]; and delaying the diagnosis time by just 1 day is associated with an increase in mortality rate by 41.3% and a lengthening of hospital stay by 26 days [1]. On the other hand, false positives may expose the patient to an unnecessary further operation and the complications associated with it. With respect to which imaging modality is best, there is opposing information in literature, some preferring contrast enemas (which are the water soluble barium enemas) [92] and others favouring CT [93].

Other methods for diagnosing AL are by measurement of the substance called C-reactive protein (CRP), which is produced in the liver and usually exists at very low levels in the body (below 3mg/L). It is usually measured using a blood test and rises in response to an inflammation in the body. A study in 2012 [94] found that a CRP test on post-operative day 2, with a cut-off of 135mg/L had a negative predictive value of 89% for post-operative infectious complications of the anastomosis. In the same year, a second study [95] confirmed the use of CRP as a predictor for AL, with a cut-off value of 140mg/L on the 3rd post-operative day. The sensitivity of this test was only 78%. The use of Procalcitonin (PCT) levels have also been investigated as a possible predictor of AL. PCT is a substance produced by specific cells of the thyroid, lungs and intestines. Again, it is nearly undetectable in normal cases, but rises in response to bacterial infection. The study in [96] claims that a PCT level above 310mg/L on the 5th post-operative day has 100% sensitivity and 100% negative predictive value in predicting AL; however, by then the leak could have already started.

Clinical signs of AL include systemic inflammatory response syndrome, fever, ileus, and elevated heart-rate and pain. On their own, these signs have low predictive values of AL [2] as previously mentioned. However, new scoring system has emerged which makes use of all these symptoms together in a ‘standardized surveillance’, along with lab findings such as CRP levels, leucocytes and

kidney function. A score of 8 or more points warrants an immediate CT scan with rectal contrast. This scoring system claims to be successful in reducing the diagnosing time to 1.5 days (from the 4 days of the control group) [97].

A new study has also created an intra-operative endoscopic mucosal grading system to predict leakage occurrence [98]. “Grade 1 is defined as a normal appearing per-anastomotic mucosa. Grade 2 is defined as ischemia or congestion involving less than 30% of either the colon or rectal mucosa and grade 3 is defined as ischemia or congestion involving more than 30% of the colon or rectal mucosa.” It was found that patients with a grade 1 anastomosis had a leak rate of 9.4% (92 patients); whereas patients with a grade 2 anastomosis had a leak rate of 40% (10 patients). Patients with a grade 3 anastomosis had their anastomosis taken down and re-created to become grade 1. This method does show promise, but requires a larger population for confirmation. On the other hand, the method does highlight the importance of a non-ischemic anastomosis for the prevention of AL. Having a good blood supply to the anastomotic wound is necessary for good healing; when this does not happen, there is blood congestion, called ischemia. Ischemia is one of the factors related to an anastomotic leak, bleeding and stricture [99]. Therefore, early detection of ischemia could potentially prevent all these complications as later seen in section 1.5.2.

Anastomotic Leakage is arguably the most devastating post-operative complication of colorectal anastomosis, but there are other complications such as surgical site infection, wound infection, ileus, bleeding, anastomotic stricture [100], [101]. Some of these problems are benign, but could become dangerous if diagnosed too late or left untreated. For example, surgical site infection is the most common post-operative complication of most surgeries. It is usually treated with anti-biotics, and similarly, wound infection. However, the latter could turn into AL and peritonitis if not spotted early [101]. Post-operative ileus is sometimes considered an inevitable complication of gastro-intestinal surgery. It is the lack of movement of the intestines, meaning that no material is being moved along the bowel, which leads to an obstruction. It is usually treated by substituting certain pain management medication (including narcotics) with local anesthetic. Anastomotic stricture is the narrowing of the anastomotic wound due to scarring. It is common of most anastomoses and is usually treated using endoscopic dilation [102]. In very rare cases the anastomosis could close completely, but this has also been treated non-surgically [103], [104]. Less rare, but also unlikely is bleeding after an anastomosis. It is usually due to the patient’s impaired clotting system and is diagnosed and treated using endoscopy [105] or colonoscopy [106]. Similarly to AL, all of these conditions require monitoring for early diagnosis and treatment. We suggest the use of MRI and MRS for the early detection of Anastomotic Leakage and potentially other complications of colorectal anastomosis.

1.4 Magnetic Resonance Imaging

Magnetic Resonance Imaging (MRI) is a powerful diagnostic method used by doctors and radiologists to view the internal structures of the human body. Using an MRI scanner, images of soft tissue, organs, blood vessels, the brain and bone can be generated. In some cases, MRI images can show problems that may not be visible with other imaging methods. When an MRI scan is performed, the patient lies inside the magnetic field of a strong magnet and RF pulses are used to generate an image of a particular 'slice' or area of the body. The main components of an MRI machine are shown in Figure 1.15. A simple description of the scanner is that it contains a coil within a coil within a coil. Firstly, there is the main field coil, generating a strong static $\mathbf{B_0}$ field. Then comes the gradient coils for imaging and spatial localisation as discussed in section 1.4.2, and finally there is the RF body coil which generates the $\mathbf{B_1}$ field. The RF body coil may also be used to receive the MR signal; however, this usually results in low image quality due to the coil not being close enough to the region of interest (ROI). Therefore, extra coils, close in proximity to the ROI, are usually used as signal receivers[1].

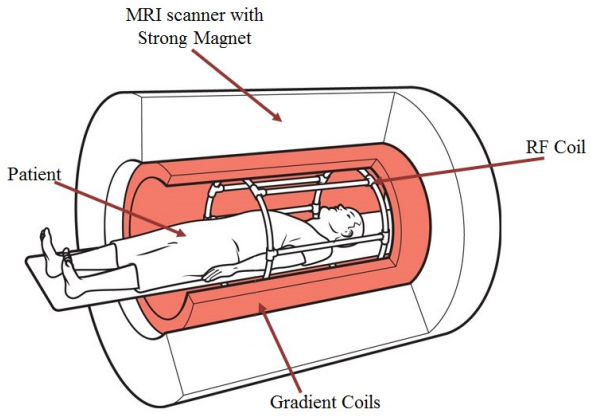

Figure 1.15 Main components of an MRI machine.

Most RF body coils are made of a birdcage resonator coil [107], [108], as seen in Figure 1.15. This consists of two circular conductive loops, connected by an even number of conductive straight elements, called rungs. Capacitors are also placed between the conductive elements, making the coil resonant. Operation is usually carried out in the first resonant mode, making the field inside the coil homogenous [109].

1.4.1 Precessing Spins

Most commercial MRI machines are concerned with the nucleus of the Hydrogen atom, which is the most abundant in the human body. This is called ^{1}H MRI since the charged element in the Hydrogen's nucleus is a single proton, having both mass and positive charge.

[1] See section 1.4.4.

MRI signal detection relies on another intrinsic property of the proton (and most other nuclei) called *spin*. The nucleus, therefore, has two important properties: Firstly, angular momentum, **p,** due to the mass of the nucleus and secondly, magnetic moment, **μ**, due to the nucleus being a charged particle. The angular momentum is given by Equ 1.1, where $\hbar = \frac{h}{2\pi}$ and h is Planck's constant. Spin angular momentum can be measured in $kg.m^2.s^{-1}$; however, it is usually given as a dimensionless property by dividing by ħ which has the same units as **p**.

$$|\mathbf{p}| = \hbar\sqrt{I(I+1)}$$

Equ 1.1

In Equ 1.1, I is the spin quantum number and depends on the structure of the nucleus. For Hydrogen, I = 1/2. The angular momentum and magnetic moment (measured in J/T) are related by Equ 1.2.

$$\boldsymbol{\mu} = \gamma \mathbf{p}$$

Equ 1.2

Here γ is the Gyromagnetic ratio, again a characteristic for each nucleus, and for Hydrogen γ = 42.58 MHz/T.

In an MRI scan, the patient is placed in a strong magnetic field, $\mathbf{B_0}$, and so we have to study the behaviour of the nuclei in this external magnetic field. We can think of the nucleus as a tiny bar magnet; and therefore, in the presence of a magnetic field, the tiny magnet will align either parallel or anti-parallel to the direction of the field. These two orientations represent a slightly lower and higher energy state respectively, and the difference in energy, ΔE, is given by Equ 1.3, and schematically represented in Figure 1.16.

$$\Delta E = \gamma \mathbf{B_0}$$

Equ 1.3

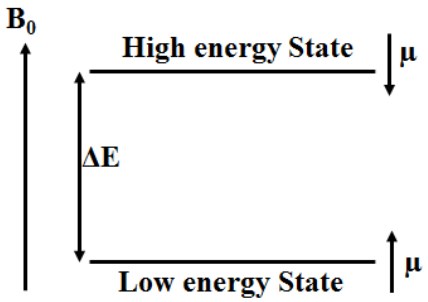

Figure 1.16 Energy levels for parallel and anti-parallel orientation of the nuclear magnetic dipole for Hydrogen

When all the nuclei have been aligned either in parallel or anti-parallel, there is a state of equilibrium and there will be a slightly higher number of parallel nuclei due to its lower energy state. The ratio of

the nuclear spins in the upper and lower energy states, as given by Equ 1.4, is nearly equal to 1 which causes the low quality raw MR signal received.

$$\frac{N_{upper}}{N_{lower}} = \exp\left(-\frac{\Delta E}{kT}\right)$$

Equ 1.4

Here N_{upper} is the number of nuclei in the anti-parallel state, N_{lower} is the number of nuclei in the parallel state, k is Boltzmann's constant and T is the absolute temperature in kelvin. From this, we can also define the excess number of nuclei in the lower energy state, denoted by ΔN.

$$\Delta N \cong N_0 \frac{\Delta E}{2kT}$$

Equ 1.5

Here N_0 is the total number of nuclei in the sample, and ΔN is approximately proportional to the difference in energy between the two states.

The alignment of the nucleus with the applied magnetic field, $\mathbf{B}_0$, produces a torque, $\mathbf{L} = \boldsymbol{\mu} \times \mathbf{B_0}$, which alters the angular momentum and causes the nucleus to precess about $\mathbf{B_0}$ as seen in Figure 1.17.

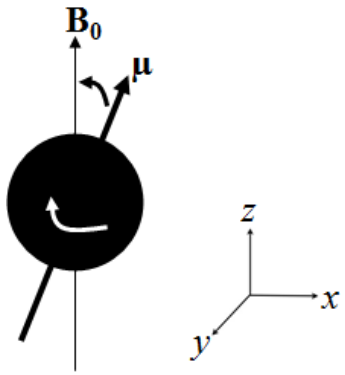

Figure 1.17 Magnetic moment precessing about the constant magnetic field B_0

The rate of change of the angular momentum is actually equal to the torque as shown by Equ 1.6

$$\frac{d\mathbf{p}}{dt} = \mathbf{L} = \boldsymbol{\mu} \times \mathbf{B_0}$$

Equ 1.6

And since $\mathbf{p} = \frac{\boldsymbol{\mu}}{\gamma}$, we have $\frac{d\mathbf{p}}{dt} = \frac{d\boldsymbol{\mu}}{\gamma\, dt}$, and we get the rate of change of the magnetic moment as

$$\frac{d\boldsymbol{\mu}}{dt} = \boldsymbol{\mu} \times \gamma \mathbf{B_0} = \boldsymbol{\omega_\mu} \times \boldsymbol{\mu}$$

Equ 1.7

Where $\boldsymbol{\omega_\mu}$ is the frequency of precession, called the Larmor Frequency and is equal to

$$\boldsymbol{\omega_\mu} = -\gamma \mathbf{B_0}$$

Equ 1.8

Here the negative sign shows the direction of rotation. Taking the magnitude of Equ 1.8, we get

$$\omega_\mu = \gamma B_0$$

Equ 1.9

We can therefore see that the precessing frequency is equal to the gyromagnetic constant multiplied by the applied magnetic field, and therefore, ω_μ is different for each nucleus. For ^{1}H imaging, under a 1.5 T magnetic field, ω_μ = 63.85MHz. This difference in the Larmor Frequency for each nucleus is what enables technicians to image the Hydrogen protons only without interacting with other nuclei in the body. However, even Hydrogen nuclei themselves can precess at slightly different frequencies in different environments. The change in environment can be due to the molecular differences since the protons being imaged are part of different molecules, each with a different electron arrangement which 'shield' the nucleus from the applied magnetic field in varying degrees, thus changing the overall precessing frequency. The other reason for the slight change in frequency is inhomogeneities in the applied B_0 field, resulting in a spatial difference in Larmor frequency.

All the Hydrogen protons will precess and align with the applied $\mathbf{B_0}$ field, and therefore, we get a Net Magnetization Vector (NMV), **M**:

$$\mathbf{M} = \sum_i \boldsymbol{\mu}_i$$

Equ 1.10

We usually write the NMV as $\mathbf{M}_z$ since, at equilibrium, the transverse component of **M** is equal to zero due to the magnetic moments having different phases. Therefore, the net magnetization actually points along the direction of the applied magnetic field, $\mathbf{B_0}$, and its magnitude is proportional to ΔN in Equ 1.5, the excess nuclei in the lower energy state. $\mathbf{M}_z$ behaves like a large magnetic dipole and we can therefore extend on Equ 1.7 and write the rate of change of the magnetization vector as

$$\frac{d\mathbf{M_z}}{dt} = \mathbf{M_z} \times \gamma \mathbf{B_0} = \boldsymbol{\omega_\mu} \times \mathbf{M_z}$$

Equ 1.11

It is this bulk precessing magnetization that we detect in an MR scan, but the system must first be perturbed in order to detect a signal. To do this, a second magnetic field, called the $\mathbf{B_1}$ field, is applied. $\mathbf{B_1}$ is perpendicular to $\mathbf{B_0}$ and it rotates about it with a frequency equal to $\boldsymbol{\omega_\mu}$, making it in synchronism with the precessing magnetic dipoles. $\mathbf{B_1}$ is often called an RF pulse since it is applied only for a few milliseconds or even microseconds. Additionally it is much weaker than the constant $\mathbf{B_0}$ field ($\mathbf{B_1}$ is in the range of 50mT, while $\mathbf{B_0}$ equals 1.5-7T). Figure 1.18 shows the effect of this RF pulse, as it makes $\mathbf{M_z}$ tilt away from $\mathbf{B_0}$, all the while still precessing about it. Note also how the RF pulse $\mathbf{B_1}$ is also precessing about $\mathbf{B_0}$ at the same frequency.

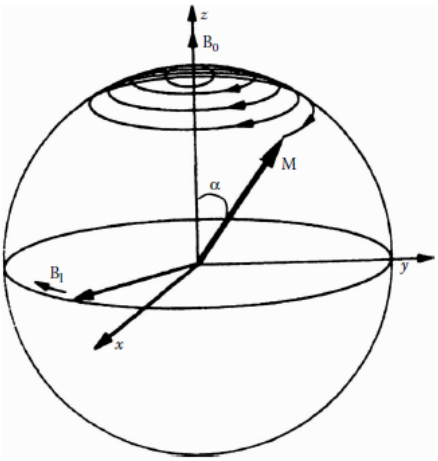

Figure 1.18 Trajectory of NMV after an RF pulse. [110]

The angle made between $\mathbf{B_0}$ and $\mathbf{M_z}$ when the pulse is switched off is called the Flip Angle (FA), shown as α in Figure 1.18. The FA can be controlled by changing the duration and/or amplitude of the $\mathbf{B_1}$ pulse. Usually $\alpha=90^o$, since this eventually generates the largest signal. In this case the longitudinal magnetization $\mathbf{M_z}$ becomes completely transverse and is denoted by $\mathbf{M_{xy}}$.

After the $\mathbf{B_1}$ field is switched off, the magnetization experiences a torque due to the constant $\mathbf{B_0}$ field and thus precesses about it at the Larmor Frequency, returning to equilibrium. $\mathbf{M}_z$ thus increases exponentially while $\mathbf{M}_{xy}$ decreases exponentially until the nuclei once again become parallel to the $\mathbf{B}_0$ field, distributed between the higher and lower energy levels in a state of equilibrium. The recovery of the longitudinal magnetisation is described in Equ 1.12, where M_0 is the magnetisation at equilibrium (before the application of the RF pulse), α is the flip angle and T1 is called the longitudinal relaxation time and denotes the time needed for $\mathbf{M_z}$ to recover to a value of 63.2% of M_0.

$$M_z(t) = M_0\left(1 - (1 - \cos\alpha)\exp\left(\frac{-t}{T1}\right)\right)$$

Equ 1.12

Similarly, the decay of the transverse magnetisation can be described by Equ 1.13 where M_0 is the initial transverse magnetisation before the application of the RF pulse, φ is the initial phase angle of the $\mathbf{B_1}$ pulse and T2, called the transverse relaxation time, is the time needed for the transverse magnetisation vector to decay to 36.7% of its original value, M_0.

$$M_{xy}(t) = M_0 \sin\alpha \exp\left(j(\omega_\mu t + \varphi)\right) \exp\left(\frac{-t}{T2}\right)$$

Equ 1.13

The relaxation time T1 is also called spin-lattice relaxation as energy is dissipated as the nuclei release their excess energy to the surroundings while returning to their initial state. T1 depends on the strength of the $\mathbf{B_0}$ field and the internal motion of the molecules. On the other hand, T2 relaxation is called spin-spin relaxation where the energy transfer occurs between the nuclei themselves rather than be dissipated to the surroundings. Initially all the nuclei are in phase precessing about the z-axis and the $\mathbf{B_0}$ field, however, due to molecular differences and the $\mathbf{B_0}$ field inhomogeneities, they grow out of phase with each other, eventually cancelling each other out. It is therefore worth emphasizing that T1 and T2 are two distinct processes, the former can be controlled by changing the strength of $\mathbf{B_0}$, but the latter is intrinsic to the imaged sample. Usually spin-spin interaction occurs in the first 50 – 200 ms after the RF pulse, whereas T1 spin-lattice dissipation takes longer. Furthermore, these times are in fact different in different environments and for different biological tissue. For example, for blood, T1 = 1200ms and T2 = 100 – 200 ms, whereas for muscle, T1 = 900 ms and T2 = 50 ms [111].

The exponentially decaying precessing magnetisation in the transverse plane, $\mathbf{M}_{xy}$, produces an alternating magnetic field in the transverse plane, which can be picked up by a suitably placed coil as an alternating voltage. This signal is called Free Induction Decay or FID and is in fact very weak due to the small value of ΔN. Signal amplification without distortion is difficult at RF frequencies, and therefore the signal is first converted to a low-frequency signal in the Hz to kHz range by subtracting a frequency component usually equal to the Larmor frequency. The new low-frequency FID is then digitally sampled and stored. This sampling duration is called the acquisition time. Usually the imaged sample contains different molecules and so the received FID will be composed of sinusoids with varying frequencies. To isolate each frequency, the FID is transformed to the frequency domain using Fourier Transformation (FT). Thus an exponentially decaying time function with a single frequency becomes a single peak at the corresponding frequency in the frequency domain; and an FID containing different frequencies will be better represented by several peaks in the frequency domain, as seen in Figure 1.19. All information in the time function is kept in the frequency domain; for instance, the rate of decay of the FID is equal to the width of the frequency spectrum at its half maximum.

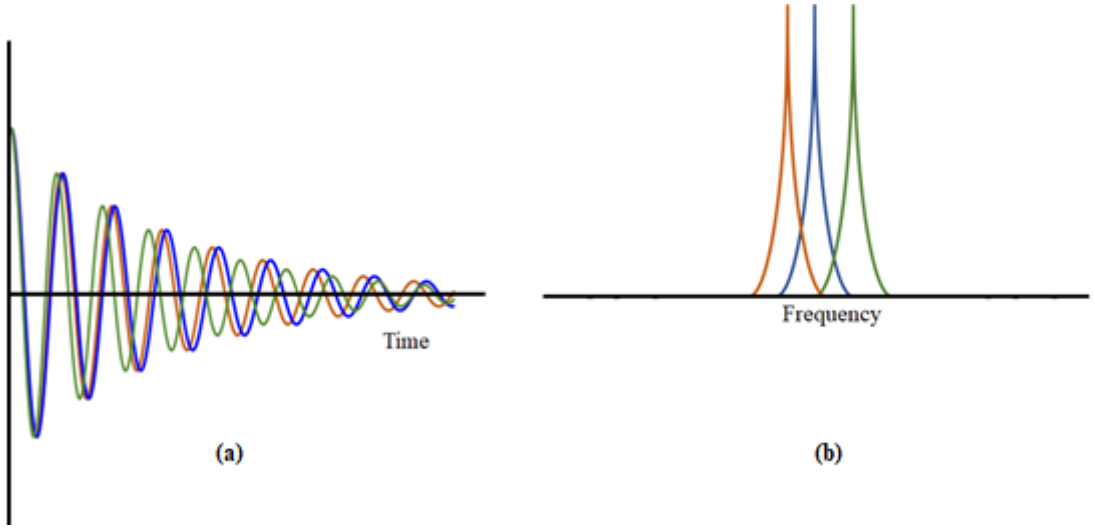

Figure 1.19 (a) FID in the time domain composed of three different frequencies. In order of frequency: orange, blue, green. (b) The same FID in the frequency domain using Fourier Transform.

1.4.2 Spatial Localisation

So far we have described the method of how a signal is received, but not how it is localised in space. Localisation is done by using magnetic field gradients. These are additional magnetic fields in the same direction as the $\mathbf{B_0}$ field, but whose amplitudes vary linearly along a chosen direction. For example, if we apply a field gradient, G_x, along the x-direction, the resulting constant magnetic field will now vary spatially according to Equ 1.14, where the new magnetic field denoted by $\mathbf{B_z}$ is the sum of the original $\mathbf{B_0}$ field and the gradient field.

$$B_z(x) = B_0 + xG_x$$

Equ 1.14

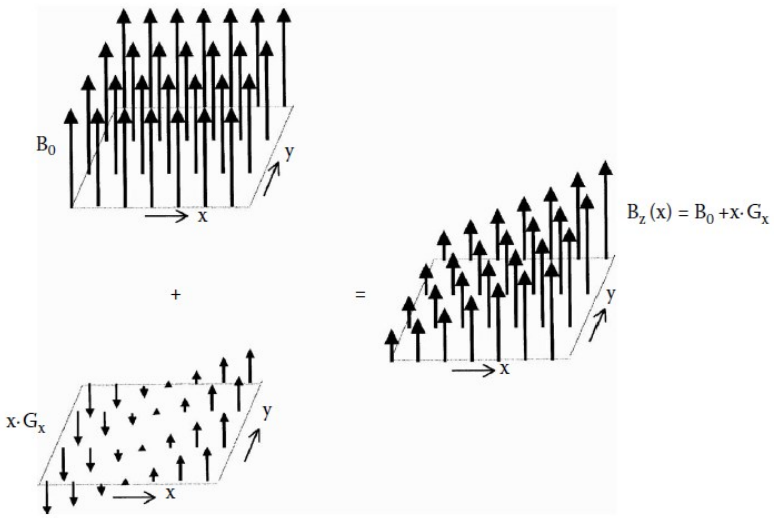

Figure 1.20 Magnetic field gradient along x axis. [Up]: uniform magnetic field B_0; [down]: the gradient field; [right]: the total magnetic field. [110]

Similarly, field gradients can also be applied in the z- and y- directions. A field gradient is the rate of change of the magnetic field in the z-axis, along the x- y- and z-directions, and therefore it has the units of Tm^{-1}. The diagram in Figure 1.20 shows how the constant B_0 field and a field gradient in the x-direction combine to produce a magnetic field in the z-direction, varying along the x-direction. It is important to note that the overall magnetic field is still in the z-direction, same as the $\mathbf{B_0}$ field; it is only the variation that can be along any axis.

The effect of the varying magnetic field is to change the Larmor frequency of the nuclei along the gradient. For G_x, the Larmor frequency varies according to Equ 1.15, and we would therefore receive an FID characterised by a distribution of resonance frequencies.

$$\omega_\mu(x) = \gamma B_z(x) = \gamma(B_0 + xG_x)$$

Equ 1.15

The field gradients are used for spatial localisation of MR signals by means of three main techniques: slice selection, phase encoding and frequency encoding. Firstly, slice selection, where each slice will eventually represent a single MR image. Consider choosing transverse slices in the xy-plane. To excite only the protons in a particular slice, and not the protons in the whole patient, a z-gradient is applied, making the Larmor frequencies vary along the patient. Now when the B_1 pulse is applied, only the protons with the matching Larmor frequency (the ones in the chosen slice) will be excited. The thickness of the slice is proportional to the bandwidth of the B_1 pulse, $\Delta\omega$, and the strength of the applied gradient, G_z. This relationship is shown in Equ 1.16.

$$\Delta z = \frac{\Delta\omega}{\gamma G_z}$$

Equ 1.16

The smaller the B_1 pulse bandwidth (i.e. the longer its duration) and the stronger the gradient, the thinner the slice will be. In the diagram of Figure 1.21, we see the effect of applying a stronger gradient (the red line) as the slice thickness, Δz decreases. We also see how varying the frequency of the B_1 pulse allows us to choose a different slice (pulse 1 has a lower frequency than pulse 2, both having the same shape and bandwidth).

The second step in MR spatial encoding is phase encoding. Here a field gradient in the y-direction, G_y, is applied. This occurs after the nuclei have been perturbed by the B_1 field and are precessing about the B_0 field in the transverse plane. G_y alters the Larmor frequency of the nuclei along the y-direction (from belly to back) and so their rate of precession about the z-axis is varied, with the nuclei experiencing a stronger field precessing faster (usually these are the nuclei at the top). When the gradient is switched off, all the nuclei return to their original Larmor frequency, but the result is that

there is a phase difference between them, with the nuclei in each 'layer' having the same phase, and thus phase encoded.

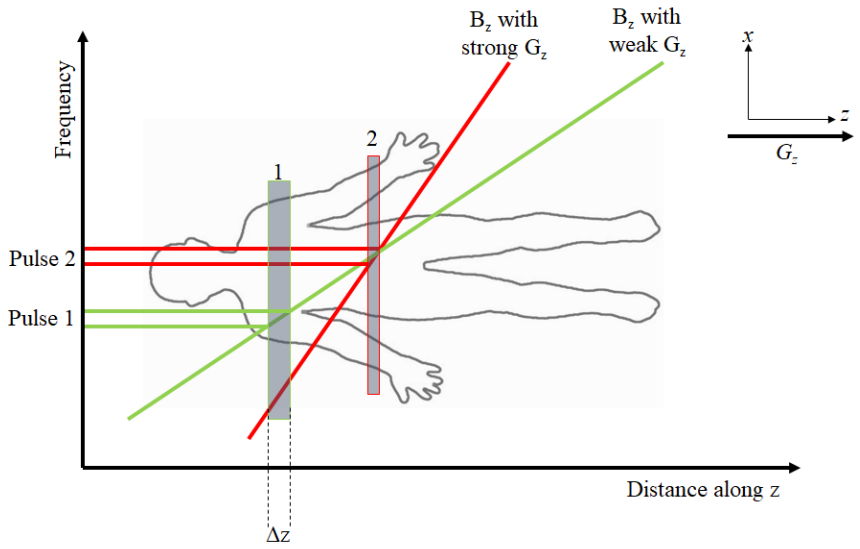

Figure 1.21 Diagram of patient in MR scanner. Pulse 1 has lower frequency, allowing selection of slice 1 if a weak gradient is applied. Pulse 2 has higher frequency allowing selection of slice 2 if a strong gradient is applied. The stronger the gradient, the thinner the slice. [111]

Finally comes the frequency encoding which is achieved using a field gradient in the x-direction[2]. Again, the gradient makes the nuclei precess with different Larmor frequencies, with nuclei in each 'column' having the same frequency. Consequently, when we receive the signal, we receive a whole spectrum of frequencies, with the higher frequencies representing the 'column' of nuclei experiencing the strongest $\mathbf{B}_z$ field.

It is relatively straightforward to extract the frequency information from the Fourier Transform; however, the phase information is less easy to extract, since each peak in the frequency spectrum carries the sum of all spins with that same frequency but different phases. The phase information is therefore extracted by applying a set of signals, rather than a single signal. The field gradient for the phase encoding for each signal is different, and a second FT is required for every echo, this time along the y-direction[3]. A timing diagram for a basic MR sequence is shown in Figure 1.22. Firstly, the RF pulse is applied and at the same time, the slice selection gradient, G_z, is turned on. In the second interval, when the RF pulse is complete, G_z is turned negative to bring the spins back into phase across the slice. The phase encoding gradient, G_y is also turned on during the second interval, and the frequency encoding gradient is turned on negatively. This is called a negative readout gradient and is used to obtain an MR echo signal. In the third interval, when the phase encoding gradient is switched off, G_x, the frequency encoding gradient (or readout gradient), is turned on.

[2] In our example, the phase encoding is done in the y-direction and frequency encoding in the x-direction. This can be reversed for some sequences.
[3] The phase encoding direction.

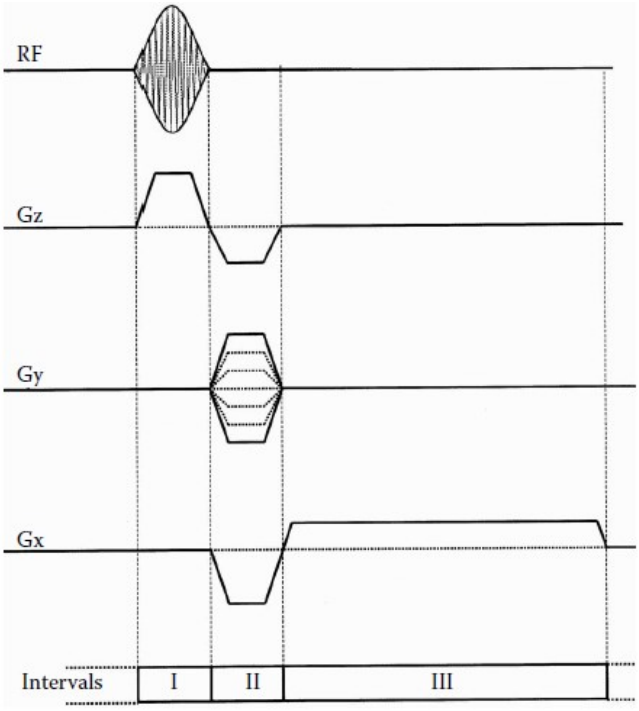

Figure 1.22 Timing diagram for basic MR sequence. In the first interval, the B_1 RF pulse is applied. During the second and third intervals, there is free precession and frequency and phase encoding is carried out. [110]

This sequence is repeated M times with differing G_y strengths to allow for phase encoding. During the scan, each time an FID is recorded, it is sampled N times to obtain a digital MR image in the end. After the signal is sampled, it is stored in what is called k-space. K-space is simply the Fourier Transform of the final MR image, such that when a 2D-FT is applied to k-space, we finally get an MR image. To understand this better, consider a 1D, infinitesimally small object with spin distribution $\rho(x)$. The FID obtained in an infinitesimal interval dx is:

$$ds(x,t) = c\rho(x)dx\exp(-j\gamma(B_0 + xG_x)t)$$

Equ 1.17

Where c is a constant of proportionality, accounting for other MR parameters such as the flip angle. The signal received from the entire sample will therefore be the sum of all ds, as seen in Equ 1.18.

$$s(t) = \int_{-\infty}^{\infty} ds(x,t) = \int_{-\infty}^{\infty} c\rho(x)\exp(-j\gamma(B_0 + xG_x)t)\,dx$$

Equ 1.18

Recall that $\omega_0 = \gamma B_0$, and so the signal received will be:

$$s(t) = c\left[\int_{-\infty}^{\infty} \rho(x)\exp(-j\gamma x G_x t)\,dx\right]\exp(-j\omega_0 t)$$

Equ 1.19

Similarly, in the y-direction, we have the FID obtained in an infinitesimal interval dy as seen in Equ 1.20. This is while the phase encoding gradient is switched on.

$$ds(y,t) = c\rho(y)d(y)\exp\left(-j\gamma\left(B_0 + yG_y\right)t\right)$$

Equ 1.20

Taking into account the fact that the sequence is repeated M times, the actual signal received is the sum of all ds with differing G_y strengths:

$$s^m(t) = c\left[\int_{-\infty}^{\infty}\rho(y)\exp\left(-jm\gamma yG_y t_{Gy}\right)dy\right]\exp(-j\omega_0 t)$$

Equ 1.21

Where t_{Gy} is the length of application of the phase encoding gradient (Second interval in Figure 1.22). Now combining both the phase and frequency encoding, each FID will have the form shown in Equ 1.22.

$$s^m(t) = c\left[\int_{-\infty}^{\infty}\int_{-\infty}^{\infty}\rho(x,y)\exp\left(-j\gamma(xG_x t + yG_y mt_{Gy}\right)dx\,dy\right]\exp(-j\omega_0 t)$$

Equ 1.22

After sampling with a time period Δt, each final sampled FID has the form in Equ 1.23, called the imaging equation, where $0 \le n \le N$ and $-M/2 + 1 \le m \le M/2$

$$s(n,m) = c\int_{-\infty}^{\infty}\int_{-\infty}^{\infty}\rho(x,y)\exp\left(-j\gamma(xG_x n\Delta t + yG_y mt_{Gy}\right)dx\,dy$$

Equ 1.23

We now make the following substitutions:

$$k_x = \gamma n\Delta t G_x$$

$$k_y = \gamma mt_{Gy}G_y$$

To get the signal in k-space as:

$$s\left(k_x,k_y\right) = c\int_{-\infty}^{\infty}\int_{-\infty}^{\infty}\rho(x,y)\exp\left(-j(xk_x + yk_y\right)dx\,dy$$

This indeed shows that the data in k-space is a sampling of the Fourier coefficients of the spin distribution $\rho(x,y)$. Therefore, applying a 2D FT would get us back to the spin distribution.

Figure 1.23 (a) shows an image of what k-space looks like in reality and Figure 1.23 (b) shows how it is filled for a sequence such as the one previously discussed in Figure 1.22.

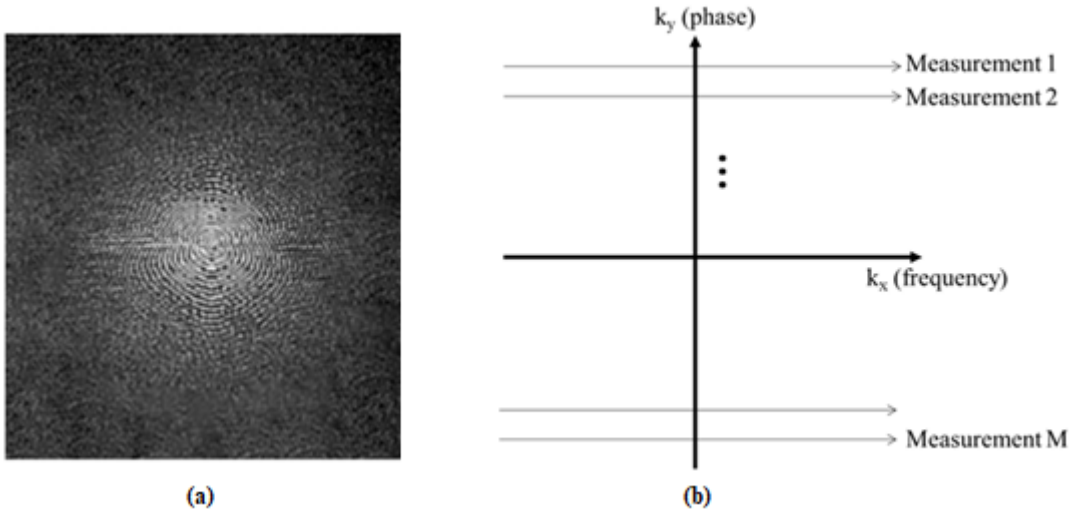

Figure 1.23 (a) Actual k-space signal. [112] **(b) k-space being filled for a basic MRI sequence.** [110]

Each time the sequence is repeated, a measurement is recorded in k-space. During the second interval, the k_y level is chosen, and during the third interval, when the readout gradient is applied, the line travels horizontally from left to right at constant speed. This is repeated until all of k-space is filled.

1.4.3 Spin Echo Sequence

Now that we know how an MR image is acquired, it is useful to also discuss an MR sequence that is most used in clinical settings and in this project: The Spin Echo Sequence. We have previously discussed how after a 90° RF pulse is applied, the Net Magnetization Vector (NMV), $\mathbf{M_z}$, parallel to the $\mathbf{B_0}$ field becomes perpendicular to it and parallel to the xy transverse plane instead. This is shown in Figure 1.24, with the NMV as the thick blue arrow. The NMV becomes $\mathbf{M_{xy}}$ still precessing about the $\mathbf{B_0}$ field. The precessing velocity of the nuclei is slightly different to the Larmor frequency due to field inhomogeneities and molecular differences; and thus the spins grow out of phase with each other as seen by the thinner different coloured arrows. In a Spin Echo sequence, a second $\mathbf{B_1}$ pulse is applied at time TE/2. This pulse is a 180° pulse and the result is to flip the spins such that the fastest red spins are now the ones lagging behind, and the slowest blue spins are now the ones with the most positive phase difference. This results in the spins realigning themselves and at time TE, the faster spins catch up with the slower ones and all the spins are in phase again. After time TE, the differing precessing velocity makes the spins lose their phase coherence once more. The signal received from this process of loss and gain of phase is called a Spin Echo (SE) rather than an FID. It is a symmetric signal with a peak where the spins are aligned and in phase, as seen in Figure 1.25.

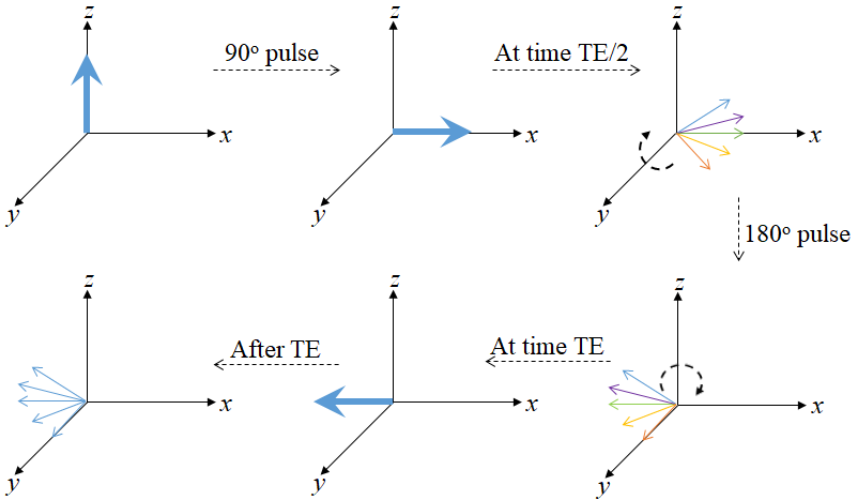

Figure 1.24 The Spin Echo sequence and the effect of a second 180° pulse on the Net Magnetization Vector [110]

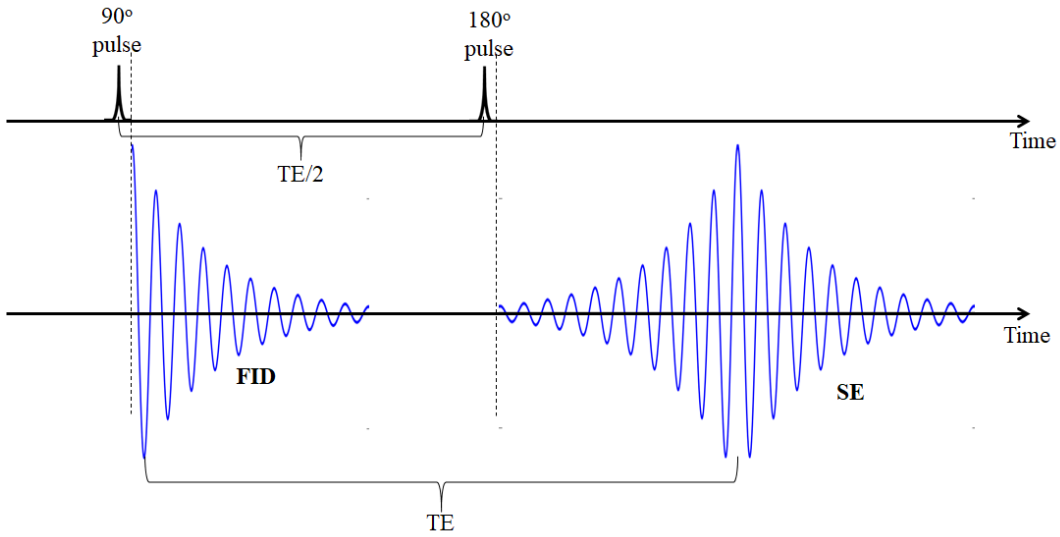

Figure 1.25 Timing diagram of a Spin Echo sequence

1.4.4 Signal to Noise Ratio

The quality of the final MR image is determined by its resolution and its Signal to Noise Ratio, or SNR [113]. The SNR is defined as the ratio between the signal intensity measured in the region of interest and the standard deviation of the signal intensity outside this region, where no tissue is present. The main source of noise in an MRI scan is the patient himself due to thermal motion. Noise is seen as an irregular granular pattern in the image and degrades the ability of the clinician to make a diagnosis; therefore a high SNR is required. Here we discuss some factors affecting the SNR. Firstly, the strength of the B_0 field itself, where the stronger it is, the larger the longitudinal magnetization is and consequently the larger the transverse magnetization and the larger the signal received. Even though there are now scanners with a field strength as high as 9T, the average hospital in the UK stocks a 3T or a 1.5T scanner, and so this is a factor that usually cannot be changed. The image pixel

size also plays a role in altering the SNR, in turn this is affected by the Field Of View (FOV) and the Matrix Size. The FOV is the physical distance over which the MR image is displayed and the matrix is the N×M matrix discussed before, where N is the number of times the frequency encoded signal is sampled and M is the number of phase encoding steps. This matrix covers the whole of the FOV, and so to get a small pixel and high resolution we need a small FOV and a fine matrix as seen in Figure 1.26.

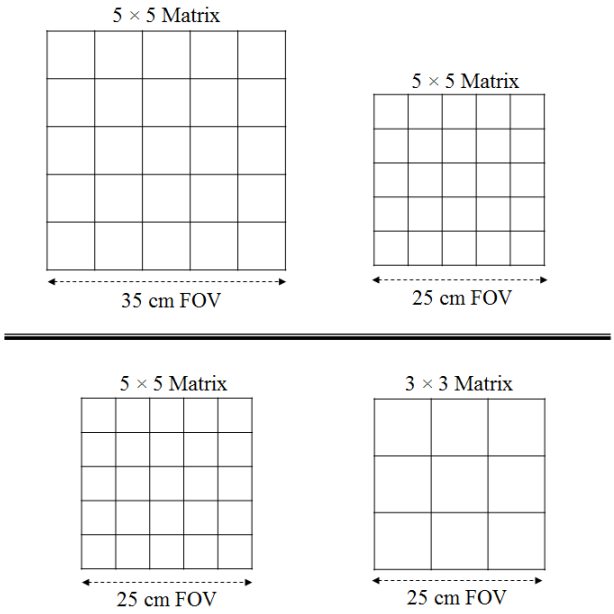

Figure 1.26 [Top] Decreasing the FOV, keeping Matrix Size constant, makes pixel size smaller. [Bottom] Decreasing Matrix Size, keeping the FOV constant, makes pixel size larger

However, a smaller pixel is also associated with lower SNR. Similarly, a thinner slice is required to achieve high image resolution but incurs a lower SNR. The dimensions of the pixel and the slice thickness together determine the dimensions of the voxel, that is the volume from which the signal is received. This signal comes from the excited spins in each voxel, and so the larger the voxel volume is, the more spins are available for excitation and the larger the signal received. Therefore, there is a compromise between resolution and SNR when it comes to the matrix size, FOV and slice thickness. Another factor that affects the SNR is the Number of Excitations or NEX. This is the number of times a signal is measured from a specific slice. The signal increases linearly with the number of excitations since it is identical for each measurement. The noise, however, is different and only increases with the square root of the NEX. Therefore, the SNR is proportional to the square-root of the NEX. However, the scan time also increases linearly with NEX and it is very important for the economic efficiency of the MRI scanner that it remains short. Finally, a method that has proven successful in increasing the SNR, without increasing the acquisition time or compromising the resolution, is using local RF coils. These are smaller coils placed as close as possible to the region of interest as seen in Figure 1.27. Being small means that they have a smaller FOV than the larger coil of the scanner, and they therefore

only pick up the noise from this small FOV, rather than from the whole FOV of the scanner. The reduced FOV also affects the signal received, but on balance, the overall effect is an increase in the SNR. The amount by which the SNR is increased depends on the design of the coil.

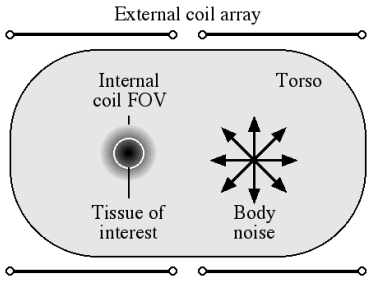

Figure 1.27 Advantage of internal coils in improving the SNR by virtue of their proximity to tissue of interest and their smaller FOV.

The local coils used can be external coils, such as that shown in Figure 1.28; a Siemens abdominal array coil regularly used by radiographers to increase the SNR of abdominal and spinal MR images. Or it could be an internal coil such as shown in Figure 1.27.

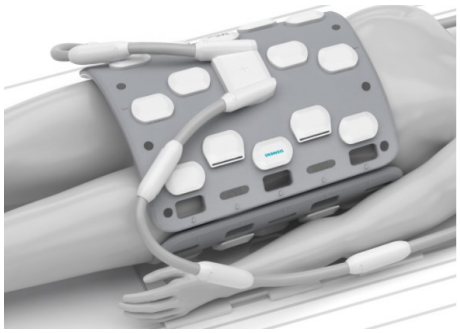

Figure 1.28 The Body Coil 60 & the Body Coil 30 from Siemens [114]

It is known that internal coils offer a greater SNR advantage over external coils due to their increased proximity to the region of interest (ROI) [115]. Examples of internal coils include intravascular [116]–[118], used inside blood vessels; transoesophageal [119], used for monitoring diseases of the oesophagus; cerebral [120]–[123], used for functional imaging of the brain; endourethral [124], used for the urinary system and endorectal [125], [126], used for the rectum.

1.5 Magnetic Resonance Spectroscopy

While MRI is used to acquire anatomic images of the body, Magnetic Resonance Spectroscopy or MRS is concerned with the chemical composition of tissue. In essence, MRI and MRS operate in a similar way, such that an MRI machine can indeed operate as an MRS machine so long as certain software is available. There are, however, some differences and these are discussed here.

Firstly and most important is that ^{1}H MRI acquires most of its signal from water and fat molecules in the body; on the other hand, ^{1}H MRS excludes signals from water and fat to analyse signals from other metabolites existing in very small quantities (mM). These metabolites can be differentiated as they precess at slightly different frequencies due to their different molecular composition as previously described. This phenomenon is called chemical shift, and is exploited in MRS. Once an FID has been transformed to the frequency domain using FT, the spectrum obtained would show peaks, each corresponding to a chemically distinct metabolite. Another difference between MRI and MRS is that usually, frequency encoding for spatial localisation by means of a readout gradient is not used in clinical MRS since now frequency is important for spectral analysis and identification of metabolites. Instead, double or triple phase encoding is utilized, or special use of coil positioning is made for selective excitation.

An MRS spectrum is shown in **Error! Reference source not found.**. This spectrum is the equivalent MRS of the area indicated by the white square in the brain MRI image and is acquired by a Point RESolved Spectroscopy (PRESS) sequence.

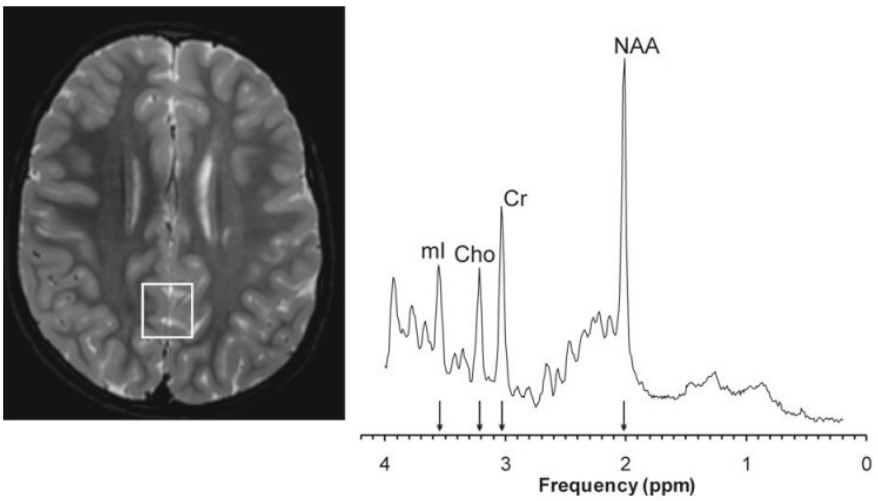

Figure 1.29 [Left] Brain MRI [Right] Spectrum of the highlighted voxel acquired by PRESS sequence MRS. [127]

The magnitude of each peak corresponds to the strength of the signal from that particular metabolite and therefore its abundance, or lack of, in the ROI. The position along the frequency axis refers to the chemical shift difference, δ, and is measured in parts per million (ppm) relative to a particular reference:

$$\delta = \frac{f_{sample} - f_{reference}}{f_{reference}}$$

Equ 1.24

The chemical shift is therefore a dimensionless property of each nucleus attached to a specific compound, and ppm is simply another way of saying $\times 10^{-6}$. In this spectrum (as in all ^{1}H MRS) the

signal from water has been suppressed – if not, it would have been present at 4.7ppm, but with a magnitude several orders of magnitude more than any other metabolite.

Note that large voxels are used compared to MRI due to the low concentrations of the metabolites to be measured (in the range of 1-5 $cm^{3,}$ compared to MRI with voxel size 1-5 mm^3) [128]. This means that the spatial localisation of MRS is not as accurate as MRI and highlights the need for higher SNR, even for MRS.

1.5.1 Phosphorus MRS

It is useful to perform spectroscopy for nuclei other than Hydrogen to give information about different metabolic compounds in the body. The second most used MRS is ^{31}P, where the $\mathbf{B_1}$ field applied rotates with a frequency of 25.8MHz for a 1.5T MR scanner. ^{31}P MRS provides unique information about cell membranes, bioenergetics and pH. The abundance of ^{31}P is 100%, meaning that all phosphorus is present in this state in the body. This an advantage when performing spectroscopy; however, its relative sensitivity is 0.07 which means that under the same conditions, it would give a signal weaker than that given by ^{1}H MR by a factor of 0.07. Fortunately, this is increased using a technique called Nuclear Overhauser Enhancement (NOE). Furthermore, since now a lower resonance frequency is required, additional hardware is needed to make an MRI machine able to carry out ^{31}P MRS.

1.5.2 Detecting Ischemia and Oedema

We have previously alluded to the importance of good blood flow in the healing of colorectal anastomosis [99], [129]. By extension, the presence of blood constriction or ischemia thus indicates a high risk of anastomotic failure. It has been shown that it is possible to detect ischemia using MRS and in a study [130] of an anaesthetized rabbit with complete superior mesenteric artery occlusion, distinct changes in peak amplitude and chemical shift of the ^{31}P spectrum were observed. The superior and inferior mesenteric arteries are the main vessels supplying blood to the colon, and so by blocking the superior mesenteric artery, ischemia is induced. In the study of [130], an array of custom coils for transmit and receive are used to carry out several sequences of MRIS (Magnetic Resonance Imaging and Spectroscopy). The main results are discussed below.

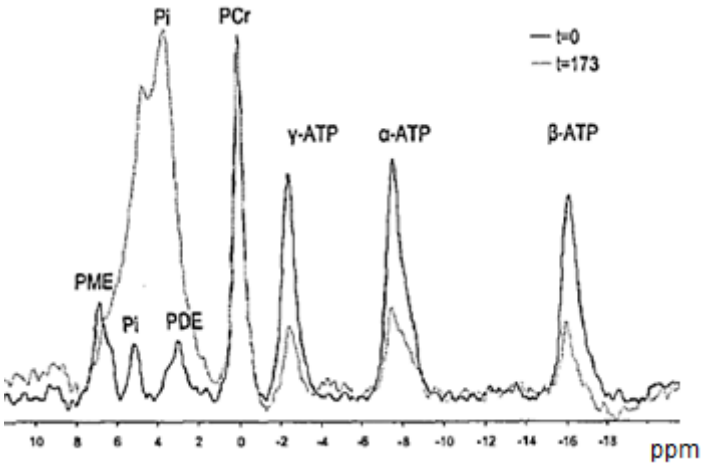

Figure 1.30 ^{31}P Spectrum before and after the onset of ischemia. [130]

In Figure 1.30, the ^{31}P MRS spectrum is shown before ischemia and after 173 minutes of the onset of ischemia. Using the PCr (phosphocreatine) as the reference at 0 ppm, there is a clear shift and magnitude change of the Pi (inorganic phosphate), as well as an amplitude change in all three ATP (adenosine triphosphate) peaks. Using the difference in Pi chemical shift, the change in pH can also be calculated as a decrease to 6.93 from 7.33. In a different study [131] it was shown that a pH less than 7.28 is indicative of a higher risk of AL by 22 times. Now using ^{1}H MRS, the lactate levels are also measured. As seen in Figure 1.31, the largest difference occurs 30 minutes after the onset of ischemia, following this, they start returning back to normal, but have not yet reached their pre-ischemic levels after 2 ½ hours.

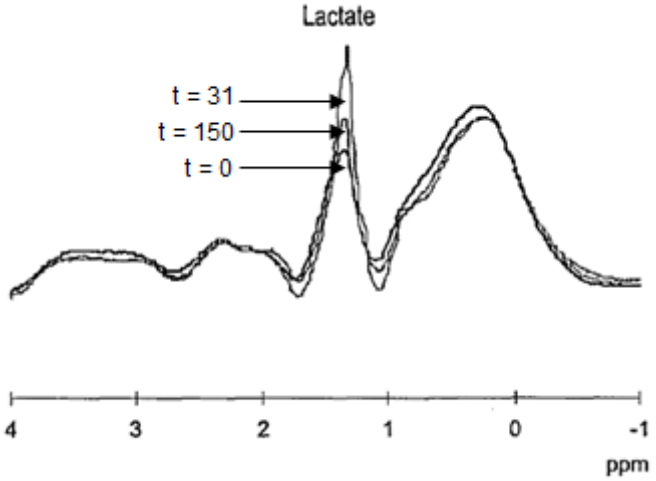

Figure 1.31 ^{1}H Spectrum before the onset of ischemia, after 31 minutes and after 2 ½ hours. [130]

These two MRS methods – with the aid of an internal coil – could therefore be used to detect ischemia at and around the anastomotic wound, which would indicate a high risk of AL. Furthermore, the same study shows an increase in the colon wall thickness by 0.2 mm. This is oedema (tissue swelling) which is also characteristic of ischemia. However, unlike the previous results, this difference is very

small and does not have a clear reference, additionally, slight oedema usually occurs after tissue manipulation as in an anastomosis operation. Nevertheless, the structural integrity of the anastomosis, as well as pooled gases and fluids, could be seen using MRI with an internal coil. Finally, using modern MR thermometry techniques [132], [133], the temperature at and around the anastomotic wound can be measured: an increased temperature indicates infection which again increases the risk of AL. MR thermometry is achievable using the usual MRI techniques, based on temperature sensitive MR parameters – such as proton resonance frequency, proton density, and T1 and T2 relaxation times – as well as temperature sensitive contrast agents [132].

1.6 Research Objective

In this introduction, we have described how colorectal anastomosis is an important and frequently used procedure in the elective and emergency settings. However, anastomotic leakage (AL) is a common major complication, associated with high morbidity and mortality. Even though a combination of clinical and radiological methods is used for the diagnosis of AL, this has not reduced the complication rates in nearly 30 years of research. It is therefore evident that a new method of predicting and diagnosing AL is needed. Currently MRI and MRS do not possess a high enough SNR to do this; however, using an internal coil, placed near the anastomotic wound, the SNR in this area could be increased enough such that oedema and structural integrity are visible in an MR image, ischemia and pH are detected using MRS, and tissue temperature is measured using MR thermometry. The aim of this research is therefore to design and implement such an internal coil.

Compression rings such as the Biodegradable Anastomosis Ring (BAR) are placed directly on the anastomotic wound and therefore provide the perfect vehicle for such a sensor. Bearing in mind the shape of the anastomotic wound, an annular sensor would be best, and fortunately one already exists. The magneto-inductive (MI) Ring, shown in Figure 1.32 is an electrical resonator formed from a number (here, 8) of identical inductively coupled loops, L, each loaded with a capacitor, C.

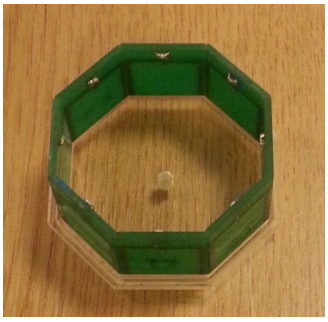

Figure 1.32 Magneto-inductive ring made from 8 inductively coupled loops[4].

[4] MI ring constructed in Chapter 3 of this thesis.

The MI ring is a periodic structure of magnetically coupled resonators that support the propagation of backward waves called MI waves. Its shape, and the fact that it is made from individual elements that are not mechanically connected, make it the perfect candidate to be used as an internal coil for the enhancement of MR signals: It will fit well within the BAR and will disintegrate and be excreted at the same time. It can be inserted at the same time as the BAR – during the initial anastomosis operation – thus eliminating the need for further exploration. The aim of this research is thus to develop an MI Ring device to be embedded in the BAR for the monitoring of colorectal anastomosis, potentially predicting anastomotic leakage. The ring should detect ^{1}H MRI signals, and must therefore be tuned to the correct frequency (63.85 MHz for 1.5 T and 127.74 MHz for 3 T). However, it must as far as possible avoid coupling directly to the $\mathbf{B}_1$ field (to avoid artefacts and ensure patient safety). To satisfy this additional condition, a more complex double ring device is developed.

The plan of this thesis is as follows. In Chapter 2, we first review some of the internal MRI coils in use and in development, including those utilizing metamaterials and MI waves. In Chapter 3, we develop a suitable device design using analytic theory, numerical simulations and simple experiments. In Chapter 4, we explain how the design can be modified to increase the rejection of unwanted fields and demonstrate a prototype fabricated from flexible thin film printed circuit boards. In Chapter 5, we show how the field of view can be calculated. Finally, in Chapter 6, the device is made MR safe and evaluated in 1.5 T and 3.0 T magnetic fields. MR images are obtained, and used to calculate the SNR improvement offered by this internal coil and to compare its field-of-view to the theoretical predictions.

The work in this research has resulted in the following publications:

H. Kamel, R. Syms, E. M. Kardoulaki, and M. Rea, “Metamaterial MRI-based Surgical Wound Monitor,” in *11th International Congress on Metamaterials*, 2017, pp. 106–108.

H. Kamel, R. R. A. Syms, E. M. Kardoulaki, and M. Rea, “Surgical wound monitoring by MRI with a metamaterial-based implanted local coil,” *EPJ Appl. Metamaterials*, vol. 5, no. 5, 2018.

2 Literature Review

In this Chapter internal RF coils, developed to improve the SNR of MR images, are reviewed and a brief assessment of the challenges in coil design is made. These include taking account of RF heating and extraction of the implanted coil from the body. These problems are eliminated by the use of magneto-inductive (MI) cables and rings. Examples of MI wave applications in MRI are thus presented then the background theory needed to design an MI ring resonator is described.

2.1 Internal Coils for MRI

Most RF receiver coils used for MRI can be represented by the equivalent circuit shown in Figure 2.1 (a). Here, we have an inductor, L, representing the coil. This is made resonant by connecting a capacitor, C, in series with it. This resonant LC circuit is tuned to the Larmor frequency, f_L, to allow it to couple to the rotating dipoles inside the body. The magnetic field generated by the precessing dipoles will therefore induce a voltage, V_s, in the loop. The resistance, R, is due to the resistivity of the coil windings and the voltage source being a lossy dielectric.

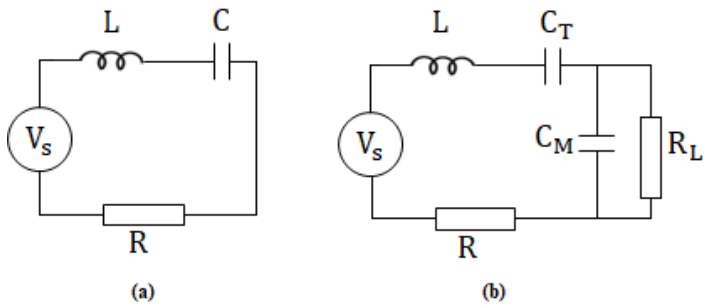

Figure 2.1 (a) Simplified equivalent circuit for an MRI RF receiver coil (b) with capacitive matching

The circuit is usually tuned by changing the value of the capacitor to achieve the required f_L as per Equ 2.1.

$$\omega_L = 2\pi f_L = \frac{1}{\sqrt{LC}}$$

Equ 2.1

To transfer all of the signal to the MR scanner, the output of the circuit has to be matched to the load. This can be done using capacitive matching as seen in the current divider circuit of Figure 2.1 (b). Here the capacitor, C, is separated into C_T and C_M – the tuning and matching capacitors respectively. The matching criterion states that the output impedance of the circuit has to equal R_L. We therefore have the relationship of Equ 2.2, from which we can find the value of C_M.

$$C_M = \frac{1}{\omega_L \sqrt{RR_L}}$$

Equ 2.2

C_T can then be calculated to satisfy Equ 2.1 such that C is the capacitors C_T and C_M in series:

$$\frac{1}{C} = \frac{1}{C_T} + \frac{1}{C_M}$$

Equ 2.3

The process of matching and tuning is usually done experimentally and other matching circuits exist for different coil configurations [134].

Internal coils for MRI offer higher SNR improvement over surface coils due to their proximity to the region of interest [115], [135], [136] . They are introduced into the body using a natural orifice and can then be retracted and re-used once properly sterilized. Examples include intravascular catheter coils [137]–[139], endoanal coils [140], endorectal coils [141], cervical coils [142] and gastro-intestinal coils [143]–[145]. Some coils are mounted on existing medical devices such as endoscopes [144]–[148] and colonoscopes [149] to offer enhanced MR imaging as well as the usual optical imaging. On the other hand, wireless implanted coils are also being developed for higher resolution brain [150], [151] , spinal cord [152] and blood vessel [153] images. In these cases, the coils are inductively coupled to an external matching circuit that is then connected to the scanner [154].

2.1.1 Coil Design: Shape and Size

There are many considerations when designing an internal coil [155]. Firstly, the shape and size of the coil; the former is usually cylindrical due to the orifice through which the coil is inserted. As for the dimensions, they are a compromise between anatomical considerations and the required extent of the coil field of view – the smaller the coil, the smaller the FOV will be. For the intravaginal coil [142] in Figure 2.2 both a saddle coil and solenoid were considered, but a solenoid was chosen for easier manufacturing. Several coil diameters were tested and a 38 mm diameter was found to offer the best solution for both ease of insertion and having a high fill factor. In this case, the tissue inside the coil represents the region of interest, but some surrounding tissue can also be seen due to the peripheral field of the coil.

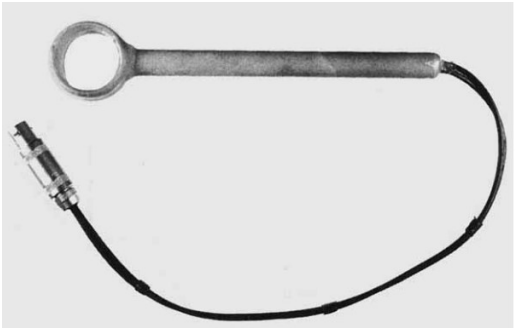

Figure 2.2 Intravaginal receiver coil for imaging the cervix [142]

For other coils, such as the endoanal coil [140] in Figure 2.3 (a), it is the surrounding tissue that is of interest. Coils made for imaging the surrounding tissue are called 'inside out' coils. Here this is a saddle coil, 75 mm long and 9 mm in diameter. As seen in Figure 2.3 (b), the signal received is highest adjacent to the coil and decreases radially becoming negligible 5 cm away.

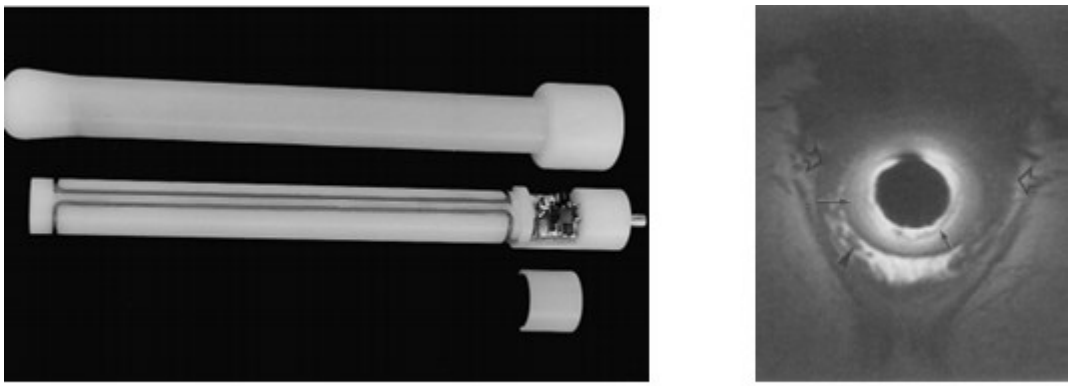

Figure 2.3 (a) Endoanal coil for imaging the anal sphincter [155] **(b) T1 weighted transverse image of a normal patient obtained in a 0.5 T scanner with the endoanal coil** [140]

Another coil design frequently used is that of the elongated loop, such as used for the endoluminal coils [143] shown in Figure 2.4 (a). These are used for imaging the walls of the GI tract and have a field of view similar to the saddle coil above. Several dimensions are investigated, as well as single and double loops and single and double layered PCBs. Keeping other variables constant, it is found that the shortest coil offers the best SNR due to its decreased resistance; and that the double loop and the double layered coils offer better penetration depth. In this experiment, the coil is also combined with a 4-element phased array coil in order to increase the signal strength and uniformity outside the field-of-view of the coil. Figure 2.4 (b) shows an MR image of a rabbit colon obtained with the combination of the phased array externally and the longest loop internally. Here the signal enhancement offered by the internal coil is clearly seen.

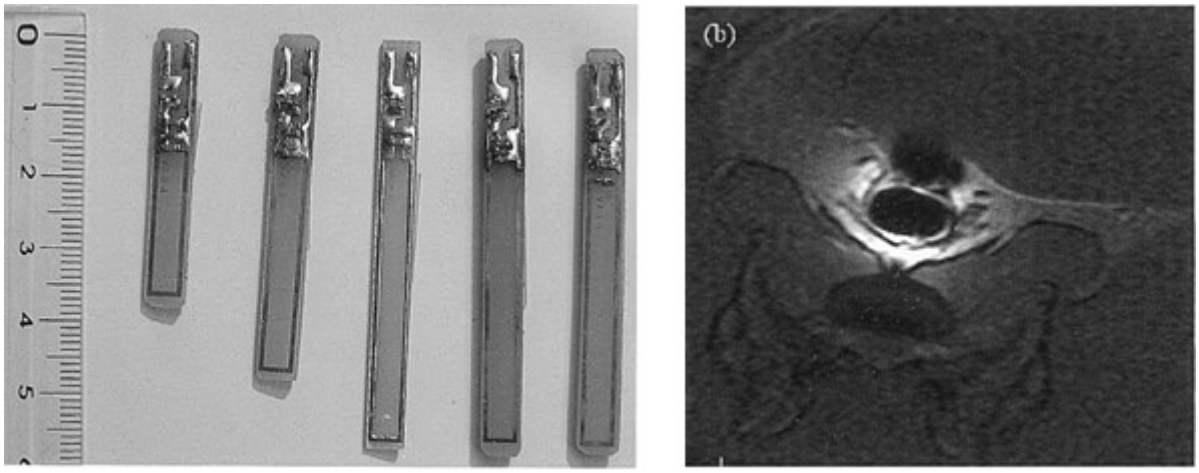

Figure 2.4 (a) Elongated loop coils, from left to right 20-, 30-, and 40 mm single loop coil, double layer and double loop coils (b) T1 weighted MR image of a rabbit colon obtained with a 4-element phased array coil associated with a 40 mm length simple loop coil [143]

Increasing the signal strength and uniformity outside the small field-of-view offered by the internal coil is sometimes needed in applications where greater spatial coverage is needed. To do this, the internal coil can be combined with an external multi-coil array, such as done with the endorectal coil of [141]. Figure 2.5 (a) shows the endorectal coil associated with the external array coil and Figure 2.5 (b) shows three MI images taken with the internal coil, then array coil and both coils respectively. Here it is seen how using both coils offers an clear advantage: the larger field-of-view means that the bladder and prostate can also be seen in the same image, saving the time and cost of acquisition of two sequences.

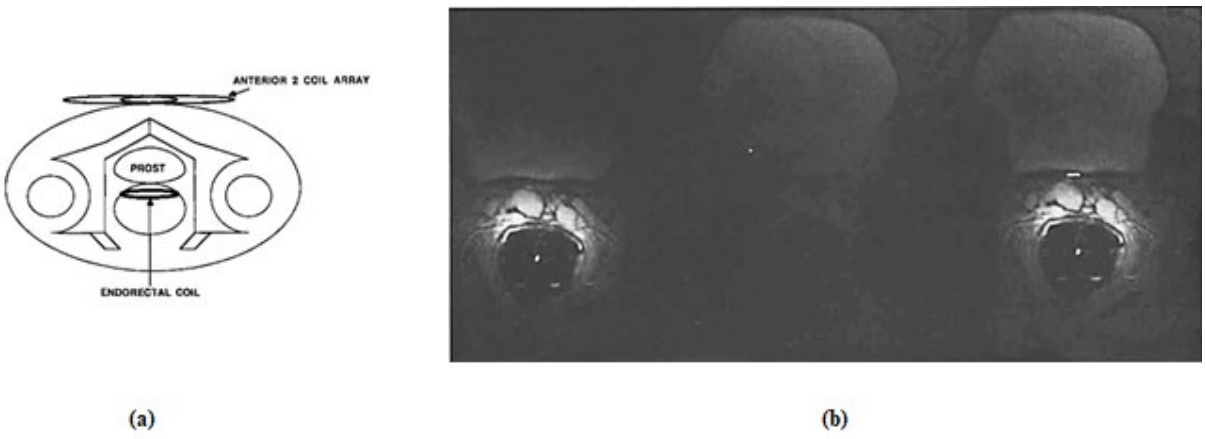

Figure 2.5 (a) Diagram showing the endorectal coil associated with the external array coil. (b) Comparison of MR images acquired with the internal coil alone, the external array coil alone and both together respectively [141]

The coils seen so far are matched and connected to the scanner directly. Wireless internal coils are made possible using an inductive matching circuit as seen in Figure 2.6. Here the left part of the circuit is the internal coil, made resonant at f_L using Equ 2.1 as previously described. The right part of the circuit, the external coil, is also made resonant using L' and C', and the impedance matching

criterion is achieved by satisfying the relationship of Equ 2.4 where M is the mutual inductance between the two parts of the circuit, adjusted by changing the position of the external circuit.

$$M = \frac{1}{\omega_L \sqrt{RR_L}}$$

Equ 2.4

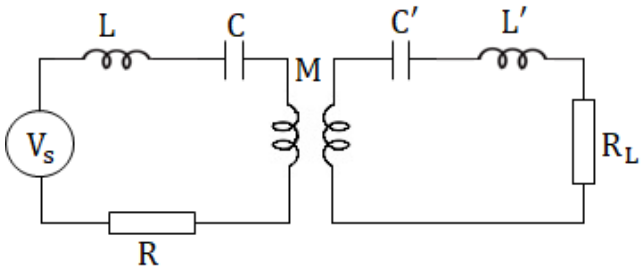

Figure 2.6 Equivalent circuit of mutual inductive matching

Such an inductive matching circuit is used in the implanted RF coil of [156] used to monitor spinal cord injury. The implanted coil is saddle-shaped, tuned using two capacitors and the external coil is rectangular, etched on a standard PCB and tuned using a single capacitor. The authors report that throughout the study period of two months, the implanted coil worked well and remained matched to the external coil. However, there was a slight frequency shift that did not affect performance.

To overcome expected frequency shifts and allow the tuning and matching of the implanted coil to be modifiable after implantation, overcoupling to an external coil with tuning and matching capabilities can be used [152]. The system is shown in Figure 2.7 where SC refers to the secondary coil (implanted coil) and PC refers to the primary coil (tuning and matching coil).

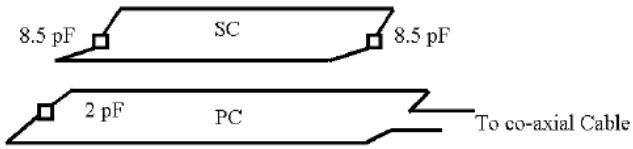

Figure 2.7 Mutual inductive matching with an internal coil (SC) and an external coil (PC) [152]

When each coil is tuned individually to the desired resonance frequency (400 MHz in the case of a 9.4 T static field), the current response in each coil depends on the coupling strength between them. This is seen in the plots of Figure 2.8 (a) and (b). As the coupling increases, the resonant current in the matching coil (I_p) decreases and its peak broadens until it eventually splits, becoming two individual peaks. At the same time, the current in the implanted coil (I_s) increases, also broadening, and again becomes two individual peaks. Overcoupling refers to the condition beyond which the peak of the current in the implanted coil (I_s) splits.

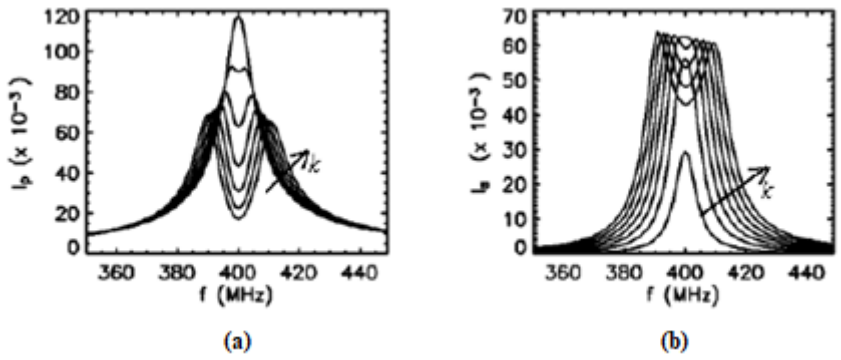

Figure 2.8 Current response of (a) external coil (b) internal coil with increased coupling

Tuning the implanted coil can now be done by tuning the matching coil and working with either the first or second resonant peak after splitting. If the first peak is required for operation (the lower frequency resonance) each individual coil is tuned to a frequency a little higher than the desired resonant frequency, then when the coils couple and the initial peak splits, the location of the first resonance can be modified by manipulating the coupling between the two coils. If the second peak is desired for operation (the higher frequency resonance), the coils are tuned to a frequency a little lower than the desired resonance frequency and the same method is used to tune the implanted coil by manipulating the coupling between the coils. This method could prove useful in our application in the future, since the sensor has to be completely implanted in the patient and being wireless is a great advantage to patient comfort and acceptance of the device.

2.1.2 Coil Design: MR compatibility

Apart from the shape and size of the coil, another important consideration is the coil's compatibility with the MR scanner. The coil itself is usually made from copper and wound round a homopolymer former (such as Delrin™ [145]), both of which are non-magnetic. However, care has to be taken when choosing the capacitors since most surface mount capacitors are magnetic and produce image artefacts. Gold, silver or palladium terminators have to be used for MR compatibility [157]. When mounting the internal coil on an existing medical device, the device also has to be non-magnetic and suitable for use inside an MR scanner. For example, for internal coils used during GI endoscopy [145], [146] a non-ferromagnetic endoscope had to be especially made for the experiments. Similarly with the non-ferromagnetic colonoscope used as a vehicle for the internal coil in [149].

Another important consideration for MR compatibility (and patient safety) is decoupling the internal coil from the B_1 field of the MR scanner. Since the coil is tuned to the Larmor frequency of the rotating dipoles, it resonates at the same frequency as the RF excitation pulses. This means that the coil would couple to these pulses, potentially causing RF heating and image artefacts. B_1 field decoupling is therefore very important and can be done using a passive [158] or active circuit [159].

For the intravaginal coil previously mentioned [142], a passive circuit is used for lower magnetic fields, while an active circuit is used for the higher magnetic field strength. The equivalent circuits are shown in Figure 2.9 (a) and (b) respectively.

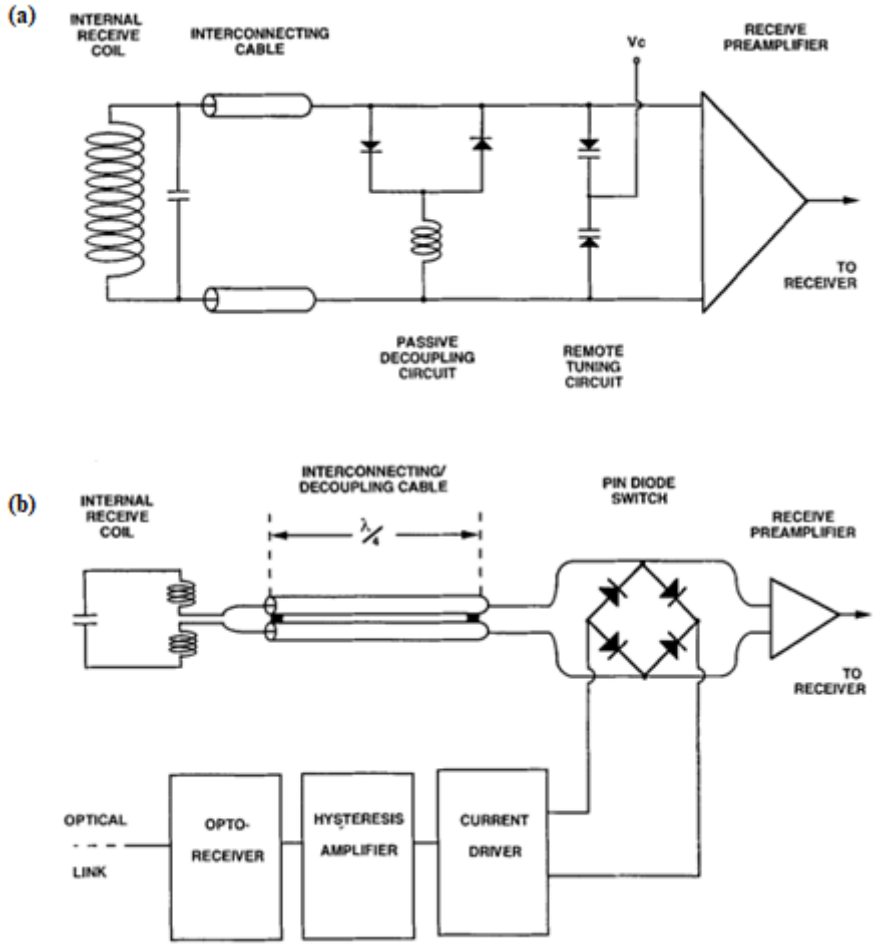

Figure 2.9 Decoupling circuits (a) Passive used with 0.15 T MRI (b) active used with 1.6 T MRI [142]

In the passive circuit, an inductor and a pair of PIN diodes are connected across from the tuning capacitor. During excitation, a high current will flow through the inductor and the diodes will be conducting, making the inductor parallel to the tuning capacitor, effectively forming a tank filter. Conversely, during detection, the induced current is low and so the diodes remain non-conducting and the decoupling inductor is open circuit, returning normal function to the LC resonator. In the active decoupling circuit, a length of coaxial cable is used, acting as an inductor when short-circuited at its end by the PIN diode switch. This happens during excitation; whilst during detection, the switch is open and the cable is connected directly to the preamplifier (Here the cable's characteristic impedance has to match the load impedance to avoid reflections through the system). Note that the active decoupling circuit can also be constructed from a decoupling inductor, similarly to the passive circuit. However, in this case, the inductor is put in series with the output and the PIN diode switch is put

across the output. Other decoupling methods, specific to certain designs are available and discussed in section 2.2.

Another important consideration of MR compatibility is induced RF heating in the wires. This has been modelled in [160], where it was found that if a bare wire is longer than 20 cm (half the wavelength for 1.5 T MRI) then the induced heating will be at a maximum. On the other hand, if the wire is insulated, the induced currents cause the temperature rise to increase with increasing wire length. In [161] the authors predict the absolute temperature of the heating of wire tips to formulate a safety margin. It is proposed that a limit is set on the specific absorption rate (SAR) to limit the temperature increase in tissue. Engineering solutions have also been proposed to eliminate RF heating. For example, in [162] , it is stated that the use of a cable length less than a quarter wavelength will induce negligible heating; however, when short cables are not possible, a coaxial cable design with embedded resonant circuits could be used. Here the cable is divided into small sections, each made resonant by a capacitor such that at the operating frequency, the cable acts as an open circuit. Cable segmentation has also been proposed in [163] where transformers are placed along the transmission line, splitting it into several short non-resonant segments. In [164] it is shown that this arrangement, of periodically interrupted transmission lines by isolation transformers, is in fact a form of metamaterial supporting magneto-inductive waves. These special waves are discussed in detail in sections 2.2 and 2.3.

2.1.3 Coil Design: Orientation

The orientation of the coil with respect to the B_0 field greatly affects its field-of-view, since the B_0 field determines the direction of the rotating dipoles. With the intravaginal [142] and endoanal coils [140] the natural anatomy of the human body allows them to be parallel to the B_0 field. However, other coils, such as endoscopic coils [144]–[146], [149], may be perpendicular to the B_0 field and therefore potentially receive no signal at all. One solution is to use an array of coils such as that for the endorectal array in [165]. Here two single-loop coils are used in different orientations, positioned along the MR machine's z-axis (parallel to the B_0 field). It is indeed confirmed that this set-up produces a higher SNR than a single coil, as seen by the plot in Figure 2.10.

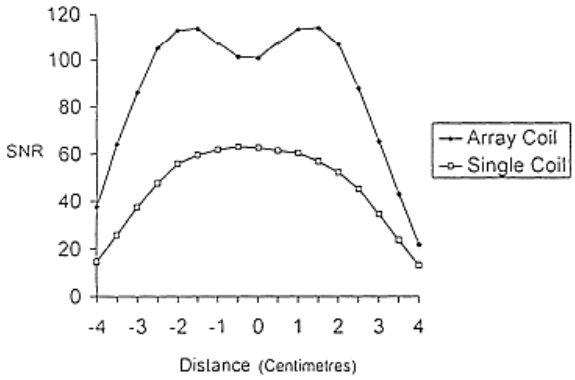

Figure 2.10 SNR of the single coil and array coil in the transverse plane [155]

Although the SNR drops where the two coils meet (at distance 0), it is still higher than for a single coil. If three orthogonal coils are used, then the orientation problem would be solved, but this is not always possible and is a problem that has to be investigated for our device since it will be implanted in the intestines and therefore difficult to predict its orientation.

2.1.4 Coil Design: Biocompatibility and Biodegradability

As well as being MR compatible, the internal coil has to be safe for use inside the human body. This includes having only biocompatible material in contact with human tissue. All conducting wires have to be properly insulated with biocompatible materials. This is done with epoxy resin which is water resistant. In addition, the former around which the coil is wound and any medical device upon which it is mounted have to be biocompatible. In this research, the aim is to implant the device in the patient and so biodegradability is as important as biocompatibility in order to eliminate the need for medical extraction after the monitoring period is over. In our case, the Biodegradable Anastomosis Ring (BAR) is made from polyglycolic acid and 12% barium sulphate [33]. The BAR has proven to be completely safe for use in the human bowel [47]. It is not only biocompatible, but also biodegradable, as it disintegrates and is excreted from the body in approximately 2 weeks.

The sensor to be mounted on the BAR has to degrade with it. One solution is to construct its coils from a biodegradable conducting material. A device constructed entirely of biodegradable material is the pressure sensor in [166] where the conductors are made of bilayers of zinc and iron. Both of these metals are biocompatible and corrode in the saline conditions of the human body; however, zinc on its own takes a very long time to degrade. In the study of [167], a zinc stent implanted in a rat aorta continued functioning with good performance even after six months. Having electrical bilayers of zinc with small percentages of iron achieves the desired higher Q-factors, while the iron stimulates the zinc corrosion. Another biodegradable metal considered for biodegradable implants is Magnesium [168]. However, the problem with these metals is that they are susceptible to the magnetic field of the MR scanner and so would not be possible for our application. Another solution is to use conductive

biodegradable polymers which are completely non-magnetic and MR compatible. In the study of [169], conductive nanoparticles of polypyrrole (PPy) are embedded in a biodegradable polymer matrix made from either polylactide (PLLA) or polycaprolactone (PCL). By increasing the amount of PPy to 39%, a resistivity of 0.0043 Ωm and 0.0016 Ωm is achieved for PLLA and PCL respectively. This translates to a Q-factor of 19 for an inductor diameter of 11 mm, obviously much lower than that found for copper.

2.2 Magneto-Inductive Waves

To avoid RF induced heating and the issues associated with using biodegradable materials for the sensor conductors, small coils that are not mechanically connected can be used. Arrangements of resonant elements that support the propagation of magneto-inductive waves are called metamaterial coil; these are described in this section.

Consider a set of coils each terminated by a capacitor as shown in Figure 2.11. The first coil is attached to a voltage source, V_s and the last is loaded with R_L, and a current I_n flows in each coil.

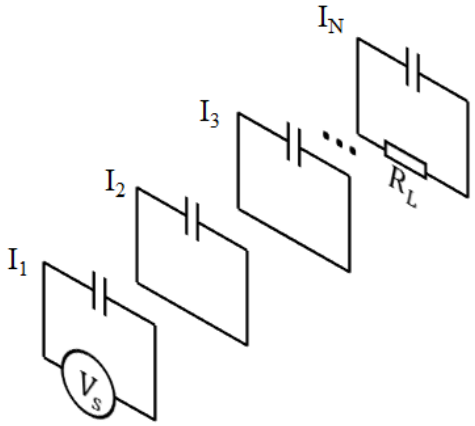

Figure 2.11 A set of coils each terminated by a capacitor

The voltage source in the first element will induce a current, I_1, to flow through it. In turn, this current will induce a current, I_2, to flow in the second element and so on. This structure can therefore be thought of as a waveguide where the 'guiding' takes place by each of the elements being coupled to all other elements [170]. Due to the magnetic coupling between the elements and the fact that it is caused by the induced voltages, the waves propagating through this waveguide are dubbed Magneto-Inductive waves (MI waves). MI waves were first discussed and theoretically analysed for an axial array in [171] and their dispersion characteristics were described. Further analyses in 2- and 3-dimensions were carried out in [172] and experimental results confirming the theoretical predictions were presented in [173]. It was then confirmed that MI waves behave in the same way as linear waves in terms of their propagation in a homogenous medium and in terms of their reflection, refraction and

diffraction [170]; however, when compared to electromagnetic waves, they are much slower, with a wavelength shorter than EM waves [174]. Many applications for MI waveguides were suggested [175]–[177] and applications in MRI are among the first and most prominent.

Even before the naming of these waves, propagating along magnetically coupled loops, their potential for use in obtaining better quality MR images was recognised. The first experiments were carried out using a hexagonal array of 19 'swiss roll' cylinders [178], where the capacitance between the turns of the spiral complete the circuit and allow current to flow. Figure 2.12 (a), (b) and (c) shows the complete hexagonal array, a single swiss roll element and the current flow through the spiral.

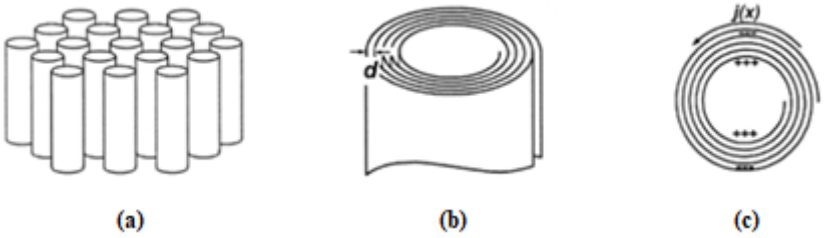

Figure 2.12 (a) The 19 element hexagonal array, (b) a single swiss roll element with separation d between the spirals, (c) cross-section of a single element and direction of current flow j(x) through the spiral. [178]

The experimental arrangement is shown in Figure 2.13 (a). Here the array of swiss rolls is used to guide the RF flux from a thumb to a small receiving coil. Figure 2.13 (b) shows an MR image taken with the body coil, with the receiving coil alone, and with the receiving coil and swiss rolls together. Comparing the last image to that taken with the body coil, there is clear signal enhancement near the tip of the thumb; thus further research into this magnetic guiding has thus been carried out [179]–[181].

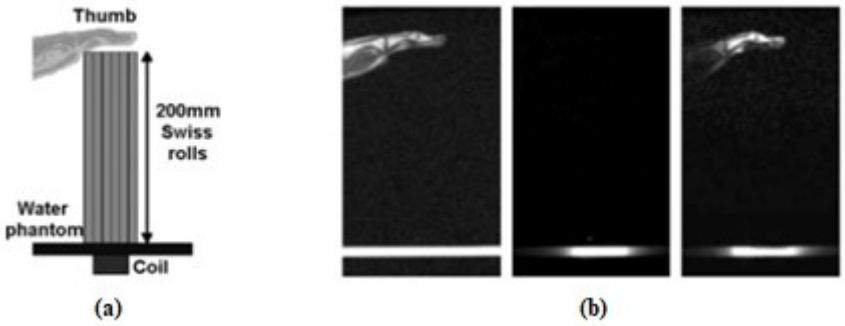

Figure 2.13 (a) Arrangement of experiment inside an MR machine, (b) results with the MR body coil, with the receiving coil alone, and with the receiving coil and swiss rolls together [178]

At the physical level, metamaterials allow a manipulation of the permittivity and permeability of electrically resonant structures. They have also been applied to other MR related research, such as the development of metamaterial lenses [182], [183] used to manipulate the spatial distribution of the RF

field or the development of parallel imaging devices [184], [185] used to achieve sub-wavelength image resolution.

Unfortunately these devices have not yet had much impact in real MRI practices. On the other hand, with the aim of producing clearer MR images and improving the diagnostic capabilities for certain diseases, MI waveguides used as catheter receivers [186], [187], with endoscope compatibility [188], [189] and MI waveguides used as duodenoscopes [190] may prove to be more attractive to the medical community. The waveguides are made of similar designs, and have equivalent circuits such as the one shown in Figure 2.14 (a), where the inductors, L, are made from copper deposited on double-sided thin-film and the capacitors, C, are made from overlapping conductive strips separated by a dielectric substrate. In Figure 2.14 (b), the grey trace represents the front of the thin film circuit and the black represents the back; and each loop has two L/2 inductors and two 2C capacitors making the required L-C circuits.

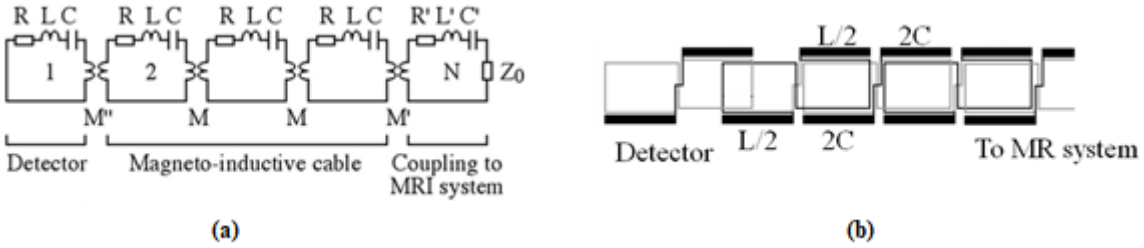

Figure 2.14 (a) Equivalent circuit of MI waveguide, (b) layout of thin film circuit [187]

The equivalent circuit is made of a detector (made from an L-C circuit), the MI waveguide itself (made from magnetically coupled L-C resonators), and a final L-C circuit which connects to the MR system. The advantage of using an MI waveguide rather than a conventional guide lies in its intrinsic patient safety since the cable is already segmented and therefore will not suffer from RF heating.

Decoupling from the B_1 field is achieved by using figure-of-eight elements [191] as seen in the layout of Figure 2.14 (b) and described in the diagram of Figure 2.15.

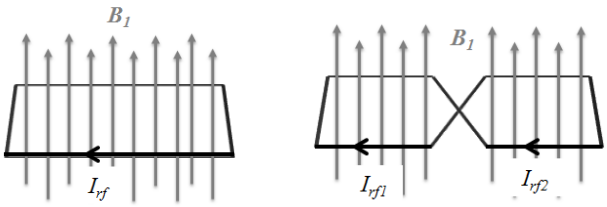

Figure 2.15 Single loop turned into a figure of eight layout

A magnetic field, B_1, through a loop will induce a current, I_{rf}, to flow in it. This coupling especially occurs if the transmit coil is larger than the receiver coil as is the case here. By replacing the single loop with a figure of eight layout, the currents induced in each loop, I_{rf1} and I_{rf2}, will be in opposite

directions and will cancel out if the areas of the new formed loops are equal and the applied B_1 field is homogenous. Thus the desired decoupling is achieved. The disadvantage here is that there will be zero sensitivity where the loop occurs as seen from the results of the MI catheter receiver of [188] shown in Figure 2.16.

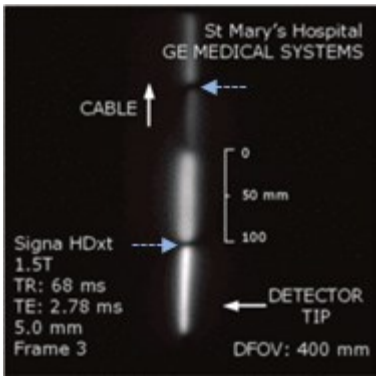

Figure 2.16 Coronal image taken with ^{1}H MRI of a cuboid phantom received with an MI catheter receiver. Dashed arrows indicate regions of zero sensitivity [188]

2.2.1 Magneto-Inductive Rings

So far, we have discussed some metamaterial devices and MI waveguides used to enhance MR images; now we consider MI rings: their first mention was in the discussion of 2D and 3D MI waveguides in [172] , and the first analysis of MI waveguides [192] came to confirm that a travelling MI wave resonance, called "rotational resonance", occurs when the circumference of the ring is equal to an integer number of MI wavelengths. The first representations of an MI ring are shown in Figure 2.17.

Figure 2.17 First representations of a magneto-inductive ring [172], [192]

Rotational resonance can be excited by a rotating nuclear dipole in the middle of the ring, and so applications to MR systems were fast suggested. However, MRS was championed over MRI due to its larger voxel size, thus potentially having a single voxel inside the MI ring. Applications to Paediatric brain MRS were suggested with 24 elements distributed round a circle with an 85 mm radius. Nonetheless, a large MI ring with flexible interconnects [193] is the first reported application of an MI

ring. Here the ring is octagonal and the flexibility allows for a larger filling factor when imaging the head, for example, which increases the sensitivity. The MI ring is shown in Figure 2.18 (a). It is made from 8 identical PCB elements with deposited copper conductors.

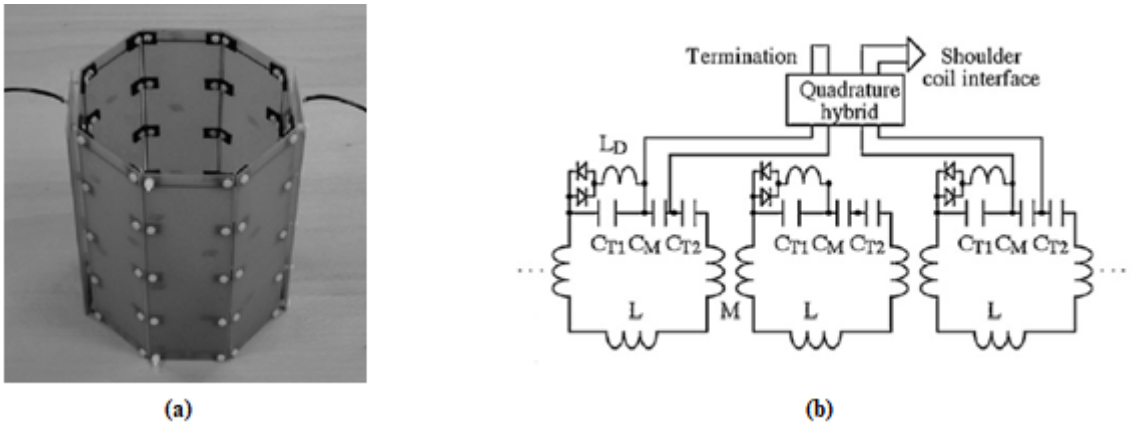

Figure 2.18 Magneto-inductive ring and equivalent circuit [193]

Its equivalent circuit is shown in Figure 2.18 (b). Here B_1 field decoupling and matching are implemented: C_{T1} and C_{T2} are used for tuning and C_M is the matching capacitor. Two taps, arranged at 90^o round the ring, are used for signal detection. The signal from each tap is combined in-phase since this provides greater uniformity than a single tap. Passive decoupling, by use of a diode-switched tank filter, is used to decouple from the excitation field.

2.3 MI Waves Theory

Having discussed applications of MI waves in improving the SNR of MR images, it is clear how they offer an advantage over conventional devices, especially with regards to eliminating RF heating, and being small enough to be biofragmented when manufactured on thin-film. In this section, some background theory [194], [195] needed for the implementation of the MI ring device is discussed. This is in preparation of the theoretical and experimental analysis of MI ring resonators in Chapter 3.

2.3.1 MI Waveguides

Planar and axial one dimensional arrays composed of N capacitively loaded loops are shown in Figure 2.19 (a) and (b). The loops are magnetically coupled to each other due to the magnetic field of each element coupling to the next and inducing a current to flow through it. Usually the elements are identical and spaced evenly, but their dimensions and the distance between them, a, is not very important so long as it is less than the wavelength of the excitation RF field. For a 1.5T MR ^{1}H scanner, the excitation frequency is at 63.85 MHz, therefore the approximate[5] wavelength is 53.5 cm.

[5] Assuming the dielectric constant of the human body to be 77.

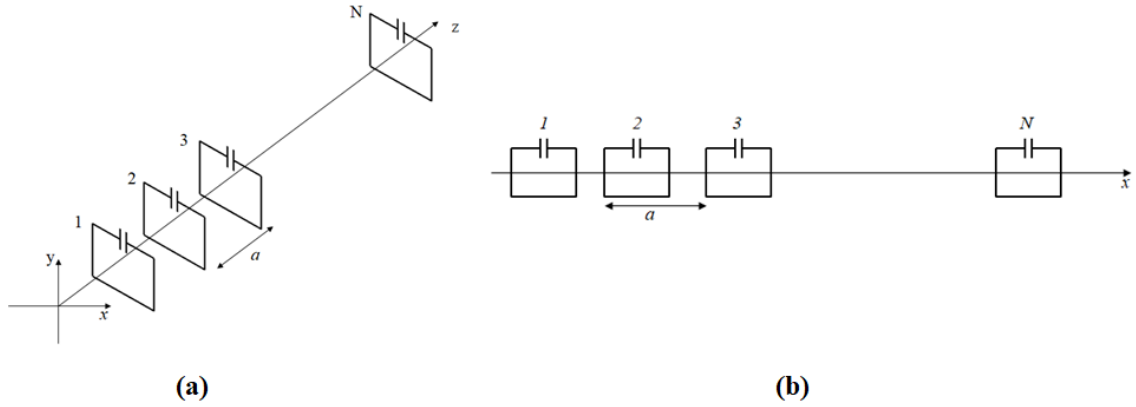

Figure 2.19 (a) Axial, (b) planar array of magnetically coupled elements

What is interesting about MI waves is that the dispersion characteristics of the wave flowing round the elements can be changed by manipulating the elements' dimensions, the distance between them, their arrangement and their resonant frequency. For example, in [196], alternating elements of the waveguide are made to have differing capacitors resulting in differing resonant frequencies. Theoretical and experimental analysis of such planar and axial configurations show that they allow the propagation of forward and backward MI waves in the lower and upper frequency bands respectively independent of their configuration. Another example, in [197], is the relative shifting between two coupled one dimensional MI waveguides. Here it is shown that the transmission of power from the input of one array to the output of the other is maximum when there is a shift of a half-a-period.

In this section, we show the derivation of the dispersion equation for one dimensional MI waveguides, followed by that for MI ring resonators in the next section. Consider three capacitively loaded loops, and their equivalent circuit, such as shown in Figure 2.20 (a) and (b). Here the period between the loops is a, L is their self-inductance and C is the capacitance. Using Kirchoff's Voltage Law (KVL), we can show that the magnetic coupling between the loops leads to the propagation of MI waves. Note that here we are ignoring losses.

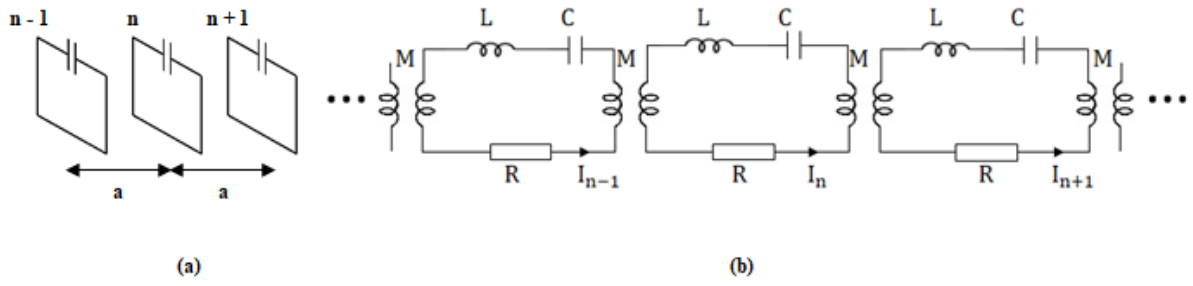

Figure 2.20 (a) Three capacitively loaded loops and (b) equivalent circuit of infinetly long waveguide

We first consider only nearest-neighbour interactions, and so when considering the voltage in element n, we account only for the currents in loops n, n-1 and n+1, and thus we have three contributions: (a)

the self-voltage $I_n Z_0$ where $Z_0 = j\omega L + \frac{1}{j\omega C}$ is the self-impedance of the loop, (b) the voltage due to the mutual inductance between elements n and n-1 equal to $j\omega M I_{n-1}$, (c) and a similar voltage due to element n+1 equal to $j\omega M I_{n+1}$. Thus we obtain

$$Z_0 I_n + Z_m (I_{n-1} + I_{n+1}) = 0$$

Equ 2.5

Where $Z_m = j\omega M$ is the mutual impedance. We assume a travelling wave solution, and so

$$I_n = I_0 \exp(-jnka)$$

Equ 2.6

Where I_0 is the magnitude of the wave and k is the propagation constant. Now, substituting Equ 2.6 into Equ 2.5, we get

$$Z_0 I_0 \exp(-jnka) + Z_m I_0 [\exp(-j(n-1)ka) + \exp(-j(n+1)ka)] = 0$$

Equ 2.7

Which with some algebraic manipulation becomes

$$Z_0 + Z_m 2\cos(ka) = 0$$

Equ 2.8

Now substituting for the impedances, we get

$$j\omega L + \frac{1}{j\omega C} + j\omega M 2\cos(ka) = 0$$

Equ 2.9

Divide by $j\omega L$ to get

$$1 - \frac{{\omega_0}^2}{\omega^2} + \kappa \cos(ka) = 0$$

Equ 2.10

Where ω_0 is the resonance for a single element and is equal to

$$\omega_0 = \frac{1}{\sqrt{LC}}$$

Equ 2.11

And κ is the coupling coefficient between two nearest neighbour elements, equal to

$$\kappa = \frac{2M}{L}$$

Equ 2.12

Thus the dispersion relationship is as shown in Equ 2.13. It can be seen that the relationship between frequency and wave number depends only on the coupling coefficient, κ, which can be altered by changing the distance between the elements and their dimensions.

$$\frac{\omega}{\omega_0} = \frac{1}{\sqrt{1 + \kappa \cos(ka)}}$$

Equ 2.13

Figure 2.21 shows a plot of the dispersion diagram for $\kappa = \pm 0.1$. Whether the coupling coefficient is positive or negative depends on the mutual inductance being positive or negative respectively. This in turn is affected by the arrangement of the elements. The mutual inductance is negative for a planar array and positive for an axial one.

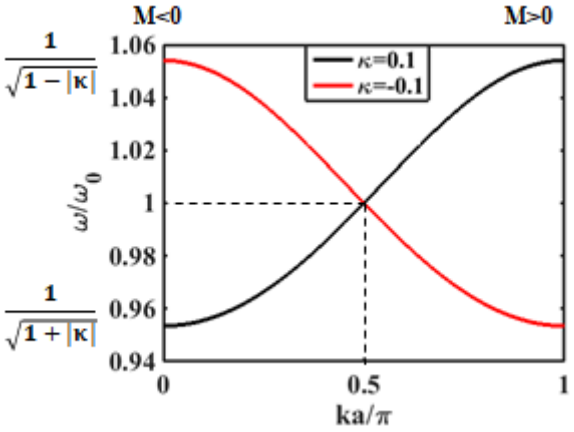

Figure 2.21 Dispersion diagram for an MI waveguide, with κ = 0.1 and -0.1

Notice that for positive mutual inductance, there is a passband for MI waves in the range shown in Equ 2.14.

$$\frac{\omega_0}{\sqrt{1 + |\kappa|}} < \omega < \frac{\omega_0}{\sqrt{1 - |\kappa|}}$$

Equ 2.14

In the presence of losses, the self-impedance of a single element becomes

$$Z_0 = j\omega L + \frac{1}{j\omega C} + R$$

Equ 2.15

where R is the resistance. k also now has a real and imaginary part

$$k = k' - jk''$$

Equ 2.16

Where k' is the propagation constant and k'' is the attenuation coefficient due to losses. Following the same method as before, we now find that KVL gives

$$j\omega L + \frac{1}{j\omega C} + R + j\omega M\, 2\cos((k' - jk'')a) = 0$$

Equ 2.17

Which after dividing by jωL and using some trigonometric identities becomes

$$1 - \frac{{\omega_0}^2}{\omega^2} - j\frac{R}{\omega L} + 2\kappa\cos(k'a)\cosh(k''a) - 2\kappa j\sin(k'a)\sinh(k''a) = 0$$

Equ 2.18

Now we separate the real and imaginary parts in Equ 2.19 and Equ 2.20 respectively.

$$1 - \frac{\omega_0^2}{\omega^2} + \kappa\cos(k'a)\cosh(k''a) = 0$$

Equ 2.19

$$\frac{1}{Q} - \kappa\sin(k'a)\sinh(k''a) = 0$$

Equ 2.20

Where $Q = \frac{Q_0\omega}{\omega_0}$ and $Q_0 = \frac{\omega_0 L}{R}$ is the quality factor of the individual single element. We can approximate the dispersion characteristics by assuming the losses are small enough, meaning the Q factor is large, then $\cosh(k''a) \approx 1$ and $\sinh(k''a) \approx k''a$; and so Equ 2.19 approximates to the no loss case, and the losses can now be calculated from Equ 2.21. Here, it can be seen that when the coupling coefficient, κ, and the Quality factor, Q, are large, the attenuation is small. Additionally, considering the change with k'a, we notice that attenuation is minimum at the resonant frequency and increases towards the band edges, nearing $k'a = 0$ and $k'a = \pi$. At these values, however, the approximation breaks down, since the attenuation is not infinitely large.

$$k''a = \frac{1}{\kappa Q\sin(k'a)}$$

Equ 2.21

Equ 2.19 and Equ 2.20 have been numerically plotted in Figure 2.22 (a) and (b) for κ = 0.1. Here it can be graphically seen that both the phase change and the attenuation vary rapidly near the band edges, and elsewhere the dispersion behaviour is very similar to that seen in Figure 2.21, when no losses are taken into account. These results have been experimentally verified in [173] for both an axial and planar configuration.

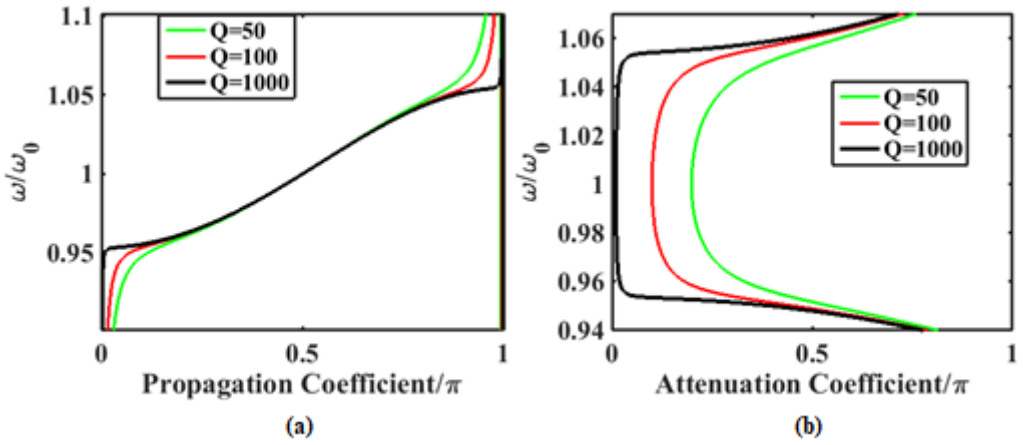

Figure 2.22 Dispersion diagrams with losses for axial configuration with κ = -0.2 (a) variation with propagation coefficients, (b) variation with attenuation coefficient

So far we have only taken into account nearest neighbour approximations. We now need to take into account higher order interactions [198], since they have an impact on the dispersion relationship when the elements are very close together. We consider an infinitely long MI waveguide as shown in Figure 2.20 (b). KVL analysis gives:

$$Z_0 I_n + Z_m(\ldots + I_{n-3} + I_{n-2} + I_{n-1} + I_{n+1} + I_{n+2} + I_{n+3} + \cdots) = 0$$

Equ 2.22

Which after substituting the corresponding impedances becomes:

$$j\omega L + \frac{1}{j\omega C} + R + j\omega 2M_1 \cos((k' - jk'')a) + j\omega 2M_2 \cos(2(k' - jk'')a) + j\omega 2M_3 \cos(3(k' - jk'')a) + \cdots = 0$$

Equ 2.23

And so, assuming losses are small as before, we get the dispersion relationship shown in Equ 2.24 and the losses equation shown in Equ 2.25.

$$\frac{\omega}{\omega_0} = \frac{1}{\sqrt{1 + \sum_m \kappa_m \cos(mk'a)}}$$

Equ 2.24

$$k''a = \frac{1}{\sum_m \kappa_m Q_m \sin(mk'a)}$$

Equ 2.25

Figure 2.23 (a) and (b) shows a FastHenry model of an eight element MI waveguide with a planar configuration and axial configuration respectively. Here each element is a 10 × 10 square coil with a width of 0.5 mm and thickness of 35 μm. The separation between the planar coils is 0.5 mm, while that between the axial coils is 5 mm.

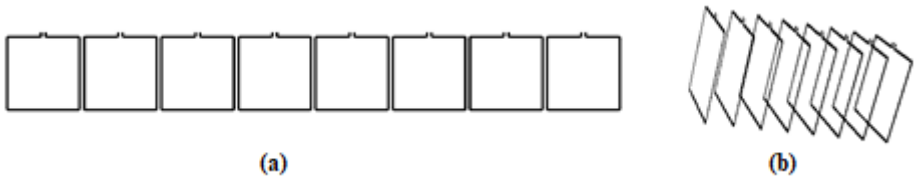

Figure 2.23 FastHenry model of 8-element MI waveguides with a (a) planar configuration and spacing between elements of 0.5mm, (b) axial configuration and spacing between elements of 5 mm

The plot in Figure 2.24 shows a comparison between taking into account higher order interactions versus nearest neighbour only for these two waveguides. The difference is not noticeable for the planar waveguide since the coupling between higher order elements is inherently small due to the large spacing dictated by the arrangement. Whereas for the axial waveguide, the spacing between the elements is small, leading to stronger coupling, even between the two furthest elements.

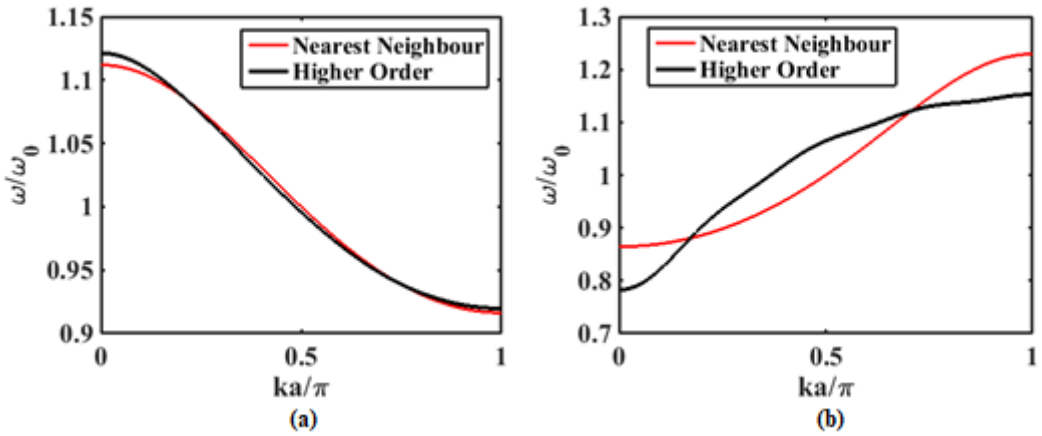

Figure 2.24 Dispersion diagrams for the 8-element waveguides in Figure 2.23 (a) and (b) respectively, taking into account (i) nearest neighbour only and (ii) higher order interactions

2.3.2 MI Ring Resonators

Moving on to MI ring resonators: as has been mentioned, “rotational resonance” will occur when the total phase shift that the MI wave accumulates round the ring is an integral multiple of 2π. Figure 2.25

(a) shows a planar view of an octagonal ring, with a magnetic dipole in its centre; and Figure 2.25 (b) shows its equivalent circuit with the usual circuit parameters.

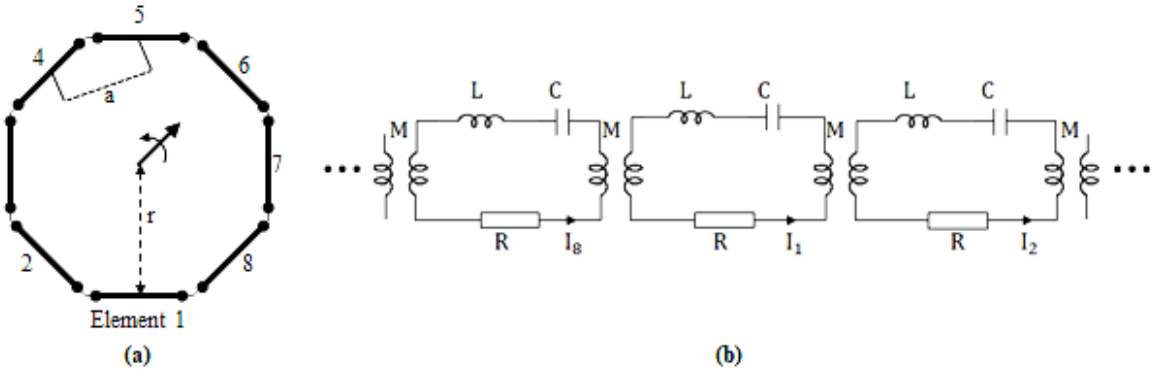

Figure 2.25 Magneto-inductive ring composed of N = 8 capacitively loaded loops (a) planar view and (b) equivalent circuit

We firstly derive the dispersion equation for the MI ring. For N magnetically coupled, capacitively loaded loops arranged as in Figure 2.25 (a) on a polygon of radius r, the distance between the elements, a, is related to the radius as follows

$$a = \frac{2\pi r}{N}$$

Equ 2.26

The wave propagating round the ring has resonance when the phase shift round the ring is equal to an integral multiple of the wavelength:

$$2\pi r = \mu\lambda$$

Equ 2.27

Where μ is an integer and $\lambda = \frac{2\pi}{k'}$ is the wavelength of the MI wave. By substituting λ and Equ 2.26 into Equ 2.27, we get

$$k'a = \frac{2\pi\mu}{N}$$

Equ 2.28

Substituting this into Equ 2.24 and making the same approximations as before for low attenuation, we obtain the frequency for rotational resonance as

$$\frac{\omega_r}{\omega_0} = \frac{1}{\sqrt{1 + \sum_m \kappa_m \cos\left(\frac{2\pi\mu m}{N}\right)}}$$

Equ 2.29

Assuming a resonance of the first order (μ=1), it can be seen that the relative value of the fundamental resonance depends only on the coupling coefficients, κ_m, and the number of elements in the ring, N. Note that the first mode is the most relevant to MRI applications as it can couple to a rotating magnetic dipole. Equ 2.29 represents the dispersion equation for a rotational ring, taking into account all neighbour interactions. If we were to consider nearest neighbour interactions only, then Equ 2.29 would be reduced to Equ 2.30. In either case, it can be seen that, unlike a waveguide, there exists allowed transmission at the particular modes, μ, only. Figure 2.26 depicts a plot of the dispersion diagram for an 8-element MI ring with the first order coupling coefficient κ = -0.2. Here it is seen that since the ring is arranged in a quasi-planar configuration, the dispersion diagram also shows a backward-propagating wave seen for the planar waveguide.

$$\frac{\omega_r}{\omega_0} = \frac{1}{\sqrt{1 + \kappa \cos\left(\frac{2\pi\mu}{N}\right)}}$$

Equ 2.30

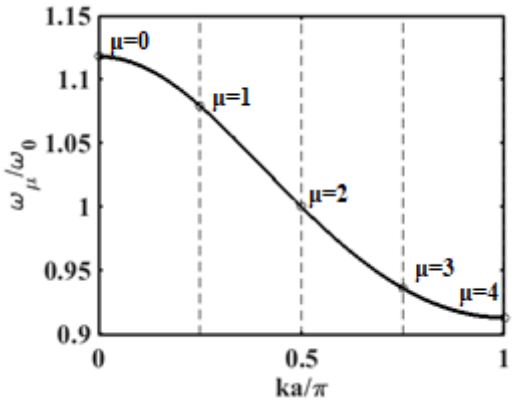

Figure 2.26 Dispersion diagram for an 8-element ring, as shown in Figure 2.25 (a), assuming nearest neighbour coupling only with κ = -0.2.

In order to excite waves at rotational resonance, we assume there exists a nucleus under magnetic resonance at the centre of the ring [192]. The nucleus can be modelled by a rotating magnetic dipole at an angular frequency ω_μ as shown in Figure 2.25 (a). If ω_μ is made to match ω_r, then the MI ring will be coupled to the magnetic dipole. The rotation of the magnetic dipole is in the plane defined by the centres of the individual loops, and so the radial component of the dipole will induce a voltage V_n in the n^{th} loop, which can be represented as in Equ 2.31 since the excitation is in the form of a wave travelling round the structure.

$$V_n = V_0 \exp\left(-j\frac{2\pi n}{N}\right)$$

Equ 2.31

Here V_0 is a constant which depends on the magnitude of the excitation and the geometry of the ring. The general relation between the induced voltages and currents is

$$\mathbf{V} = \bar{\mathbf{Z}}\mathbf{I}$$

Equ 2.32

Where **V** and **I** are vectors of length N and $\bar{\mathbf{Z}}$ is an N×N matrix containing the mutual inductances, $Z_m = j\omega M$. Using nearest neighbour approximation, $\bar{\mathbf{Z}}$ will have the following form:

$$\bar{\boldsymbol{Z}} = \begin{pmatrix} Z_0 & Z_m & 0 & 0 & \cdots & \cdots & \cdots & \cdots & Z_m \\ Z_m & Z_0 & Z_m & 0 & \cdots & \cdots & \cdots & \cdots & 0 \\ 0 & Z_m & Z_0 & Z_m & 0 & \cdots & \cdots & \cdots & 0 \\ 0 & 0 & Z_m & Z_0 & Z_m & 0 & \cdots & \cdots & 0 \\ \cdots & \cdots & \cdots & \cdots & \cdots & \cdots & \cdots & \cdots & \cdots \\ 0 & \cdots & \cdots & \cdots & Z_m & Z_0 & Z_m & 0 & 0 \\ 0 & \cdots & \cdots & \cdots & \cdots & Z_m & Z_0 & Z_m & 0 \\ 0 & 0 & \cdots & \cdots & \cdots & 0 & Z_m & Z_0 & Z_m \\ Z_m & 0 & \cdots & \cdots & \cdots & 0 & 0 & Z_m & Z_0 \end{pmatrix}$$

Equ 2.33

To obtain the relationship between the induced currents and voltages, we first note that, due to circular symmetry, the absolute values of all currents must be identical and the phases match those of the induced voltage. Now working an example for n = 2, we have

$$V_2 = Z_0 I_2 + Z_m(I_1 + I_3)$$

Equ 2.34

Bearing in mind Equ 2.31 and that the current and voltage phases match and the current magnitudes are equal, we obtain

$$V_2 = \left[Z_0 + 2Z_m \cos\left(\frac{2\pi}{N}\right)\right] I_2$$

Equ 2.35

And

$$\mathrm{Im}\left[Z_0 + 2Z_m \cos\left(\frac{2\pi}{N}\right)\right] = 0$$

Equ 2.36

Thus we obtain the well-known relationship in Equ 2.37 which is valid for all other elements as well.

$$I_2 = \frac{V_2}{R}$$

Equ 2.37

It states that the current in one of the elements of an MI ring, under rotational resonance, is the same as that for the uncoupled individual element when excited by the same voltage at its resonant frequency ω_0.

2.4 Summary

A variety of internal coils have been reviewed and a clearer picture of the challenges facing the design of the MI ring resonator device has been formed. It is first worth noting that there does not exist a device capable of offering the higher SNR needed for MR images without compromising the integrity of the colorectal anastomosis. The coils reviewed for imaging the GI wall are the closest alternative [143], [146], [149], [199], but they have some disadvantages: It would be difficult to thread a catheter or a colonoscope past the colon and so imaging the small intestine with these coils is nearly impossible. Moreover, a colonoscopy is another operation altogether which the patient may not be comfortable with after the anastomosis surgery. Therefore, an implantable coil, inserted during the operation itself and mounted on the Biodegradable Anastomosis Ring (BAR) is ideal.

Using an MI ring resonator also seems ideal, not only due to its shape, but also due to its unconnected individual coils which will disintegrate with the BAR. Furthermore, the individual small coils comprising the ring will limit RF heating. On the other hand, there are issues with how to decouple the device from the B_1 field, since its small size makes connecting a decoupling circuit difficult and so figure-of-eight elements is a viable option. Another problem is with signal collection and matching to the MR scanner: quadrature taps can be used such as in [193], but wireless matching is required for patient comfort. Finally, the implanted coil can assume virtually any orientation in the body and so investigating how to make the FOV unaffected by coil orientation is also a challenge.

3 Magneto-Inductive Ring Resonators

Any internal coil must be decoupled from the B_1 field of the MRI scanner to avoid image artefacts and RF induced heating. In this Chapter we first discuss how using a coupled pair of magneto-inductive ring resonators provides a mechanism for B_1 field decoupling. We then develop two different coupled MI ring resonators made from two types of element, and compare their performance based on S-parameter measurements and dispersion diagrams. In particular, we attempt to determine the resonant frequency of the lowest order spatially symmetric and anti-symmetric modes, and investigate how their positions in the overall resonance spectrum can be manipulated to achieve decoupling and detection at the same frequency.

3.1 B_1 Field Decoupling

We have previously discussed several methods of decoupling an internal MRI detection coil from the scanner's B_1 field, which rotates at exactly the same frequency as the rotating nuclear dipoles to which the detector should couple. The methods mentioned were active [159] and passive [158] decoupling using a diode-switched tank filter, which both reduce the current in the coil that must follow from an induced voltage, and the use of figure-of-eight elements, which reduces the induced voltage itself to zero by cancellation [191]. In this Section, we consider possible options for the decoupling system needed in an annular surgical wound monitor. Clearly, the design must to be as simple as possible to allow the device to be embedded in a Biodegradable Anastomosis Ring (BAR). Thus we initially consider the following three options for decoupling:

a) A single MI ring resonator, based on figure-of-eight elements
b) A coupled pair of ring resonators, based on rectangular elements
c) A coupled pair of ring resonators, based on figure-of-eight elements

To understand how the use of a coupled ring resonator system can achieve decoupling, we must first consider the resonant modes of a single ring, constructed from a set of capacitively loaded loops. Figure 3.1 shows projection and plan views of an 8-element octagonal ring. In general, the number of resonant elements in the ring, N, determines the number of spatial modes that the ring can support, M. Generally, M = N; however, for symmetric ring resonators, there is a reduction in the number of observably different resonant frequencies, since several pairs of modes resonate at identical frequencies. This behaviour is known as modal degeneracy.

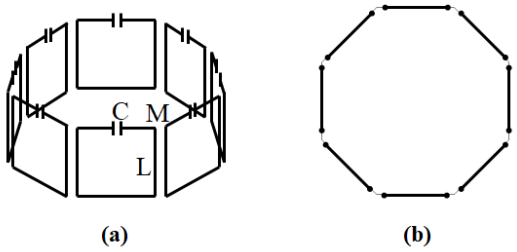

Figure 3.1 8-element octagonal MI ring (a) projection and (b) plan view.

To illustrate this, Figure 3.2 shows the dispersion diagram of an MI waveguide with quasi-planar coupling, due to nearest neighbour coupling $\kappa = -0.2$. The characteristic is plotted over a complete 2π period, and the discrete conditions for ring resonance $Nka = 2\mu\pi$ in a single octagonal ring are identified. These resonances clearly lie at angular frequencies ω_μ corresponding to $k_\mu a = 2\mu\pi/N$, where μ is an integer.

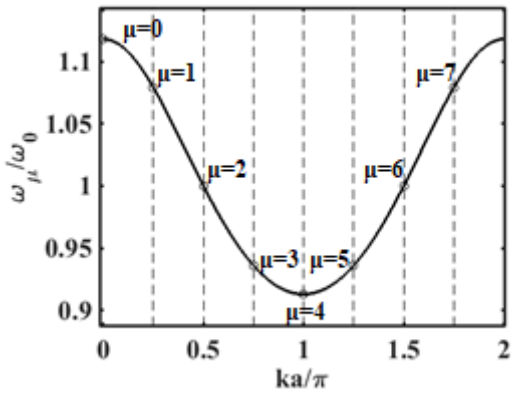

Figure 3.2 Dispersion diagram for an octagonal MI ring resonator with $\kappa = -0.2$

The first and seventh modes are at the same frequency, as are the second and sixth modes and the third and fifth modes. Thus for an 8-element polygonal ring, there are only 5 distinct resonant modes. In fact, for any symmetric MI ring with an even number of elements, we have:

$$M = \frac{N}{2} + 1$$

Equ 3.1

If, however, the MI ring has an odd number of elements, the number of distinct modes is different. In this case, similar arguments lead to:

$$M = \frac{(N+1)}{2}$$

Equ 3.2

For a single MI ring, the first mode (whose mode number is $\mu = 1$) will couple to the rotating dipoles in the body; and all other modes have to be rejected. To that end, the smaller the number of elements – and hence the smaller the number of resonant modes – the better. On the other hand, if the ring is to be made from rigid elements (for example, printed circuit boards or PCBs), the number of elements determines the 'smoothness' of the ring; and here the larger the number of elements, the better. A good compromise is provided by an eight-element octagonal MI ring, with five resonant modes.

When a pair of coupled ring resonators are used, an additional degree of spatial structure is introduced into the mode shape, and the overall current patterns may be symmetric or anti-symmetric in form. For symmetric modes, the currents in the two rings are equal, while for anti-symmetric modes the currents have equal amplitude but opposite sign. A coupled ring resonator system based on octagonal rings will therefore support ten modes, five symmetric and five anti-symmetric. If the excitation is the same in both rings, only the symmetric modes can arise. Conversely, if the excitation has equal amplitude and opposite sign in each ring, the induced voltages will also be opposite to each other, and only the anti-symmetric modes will be excited.

Figure 3.3 shows a coupled octagonal ring resonator system, immersed in the uniform B_1 field used in the excitation phase of MRI. In this case, the induced voltages in the two rings will be identical, and the lowest order symmetric mode will be excited. To avoid this, and hence to achieve decoupling, this mode must be tuned away from the Larmor frequency ω_L (63.85 MHz for a 1.5 T scanner, or 127.74 MHz for 3.0 T). However, the local magnetisation generated during signal reception is non-uniform, and can be detected using the lowest-order anti-symmetric mode, provided this is tuned to ω_L.

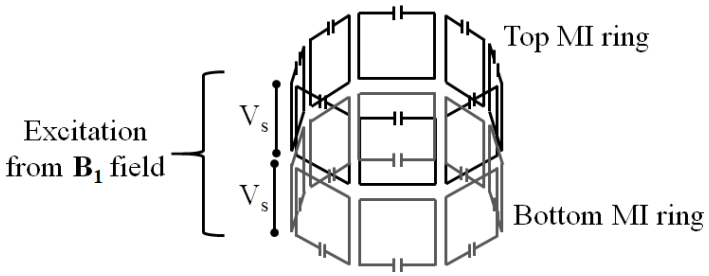

Figure 3.3 Coupled MI ring resonator system for B_1 field decoupling

Figure 3.4 shows a number of possible configurations for annular surgical wound monitors based on MI ring resonators. In each case, the monitor is inside the bowel, close to the wound site. In Figure 3.4 (a), a single ring is used, based on the figure-of-eight elements needed to achieve decoupling by voltage cancellation. The disadvantage of this configuration is that symmetric placement is incompatible with the two-part construction of a bowel anastomosis ring, while the figure-of-eight element shape will lead to a null in sensitivity at the wound site itself. In Figure 3.4 (b), a pair of coupled rings is used, based on rectangular elements. This arrangement is now immediately compatible with BAR construction. Since non-zero voltages will now be induced,

decoupling must be achieved by detuning the lowest order symmetric mode away from resonance, as described above. However, the use of an anti-symmetric mode for detection again reduces sensitivity immediately adjacent to the wound. In Figure 3.4 (c), a pair of coupled rings is used, based on figure-of-eight elements. This arrangement returns sensitivity to the wound site itself, but is larger. However, it is important to remember that ischemia, oedema and leakage can all occur at some distance from the wound, and the desired field-of-view is currently unclear. At this early stage of design, therefore, the best and simplest option is almost certainly provided by a coupled ring system based on rectangular elements.

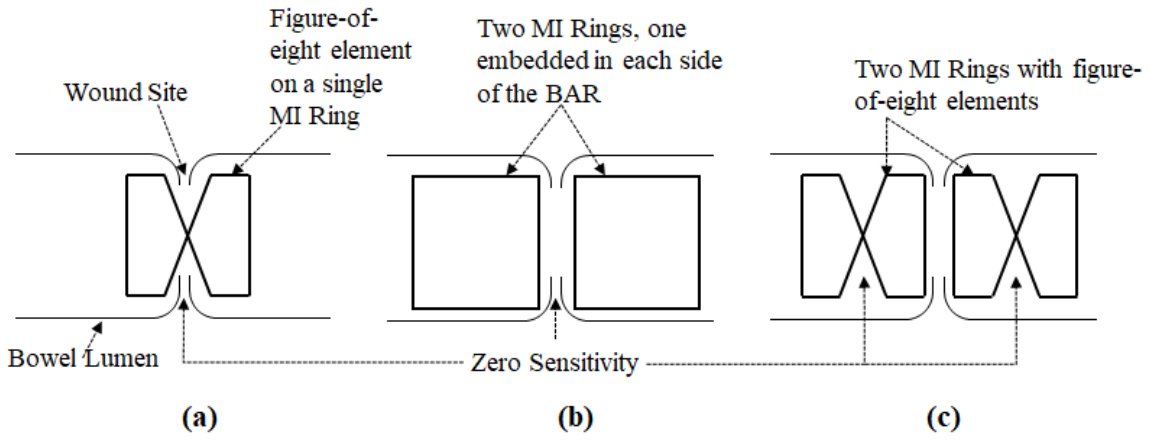

Figure 3.4 Annular surgical wound monitors based on a (a) a single MI ring with figure-of-eight elements, (b) a pair of coupled MI Rings with rectangular elements, (c) coupled MI rings with figure-of-eight elements.

3.2 Device Design and Testing

In this Section, the design of the coupled MI ring resonator system is considered in detail, and methods for theoretical simulation and experimental verification are explained. The set-up for the experiment and the simulation programs are explained below.

3.2.1 Experimental Set-up

Figure 3.5 shows the experimental resonant elements used in the initial prototype coupled ring system. The elements are constructed as rigid double-sided PCBs based on Cu conductors and FR4 substrates. Etched spiral conductor tracks form the inductors, and discrete surface mount capacitors are soldered onto landing sites to complete the circuit. To investigate the effect of a single coil on the overall performance of the coupled resonator system, two different inductor layouts are used: Type A is a double-sided square coil with three turns on either side, while Type B is a similar rectangular coil with two turns on either side. These elements were available from earlier projects, and had already demonstrated good performance in experiments involving magneto-inductive waves. In each case,

eight similar elements are needed to construct a single eight-element MI ring resonator, while sixteen similar elements form the corresponding coupled ring system.

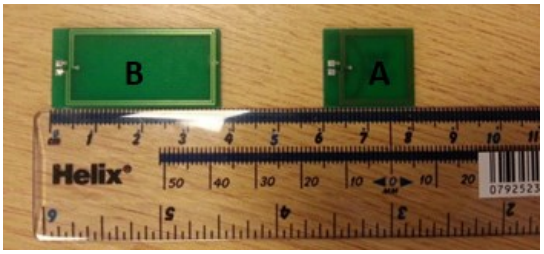

Figure 3.5 PCB inductors used to construct resonant elements for early prototype ring resonators.

Figure 3.6 shows the experimental rig used to arrange these elements into single and coupled ring resonator configurations. **Figure 3.6** (a) shows a cross-sectional diagram of the internal arrangement of a couple MI ring system and **Figure 3.6** (b) shows a photograph of a system under test. Single rings are assembled by slotting eight PCB elements into octagonal grooves machined into a Perspex baseplate. Machined cut-outs provide spaces for capacitors, and a concentric outer groove allows the mounting of additional transducers for excitation and detection. Two such rings are mounted one above the other to form a coupled ring resonator system, using plastic pillars and plastic studding to adjust their relative height.

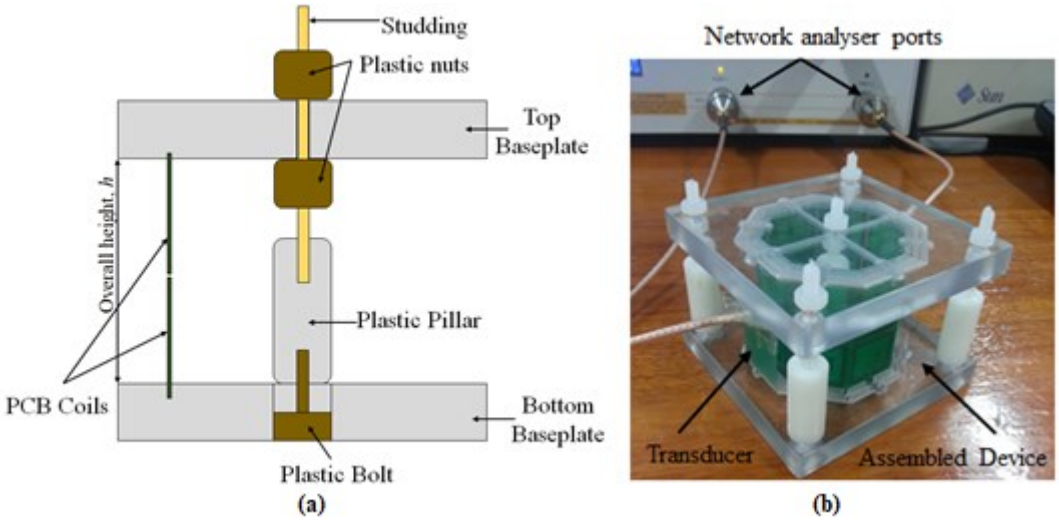

Figure 3.6 (a) Cross-section of rig[6]. (b) Assembled device under test using a network analyser

3.2.2 Simulation

To aid in design and allow interpretation of experimental results, full simulations are carried out. The first step involves simulation of the resonant elements themselves, with the aid of the electromagnetic field solver FastHenry2. This freely available software, originally designed for estimating circuit

[6] Many thanks to Mr. Phil Jones, mechanics technician at Imperial College, for manufacturing the rig to the exact specifications.

parasitics, was developed at MIT and allows the calculation of self-inductances, L_n, resistances R_n and mutual inductances, $M_{n,m}$, for any set of N coupled coils. The node coordinates and track connectivity for the coil set are first read from a layout description file, and the result is given in an N×N inductance matrix, $\bar{\mathbf{Z}}$. Reciprocity implies that $M_{n,m} = M_{m,n}$. For a ring resonator, the self-inductances L_n and resistances R_n are all identical and can be written as L and R. Similarly the mutual inductances $M_{n,n+1}$ and $M_{n,n-1}$ between nearest neighbours are all identical and can be written as M_1, while the mutual inductance between second-neighbours can be written as M_2. Thus, the matrix $\bar{\mathbf{Z}}$ has the form shown in Equ 3.3.

$$\bar{\mathbf{Z}} = \begin{pmatrix} R+jL & M_1 & M_2 & M_3 & \cdots & \cdots & \cdots & \cdots & M_N \\ M_1 & R+jL & M_1 & M_2 & \cdots & \cdots & \cdots & \cdots & \cdots \\ M_2 & M_1 & R+jL & M_1 & M_2 & \cdots & \cdots & \cdots & \cdots \\ M_3 & M_2 & M_1 & R+jL & M_1 & M_2 & \cdots & \cdots & \cdots \\ \cdots & \cdots & \cdots & \cdots & \cdots & \cdots & \cdots & \cdots & \cdots \\ \cdots & \cdots & \cdots & \cdots & M_1 & R+jL & M_1 & M_2 & M_3 \\ \cdots & \cdots & \cdots & \cdots & \cdots & M_1 & R+jL & M_1 & M_2 \\ \cdots & \cdots & \cdots & \cdots & \cdots & M_2 & M_1 & R+jL & M_1 \\ M_N & \cdots & \cdots & \cdots & \cdots & M_3 & M_2 & M_1 & R+jL \end{pmatrix}$$

Equ 3.3

For example, Figure 3.7 shows a FastHenry model of a single MI ring made from the square Type A coils. Additional coils (not shown) may be added to simulate the inductive probes used to interrogate the device. Here each individual coil is defined using 16 sets of coordinates, and varying the dimensions of the coils and/or the distance between them requires re-definition of these coordinates in the x-, y-, and z-axes. With sixteen coils – eight for each MI ring – this process is time consuming. The coordinates are therefore generated using a Matlab script, where only the dimensions of the coils and the distance between them are parameters and the FastHenry coil coordinates are the output. FastHenry is then used to calculate the $\bar{\mathbf{Z}}$-matrix, and Matlab is used to extract the values of L, R and M_n from the $\mathbf{Z}$ matrix, process these values to calculate the frequency dependence of the S-parameters, extract the resonant frequencies and plot the dispersion diagram.

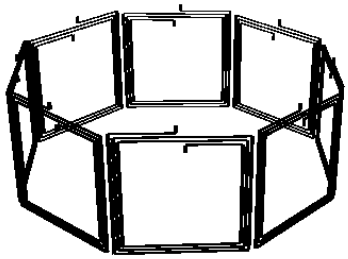

Figure 3.7 FastHenry model of an octagonal MI ring resonator made from square Type A coils

3.3 Single Magneto-Inductive Ring Resonator

3.3.1 Single Element

In order to understand the operation of an MI ring, the characteristics of a single resonant elements are first required. The dimensions of the coils to be tested are detailed in Figure 3.8 and Table 3.1. Here L_v and L_h are the vertical and horizontal lengths of the outer-most turn of the coil, s is the separation between the turns, u is the elevation for the capacitor connection, and c and b are the distance from the outermost turn of the coil to the edges of the PCB. The last parameters determine the separation of individual elements and rings, respectively

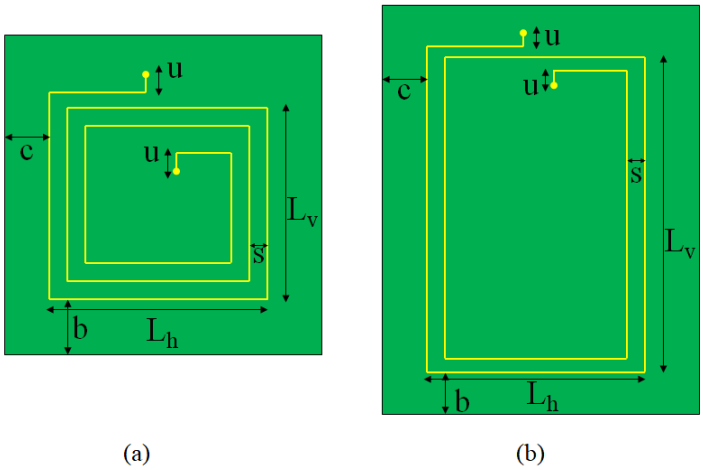

Figure 3.8 Key dimensions of double-sided PCB elements: (a) Type A square three-turn coil (b) Type B rectangular two-turn coil.

Table 3.1 Dimensions of PCB coils to be tested.

	Type A	**Type B**
L_h (mm)	16	16
L_v (mm)	16	32
w (mm)	0.5	0.5
h (mm)	0.035	0.035
u = b = c (mm)	1	1
s (mm)	0.5	0.5

The two coils to be investigated are therefore identical except for the number of turns and the length of L_v; for the rectangular coil $L_v = 2L_h$, whereas for the square coil, $L_v = L_h$. Both coils can be represented in terms of the equivalent circuit of Figure 3.9, where L is the self-inductance of the coil, R is its self-resistance and C_{coil} is the self-capacitance caused by the stray capacitance between neighbouring turns. This self-capacitance causes the coil to resonate without the addition of a mounted capacitor, C_{test}, albeit at a higher frequency than that expected for normal operation.

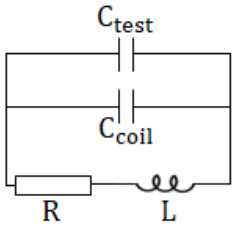

Figure 3.9 Equivalent circuit of a PCB-based resonant element.

The equivalent circuit parameters may easily be extracted experimentally, by measuring the resonant frequency and Q-factor using a pair of inductive probes, one for excitation and the other for detection. In the process, it is important to load the element lightly, so that the resonant frequency is not shifted and the Q-factor is not degraded. It is usually sufficient to make measurements with a set of different capacitors C_{test}, whose losses are normally neglected. The parameters, C_{coil} and L, may then be extracted as follows. We first reconsider the formula for L-C resonance $\omega_0^2 = 1/LC$, knowing that now $C = C_{test} + C_{coil}$. This formula may be re-arranged as:

$$C_{test} = \frac{1}{\omega_0^2 L} - C_{coil}$$

Equ 3.4

Equ 3.4 predicts a straight-line relation between C_{test} and $1/\omega_0^2$, where 1/L is the gradient of the line and C_{coil} is the y-intersect. If experimental values of C_{test} are plotted against corresponding values of $1/\omega_0^2$, C_{test} and L may then be extracted by regression.

For example, Figure 3.10 shows such a plot for the type B rectangular coil. Here the discrete points represent experimental data, while the continuous line represents the best fit. In this case, C_{coil} = 1.99 pF. This capacitance is relatively small, but it will strongly affect performance if the desired resonance lies close to the self-resonance arising from a combination of L and C_{coil}.

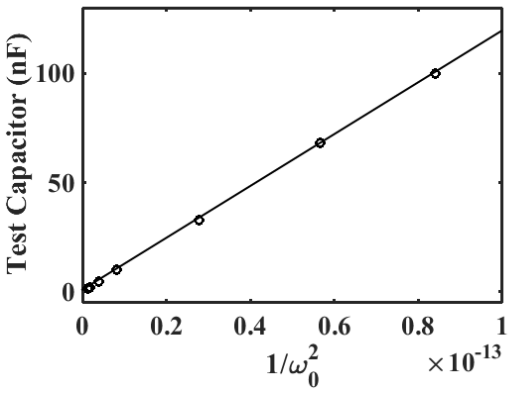

Figure 3.10 Test Capacitance against $\frac{1}{\omega_0^2}$ plot for the type B element

To demonstrate the existence of such a self-resonance, we can use inductive probes and a network analyser to record the frequency dependence of the transmission S-parameter S_{21} through the coil with no added capacitor. Figure 3.11 shows the results, for a Type B element. As can be seen, there is a resonant peak at 124.7 MHz. The coil cannot therefore be tuned to operate at a higher frequency than this, and consequently could almost certainly not be used to construct a resonant MRI detector for operation at 3.0 T. This shows the importance of C_{coil}, no matter how small it may be.

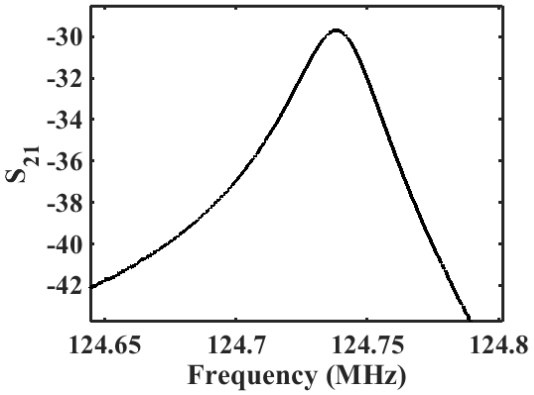

Figure 3.11 Frequency dependence of the transmission S-parameter S_{21} for a type B coil with no added capacitor.

The gradient of plots of the type shown earlier in Figure 3.10 can be used to extract the self-inductance L of the coil, In this case, the gradient is 1.2×10^6, implying that that L = 0.83μH for Type B rectangular elements. Alternatively, the resonant frequency could simply be measured using a capacitor C_{test} large enough that the value of C_{coil} does not affect measurements. The capacitors used here range from 220 pF to 22 nF. We then record the resonance, $\omega_0 = 2\pi f_0$, for each capacitor and use the relation $L = 1/\omega_0^2 C$ to calculate the average self-inductance. The results are L = 1.1μH and L = 0.82μH for Type A and Type B elements respectively. The inductance may also be estimated using FastHenry. Using this approach, L = 1 μH and L = 0.87μH are obtained for Type A and Type B

elements respectively. The two central columns in Table 2 summarise these results; theoretical estimates are clearly in good agreement with experimental values.

Note that the relationship between inductance and number of turns is given by Equ 3.5 where N is the number of loops, μ is the relative permeability, A is the coil area and l is the coil length.

$$L = \frac{N^2 \mu A}{l}$$

Equ 3.5

This relationship is originally formulated for three-dimensional coils, but it also holds for planar coils up to a certain number of turns. By having a coil on both sides of the PCB, the number of turns has been doubled and the inductance has been quadrupled. This relation is effectively verified by the final column of FastHenry estimates in Table 2.

Table 3.2 Measured and simulated inductance for single and double-sided PCBs

	Measured Inductance (μH)	**Simulated Inductance (μH)**	**Simulated Inductance for one sided PCBs (μH)**
Type A	1.10	1.00	0.31
Type B	0.82	0.87	0.24

Self-resistance is extracted by measuring the coil's quality factor (or Q-factor), a dimensionless property of a resonator that describes damping effects. The Q-factor also determines how sharply the final device will be tuned. The Q-factor can be defined either as a ratio between the resonant frequency and the bandwidth, or as a ratio between the parameters L and R as given in Equ 3.6:

$$Q_0 = \frac{f_0}{\Delta f} = \frac{\omega_0 L}{R}$$

Equ 3.6

The assumption of constant parameter values suggest that that Q_0 is linearly dependent on the resonant frequency; however, this is only true at low frequency. At higher frequency, the coil resistance, R, becomes frequency dependent due to the skin effect. R is inversely proportional to the skin depth, δ, which is itself directly proportional to $\sqrt{f}$, as shown in Equation 7. Under these conditions, Q_0 is proportional to the square root of the frequency.

$$R \propto \frac{1}{\delta} \propto \frac{1}{\sqrt{f}}$$

Equ 3.7

For example, Figure 3.12 shows the experimental variation of the Q-factor with resonant frequency for Type B elements. Here different capacitors are used to obtain different resonant frequencies, and the Q-factor is read directly from the network analyser. Up to a frequency of about 35 MHz the skin effect does not influence the Q-factor much, and Q is proportional to f as shown by the thin continuous line. Above this frequency, the relationship changes to a dependence on √f as shown by the thick continuous line. However, at frequencies nearing the self-resonance of the coil, the Q-factor actually decreases, as shown by the dashed line, due to resonantly amplified losses.

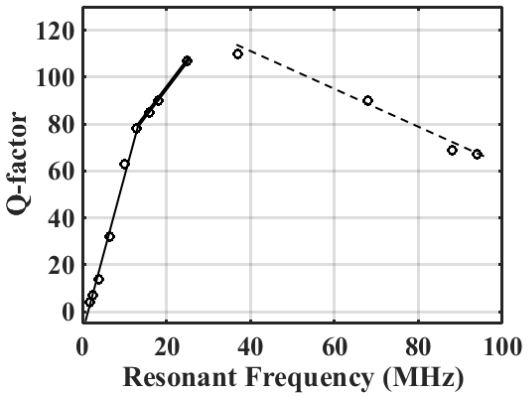

Figure 3.12 Q-factor against resonant frequency for the type B element

From Equ 3.3, it can be seen that R can indeed be extracted from the $\bar{\mathbf{Z}}$ matrix of the FastHenry solution. However, this time, there is a large discrepancy between the simulated and experimental results. Table 3.3 shows a comparison between these values. The measured resistance is clearly much higher than the predicted one. The discrepancy is attributable to two effects: the use of thin-film copper (which has a lower conductivity than bulk Cu) in the experimental elements, and loading from the transducers. Neither effect is taken into account in FastHenry.

Table 3.3 Comparison between resistances predicted by FastHenry with experimentally measured values.

	Expected Resistance (Ohms)	Measured Resistance (Ohms)
Type A[7]	0.7474	2.0663
Type B[8]	0.7091	3.0019

Note that the table records the resistance measured with C = 47 pF and 6.8 pF for Type A and Type B coils respectively. With C = 6.8 pF, f_0 = 59 MHz and the Type B elements can form a perfectly tuned single MI ring for ^{1}H MRI at 1.5 T. However, for the type A elements, f_0 = 23.2 MHz and here the effect of lower resonant frequency is investigated; this may be required if the double MI ring device is to be tuned for ^{31}P MRS with a Larmor frequency of 25.84 MHz at 1.5T.

[7] Measured and simulated at 22 MHz with C = 47pF
[8] Measured and simulated at 59 MHz with C = 6.8pF

3.3.2 Coupling Coefficients

The coupling coefficient is a dimensionless quantity that gives an indication of how strong the mutual inductance between two elements is. Figure 3.13 shows the equivalent circuit of two identical coupled resonant elements. Here L is the self-inductance, C is the test capacitance, M is the mutual inductance between the elements, and I_1 and I_2 are the currents flowing in each element. M can be positive or negative depending on the orientation of the elements to each other: for the axial configuration, M is positive, and for the planar configuration M is negative.

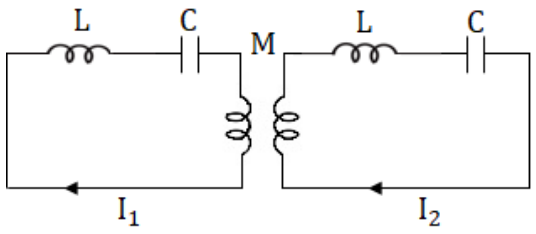

Figure 3.13 Equivalent circuit of two coupled resonant elements.

The coupling coefficient κ is given by:

$$\kappa = \frac{2M}{L}$$

Equ 3.8

This value represents the nearest-neighbour coupling coefficient κ_1 in a multi-element system. Similar values obtained with more widely spaced elements can represent the non-nearest neighbour coefficients in a multi-element system such as a ring resonator. These coupling coefficients must generally all be determined to characterise the overall interaction and estimate the dispersion relationship. This in turn will aid in tuning the elements to the required resonance frequency.

The dispersion relationship for a single MI ring has been derived in Chapter 2 and is repeated here in Equ 3.9. Here $\omega_{r\mu}$ is the μ^{th}-order ring resonance, ω_0 is the resonance of a single element, κ_m is the m^{th} order coupling coefficient and N is the number of elements in the ring.

$$\frac{\omega_{r\mu}}{\omega_0} = \frac{1}{\sqrt{1 + \sum_m \kappa_m \cos\left(\frac{2\pi\mu m}{N}\right)}}$$

Equ 3.9

To find the coupling coefficient between two elements, we refer to their equivalent circuit as seen in Figure 3.13. Neglecting excitation and losses, KVL gives the two circuit equations shown in Equ 3.10

$$I_1\left(j\omega L + \frac{1}{j\omega C}\right) + I_2 j\omega M = 0$$

$$I_1 j\omega M + I_2\left(j\omega L + \frac{1}{j\omega C}\right) = 0$$

Equ 3.10

These two equations can be represented in matrix format as shown in Equ 3.11.

$$\begin{pmatrix} j\omega L + \frac{1}{j\omega C} & j\omega M \\ j\omega M & j\omega L + \frac{1}{j\omega C} \end{pmatrix} \begin{pmatrix} I_1 \\ I_2 \end{pmatrix} = 0$$

Equ 3.11

This equation has a non-trivial solution (i.e. non-zero currents) only when the determinant of the matrix is equal to zero as implied by Equ 3.12.

$$\begin{vmatrix} j\omega L + \frac{1}{j\omega C} & j\omega M \\ j\omega M & j\omega L + \frac{1}{j\omega C} \end{vmatrix} = 0$$

Equ 3.12

Solving the determinant, we obtain the two resonances shown in Equ 3.13. Here ω_1 corresponds to the (L + M) term and to the symmetric mode with $I_1 = I_2$, while ω_2 corresponds to the (L - M) term and to the anti-symmetric mode with $I_1 = -I_2$.

$$\omega_{1,2} = \frac{1}{\sqrt{C(L \pm M)}}$$

Equ 3.13

With some algebraic manipulation, it can be found that

$$MC = \frac{\omega_2^2 - \omega_1^2}{2\omega_1^2\omega_2^2}$$

$$LC = \frac{\omega_2^2 + \omega_1^2}{2\omega_1^2\omega_2^2}$$

Equ 3.14

Dividing MC by LC then gives the relationship between the coupling coefficient and the two resonant frequencies, as shown in Equ 3.15.

$$\kappa = 2\frac{\omega_2^2 - \omega_1^2}{\omega_2^2 + \omega_1^2}$$

Equ 3.15

Figure 3.14 details the coupling coefficients that arise in an eight-element coupled ring system. Figure 3.14 (a) shows the coefficients κ_{si} associated with coupling between the elements in the same ring, while Figure 3.14 (b) shows the coefficients κ_{di} associated with coupling between different rings. Here we call κ_{si} the intra-ring coupling coefficients and κ_{di} the inter-ring coupling coefficients. For the former, the first order is denoted as κ_{s1}, the second order as κ_{s2} and so on.

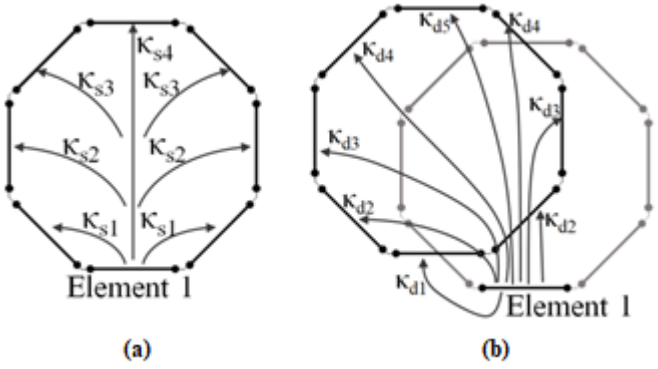

Figure 3.14 8-element MI Ring with annotated coupling coefficients: a) intra-ring, and b) inter-ring.

To measure these coupling coefficients, two elements are arranged as they would be in the octagonal ring, the frequency dependence of S_{21} measured, and the resonant peaks of the two moded system are extracted. The coupling coefficient is computed using these values following Equ 3.15. Figure 3.15 shows the experimental arrangement, using Type B rings. Figure 3.15 (a) shows the arrangement used to measure the first order intra-ring coefficient and the Figure 3.15 (b) shows the arrangement to measure the second order inter-ring coefficient.

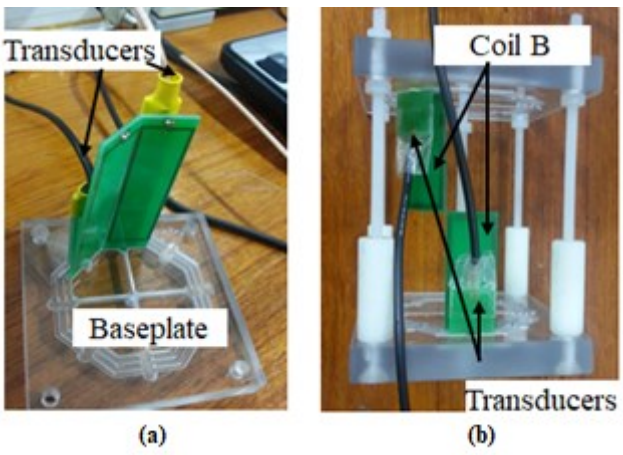

Figure 3.15 Arrangement for measuring coupling coefficients (a) nearest neighbour intra-ring, (b) second nearest neighbour inter-ring.

Figure 3.16 (a) shows the resonance spectrum for Type A elements arranged to determine κ_{s1}. Here we see the two peaks as expected, with the lower being the symmetric mode and the higher the anti-symmetric mode. The two are clearly discernible and we are able to calculate the corresponding coupling coefficient. Figure 3.16 (b) shows the resonance spectrum for elements arranged to determine κ_{s2}. Here the two peaks are much closer and have merged together, making it difficult to identify exactly their resonance frequency. This is also the case for the higher order couplings. To combat this, the load on the elements can be reduced by using smaller transducers and spacing them far from the elements to maximise the Q-factor. Thus, it is possible to get the second order coupling coefficients; however, the higher order couplings are still too small to measure for Type A elements.

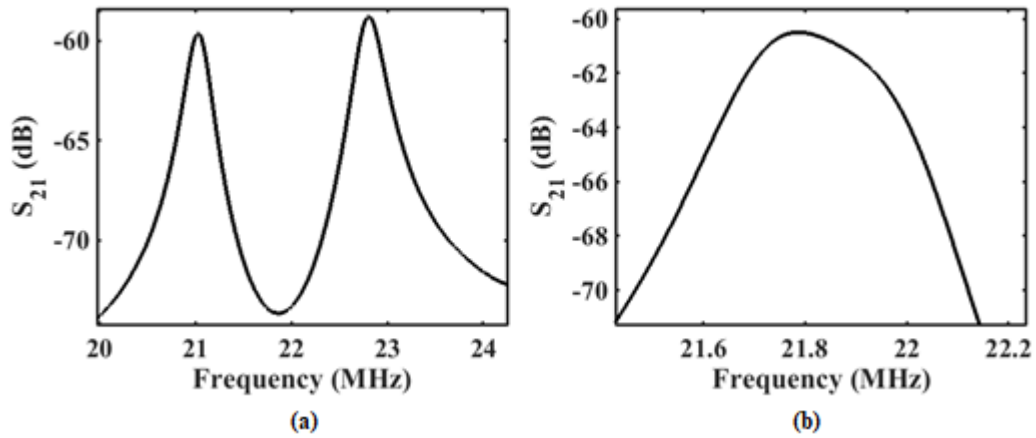

Figure 3.16 Frequency variation of S_{21} for (a) two nearest neighbour elements and (b) second nearest neighbour elements in a single ring.

Using similar methods, a reasonably complete set of coupling coefficients can be extracted, for both types of coil. Table 3.4 compares the measured and simulated coupling coefficients. The slight difference between the theoretical and experimental values is most probably due to errors in arranging the elements perfectly in a ring during the experiment; however, the agreement is satisfactory.

Table 3.4 Coupling coefficients for type A and type B elements in a single ring.

	Type A Measured	Type A Simulated		Type B Measured	Type B Simulated
κ_{s1}	-0.15	-0.17	κ_{s1}	-0.25	-0.28
κ_{s2}	-0.018	-0.019	κ_{s2}	-0.037	-0.036
κ_{s3}		-0.01	κ_{s3}	-0.024	-0.020
κ_{s4}		-0.0082	κ_{s4}		-0.017
κ_{d1}	-0.15	-0.18	κ_{d1}	-0.098	-0.13
κ_{d2}		0.036	κ_{d2}	-0.033	0.032
κ_{d3}		0.0098	κ_{d3}		0.01
κ_{d4}		0.0063	κ_{d4}		0.0068
κ_{d5}		0.0055	κ_{d5}		0.0062

By comparing the intra-ring coupling for the two coil types, we notice that even though the square type A coils have three turns and the rectangular type B coils have only two turns, the latter have higher intra-ring coupling coefficients due to their larger L_v. On the other hand, this large L_v is also the reason why the inter-ring coupling for the type B coil is less than that of the type A coil. In the next section we investigate how these values affect the overall S-parameters of the MI rings constructed from these coils.

3.3.3 Resonant Modes

In order to tune the device, we must first identify the resonant frequency of the important primary mode. This is done by examining the complete spectrum of resonant modes, which can be found from the frequency dependence of the scattering parameter S_{21} between two probes. Figure 3.17 shows the set-up used. Here tr_1 and tr_2 are the transmitting and receiving transducers, which are placed on either side of a coil diameter to minimise direct coupling and maximise uniformity of the spectral peaks. .

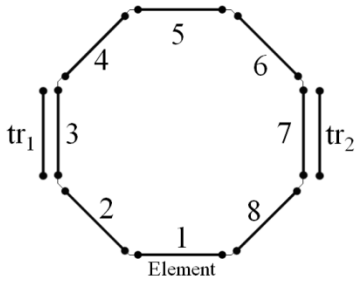

Figure 3.17 Arrangement for measuring the resonant mode spectrum of a single ring.

The mode spectrum can be found theoretically and experimentally. Firstly, the frequency dependence of S_{21} can be computed theoretically for a single ring using Matlab. The self-inductance, self-resistance, and mutual inductance between all elements of the ring are first obtained using FastHenry, together with the mutual inductance between the elements and the transducers tr_1 and tr_2.

There are four distinct mutual inductances as discussed in the previous section. Note that they are all negative – behaving like a planar waveguide – except for the coupling between opposing elements, where the coupling is positive – behaving like an axial waveguide. Note also that the coupling weakens as the elements get further apart. The L, M_n and R values are then used in a $\bar{\mathbf{Z}}$-matrix similar to that shown in Equ 3.3, but including the self-impedance of the transducers, Z_{0tr} and the mutual impedance between the transducers and their closest neighbouring elements, Z_{mtr} (in this case elements 3 and 7 as shown in Figure 3.17). The **Z**-matrix for a single octagonal ring with two transducers is therefore a 10×10 matrix.

To complete the circuit for each of the eight coils of the MI ring, we need a capacitor, C. To calculate the correct value, we use the fact that the rotational resonance of the ring, f_r, should equal the nuclear

resonance of the rotating dipoles, f_n. These should also equal the resonant frequency of the first mode, $f_{\mu=1}$. Thus we have the relationship in Equ 3.16 where $\omega = 2\pi f$.

$$\omega_r = \omega_n = \omega_{\mu=1}$$

Equ 3.16

However, it is $\omega_{\mu=1}/\omega_0$ that is available to us from the dispersion diagram, as seen from the y-axis in the plot of Figure 3.18.

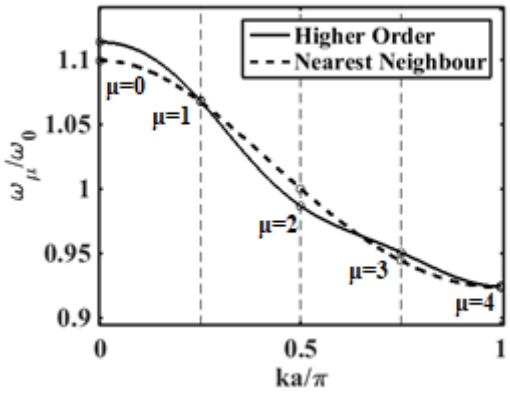

Figure 3.18 Dispersion diagram for an octagonal MI ring with Type A elements.

We therefore use instead the relationship in Equ 3.17. Here the dispersion equation is solved for the first mode, μ=1, for the Type A element ring.

$$\frac{\omega_{\mu=1}}{\omega_0} = \frac{\omega_r}{\omega_0} = 1.068$$

Equ 3.17

Rearranging Equ 3.17, while keeping the $\omega_{\mu=1}/\omega_0$ term intact, the ω_0 value can be obtained as:

$$\omega_0 = \frac{\omega_r}{\omega_{\mu=1}/\omega_0} = \frac{63.85\text{MHz} \times 2\pi}{1.068}$$

Equ 3.18

Knowing ω_0 we can calculate the capacitance needed to place the primary resonance at the correct frequency from the relationship $C = 1/\omega_0^2 L$. For example, the values needed for ^{1}H MRI at 1.5 T (63.85 MHz) are 7.09 pF for type A elements and 8.94 pF for type B elements. Now we have the complete **Z**-matrix. We know that

$$\mathbf{I} = \bar{\mathbf{Z}}^{-1}\mathbf{V}$$

Equ 3.19

Where **I** and **V** are the current and voltage vectors respectively. The voltage across each element is zero, except for the transmission transducer, where we put unity voltage ($Vt_{r1} = V_s = 1$). Consequently so the voltage vector has all elements zero except for the element before last.

Using Equ 3.19 we can calculate the current flowing through each element and we denote I_{in} as the current through the transmitter (tr_1) and I_{out} as the current through the receiver (tr_2). It can be shown that – for any two-port network with a single device under test – the voltage reflection and transmission coefficients (R_v and T_v) are:

$$R_v = 1 - \frac{2I_{in}R_L}{V_s}$$

Equ 3.20

$$T_v = \frac{I_{out}R_L}{V_s - I_{in}R_L}(1 + R_v)$$

Equ 3.21

Where V_s is the source voltage and R_L is the load impedance equal to 50 Ω. Converting these values to dB, we can obtain the reflection and transmission scattering parameters as shown in Equ 3.22. These can then be plotted across the frequency range of interest using Matlab:

$$S_{11} = 10\log_{10}(|R_v|^2)$$

Equ 3.22

$$S_{21} = 10\log_{10}(|T_v|^2)$$

Equ 3.23

Figure 3.19 shows the frequency variation of the S-parameters S_{11} and S_{21} for an MI ring with Type A elements. As expected, there are five resonances, and the required resonance (the second largest frequency, highlighted on the plot) is located at the correct absolute frequency for ^{1}H MRI at 1.5 T.

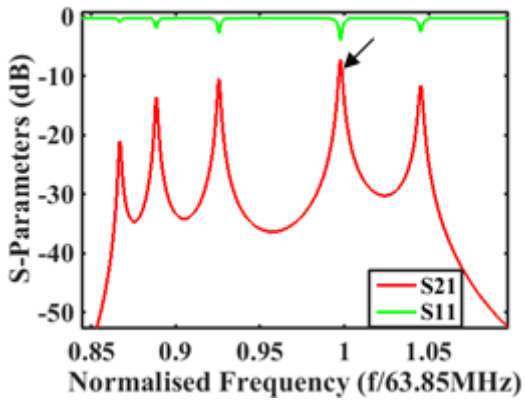

Figure 3.19 Simulated frequency dependence of scattering parameters for a Type A octagonal ring.

The frequency dependence of S-parameters for a single ring can also be measured experimentally. For the Type A elements, we have used a tuning capacitor value of C = 47pF and this places $f_{\mu=1}$ at 23.07 MHz. This is not perfectly tuned for ^{31}P MRS at 1.5 T, but is close enough in frequency to allow a fair comparison with a higher frequency ring. For the type B elements, we use C = 6.8pF to account for the value of C_{coil} which also affects tuning. This places $f_{\mu=1}$ at 64.06 MHz. Figure 3.20 shows the frequency dependence of S_{21} for both types of coil.

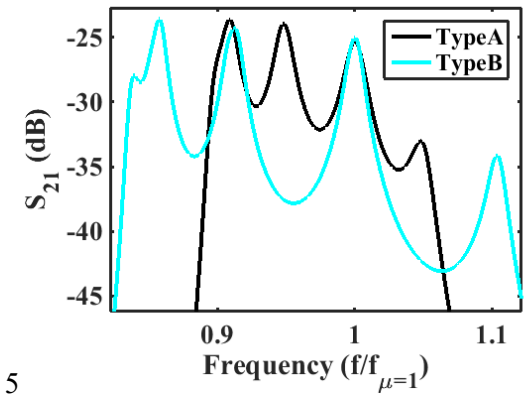

Figure 3.20 Measured frequency dependence of S_{21} for different octagonal rings based on Type A and Type B elements.

Again, there are five resonances as expected; however, the Q-factor is much smaller than theoretically expected, shown from the wider peaks. As previously discussed, this may be partly due to loading from the transducers and partly due to low-conductivity elements. By comparing the plots for the type A and type B rings, we also notice that the latter has a larger bandwidth due to the higher value of its higher primary coupling coefficient κ_{s1}.

Additionally, the Type A coil is tuned to a lower frequency than the Type B coil and this has decreased the Q-factor of its resonances even more, with the Q-factor of the first anti-symmetric mode of Type A and B rings being 59.15 and 76.26 respectively. It is also noticeable that, especially at the lowest and highest resonance, the Q-factors and peak highs reduce further. This is theoretically expected from the attenuation relationship discussed in Chapter 2. Figure 3.21 shows the plot of attenuation against frequency; attenuation is clearly highest at the band edges.

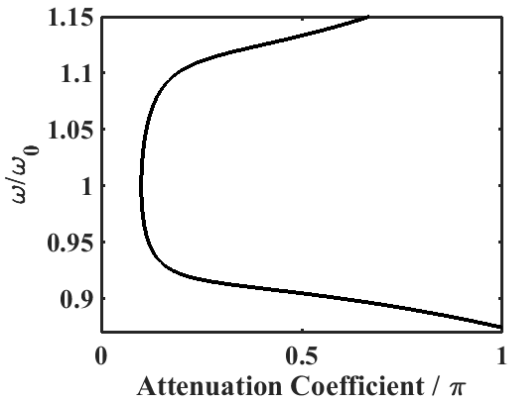

Figure 3.21 Frequency variation of attenuation coefficient, for $\kappa = -0.2$ and $Q_0 = 50$.

3.4 Coupled Magneto-Inductive Ring Resonator

We now consider a coupled MI ring resonator system, as seen in in **Figure 3.6** (b). Here the two MI rings are arranged above each other with the capacitor elevations for each ring facing away from each other to minimise the distance between the rings and maximise the inter-ring coupling. These additional inter-ring couplings must be taken into account when calculating the dispersion relationship or the S-parameters of the coupled MI ring resonator system, as discussed in the following two sections.

3.4.1 Dispersion Relationship

The dispersion relationship for a single MI ring has been derived in Chapter 2. Now we extend the theory to derive the dispersion relationship for two MI rings and confirm the number of modes to expect for the double ring configuration. Figure 3.22 shows the physical arrangement and equivalent circuit. We start with the nearest neighbour coupling assumption as shown in Figure 3.22 (a), with M_s being the nearest neighbour mutual inductance between elements of a single ring and M_d the nearest neighbour mutual inductance between the two rings. An equivalent circuit representation is shown in Figure 3.22 (b).

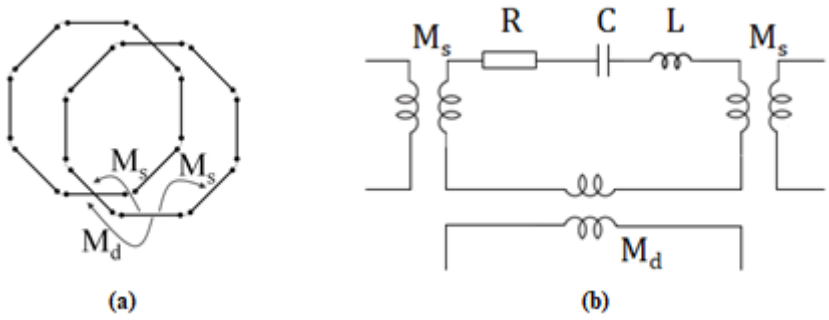

Figure 3.22 (a) Two coupled MI rings, showing only nearest neighbour inter-ring coupling; (b) equivalent circuit for a single element.

We use this to work out the dispersion relationship, and consider the case of two infinitely long waveguides arranged on top of each other, with coupling M_s and M_d as described above. This is then a good approximation for the two ring case. We also ignore losses, assuming R approximates to zero.

For the first waveguide, we can obtain the following relationship by applying KVL on one element

$$Z_0 I_{n1} + Z_{Ms}(I_{n1-1} + I_{n1+1}) + Z_{Md} I_{n2} = 0$$

Equ 3.24

Here $Z_0 = j\omega L + 1/j\omega C$ is the self-impedance of a single element, $Z_{Ms} = j\omega M_s$ is the nearest neighbour mutual inductance between elements of a single waveguide, and $Z_{Md} = j\omega M_d$ is the nearest neighbour mutual inductance between the two waveguides. We assume a travelling wave solution for the currents I_{n1} and I_{n2} in the two guides in the form:

$$\begin{pmatrix} I_{n1} \\ I_{n2} \end{pmatrix} = \begin{pmatrix} I_{01} \\ I_{02} \end{pmatrix} \exp(-jnka)$$

Equ 3.25

Substituting this solution into Equ 3.24, we obtain:

$$Z_0 I_{01} \exp(-jnka) + Z_{Ms} I_{01}\{\exp(-j(n-1)ka) + \exp(-j(n+1)ka)\} + Z_{Md} I_{02} \exp(-jnka) = 0$$

Equ 3.26

After some algebraic manipulation we obtain the partial dispersion equation:

$$Z_0 I_{01} + Z_{Ms} I_{01} 2\cos(ka) + Z_{Md} I_{02} = 0$$

Equ 3.27

Carrying out similar steps for the second waveguide we obtain a second partial dispersion equation:

$$Z_0 I_{02} + Z_{Ms} I_{02} 2\cos(ka) + Z_{Md} I_{01} = 0$$

Equ 3.28

These two simultaneous equations can be represented in matrix format as:

$$\bar{\mathbf{Z}}\mathbf{I} = 0$$

Equ 3.29

Where $\bar{\mathbf{Z}}$ is the 2 x 2 matrix:

$$\bar{\mathbf{Z}} = \begin{pmatrix} Z_0 + Z_{Ms}2\cos(ka) & Z_{Md} \\ Z_{Md} & Z_0 + Z_{Md}2\cos(ka) \end{pmatrix}$$

Equ 3.30

And **I** is the column vector:

$$\mathbf{I} = \begin{pmatrix} I_{01} \\ I_{02} \end{pmatrix}$$

Equ 3.31

To obtain a non-trivial solution to Equ 3.29, we can use the condition $\det(\bar{\mathbf{Z}}) = 0$ which gives:

$$[Z_0 + Z_{Ms}2\cos(ka)]^2 - [Z_{Md}]^2 = 0$$

Equ 3.32

Equ 3.32 is a difference between two squares; consequently it has the two solutions:

$$[Z_0 + Z_{Ms}2\cos(ka)] \pm Z_{Md} = 0$$

Equ 3.33

Now substituting the values for Z_0, Z_{Ms} and Z_{Md} we get:

$$j\omega L - \frac{j}{\omega C} + 2j\omega M_s\cos(ka) \pm j\omega M_d = 0$$

Equ 3.34

Which after algebraic manipulation yields the dispersion relationship as

$$\frac{\omega_\mu}{\omega_0} = \frac{1}{\sqrt{1 + \kappa_s\cos(ka) \pm {}^1\!/_2\,\kappa_d}}$$

Equ 3.35

Where $\kappa_s = \frac{2M_s}{L}$ is the coupling coefficient between elements of a single ring and $\kappa_d = \frac{2M_d}{L}$ is the coupling coefficient between the two rings. $ka = \frac{2\mu\pi}{N}$ is the propagation constant and $\mu = 1,2,\ldots,\frac{N}{2} + 1$ is the mode number where N is the number of elements in a single ring, in this case eight.

Therefore, we should expect to see ten modes overall, five symmetric modes and five anti-symmetric modes, each with its own resonance. Following further manipulation of Equ 3.27 and Equ 3.28, it can be shown that there are two current patterns, with $I_{01} = \pm I_{02}$, associated with the symmetric and anti-symmetric modes respectively.

Taking into account higher order coupling as well, it is straightforward to show that the dispersion equation becomes:

$$\frac{\omega_\mu}{\omega_0} = \frac{1}{\sqrt{1 + \sum_{m=1}^{N/2} \kappa_{sm} \cos\left(\frac{2\pi\mu m}{N}\right) \pm \left[\frac{\kappa_{d1}}{2} + \sum_{m=2}^{N/2+1} \kappa_{dm} \cos\left(\frac{2\pi\mu(m-1)}{N}\right)\right]}}$$

Equ 3.36

Figure 3.23 shows the dispersion diagram, assuming the following parameters: κ_{sm} the m^{th} order intra-ring coupling coefficient, κ_{sm} the m^{th} order inter-ring coupling coefficient, N the number of coils in a single MI ring resonator, and μ the mode number. In contrast to the single-ring case, there are two branches, with the branch corresponding to the symmetric modes being generally higher in frequency than the branch for the anti-symmetric modes. For this configuration, the variation obtained by including higher order coupling coefficients (drawn in black) is very similar to the corresponding variation obtained assuming nearest neighbours alone (red).

Focusing on the former, we notice that some modes are close to each other in frequency and may actually appear as a single resonance in the mode spectrum. These are the first anti-symmetric mode and the second symmetric mode; and the zeroth anti-symmetric mode and the first symmetric mode. The required mode to couple to the rotating dipoles in the body during detection is the first anti-symmetric mode and it is essential that it is discernible from the other modes.

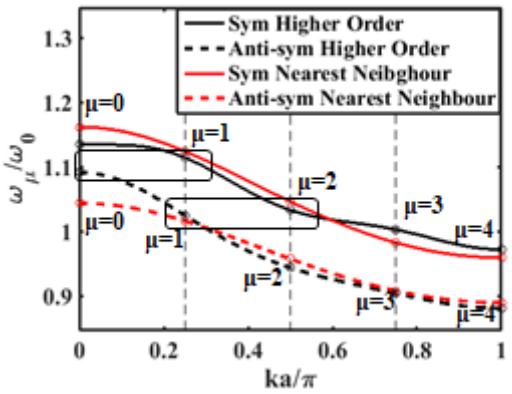

Figure 3.23 Dispersion diagrams for coupled MI ring resonators based on Type A elements.

3.4.2 Symmetric and Anti-symmetric Modes

Theory

The mode spectrum for a coupled MI ring resonator system can be predicted theoretically using an extension to the methods used for the single MI ring case. The set-up is shown in Figure 3.24 (a), where the two rings are assumed to lie on top of each other and the transducers can couple separately to either of the rings. The Z-matrix in this case then becomes an 18×18 matrix: the upper left 16×16 matrix is for the elements of the two rings and the last two rows and columns are reserved for the transducers.

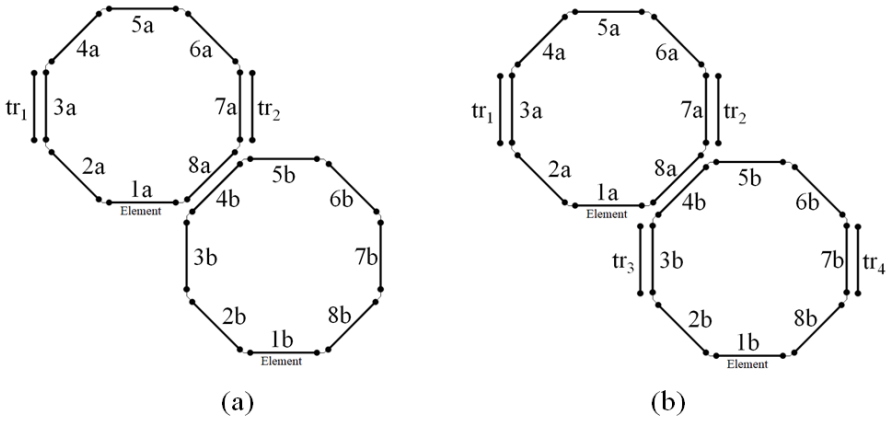

Figure 3.24 Set-up for exciting two MI rings. Ring a is at the bottom and ring b is at the top. (a) Exciting all resonant modes. (b) Exciting symmetric and anti-symmetric modes separately.

Figure 3.25 shows the frequency variation of S_{21} for a coupled MI ring resonator system based on Type A elements obtained in this way. Here there are only nine visible resonances and it is unclear which resonance belongs to which mode. In order to clarify this, the symmetric and anti-symmetric modes must be excited separately.

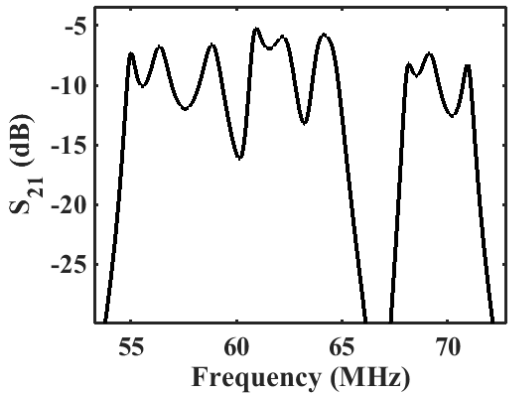

Figure 3.25 Simulated frequency dependence of S_{21} for a coupled MI ring resonator system based on Type A elements.

Figure 3.24 (b) shows the arrangement for exciting each type of mode separately. Here we make use of an extra two transducers positioned opposite elements 3b and 7b. Coils tr_1 and tr_3 are used as transmitters and tr_2 and tr_4 as receivers. To excite the symmetric modes only, the same voltage is applied to tr_1 and tr_3 such that $V_{tr1} = V_{tr3} = 1$. Conversely to excite the anti-symmetric modes only, the

opposite voltage is applied to tr_1 and tr_3 such that $V_{tr1} = -V_{tr3} = 1$. We can receive either with tr_2 or tr_4 with no difference to the results.

Figure 3.26 shows the resulting frequency dependence of S_{21}, with results for symmetric and anti-symmetric modes plotted separately in red and black, respectively. As expected, the symmetric modes are generally higher up in frequency than the anti-symmetric modes and there are five of each, yielding ten modes overall. The plot resembles that seen in Figure 3.25. However, it can be clearly seen that the resonances of symmetric mode 2 and anti-symmetric mode 1 are very close to each, and merge together when all modes are excited simultaneously. Similarly, symmetric mode 1 and anti-symmetric mode 0 are also very close, as expected from the dispersion relationship in Figure 3.23.

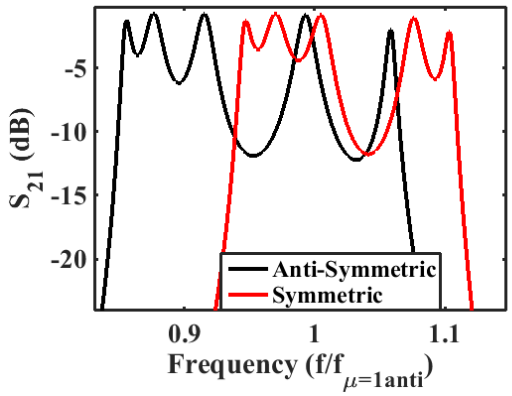

Figure 3.26 Simulated mode spectra for a coupled MI ring system, with the symmetric and anti-symmetric modes super-imposed

It is desirable to be able to pinpoint the symmetric and anti-symmetric modes without having to excite each separately as has been done above. To that end, we need the last symmetric mode ($\mu = \frac{N}{2} = 4$) to be higher up in frequency than the zeroth anti-symmetric mode ($\mu = 0$). This requires:

$$\frac{\omega_{\mu=N/2}}{\omega_0}_{\text{Sym}} > \frac{\omega_{\mu=0}}{\omega_0}_{\text{Anti}}$$

Equ 3.37

Substituting in the dispersion equation with the correct sign for the symmetric and anti-symmetric modes, we get:

$$\frac{1}{\sqrt{1+\kappa_s\cos(ka_{sym})+\frac{1}{2}\kappa_d}} > \frac{1}{\sqrt{1+\kappa_s\cos(ka_{anti})-\frac{1}{2}\kappa_d}}$$

Equ 3.38

We can remove the division by inverting the greater than sign. Removing the square root and substituting the correct values for the modes, we then get:

$$\kappa_s \cos\left(\frac{2\pi\, {}^{N}/_{2}}{N}\right) + \frac{1}{2}\kappa_d < \kappa_s \cos\left(\frac{2\pi.0}{N}\right) - \frac{1}{2}\kappa_d$$

Equ 3.39

Finally, solving the inequality leads to the following relationship in between the first order intra-ring and inter-ring coupling coefficients:

$$2\kappa_s > \kappa_d$$

Equ 3.40

Note that here both κ_s and κ_d are negative values, and so in absolute values we would need to fulfil the condition in Equ 3.41, which states that the coupling between the two rings must be stronger than twice the coupling between individual elements in a single ring, or:

$$2|\kappa_s| < |\kappa_d|$$

Equ 3.41

This condition only holds exactly with nearest neighbour elements alone, but is still a good guide when including higher order coupling too. To achieve it in practise, we need elements whose extent along the ring circumference is greater than that in the perpendicular direction. Figure 3.27 shows a FastHenry model of a coupled ring system based on such elements, with L_v = 16 mm and L_h = 64 mm. It is clear that the overall device must now be relatively large in diameter, and shallow.

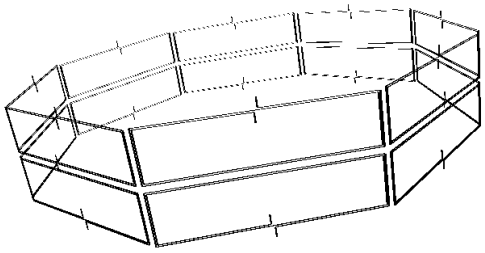

Figure 3.27 FastHenry model of a coupled ring configuration with L_v = 16 mm and L_h = 64mm and two-turn coils

Figure 3.28 (a) shows the dispersion relationship for this device calculated from known coupling coefficients. The two sets of modes are now well separated in frequency, with all the symmetric modes being higher up in frequency than the anti-symmetric modes. This is confirmed by the mode spectra shown in Figure 3.28 (b). Even when all the modes are excited at the same time, the mode needed for MRI signal detection (the anti-symmetric mode with μ=1) can be recognised easily.

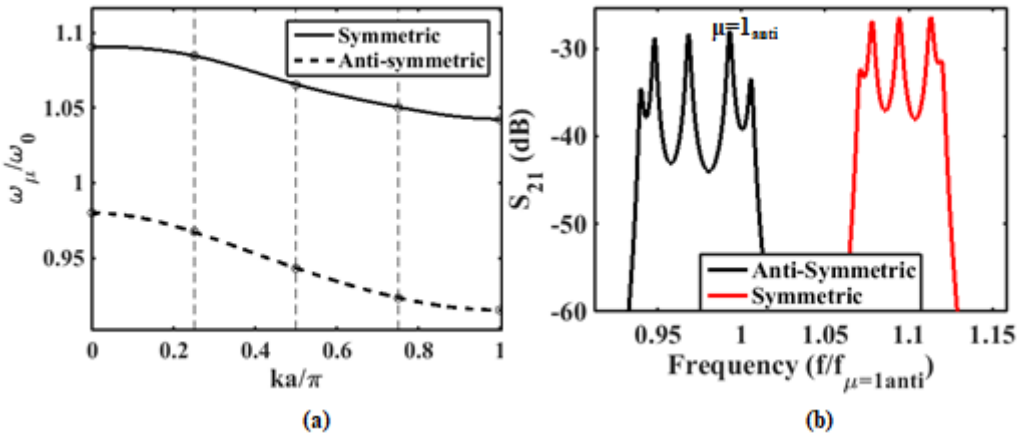

Figure 3.28 Simulated (a) Dispersion diagram and (b) mode spectra for coupled MI ring system based on high aspect ratio elements.

Experiment

We now need to confirm the results obtained theoretically with experimental measurements. To that end, two coupled MI ring resonators were constructed using the rig in **Figure 3.6**(b). One is made from type A elements and one from type B elements.

The set-up for measuring mode spectra has previously been shown in **Figure 3.6** (a). Figure 3.29 shows the results for devices made with both Types of element. For the system made from Type A elements, there are eight visible resonances; however, again due to the poor Q-factor at the band edges, the lowest frequency resonance cannot be clearly distinguished. For the Type B system, there are also eight visible resonances. Comparing the two, we can see that reduced first order intra-ring coupling has again made the bandwidth of the Type A device less than that of the Type B device. Additionally, the Q-factor for all resonances is generally less for Type A than Type B.

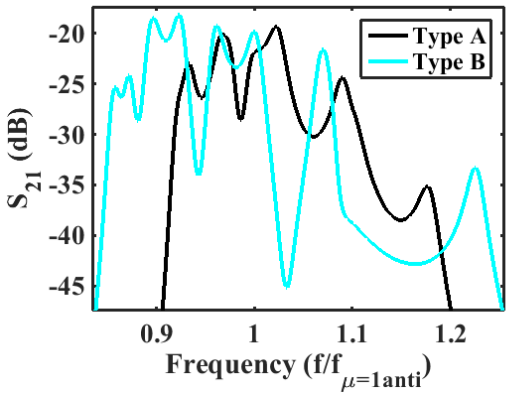

Figure 3.29 Measured mode spectra for coupled MI ring resonator systems made from type A and type B elements.

The next step is to determine which resonances correspond to the symmetric mode and which to the anti-symmetric mode. As previously discussed, we need two transmitters to excite the symmetric and

anti-symmetric modes separately. Figure 3.30 shows two suitable arrangements. The symmetric configuration mimics a single large transducer, exciting both rings equally. The anti-symmetric configuration mimics a figure-of-eight shaped transducer, exciting each ring with opposite polarity.

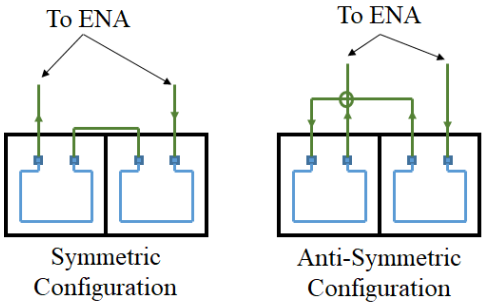

Figure 3.30 Transducer configurations used to excite symmetric and antisymmetric modes separately.

Practically, transducer positions are adjusted until only the required modes are visible. **Figure 3.31** shows the resulting mode spectra. **Figure 3.31** (a) shows results for Type A elements, and **Figure 3.31** (b) for type B elements. In each case, the highest order resonance (at the lowest frequency) is barely visible. Again, this is due to high attenuation at the band edges following from the low Q-factor. Apart from this, five resonances are visible for each type of mode. When superimposed, these sets do make the same plot as for the full excitation. Unfortunately, the first anti-symmetric mode (arrowed) is still buried among other resonances. Consequently, it may be difficult isolate it and reject other modes.

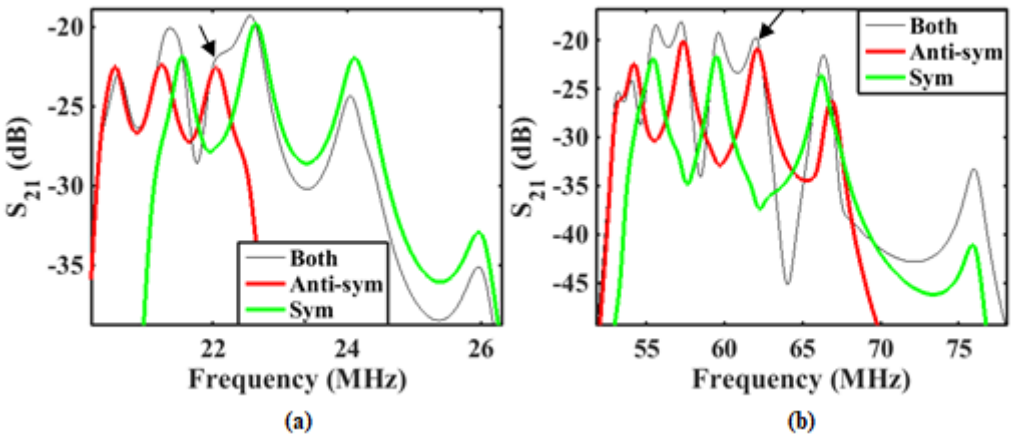

Figure 3.31 Measured S-Parameters showing the symmetric and anti-symmetric modes excited separately (a) rings made from type A elements. (b) rings made from type B elements.

Comparison with theory

In order to be certain of the position of each resonant mode, we compare the theory with the experimental results. Figure 3.32 (a) compares the complete experimental and theoretical mode

spectra for the Type A device and Figure 3.32 (c) does the same for the Type B device . Here, the experimental coupling coefficients, inductances and resistances have been used to produce the theoretical plots. There is good agreement between the theoretical and experimental results. Small discrepancies could be attributed to slight errors in the position of the transducers, which affects the relative height of resonant peaks. Figure 3.32 (b) and (d) shows the separate spectra for symmetric and anti-symmetric modes in the Matlab simulation. The plots indicate that the first anti-symmetric mode is at the fourth highest resonance for the Type A device and the sixth highest resonance for the Type B device, in agreement with experimental observation. Consequently, although we have ascertained the position of the first anti-symmetric mode, it is clear that it will be very difficult to reject nearby modes since they are so close in frequency.

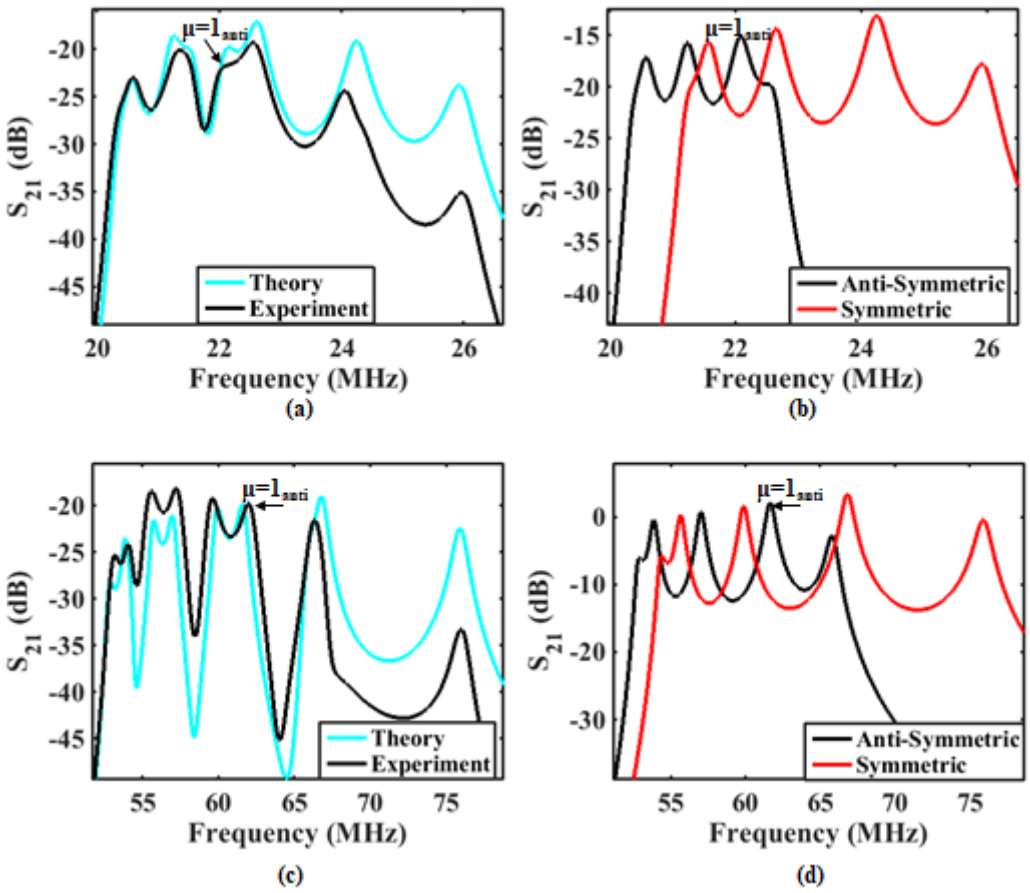

Figure 3.32 (a),(c) Comparison of the experimental and Matlab simulated S_{21} plots for type A and type B double MI ring device respectively (b),(d) Isolating the symmetric and anti-symmetric modes in simulation for the type A and type B respectively

3.4.3 Improved Design

The results above suggest that the assumed PCB layout has been only partially successful in isolating the important first-order anti-symmetric mode from other neighbouring modes. An improved design is therefore required to increase the mode separation.

Closer PCB Elements

We first investigate the effect of increasing the coupling between the elements of a single ring. To do this, the edges of Type A PCB elements were filed away, to allow closer fitting, and mounted in a modified baseplate. Figure 3.33 shows the mode spectrum of the resulting coupled ring system. It was expected that the bandwidth of the new device would be larger than the original device and therefore that the first anti-symmetric mode would be easier to isolate. Indeed this is the case, however, the resonances visible are now also different, since the ratio of κ_s/κ_d has now also changed. The first anti-symmetric mode is too close to the second symmetric mode. Therefore, even with this new design it may not be possible to isolate the first-anti symmetric mode in the MRI scanner.

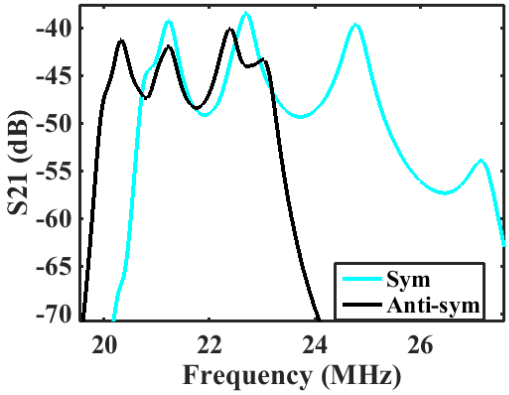

Figure 3.33 Mode spectrum for improved coupled MI ring system, showing improved separation of symmetric and anti-symmetric modes.

Horizontally Arranged Elements

Another way to increase isolation of the first anti-symmetric mode is to separate the symmetric and anti-symmetric modes further in frequency by altering the aspect ratio of the elements as previously shown in Figure 3.27. Taking the current dimensions of the element types available into account, we concentrate on elements of type B. Figure 3.34 (a) shows how these may be arranged 'horizontally' to achieve the requirement of $|\kappa_{d1}| > |2\kappa_{s1}|$.

Figure 3.34 (b) shows the resulting mode spectrum. Here it can be seen that increased separation of the symmetric and anti-symmetric modes has indeed been achieved, with the five symmetric resonances clearly visible (the lowest frequency symmetric resonance has low Q-factor as previously discussed). However, the anti-symmetric modes are now much closer together, occupying a much smaller bandwidth, which does not help in isolating the first anti-symmetric mode. Even though this experiment is quite crude, it allows us to conclude that it is not simply the separation of the symmetric and anti-symmetric modes that will allow isolation of the first anti-symmetric mode, but we also require the first anti-symmetric mode resonances to occupy a larger bandwidth. Methods of achieving this are considered in the next Chapter.

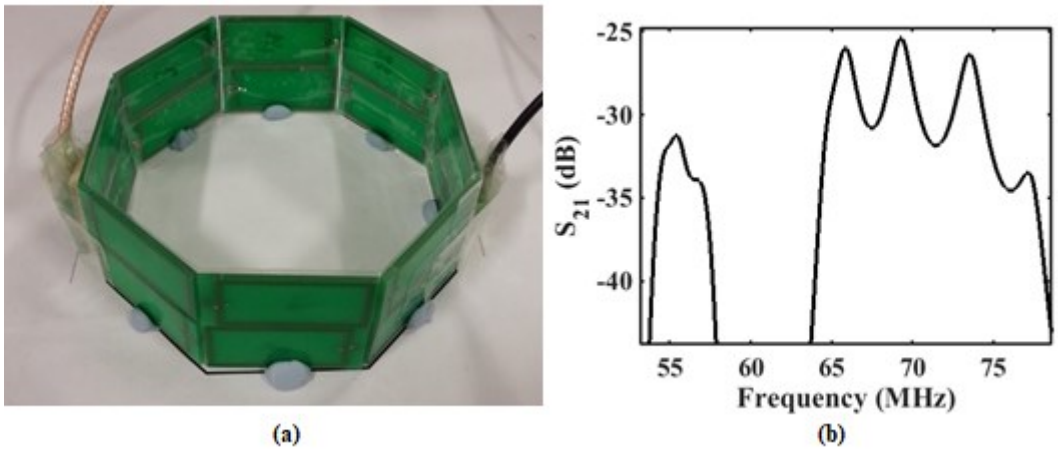

Figure 3.34 (a) Coupled MI ring resonator system constructed from Type B elements arranged horizontally (b) corresponding frequency variation of S_{21}

4 Manipulating the Mode Spectrum

We have previously seen that the coupling together of two magneto-inductive rings introduces an additional dimension to the spatial structure of resonant modes. Particularly, the existence of an anti-symmetric mode, which can be used for local signal detection but which will reject uniform fields, potentially provides a mechanism for purely passive decoupling. However, the close separation in frequency of other modes (including a spatially symmetric mode that will most definitely couple to B_1 fields) reduces the effectiveness of this decoupling mechanism, allowing RF heating and generation of local artefacts. In this Chapter, we explore different possibilities for manipulating the mode spectrum, to maximise decoupling effects. We first perform a detailed survey of the doubly planar coupling geometry considered so far. We then introduce a more effective alternative, involving a mixture of axial and planar coupling. Finally, we present an experimental demonstration to confirm theoretically predicted performance.

4.1 Rejection of Symmetric Modes

We have so far constructed two devices, one made from square and the other from rectangular coils. Both have their resonant elements coupled in a quasi-planar configuration, for both intra- and inter-ring coupling, and their mode spectra confirm that the first anti-symmetric mode is too close in frequency to other modes. In fact, the decoupling performance of any design may be evaluated in terms of the rejection of other modes at the resonant frequency of the first anti-symmetric mode.

Rejection may be quantified from the mode spectrum, in terms of the difference in magnitude between the resonant peak of the first anti-symmetric mode, and response of the nearest unwanted symmetric mode. For example, Figure 4.1 shows the mode spectrum for a Type A device, measured as described before and separated into symmetric and anti-symmetric groups. To avoid direct coupling to the lowest order symmetric mode, its rejection should be at least 30 dB, so that induced voltages are reduced by a factor of $\sqrt{10^3} = 31.6$. However, the rejection here, indicated by the arrowed line, is only 7 dB. To increase the rejection, we should try to achieve both of the following: (a) complete frequency separation of the symmetric and anti-symmetric modes and (b) an increase in bandwidth of the anti-symmetric mode spectrum, separating individual modes further in frequency.

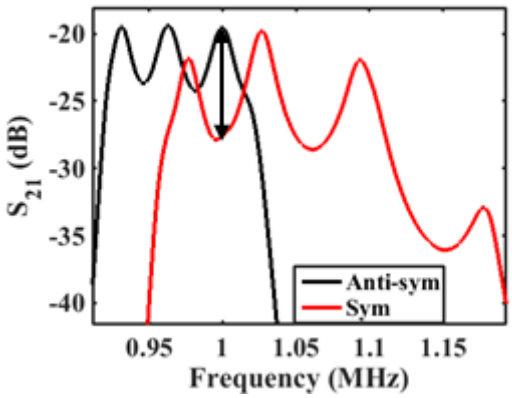

Figure 4.1 Mode spectrum for a coupled MI ring system made with Type A elements.

We study the first point by considering the dispersion relationship for a coupled MI ring system given again in Equ 4.1, where κ_{sm} is the m^{th} order intra-ring coupling coefficient, κ_{dm} is the m^{th} order inter-ring coefficient, μ is the mode number and the positive sign is used for the symmetric modes and the negative for the anti-symmetric modes.

$$\frac{\omega_{\mu\pm}}{\omega_0} = \frac{1}{\sqrt{1 + \sum_{m=1}^{N/2} \kappa_{sm} \cos\left(\frac{2\pi\mu m}{N}\right) \pm \left[\frac{\kappa_{d1}}{2} + \sum_{m=2}^{N/2+1} \kappa_{dm} \cos\left(\frac{2\pi\mu(m-1)}{N}\right)\right]}}$$

Equ 4.1

To isolate symmetric and anti-symmetric modes, we must satisfy the condition in Equ 4.2, which implies that the last symmetric mode has a higher resonant frequency than the zeroth anti-symmetric mode:

$$\frac{\omega_{\mu+=4}}{\omega_0} > \frac{\omega_{\mu-=0}}{\omega_0}$$

Equ 4.2

Substituting the relevant mode numbers into the dispersion relation then yields the inequality in Equ 4.3, a condition on the coupling coefficients themselves rather than the mode frequencies:

$$1 + \sum_{m=1}^{4} \kappa_{s\,m} \cos\left(\frac{2\pi m \,.\, 4}{8}\right) + \frac{\kappa_{d1}}{2} + \sum_{m=2}^{5} \kappa_{d\,m} \cos\left(\frac{2\pi(m-1) \,.\, 4}{8}\right)$$
$$> 1 + \sum_{m=1}^{4} \kappa_{s\,m} \cos\left(\frac{2\pi m \,.\, 0}{8}\right) - \frac{\kappa_{d1}}{2} - \sum_{m=2}^{5} \kappa_{d\,m} \cos\left(\frac{2\pi(m-1) \,.\, 0}{8}\right)$$

Equ 4.3

Equ 4.3 may be simplified as follows. The cosine of an even multiple of π is unity, while the cosine of an odd multiple of π is -1. Thus the left hand side of the inequality can be written out as 1 - κ_{s1} + κ_{s2} -

$\kappa_{s3} + \kappa_{s4} + \kappa_{d1}/2 - \kappa_{d2} + \kappa_{d3} - \kappa_{d4} + \kappa_{d5}$. Using the additional condition that cos(0) = 1, the right hand side can be simplified to $1 + \kappa_{s1} + \kappa_{s2} + \kappa_{s3} + \kappa_{s4} - \kappa_{d1}/2 - \kappa_{d2} - \kappa_{d3} - \kappa_{d4} - \kappa_{d5}$. Cancellation then yields the surprisingly simple result shown in Equ 4.4:

$$\kappa_{d1} + 2\kappa_{d3} + 2\kappa_{d5} < 2\kappa_{s1} + 2\kappa_{s3}$$

Equ 4.4

However, it is usually the case that the coupling coefficients reduce in magnitude as their order increases, so that κ_{d1} is much greater than κ_{d3} and κ_{d5}, while $\kappa_{s1} >> \kappa_{s3}$. Equ 4.4 therefore simplifies to Equ 4.5, the conclusion previously reached for the nearest-neighbour approximation in Chapter 3.

$$\kappa_{d1} < 2\kappa_{s1}$$

Equ 4.5

It is important to note that both κ_{s1} and κ_{d1} are negative here. If κ_{s1} is positive instead, the dispersion diagram will alter, with each branch tending to that obtained for an axially-coupled MI waveguide. For example, Figure 4.2 shows the dispersion diagram obtained for the typical parameters $\kappa_{s1} = + 0.2$ and $\kappa_{d1} = -0.2$. Here we note that the lowest-order mode of the anti-symmetric branch (arrowed) is now at a much lower frequency than was seen in the planar-planar case, separating it further from nearby modes.

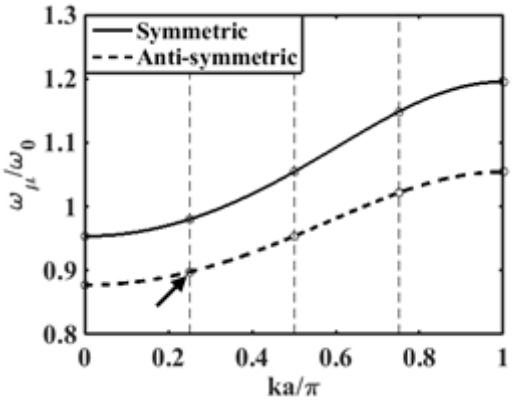

Figure 4.2 Dispersion diagram for a coupled MI ring resonator system with $\kappa_{s1} = 0.2$ and $\kappa_{d1} = -0.2$.

To separate the symmetric and anti-symmetric modes completely, we must now satisfy the condition in Equ 4.6. Here the zeroth symmetric mode must be higher in frequency than the last anti-symmetric mode.

$$\frac{\omega_{\mu+=0}}{\omega_0} > \frac{\omega_{\mu-=4}}{\omega_0}$$

Equ 4.6

After similar manipulations and approximations, we obtain:

$$2\kappa_{s1} < -\kappa_{d1}$$

Equ 4.7

It is clear that Equ 4.5 and Equ 4.7 are the same in terms of absolute value. Therefore, we reach the general conclusion that the requirement for separating the two mode spectra is:

$$2|\kappa_{s1}| < |\kappa_{d1}|$$

Equ 4.8

We now consider the second point of increasing the bandwidth of the anti-symmetric modes. This can most directly be achieved by increasing the first-order coupling coefficient, κ_{s1}. Figure 4.3 illustrates this by showing the dispersion diagrams of two different coupled MI ring systems. In each case, κ_{d1} = -0.2; however in Figure 4.3 (a) κ_{s1} = -0.15, while in Figure 4.3 (b) κ_{s1} = -0.3. Numerical extraction then suggests that the increase in first order intra-ring coupling coefficient between (a) and (b) doubles the normalised bandwidth from $\Delta\omega/\omega_0$ = 0.13 to 0.27.

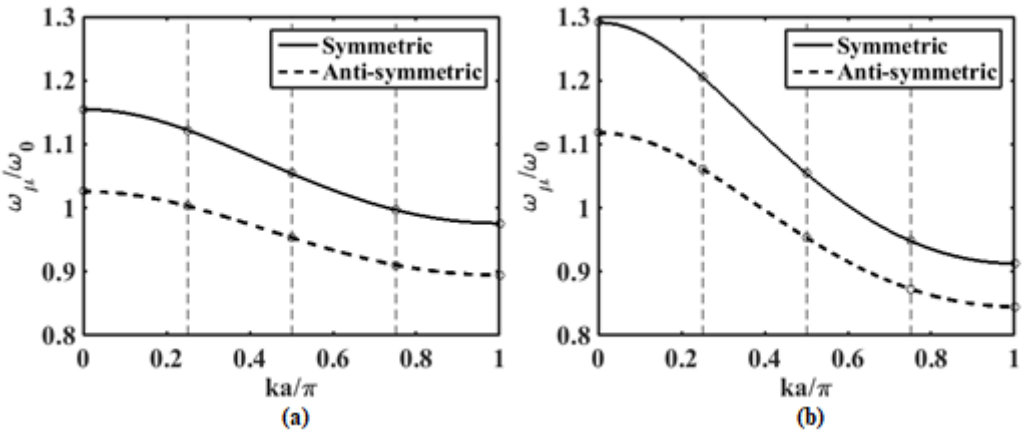

Figure 4.3 Dispersion diagram for coupled MI ring systems with κ_{d1} = -0.2 and (a) κ_{s1} = -0.15, (b) κ_{s1} = -0.3.

In practice, however, the first-order intra-ring coefficients can only be increased by reducing the element separation, and the achievable increase may still be insufficient. Another much more effective method is to use positive coupling, previously exploited in MI cables [189] and achieved by overlapping the intra-ring elements. For example, Figure 4.4 (a) and (b) compare planar and quasi-axial configurations for single-turn rectangular elements, with L_v and L_h being the vertical and horizontal length, respectively, and d being the overlap (or, if negative, the separation). Note that a vertical offset has been introduced in Fig. 4b for clarity; in practise, a similar offset will be required to minimise parasitic capacitance [200], as discussed later.

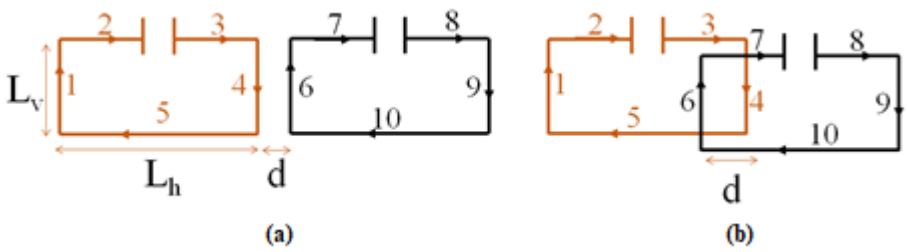

Figure 4.4 (a) Planar and (b) axial configurations for a single pair of rectangular elements.

The total mutual inductance between these two coils, M, can be described as the sum of the mutual inductances between the individual wires of the elements as shown in Equ 4.9. Here $M_{p,q}$ is the mutual inductance between individual wires p and q, with the contribution being positive when the current in the two wires is flowing in the same direction, and negative otherwise.

$$M = M_{1,6} + M_{4,9} - M_{4,6} - M_{1,9} + M_{5,10} + M_{2,7} + M_{2,8} + M_{3,7} + M_{3,8}$$

Equ 4.9

With no overlap, $M_{4,6}$ is the strongest term and the overall mutual inductance is therefore negative. In fact, it is so much larger than $M_{1,6}$, $M_{4,9}$, $M_{5,10}$ and $M_{3,7}$ that these terms can normally be ignored. However, as the coils are overlapped and the distance d increases, $M_{4,9}$ and $M_{1,6}$ increase, as well as $M_{3,7}$ and $M_{5,10}$. At a particular value of d, $M_{4,9} + M_{1,6} + M_{3,7} + M_{5,10}$ starts to exceed $M_{4,6} + M_{1,9}$, making the total mutual inductance positive. A promising strategy to isolate the first anti-symmetric mode may therefore be to use MI ring resonators with overlapping intra-ring elements to maximise bandwidth, and balance the large value of κ_{s1} needed with a large value of κ_{d1} to separate the symmetric and anti-symmetric mode spectra. We now investigate this strategy in detail.

4.2 Design Considerations

To try to identify the optimum design, we investigate the effect of the dimensions L_v and L_h and spacings d of single-turn rectangular elements on their characteristics. To do this, many coil geometries were simulated with FastHenry and Matlab using methods previously described. The results are presented in the form of parameter variations, dispersion diagrams and mode spectra. The variations examined are as follows:

Firstly, the dimensions L_v and L_h of the individual elements are altered, to determine the dependence of inductance, resistance and coupling coefficients on these dimensions. It is particularly expected that at some ratio L_v/L_h, the inter-ring coupling coefficient will be twice that of the intra-ring coefficient, separating the symmetric and anti-symmetric modes completely in frequency. Secondly, the loop area $L_v \times L_h$ is varied and it is expected that a different set of coupling coefficients will be found. Thirdly, the elements of a single ring will be overlapped, with the aim of increasing the bandwidth of the anti-

symmetric mode. Finally, the two rings will themselves be overlapped to observe what effect this will have on rejection and whether it could offer any improvement.

4.2.1 Coil Dimensions

We start by varying the ratio L_v/L_h, keeping the area of the loop, $L_v \times L_h$, constant. At this stage, a large variation in L_v/L_h is used, however, in reality this range is constrained due to the requirement for compatibility with the BAR. Table 1 shows the values of L_v, L_h and L_v/L_h investigated. In each case, a coupled MI ring resonator system was simulated in FastHenry, and the inductance, resistance and coupling coefficients were extracted. Here the track width is 0.5 mm, the thickness is 35 μm and a copper conductivity of 5.96×10^7 Sm^{-1} is used. The distance between the first neighbouring inter- and intra-ring elements is kept at 2 mm (except when there is overlap, as discussed in the next sections).

Table 4.1 Dimensions of investigated elements.

L_v (mm)	L_h (mm)	L_v / L_h
5	102.4	0.05
10	51.2	0.20
15	34.1	0.44
20	25.6	0.78
25	20.5	1.22
35	14.6	2.39
40	12.8	3.13
60	8.5	7.03
100	5.1	19.53

Figure 4.5 shows the variation of the self-inductance, L, for a rectangular coil, as a function of the aspect ratio L_v/L_h, plotted using a logarithmic scale for the x-axis. It is clear that the variation is a quadratic, whose symmetry merely reflects the fact that the self-inductance cannot depend on whether the element is 'standing up' or 'lying down'.

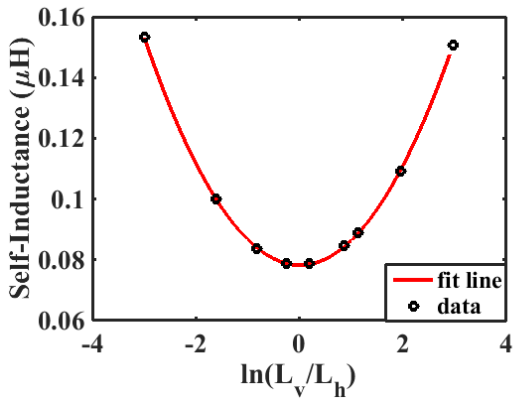

Figure 4.5 Variation of self-inductance with $\ln(L_v/L_h)$.

Of course, it is well known that the inductance of a wire is inversely proportional to its length, and this seems to be mirrored in these results; the square coil has the minimum perimeter, and consequently minimum inductance. In fact, an analytic equation of the self-inductance of a rectangular coil with tracks of rectangular cross-section is also known, and shown in Equ 4.10, where μ_0 is the free-space permeability, and w and h are the width and height of the track [201]:

$$L = \frac{\mu_0}{\pi}\left[\begin{array}{l} -2(L_h + L_v) + 2\sqrt{{L_v}^2 + {L_h}^2} - L_v \ln\left(\frac{L_v + \sqrt{{L_v}^2 + {L_h}^2}}{L_h}\right) \\ -L_h \ln\left(\frac{L_h + \sqrt{{L_v}^2 + {L_h}^2}}{L_v}\right) + L_v \ln\left(\frac{2L_v}{w+h}\right) + L_h \ln\left(\frac{2L_h}{w+h}\right) \end{array}\right]$$

Equ 4.10

Numerically, we have verified that the variation of inductance with element dimensions predicted using Equ 4.10 matches that obtained using FastHenry. Figure 4.5 (b) shows the results plotted in red over the simulated points. Those are obtained using the parameters w = 0.5 mm, h = 35 μm, with L_v ranging from 5 mm to 100 mm in steps of 1 mm.

We now consider the self-resistance of the rectangular coil. Figure 4.6 shows its variation with the aspect ratio L_v/L_h. Here we see a similar variation to the self-inductance, and a best-fit quadratic polynomial is plotted in red over the simulated results. The resistivity of a wire is inversely proportional to its length and therefore we see a quadratic relationship between R and the natural logarithm of L_v/L_h, with a minimum at $L_v/L_h = 1$, again illustrating that the resistance is the same whether the coil is 'standing up' or 'lying down'.

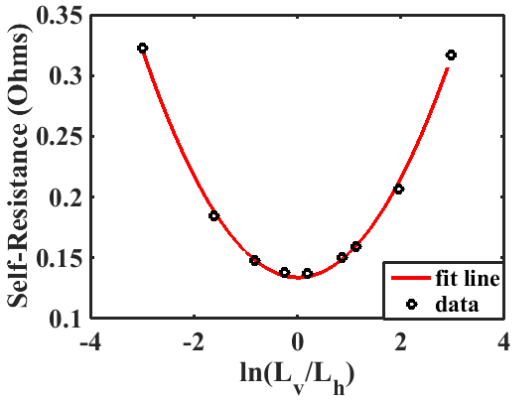

Figure 4.6 Variation of self-resistance with L_v / L_h.

We continue, using FastHenry models of the coupled MI ring resonator system, to calculate the intra- and inter-ring coupling coefficients and their variation with element dimensions. It is expected that all

intra-ring coefficients increase as L_v (and therefore L_v/L_h) increases. Figure 4.7 (a) and (b) show the variation of κ_{s1}, and κ_{s2} and κ_{s3} with L_v/L_h, for the same track and separation parameters as before. Here we have plotted best-fit curves over the simulated results to aid in pattern visualization. As L_v increases, all the intra-ring coupling coefficients increase negatively, with the negative sign resulting from the quasi-planar configuration in a single ring. From the scale of the y-axis, we see that κ_{s1} is much greater than κ_{s2} and κ_{s3}, and that κ_{s2} is greater than κ_{s3}.

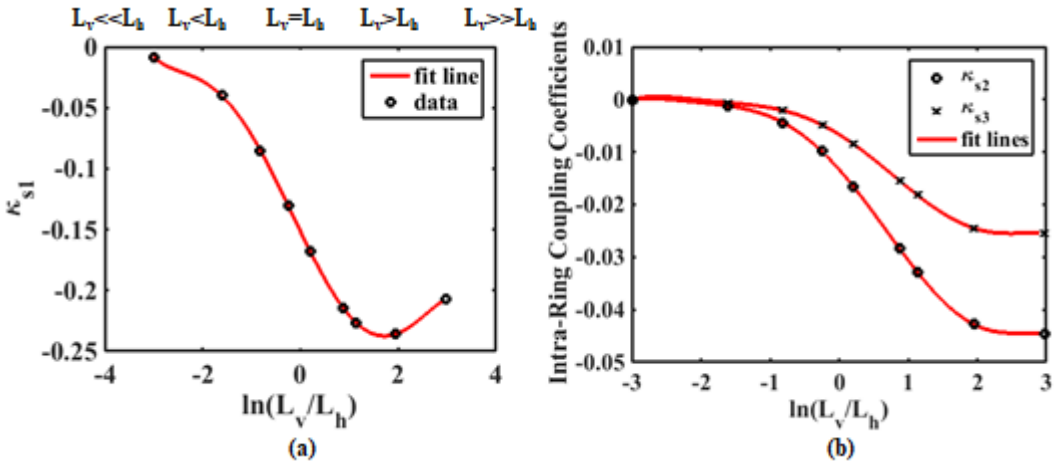

Figure 4.7 Variation of (a) first order and (b) second and third order intra-ring coupling coefficients with L_v/L_h.

From Figure 4.7 (a), we observe that when L_v is very large and L_h is very small (equal to 100 mm and 5.12 mm, for example), the magnitude of the first-order coefficient decreases again. This can be understood by first observing the variation of the first-order intra-ring mutual inductance with L_v/L_h as seen in Figure 4.8. Here it can be seen that the mutual inductance is monotonically decreasing as expected. It, therefore, becomes clear that the decrease in magnitude of κ_{s1} – for very large L_v – is due to the large increase in magnitude of the self-inductance as seen in Figure 4.5.

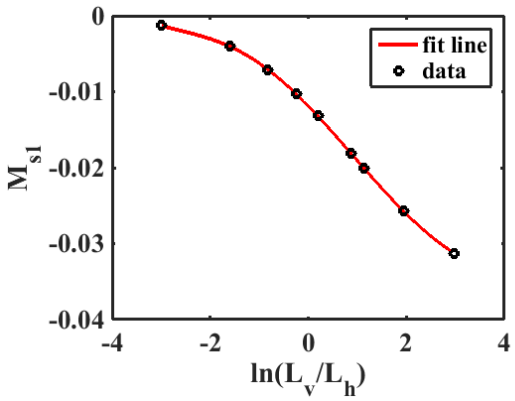

Figure 4.8 Variation of the first order intra-ring mutual inductance with L_v/L_h.

We now consider the coupling between the two different MI ring resonators. Figure 4.9 (a) shows the variation of the first order inter-ring coupling coefficient with the ratio L_v/L_h. Once again, the same

track parameters have been used, and the inter-ring separation d is assumed to have the same value as the intra-ring separation. A best-fit curve has been matched to the results. Here we see that the variation is opposite to that observed for intra-ring coupling, since inter-ring coupling depends more on changes in L_h rather than L_v. Therefore, κ_{d1} decreases as L_h decreases, and the rate of decrease slows as L_h becomes very small.

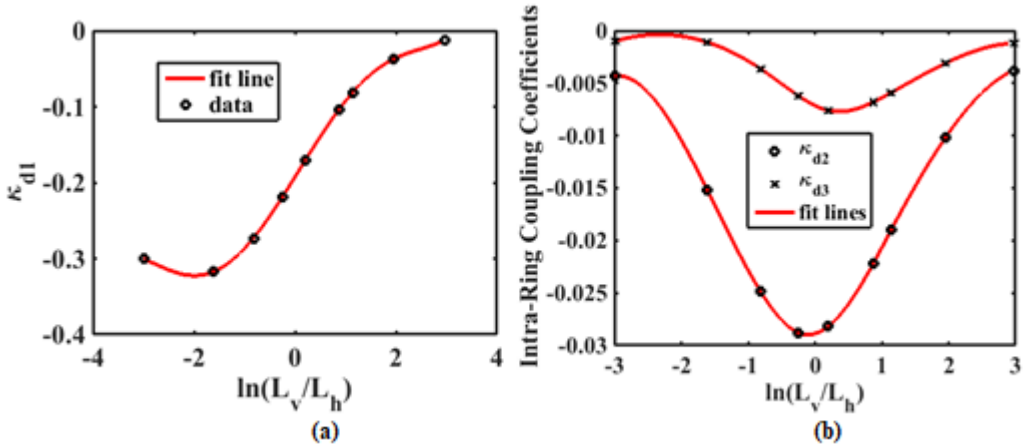

Figure 4.9 Variation of (a) first order and (b) second and third order inter-ring coupling coefficients with L_v /L_h.

As was previously observed, κ_{s1} decreases for very large L_v and small L_h; here κ_{d1} decreases for very large L_h and small L_v. The same reasoning can be applied as before. Figure 4.10 shows the variation of the first order inter-ring mutual inductance with L_v/L_h. As L_h decreases, the magnitude of M_{d1} decreases, again with the rate of decrease reducing as L_h becomes very small. Therefore, the decrease in κd1 for very large Lh is due to the shape of the self-inductance curve shown in Figure 4.5.

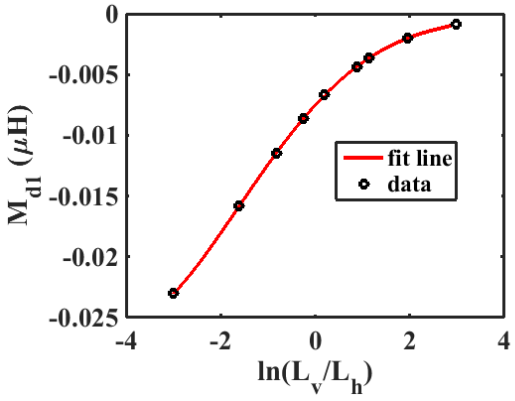

Figure 4.10 Variation of the first order intra-ring mutual inductance with L_v /L_h.

Considering the second and third order inter-ring coupling coefficients, we see a very different pattern for the geometric variation of κ_{d1}. Figure 4.9 (b) shows the variation of κ_{d2} and κ_{d3} with L_v /L_h. Here we see that the second and third order inter-ring coefficients increase in magnitude as L_h becomes smaller, and the elements come closer together. To explain this, we consider Figure 4.11, which

shows a planar view of three pairs of coupled elements from a coupled MI ring resonator system. Here d = 2 mm is the common intra- and inter-ring element separation as before, and L_v and L_h have their usual meaning. We see that as L_h becomes smaller, elements 1a and 2b, and elements 3a and 2b (the second and third inter-ring neighbours respectively) ,move closer together, increasing κ_{d2} and κ_{d3}. However, at approximately $L_v / L_h = 1$, L_h becomes too small to provide much inter-ring coupling. Consequently, the decrease in L_h causes κ_{d2} and κ_{d3} to fall again.

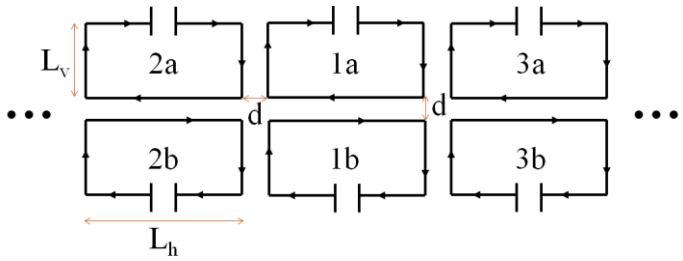

Figure 4.11 Section of a coupled MI ring resonator system

The opposing variations of κ_{s1} and κ_{d1} with element dimensions indicate that there must be a trade-off between the two. Figure 4.12 shows the relation between κ_{s1} and κ_{d1} for two different loop areas $L_v \times L_h$. In each case, the relation is linear in the shaded region, becoming curved for extreme elements. The linear relation is due to the fact that for the same area element, a large L_v is needed for a large κ_{s1}, but this makes L_h small and therefore κ_{d1} small. Similarly to have a strong κ_{d1}, we need a large L_h, which makes L_v smaller, weakening κ_{s1}. When the element area decreases, the extent of the linear region decreases and the compromise becomes larger, thus for the same κ_{s1} we now obtain a weaker κ_{d1}.

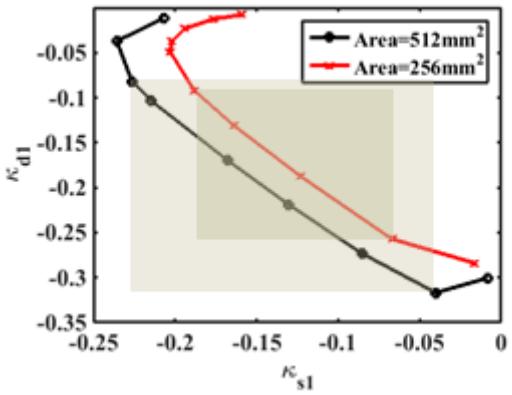

Figure 4.12 Relation between first order inter- and intra-ring coupling coefficients.

4.2.2 Intra-ring Coil Overlap

We now consider the effect of overlapping the elements of each ring resonator in the coupled system. The aim is to reverse the order in frequency of the anti-symmetric modes, lowering the resonance of the first such mode and hence isolating it from others. Figure 4.13 (a) shows a planar view of four

elements from a single ring resonator with intra-ring overlap; and Figure 4.13 (b) shows a plan view of the whole ring. We denote the extent of overlap as L_h/m, where m is a new parameter. To investigate its effect, we consider the values of m = 5 and m = 3, with the latter implying greater overlap. However, we keep to the inter-ring separation fixed at 2 mm.

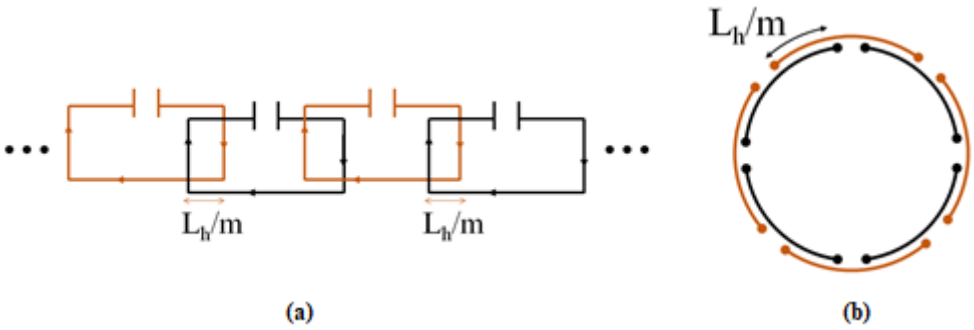

Figure 4.13 (a) Four overlapping elements from the same ring resonator, (b) a plan view of a single ring showing the arrangement of the overlapping elements.

We now investigate the effects of the intra-ring overlap on the characteristics of the elements and the coupling coefficients. Firstly, considering the self-inductance and the self-resistance: these remain constant, no matter how much the elements are overlapped, since these properties are inherent and do not depend on interactions with other elements.

Moving on to the intra-ring coupling coefficients: Firstly, Figure 4.14 shows the variation of the first order coefficient with the ratio L_v/L_h for the cases of i) no overlap and ii) and iii) the two different values of intra-ring overlap. Here, all simulated results are matched to best curve fits. κ_{s1} becomes positive when the elements are overlapped, and increases as the overlap increases. The shape of the plot is approximately the same for the three cases, meaning that when there is an overlap, the positive κ_{s1} actually decreases as L_v/L_h increases. Additionally, when the overlap is $L_h/5$, κ_{s1} is positive when L_v/L_h is very small, decreasing to 0.0084 when L_v = 35 mm and L_h = 14.63 mm. After this, for larger L_v/L_h, κ_{s1} actually becomes negative, increasing in magnitude as L_v/L_h increases.

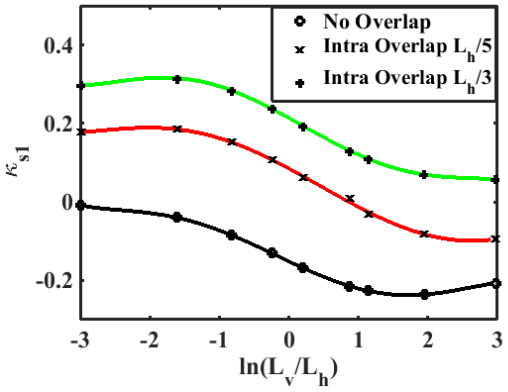

Figure 4.14 Variation of the first order intra-ring coupling coefficient with L_v / L_h, for i) no intra-ring overlap, and overlap of ii) $L_h/5$ and iii) L_h /3.

A possible explanation for the decrease in the positive κ_{s1} as L_v/L_h increases can again be reached by studying Figure 4.4 (b) and considering how the components of M in Equ 4.9 alter with L_v/L_h. As L_v increases and L_h decreases, $M_{1,6}$ and $M_{4,9}$ increase due to the wires getting longer and coming closer together. $M_{4,6}$ and $M_{1,9}$ also increase. On the other hand, $M_{5,10}$ and $M_{3,7}$ decrease since L_h is becoming smaller. Recalling that the elements lie in slightly different planes, the dominant terms are now $M_{5,10}$, $M_{3,7}$ and $M_{4,6}$. The term $M_{4,6}$ subtracts from the overall inductance, while $M_{5,10}$ and $M_{3,7}$ add to it. As L_v/L_h increases, $M_{4,6}$ becomes stronger than $M_{5,10}$ + $M_{3,7}$ and thus the overall mutual inductance decreases, even becoming negative if the overlap is insufficient (as it is for m = 5).

Figure 4.15 (a) and (b) shows the variation of the second and third order intra-ring coupling coefficients respectively with L_v/L_h for the cases of i) no overlap and ii) the same two values of intra-ring overlap. Here, simulated results are matched to a best curve fit. As expected, κ_{s2} and κ_{s3} increase when there is an intra-ring overlap because all the elements of a single ring must come closer together in this case. Additionally, κ_{s2} and κ_{s3} remain negative because there is no overlap between second and third neighbours.

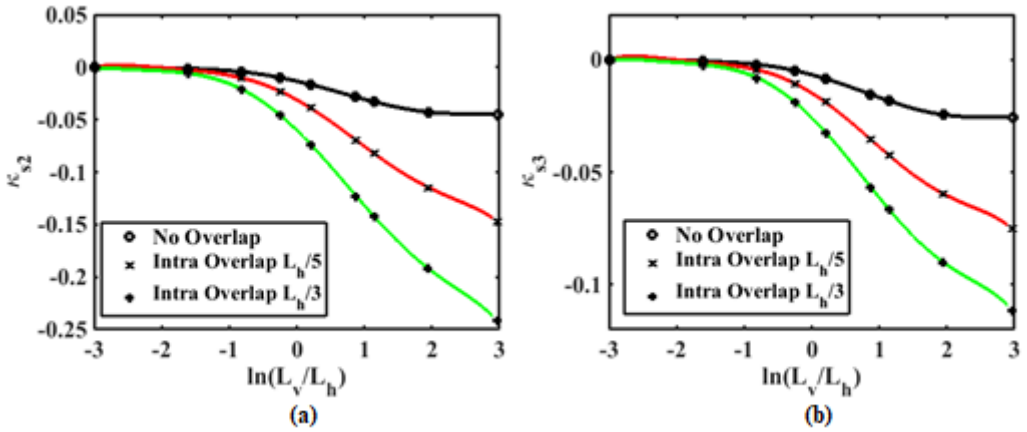

Figure 4.15 Variation of (a) second and (b) third order intra-ring coupling coefficient with L_v/L_h, for the cases of (i) no intra-ring overlap, and overlap of (ii) $L_h/5$ and (iii) $L_h/3$.

We now concentrate on the effect of intra-ring overlap on the inter-ring coupling coefficients. Figure 4.16 (a), (b) and (c) shows the variation of the first, second and third order coupling coefficients respectively with L_v/L_h for i) no overlap and ii) the same two values of intra-ring overlap. From Figure 4.16 (a), we see that the first order inter-ring coefficient, κ_{d1}, remains unchanged, whatever the overlap, clearly because the distance between the first neighbouring inter-ring elements remains unaltered. On the other hand, when there is overlap, the second and third inter-ring neighbours move closer together, so κ_{d2} and κ_{d3} become stronger as seen in Figure 4.16 (b) and (c).

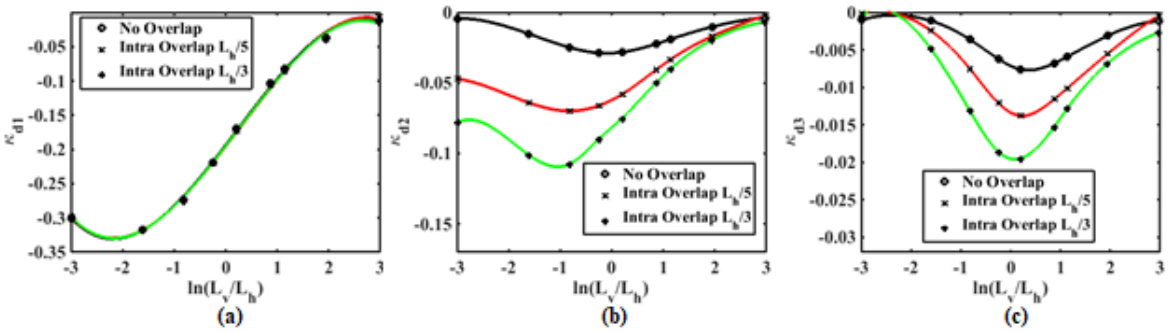

Figure 4.16 Variation of (a) first, (b) second and (c) third order inter-ring coupling coefficient with L_v/L_h, for (i) no intra-ring overlap, and overlap of (ii) $L_h/5$ and (iii) $L_h/3$.

Since κ_{d1} has remained the same with intra-ring overlap, while κ_{s1} has become positive and increased, we expected the 'locus' of the relationship between κ_{s1} and κ_{d1} to have retained approximately the same shape, but have shifted to the right. Figure 4.17 shows the effect of overlap on the trade-off between κ_{s1} and κ_{d1}. For the same κ_{d1}, we can now achieve a higher κ_{s1} due to overlapping the elements of the same ring, with greater overlap now offering a higher achievable value of κ_{s1}.

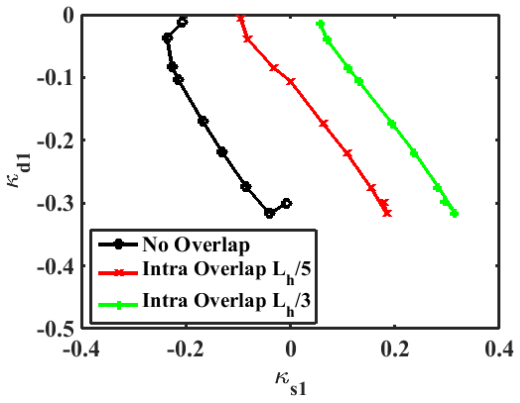

Figure 4.17 Relationship between first order inter- and intra-ring coupling coefficients, for the cases of (i) no overlap, and intra-ring overlaps of (ii) $L_h/5$ and (iii) $L_h/3$.

4.2.3 Inter-ring Coil Overlap

We now consider the alternative strategy of overlapping the two rings themselves. Figure 4.18 (a) shows a planar view of part of a coupled ring system with inter-ring element overlap. Here, we assume that the amount of overlap can again be expressed as L_v/m, with m changing from 5 to 3. Here, we keep the distance d separating the first order intra-ring elements fixed at 2 mm. Figure 4.18 (b) shows a 3D view of an entire coupled MI ring system, with inter-ring overlap.

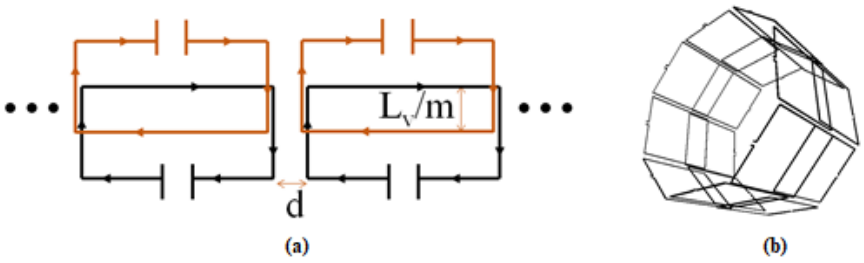

Figure 4.18 (a) Two pairs of overlapping elements from a coupled ring resonator system, (b) FastHenry model, showing elements with inter-ring overlap.

As before, the self-inductance and the self-resistance are independent of inter-ring overlap, since these characteristics are inherent. We therefore focus on the changes to the coupling coefficients, starting with the first order inter-ring coefficient. Figure 4.19 shows the variation of κ_{d1} with L_v/L_h for i) no overlap, and ii) and ii) different values of inter-ring overlap. The results are matched to a best curve fit. The overall shape of the curve is approximately independent of the overlap, but shifts up as L_v/L_h increases.

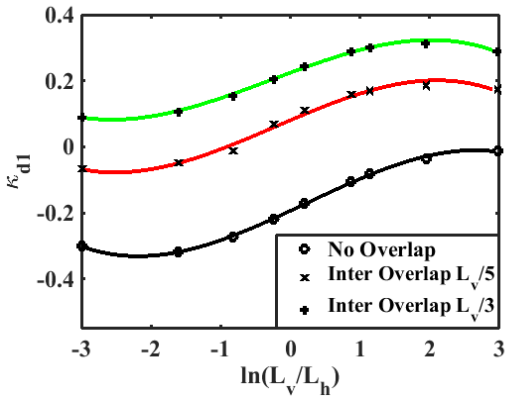

Figure 4.19 Variation of first order inter-ring coupling coefficient with L_v /L_h, for the cases of (i) no inter-ring overlap, and inter-ring overlap (ii) of L_v /5 and (iii) L_v /3.

As before, to explain the shape of the plot, we consider how each component of the mutual inductance between the elements changes as L_v/L_h increases. Figure 4.20 shows a pair of coupled coils from a coupled ring system with inter-ring overlap. As before, a small horizontal offset has been introduced for clarity, and the individual wires have been numbered.

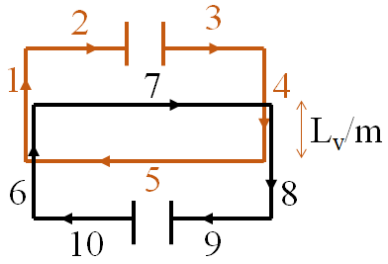

Figure 4.20 A pair of overlapping elements from different rings in a coupled ring system.

Equation 13 details the important contributions to the overall mutual inductance M. As L_v increases, the positively-valued terms $M_{1,6}$ and $M_{4,8}$ increase, while the negatively valued $M_{1,8}$, $M_{4,6}$ also increase due to the wires becoming longer. At the same time, when L_h decreases, the negative $M_{5,7}$ decreases, and the positive terms $M_{2,7}$, $M_{3,7}$, $M_{5,9}$ and $M_{5,10}$ also decrease. In turn, this leads to M becoming positive and increasing, since $|M_{1,6} + M_{4,8}| > |M_{1,8} + M_{4,6}|$ and $|M_{5,7}| > |M_{2,7} + M_{3,7} + M_{5,9} + M_{5,10}|$.

$$M = M_{1,6} + M_{4,8} - M_{1,8} - M_{4,6} - M_{5,7} + M_{2,7} + M_{3,7} + M_{5,9} + M_{5,10}$$

Equ 4.11

Figure 4.21 shows the variation of the second and third order inter-ring coupling coefficients with L_v /L_h for the two usual cases, i) no overlap and ii) and ii) two different values of inter-ring overlap. The simulated results are matched with a best-fit curve. Here we see that κ_{d2} and κ_{d3} also increase with inter-ring overlap, due to second and third neighbours moving closer. Conversely, κ_{d2} and κ_{d3} remain negative since there is no overlap between these neighbours. It is also noted that the point at which the coupling coefficients decrease again – due to L_h becoming too small to provide much coupling –

shifts to the right. This is because, with the inter-ring overlap, the mutual inductance between the horizontal wires affects M relatively less than without the overlap, and it takes longer for κ_{d2} and κ_{d3} to start decreasing.

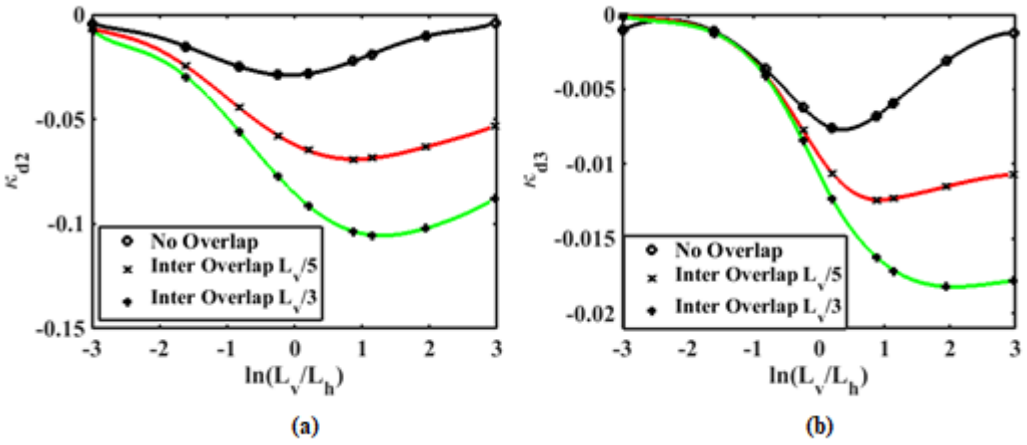

Figure 4.21 Variation of (a) second and (b) third order inter-ring coupling coefficient with L_v / L_h, (i) no inter-ring overlap, and overlap of (ii) L_v /5 and (iii) L_v /3.

Figure 4.22 (a), (b) and (c) show how the first, second and third order intra-ring coupling coefficients vary with L_v /L_h for the usual three cases. Here we see that all of the intra-ring coefficients remain essentially constant with overlap, because the distance between the first, second and third neighbours of the same ring are unchanged. The slight differences shown in Figure 4.22 (b) and (c) caused by overlap is due to the small increase in distance between neighbouring elements, since the coils in each ring must lie in different planes to accommodate an overlap.

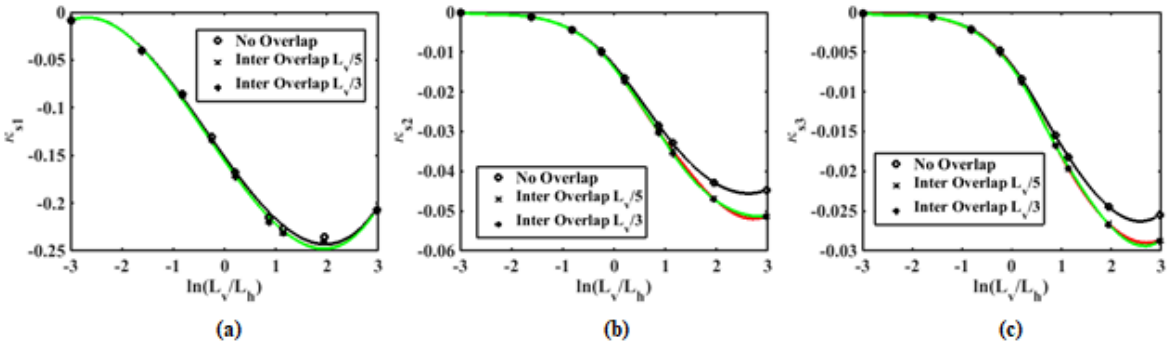

Figure 4.22 Variation of (a) first, (b) second and (c) third order intra-ring coupling coefficients with L_v /L_h, for (i) no inter-ring overlap, and overlap of (ii) L_v/5 and (iii) L_v/3.

Figure 4.23 shows the trade-off between κ_{s1} and κ_{d1}. Here we can see that the 'locus' of the relationship shifts upwards, due to the increased value of κ_{d1}. This effect implies that, for the same κ_{s1}, we can now achieve a higher κ_{d1} by overlapping the elements of the two rings.

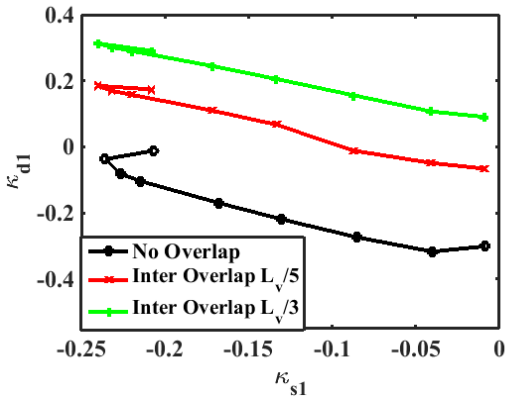

Figure 4.23 Relationship between first order inter- and intra-ring coupling coefficients (i) no overlap between elements, and overlap of (ii) $L_v/5$ and (iii) $L_v/3$.

It seems, therefore, that there is benefit to be gained from overlapping elements. However, it is still unclear which arrangement is best. One point worth mentioning is that with intra-ring overlap, there was an increase in the second and third order coupling coefficients, as well as all the intra-ring coefficients. Conversely, with the inter-ring overlap, the inter-ring coefficients did increase, but all the intra-ring coefficients remained constant. Therefore, intra-ring overlap seems to offer an extra advantage not seen with inter-ring overlap.

4.2.4 Design Optimisation

Results so far give an idea the effect of intra- and inter-ring overlap on the coupling coefficients of a coupled MI ring resonator system. Now it is necessary to decide which design will most effectively isolate the first anti-symmetric mode. To aid in this, we now study the resonance spectra obtained using a subset of designs. Figure 4.24 (a), (b) and (c) show mode spectra for element dimensions of L_v = 20 mm and L_h = 25.6 mm and the same track parameters and separations as before, for the three cases of i) no overlap, and ii) and iii) intra- and inter-ring overlap, by $L_h/5$ and $L_v/5$, respectively.

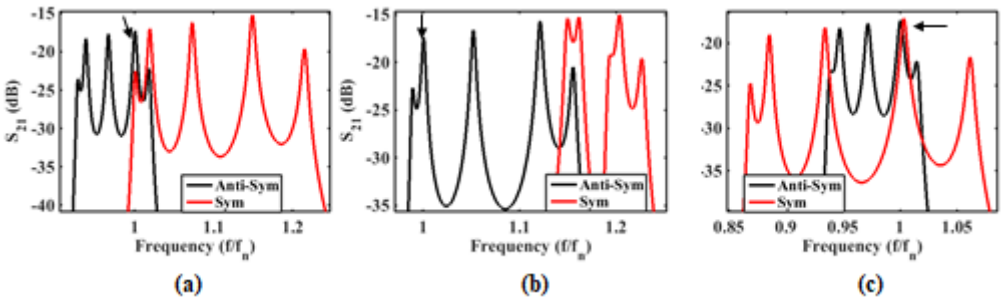

Figure 4.24 Mode spectra for a coupled MI ring resonator systems with L_v = 20 mm and L_h = 25.6 mm, for (a) no element overlap, (b) intra-ring overlap by $L_h/5$, (b) inter-ring overlap by $L_v/5$.

From Figure 4.24 (a), the no overlap case, the first anti-symmetric mode is the second highest resonance in the anti-symmetric set. For the dimensions considered, this mode of interest coincides

with the lowest frequency symmetric mode, which means that there will certainly be B_1 coupling. For other dimensions this may not be the case, but it is an indication that the first anti-symmetric mode is not well isolated. With the intra- and inter-ring overlap, the first order intra- and inter-ring coupling coefficients become positive, which affects the position of the modes. The effect can be studied most easily using the relevant dispersion diagrams, using the same parameters.

Figure 4.25 (a) shows the dispersion diagram for the coupled ring system with intra-ring overlap. Here, the first anti-symmetric mode is labelled and is separated in frequency from all symmetric modes. Furthermore, by shading the range occupied by the symmetric modes, we see that it is only the fourth anti-symmetric mode that occupies this range and all other anti-symmetric modes lie outside it.

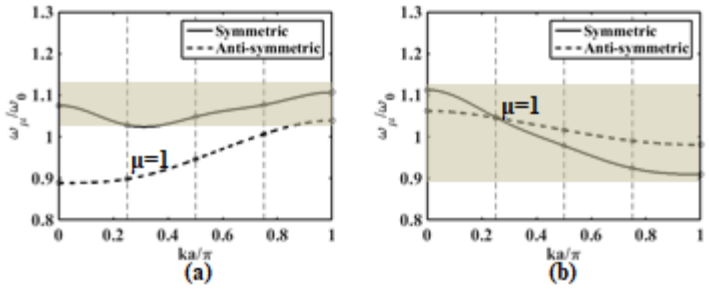

Figure 4.25 Dispersion diagram for coupled ring resonator system with L_v = 20 mm and L_h = 25.6 mm (a) with intra-ring element overlap of L_h /5, (b) with inter-ring element overlap of L_v /5.

We can, therefore, identify the position of the first anti-symmetric mode in Figure 4.24 (b) as shown by the arrowed line, and it is evident that the rejection of uniform fields will inevitably improve using this configuration. In addition to this, Figure 4.24 (b) shows that the bandwidth occupied by the anti-symmetric modes has increased as required. Conversely, the bandwidth occupied by the symmetric modes has decreased; but this does not have a negative impact on the working of the device.

In contrast, with inter-ring overlap, we obtain undesired results. Figure 4.24 (c) shows the anti-symmetric modes all nestled within the symmetric modes, with the former occupying a smaller and the latter having a larger bandwidth. From the dispersion diagram in Figure 4.25 (b) we confirm that since the intra-ring coupling coefficients have not changed sign, the frequency order of the anti-symmetric modes remains the same as it was without overlap. The first anti-symmetric mode is shown by the arrowed line in Figure 4.24 (c), and, again, for the dimensions considered, falls at the same frequency as the first symmetric mode. Once again, this may not occur for other dimensions, but having anti-symmetric modes within the frequency range of symmetric modes increases the likelihood.

Similar observations can be made for all other element dimensions shown in Table 4.1. Thus we draw the conclusion that an intra-ring overlap offers the best chance in isolating the first anti-symmetric mode and rejecting symmetric modes. Figure 4.26 (a) and (b) show the mode spectra and the

dispersion diagram of the coupled MI ring resonator system with the same dimensions, but with an intra-ring overlap of $L_h/3$. By comparing these plots with those for $L_h/5$ in Figure 4.24 and Figure 4.25, we see that the larger overlap offers an improvement by making the anti-symmetric modes occupy an even larger bandwidth and pushing the first such mode further away from others. With an overlap of $L_h/3$ the anti-symmetric mode is 0.0128 away from its closest neighbour, while with an overlap of $L_h/5$ this decreases to 0.0096. Therefore, the best design would be to overlap the elements of each MI ring as much as possible.

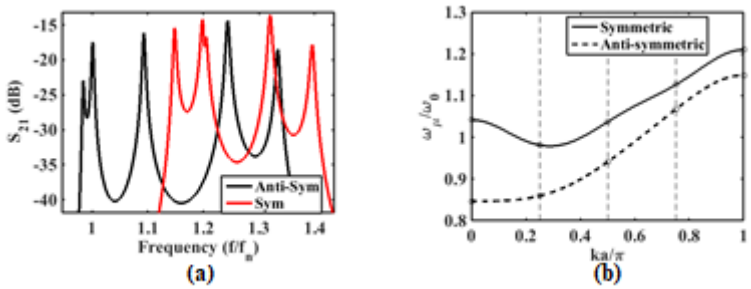

Figure 4.26 (a) Mode spectra and (b) dispersion diagram for coupled MI ring resonator system with L_v = 20 mm, L_h = 25.6 mm and an intra-ring overlap of $L_h/3$.

4.2.5 Device Dimensions

We have learnt from Figure 4.12 that increasing element larea offers a better compromise between the values of κ_{s1} and κ_{d1}. However, in practice, we are constrained by the dimensions of the Biodegradable Anastomosis Ring Figure 4.27 shows a BAR with its dimensions annotated [35]. Clearly these are chosen for anatomical compatibility, and must be considered when making any decision on the dimensions of the coupled MI ring resonator system and its individual coils, as follows.

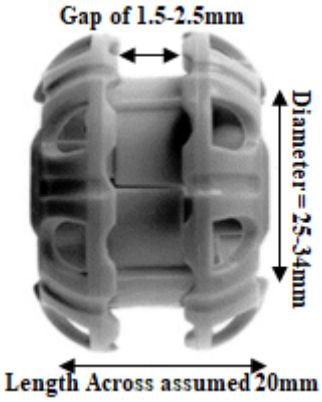

Figure 4.27 The BAR with annotated dimensions. [34]

The length of 20 mm determines the length of L_v. If we assume that each half of the BAR is identical, we can limit L_v to 10 mm. Now, the gap between the two halves of the BAR ranges from 1.5 to 2.5

mm to accommodate different bowel thicknesses, and this determines the distance between the two MI rings. Similarly, the BAR diameter has a range of 25 to 34 mm to accommodate different bowel diameters, including the small and large intestines. This limits the range of L_h. However, the amount of overlap also affects this length.

We know that the greater the overlap, the better isolated the first anti-symmetric mode will be. Additionally, the greater the overlap, the larger L_h can be, within the BAR dimensions. Therefore, we choose an overlap of $4L_h/9$, with m = 9/4. This value satisfies another important constraint on m, namely that m < 2 so that the second neighbours do not touch. Since the circumference of the ring is C = πD, where D is the diameter and $C = 8L_h - (8 \times 4L_h/9) = 40L_h/9$, we can obtain the relationship in Equ 4.12 between L_h and the diameter of the device for $4L_h/9$ intra-ring overlap. This limits the allowable range of L_h to between 17.5 and 24 mm.

$$L_h = \frac{9\pi D}{40}$$

Equ 4.12

We first let L_v = 7 mm and choose the two extreme values for L_h to investigate the best dimensions. With L_h = 24 mm, we have a larger element area and would expect a larger self-inductance and self-resistance, as well as stronger intra- and inter-ring coupling. Additionally, the value of $\ln(L_v/L_h)$ = -0.92 and -1.23 for L_v = 7 mm and L_h = 17.5 mm and 24 mm respectively. Reviewing the results of previous sections, specifically Figure 4.14 to Figure 4.16, we see that the larger L_h increases κ_{s1} and κ_{d1} even more, but decreases the second and third order intra- and inter-ring coefficients. To see the overall effect on isolating the first anti-symmetric mode, we compare the resonance spectra and dispersion diagrams for the two different coupled MI ring systems.

Figure 4.28 (a) and (c) shows the mode spectra for the two coupled MI rings with $4L_h/9$ intra-ring overlap, L_v = 7 mm and L_h = 17.5 mm and 24 mm respectively. As expected the large overlap has resulted in good rejection of symmetric modes with 41.5 dB and 46.9 dB for the smaller and larger elements respectively. Additionally, the first anti-symmetric mode is completely isolated in frequency from all symmetric modes. Furthermore, for the device with the larger elements, the difference in frequency between the first and zeroth anti-symmetric modes is greater.

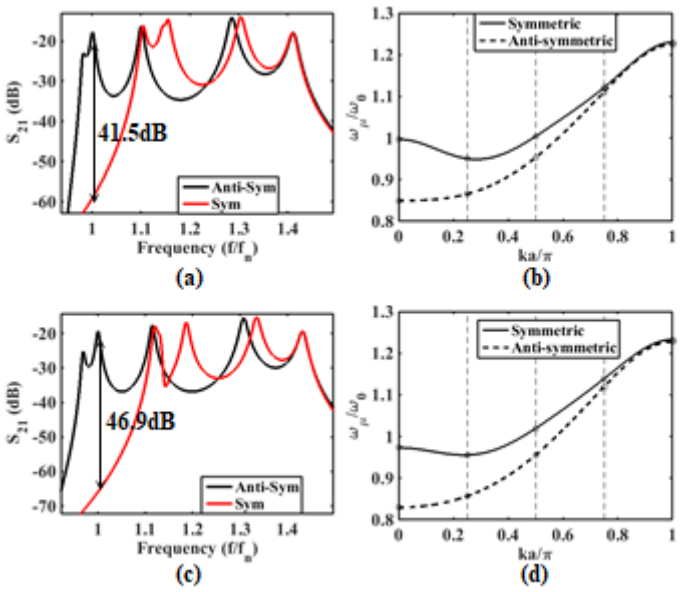

Figure 4.28 (a), (c) Mode spectra for coupled MI ring resonator systems with $4L_h/9$ intra-ring overlap, $L_v = 7$ mm and $L_h = 17.5$ mm, 24 mm respectively. (b), (d) corresponding dispersion diagrams.

Figure 4.28 (b) and (d) shows the corresponding dispersion diagrams. Here we can calculate that the distance in normalised frequency between the first anti-symmetric mode and the zeroth anti-symmetric mode is[9] 0.0162 and 0.0271 for the smaller and larger elements respectively, representing a 67% increase for the larger device. Here it can also be seen that the zeroth and first symmetric modes have changed positions in frequency. This alteration is more pronounced in the smaller device; effectively making the symmetric modes be generated by both backward and forward MI waves.

This phenomenon is not well understood and it is unclear if it will have any effect on operation, and so – for now – it is best to avoid designs giving such results. Decreasing the ratio L_v/L_h eliminates the problem. We therefore choose $L_v = 4$ and $L_h = 24$ mm, a combination known to give satisfactory performance. Figure 4.29 (a) and (b) show the mode spectra and the dispersion diagram for the coupled ring system with these element dimensions. From the dispersion diagram we confirm that both the symmetric and anti-symmetric modes exhibit forward wave behaviour and that the normalised frequency difference between the first anti-symmetric mode and its nearest mode is 0.028. From the mode spectra we calculate the rejection to be 49.3 dB implying a better performing device.

[9] Multiplying these numbers by $\omega_0/2\pi$ gives the value in Hz.

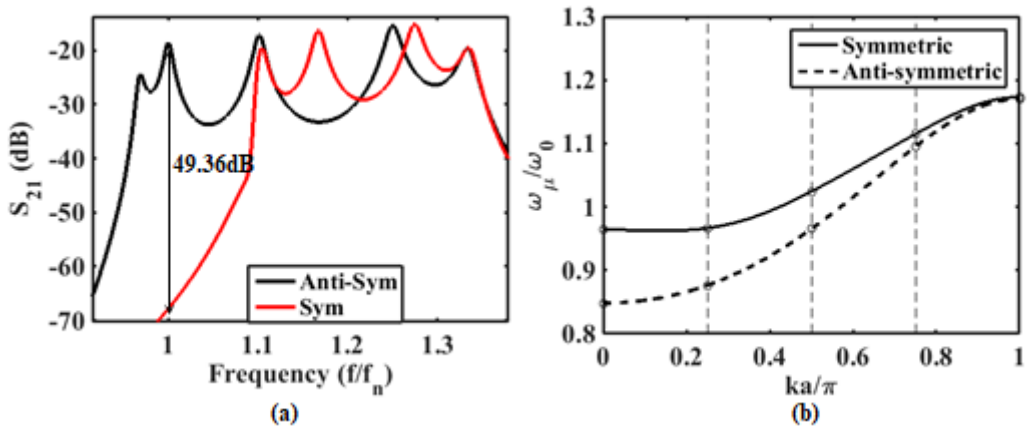

Figure 4.29 (a) Mode spectra and (b) dispersion diagram for coupled MI ring resonator system with L_v = 4 mm and L_h = 24 mm and intra-ring overlap of $4L_h/9$.

4.3 Device Fabrication

We now consider the construction of experimental devices based on the design rules developed above. Figure 4.30 shows the FastHenry model of the proposed device, namely a coupled MI ring resonator system, with the coils of each ring overlapped by $4L_h/9$. The overall diameter is 34 mm and the length is 18 mm, including the capacitor elevations. There are two layers to the device, an inner and outer layer, to allow for the intra-ring overlap. The offset of 1 mm between the two layers reduces the parasitic capacitance that would be obtained if the tracks were positioned exactly on top of each other.

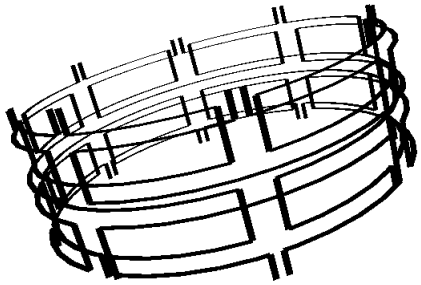

Figure 4.30 FastHenry model of coupled MI ring device, diameter = 34 mm, length = 18 mm, L_v = 4 mm, L_h = 24 mm

Fabrication requires a flexible PCB and a supporting plastic scaffold. Figure 4.31 shows a scale diagram of the track layout. The upper (black) track shows the inner coils of the coupled MI ring resonator system, while the lower (red) track shows its outer coils. Bearing in mind the thickness of the flexible PCB, the inner elements must either be closer together than the outer elements, or have a shorter L_h. The first option means that the higher order coupling coefficients will be slightly different; while the second implies that the self-inductance of inner coils would be slightly lower than that of outer coils. The first choice is considered likely to have less of an impact on performance. Thus for a diameter of 34 mm, with L_h = 24 mm, and track width of 0.5 mm, the spacing between the inner elements is 2.67 mm and the spacing between the outer elements is 2.76 mm.

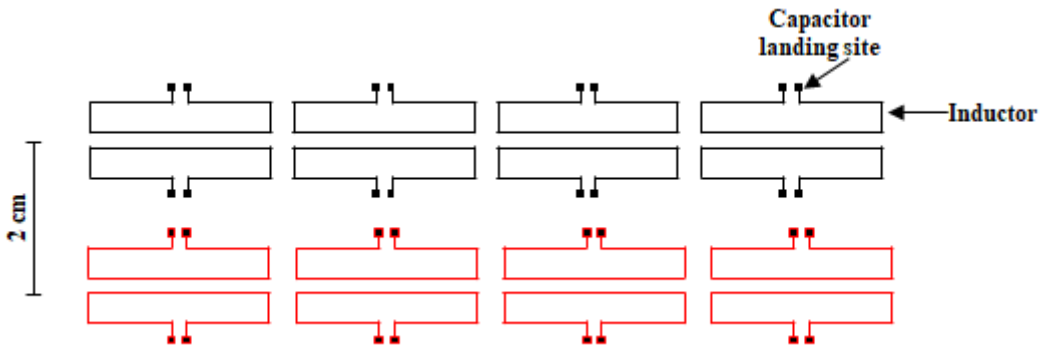

Figure 4.31 Circuit tracks to be printed for device fabrication. Coils are drawn to scale.

Once the tracks have been printed on flexible PCB, they can be overlaid. Figure 4.32 shows how the two layers are positioned on top of each other, so that inter-ring elements have an overlap of $4L_h/9$. Once the flexible PCB is wrapped round the plastic ring with an outer diameter of 34 mm, all the intra-ring coils will have the desired overlap.

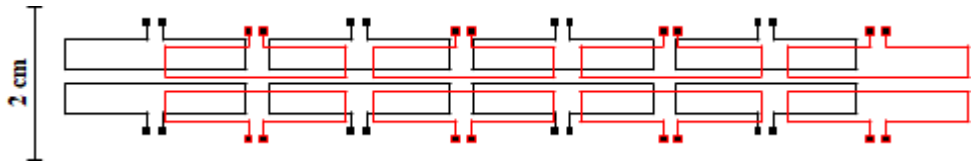

Figure 4.32 Circuit tracks overlapped to form an 'unwrapped' coupled MI ring

The flexible PCB used to print the track is a flexible laminate from Mega Electronics [202]. Figure 4.33 (a) shows a photograph of the laminate, while Figure 4.33 (b) details its cross-section. The laminate consists of a 50 µm polyester base carrying a 35 µm copper coating and a photosensitive resist covered by a light-proof seal. Each sheet is 30.5 × 50 cm and is singulated into individual circuits of the correct size after development and etching.

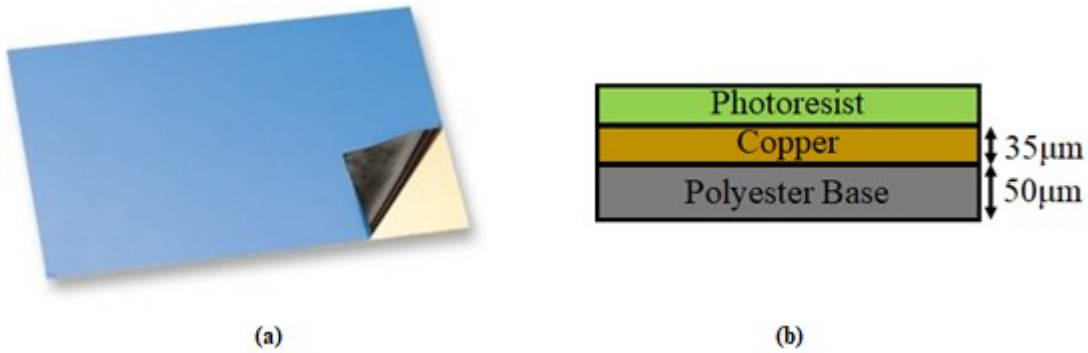

Figure 4.33 (a) Flexible laminate [202]**, and (b) cross-section showing thickness of layers.**

4.3.1 Manufacturing the MI Rings

The following steps are used to produce a circuit. The track layout is first printed on a specially formulated sheet that allows for the production of PCBs directly from a laser printer. Here we have used LaserJet sheet, again from MegaElectronics [203]. The printed circuit is then placed face upward on a UV light tray and the flexible laminate is placed on top, photoresist side down. The laminate has a positive photoresist, allowing the area exposed to light to be removed by development, while the tracks shielded from the light by the printed mask remain unaffected. After exposure, the tracks may be seen as very faint lines in the resist. The resist is then developed in a tray of sodium hydroxide solution, which is gently rocked from side to side to ensure uniform development.

Once all the exposed photoresist has been dissolved, the laminate is removed from the tray, washed and, immersed in copper etchant. Here a sodium persulphate solution is used, and the tray is contained in a warm water bath, since the optimum etchant temperature is between 40^{o}C and 55^{o}C. Again, the tray is gently rocked to aid in etching. Originally, the etchant is transparent and changes to light blue as the copper starts dissolving. Figure 4.34 shows the tray with the light blue sodium persulphate solution. This white tray is contained in another larger black tray filled with warm water. Here the flexible laminate is also shown and we see the copper dissolving from the outside inwards.

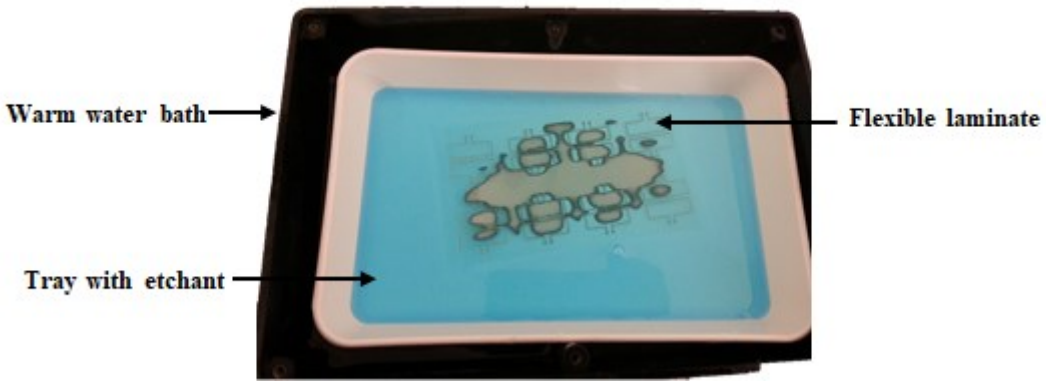

Figure 4.34 Flexible laminate with conducting printed circuit in etchant solution

Once all the exposed copper has been removed and only the circuit tracks – protected by the photoresist – remain, the flexible laminate is removed from the etching tray and washed. Finally, residual photoresist is removed, and the sheet is separated into strips. Figure 4.35 shows two such strips ready for use. Surface-mount capacitors (whose values are chosen to achieve the desired resonant frequency) are then soldered to the landing sites using lead-tin solder. Small cut-outs are made in the plastic sheet, to allow overlay without these capacitors interfering with the arrangement.

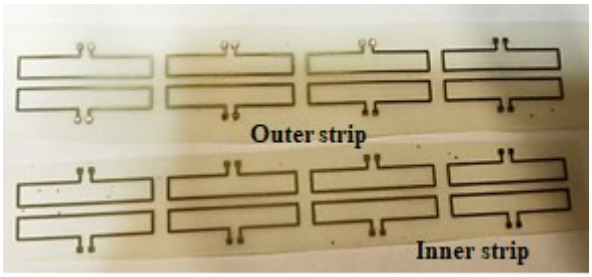

Figure 4.35 PCBs for a coupled MI ring system with L_v = 4 mm and L_h = 24 mm

The coupled ring system is then assembled. An annular plastic scaffold representing a BAR is first machined in the workshop with an appropriate outer diameter and additional mounting points. Strips containing inner and outer elements are positioned as previously shown in Figure 4.32, are wrapped round the plastic scaffold and attached with adhesive. Figure 4.36 shows a completed coupled MI ring device made from elements with dimensions 4 × 24 mm and having a diameter of 34 mm.

Figure 4.36 Final coupled MI ring device with L_v = 4 mm, L_h = 24 mm, diameter = 34 mm, length = 18 mm

Initial benchtop evaluation is then carried out. Figure 4.37 (a) shows the arrangement for measuring the resonance spectrum. A machined plastic base plate is used to provide. mounting features for a pair of measurement transducers. Each pair of elements is tagged with a number, providing four identifiable diameters across which measurements can be taken. Figure 4.37 (b) shows a diagram representation of the set-up, indicating the element tagging and the position of the transducers across the diameter 1-5. Generally, consistent results were obtained at each position.

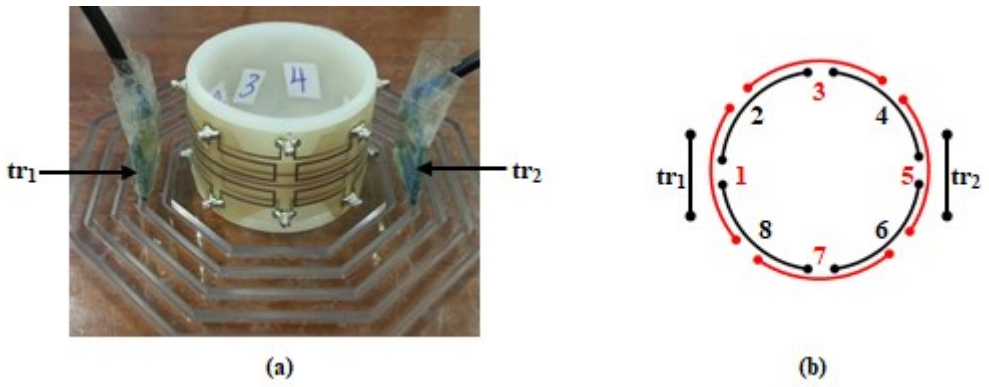

Figure 4.37 Set-up for measuring the resonance spectrum of a coupled MI ring device: (a) experimental arrangement, and b) element numbering system.

Figure 4.38 shows the measured mode spectra for this device. Here the ring is not tuned to a particular design frequency. Instead, capacitors of approximately the correct value (150 pF) are simply connected to all coils to allow for rotational resonance. In this case, the inductance of a single coil is equal to 36.3 nH and thus $f_0 = 68.24$ MHz. The average Q-factor for a single element at this frequency is 39. Examining the mode spectra, we find, as expected, that the first anti-symmetric mode is the second lowest resonance and has a Q-factor of 41. The rejection of the nearest symmetric mode is 19 dB, implying that the voltage induced by uniform B_1 fields will be reduced by a factor of 9. This is a vast improvement over the measured rejection of the early devices with no overlap; however, it is lower than the theoretically predicted value and also lower than what is required practically. Therefore, considering other dimensions – perhaps larger – is an option.

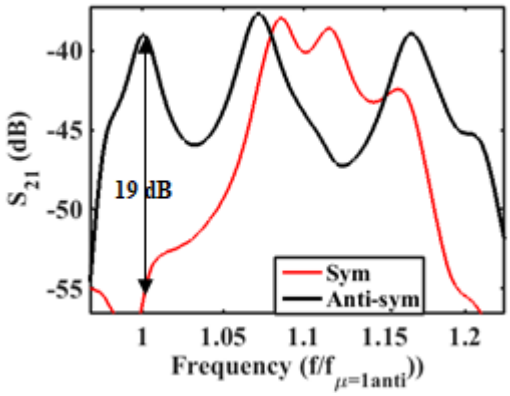

Figure 4.38 Measured mode spectra for the experimental coupled MI ring device.

Since the predicted and measured rejections differ, the corresponding coupling coefficients were measured. To do so, individual elements were detached and placed as they would be in the first, second and third order neighbour positions etc. Figure 4.39 shows how this is done for κ_{s1}, κ_{s2} and κ_{d1}. Here a paper printout of the circuit layout is used to guide the placement of the coils. Then the coils, along with the guide, are placed between the transducers connected to the network analyser.

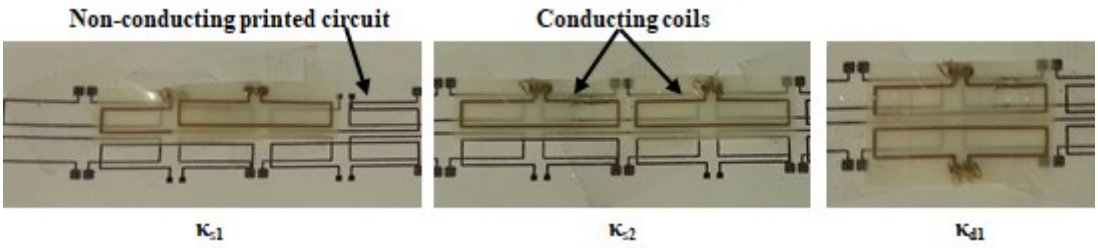

Figure 4.39 Arrangement for measuring coupling coefficients.

Table 4.2 compares the measured and theoretical coupling coefficients. Here it can be seen that the experimental values are indeed less than the theoretical ones. One possible explanation is alterations to the track width caused by the relatively crude lithography and etching used for PCB manufacture.

Table 4.2 Theoretical and experimental coupling coefficients for prototype coupled MI ring.

Intra-ring Coupling Coefficients			Inter-ring Coupling Coefficients		
	Experiment	Theory		Experiment	Theory
κ_{s1}	0.18	0.26	κ_{d1}	-0.08	-0.14
κ_{s2}	-0.01	-0.016	κ_{d2}	-0.01	-0.075
κ_{s3}		-0.0037	κ_{d3}		-0.0096
κ_{s4}		-0.0029	κ_{d4}		-0.003
			κ_{d5}		-0.0022

Figure 4.40 compares the theoretical and experimental dispersion diagrams. We can see that due to the decreased coupling coefficients, the overall bandwidth is less than what is expected theoretically. In fact, the experimental normalised bandwidth is 0.23 while the theoretical value is 0.32. This translates to a difference of: (0.32 – 0.23) x 63.85 = 5.75 MHz at 1.5 T. The most likely explanation is parasitic capacitance from the overlapped tracks [200], and this is explored further in the next section.

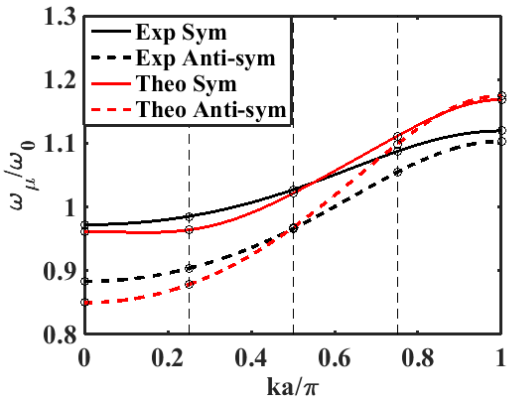

Figure 4.40 Dispersion diagram for prototype coupled MI ring device.

4.3.2 Effect of the Track Width

To determine the possible effects of track dimensions on device performance, devices were fabricated with two further track widths. Figure 4.41 (a) and (b) show images of these devices, which have track thickness of 0.35 mm and 1 mm respectively.

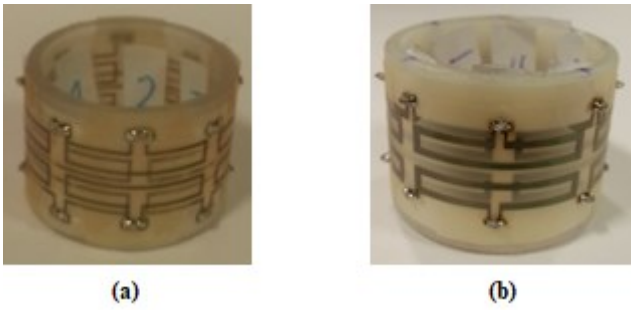

Figure 4.41 Coupled MI ring devices with track widths of (a) 0.35 mm and (b) 1 mm.

Devices were constructed as previously described, and the coupling coefficients and resonance spectra were then measured. Table 4.3 compares the measured and theoretical coefficients. Here we note that the corresponding values are very similar for the device with the thin tracks, experimental coefficients are lower than theoretical ones for thick tracks. This result indicates that the experimental reduction in bandwidth is due to track width, and consequently to parasitic capacitance.

Table 4.3 Experimental and theoretical coupling coefficients for coupled MI ring devices with different track widths

	w = 0.35 mm		**w = 1 mm**	
	Experiment	**Theory**	**Experiment**	**Theory**
κ_{s1}	0.24	0.24	0.17	0.27
κ_{s2}	-0.015	-0.015	-0.01	-0.020
κ_{s3}		-0.0034		-0.0045
κ_{s4}		-0.0027		-0.0036
κ_{d1}	-0.12	-0.12	-0.087	-0.16
κ_{d2}	-0.071	-0.071	-0.05	-0.077
κ_{d3}		-0.0088	-0.0061	-0.118
κ_{d4}		-0.0027		-0.0036
κ_{d5}		-0.0021		-0.0028

Figure 4.42 shows the resonance spectra for devices with differing track widths. Here, all modes are shown. Clearly, the device with 0.35 mm track width has the largest bandwidth, followed by the device with 0.5 mm tracks and finally that with 1 mm tracks. This is unexpected, since the device with the widest bandwidth should have the largest coupling coefficients, resulting in its mode spectrum occupying the largest range of frequencies.

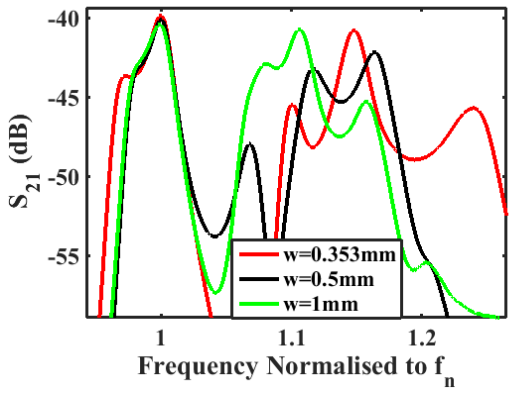

Figure 4.42 Comparison of resonance spectra for the coupled MI ring device with different track widths

Figure 4.43 (a) shows a portion of the track layout, highlighting the overlap regions. The effect is shown in the equivalent circuit in Figure 4.43 (b), which shows four of the coils forming the coupled MI ring. In addition to the usual circuit parameters, there is now a stray capacitance, C_s, between each pair of intra-ring elements; in linear MI cable systems, this has been shown to have a significant effect on bandwidth . Unfortunately, the effect of the stray capacitance cannot be compensated for using a change in capacitance, C, and so using such wide tracks is discouraged.

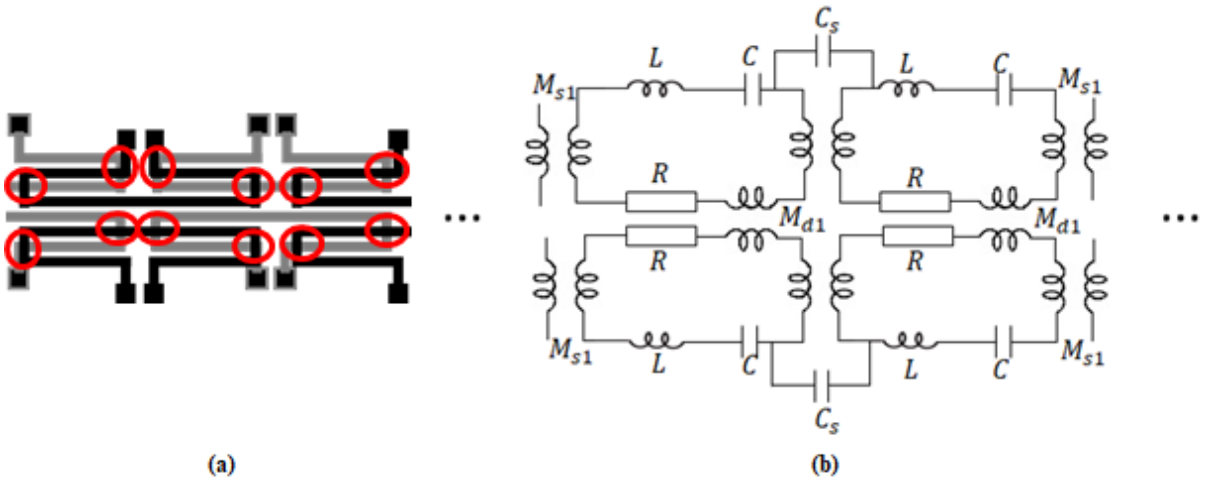

Figure 4.43 (a) Track layout of coupled MI ring showing position of track overlap, (b) equivalent circuit, showing the stray capacitance, C_s.

We must now make a choice between the devices with w = 0.35 mm and 0.5 mm. Table 4.4 compares their performance. Here we notice that they are very close in terms of rejection, isolation of the first anti-symmetric mode from its nearest unwanted neighbour and Q-factor. Thus, although it appears that parasitic capacitance can indeed be blamed for the observed effects, there is no significant performance advantage to be obtained from reducing the track width. However, the best rejection achieved so far is 19.6 dB, lower than the value needed to suppress artefacts during MRI.

Table 4.4 Performance comparison of coupled MI ring devices with different track widths.

	w = 0.35 mm	w = 0.5 mm
Rejection (dB)	19.6	19.2
Normalised frequency difference from nearest undesired resonance	0.025	0.021
Q-factor at the desired anti-symmetric mode	40.1	40.7

4.3.3 Larger Device Dimensions

To attempt to increase the rejection of symmetric modes, a larger device was constructed, with an overall diameter of 49.5 mm, a length of 22 mm, and element dimensions of L_v = 6 mm and L_h = 35 mm. These dimensions are no longer compatible with human anatomy, but will provide a useful yardstick for comparison with smaller devices. The overlap of $4L_h/9$ and the track width of 0.5 mm were retained. Figure 4.44 shows this larger device.

Figure 4.44 Larger coupled MI ring device: diameter = 49.5 mm, length = 22 mm, L_v = 6 mm, L_h = 35 mm.

Figure 4.45 (a) shows the measured mode spectrum of this device, and Figure 4.45 (b) shows a comparison between the theoretical and experimental dispersion diagrams. From Figure 4.45 (a), we calculate the rejection to be 24.7 dB and the Q-factor at the first anti-symmetric resonance to be 67. Both values are an improvement over the smaller devices. Additionally, from the dispersion diagram, we see that the theoretical and experimental coupling coefficients are nearly identical, indicating that the effect of track width reduces as overall device size in increases.

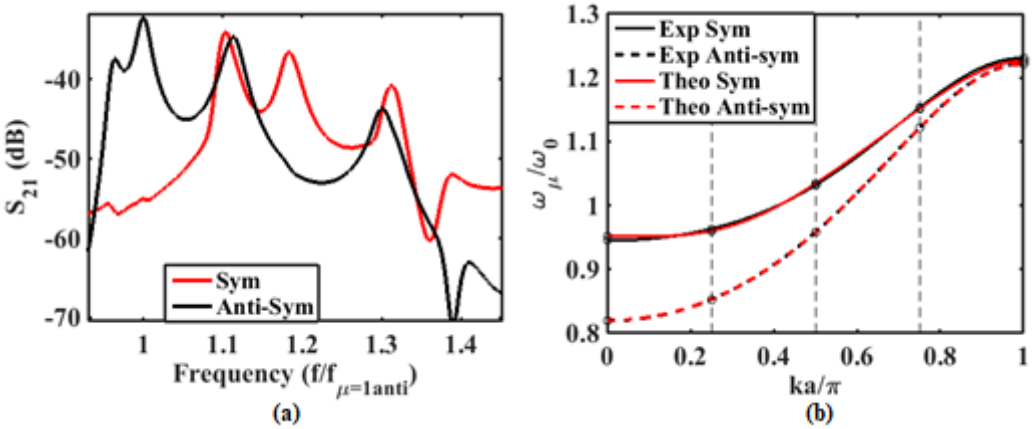

Figure 4.45 (a) Mode spectra and (b) dispersion diagram for larger coupled MI ring device.

4.4 Conclusions

In conclusion, a systematic search of the effects of geometric parameters on the performance of coupled ring resonator systems appears to have identified arrangements likely to allow reasonable magnetic resonance imaging performance. To confirm this, we review the performance of small and large systems, both with a track width of 0.5 mm. Figure 4.46 compares the resonance spectra for the two devices. Here the larger device's higher Q-factor is more evident, as well as its larger bandwidth. It is thus more likely that the larger device will perform better. However, since the small device fits inside the human bowel and BAR, while the larger device does not, both will be tested inside the MRI scanner to confirm that they offer a higher SNR than an external coil. In the next Chapter we calculate the field-of-view of the devices before evaluating their experimental imaging performance in the last technical Chapter.

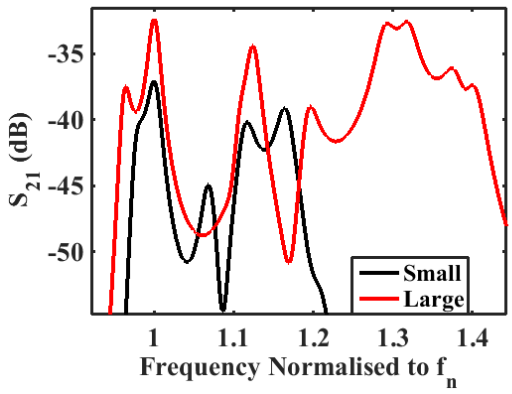

Figure 4.46 Resonance spectra of small and large coupled MI ring devices, with w = 0.5 mm.

5 Field Of View

Broadly speaking, the field of view (FOV) of any MRI reception coil is the volume within which the magnetic moment of a group of precessing dipoles is able to induce a significant voltage in the coil. In more detail, it represents the useful volume of the spatially varying sensitivity or reception pattern of the coil. For the implanted sensor considered here, we require methods to calculate the FOV and match it to the tissue of interest. Particularly, it is desirable that the sensitivity of the device is highest where the annular wound in the bowel lumen is located, and falls off radially away, to reduce the amount of detected body noise.

In this Chapter, we start by calculating the general expression for the reception pattern of any coil. We then use this to calculate the FOV of the coupled MI ring device, analysing where the sensitivity is highest, where it is zero and the rate at which it decreases. We then consider how the coupling between the external MRI receive coil and the internal MI ring coil affects its FOV. This is done for the cases of a single MI ring resonator and a coupled MI ring system, highlighting how the anti-symmetric operation of the latter affects the receiver type we are able to use. Finally, the sensitivity of the side-view of the coupled MI ring device is examined to confirm any zero-sensitivity regions and conclude what should be seen in subsequent MRI testing.

5.1 Coil Reception Pattern

It is generally difficult to calculate the voltage, V_s, induced in the coil by a magnetic moment, **m**, located in arbitrary position in space. However, the reciprocity principle (which implies that the electromagnetic effect at a point Y due to a source at point X is directly related to the effect at X due to a source at Y) provides a convenient method to calculate the sensitivity pattern from the magnetic field created when the reception coil is driven [138]. We illustrate this first in general and then with a number of examples.

The reciprocity principle implies that the signal voltage $V_s(t)$ induced in the coil by a time-varying magnetic moment, $\mathbf{m}(t)$, is given by

$$V_s(t) = -\frac{d}{dt}\left[\mathbf{B} \,.\, \mathbf{m}(t)\right]$$

Equ 5.1

Where **B** is the magnetic field produced by the unit current at the location of **m.** Assuming that the static magnetic field $\mathbf{B_0}$ is in the z-direction, magnetic dipoles precess about the z-axis at the Larmor frequency ω_L, with a transverse magnetization $\mathbf{M}_{xy}$ per unit volume. The most important contribution

to **B** is then the transverse component $\mathbf{B}_{xy}$ lying in the x-y plane. For a volume dv of dipoles, the induced voltage in the coil is now equal to:

$$V_s(t) = -\frac{d}{dt}\left[\mathbf{B_{xy}} \,.\, \mathbf{M_{xy}}(t)\right] dv$$

Equ 5.2

Now, the variation $\mathbf{B}_{xy}$ produced by the coil can be written as:

$$\mathbf{B_{xy}} = \mu_0(H_x\hat{\imath} + H_y\hat{\jmath})$$

Equ 5.3

Where μ_0 is the permeability of free space, H_x and H_y are the x and y components of the magnetic field, and $\hat{\imath}$ and $\hat{\jmath}$ are the unit vectors in the x and y directions respectively. We can rewrite the magnetisation vector in terms of its components in the x- and y- axes as:

$$\mathbf{M}_{xy}(t) = M\left(\hat{\imath} + j\,\hat{\jmath}\right)\exp(j\omega_L t)$$

Equ 5.4

For a 90^o flip angle – commonly used in spin-echo imaging - the magnetization is entirely transverse, so $M = M_0$, where M_0 is the magnetization per unit volume. Taking the dot product between $\mathbf{B}_{xy}$ and $\mathbf{M}_{xy}$, we obtain:

$$\mathbf{B_{xy}}.\mathbf{M_{xy}}(t) = \mu_0 M_0(H_x + jH_y)\exp(j\omega_L t)$$

Equ 5.5

After differentiating, we can then obtain the induced voltage as:

$$V_s(t) = -j\omega_L\mu_0 M_0\ \left[\left(H_x + jH_y\right)\exp(j\omega_L t)\right] dv$$

Equ 5.6

For the purposes of the FOV calculations, we can disregard the time dependence and write the induced voltage in phasor form as:

$$V_s = -j\omega_L\mu_0 M_0\left(H_x + jH_y\right) dv$$

Equ 5.7

The magnitude of this voltage is then:

$$|V_s| = \omega_L \mu_0 M_0 \sqrt{{H_x}^2 + {H_y}^2}\ dv$$

Equ 5.8

Since the majority of the terms above are constants, we may focus on the spatially dependent term $\sqrt{{H_x}^2 + {H_y}^2}$ to describe the sensitivity pattern of the coil.

5.2 FOV of MI Ring Resonator

The magneto-inductive sensor described in this thesis consists of a complicated three-dimensional arrangement of coupled resonators. Calculation of the FOV for such a system is normally a lengthy procedure, which requires a full 3D calculation of the vector magnetic field produced by the coil. Here we simplify matters by judicious use of two-dimensional approximations, in which the 3D structure is modelled in 2D, as a set of parallel wires for which the fields can be found analytically. We first calculate the FOV of a single wire, followed by the FOV for an individual coil. We then extend the approach to a whole MI ring resonator, and finally to a ring with overlapped coils.

5.2.1 A Single Wire

We start by considering an infinitely long wire, with current, I = 1, flowing through it. Figure 5.1 shows a cross-section of the wire, with current flowing out of the plane of the paper, and the magnetic field produced by the current in the anti-clockwise direction.

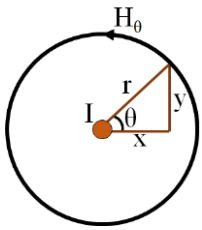

Figure 5.1 Cross-section of an infinitely long wire, with current flowing out of the plane of the paper.

It is trivial to show using Ampere's Law that the magnetic field H_θ is circumferential, and falls off inversely with radial distance r following Equ 5.9:

$$H_\theta = \frac{I}{2\pi r}$$

Equ 5.9

For the purposes of the FOV calculation, which uses Cartesian coordinates, this field can be resolved into its x- and y-components as follows:

$$H_x = \frac{-I}{2\pi r}\sin(\theta)$$

Equ 5.10

$$H_y = \frac{I}{2\pi r}\cos(\theta)$$

Equ 5.11

Knowing that $r = \sqrt{x^2 + y^2}$, $\cos(\theta) = \frac{x}{r}$ and $\sin(\theta) = \frac{y}{r}$, we can write H_x and H_y as

$$H_x = \frac{-I}{2\pi}\frac{y}{(x^2 + y^2)}$$

Equ 5.12

$$H_y = \frac{I}{2\pi}\frac{x}{(x^2 + y^2)}$$

Equ 5.13

The spatial variation of sensitivity can then be found as:

$$S = \sqrt{{H_x}^2 + {H_y}^2} = \frac{1}{2\pi(x^2 + y^2)}\sqrt{x^2 + y^2} = \frac{I}{2\pi\sqrt{x^2 + y^2}}$$

Equ 5.14

Figure 5.2 shows a 2D contour map of the function S, which defines the spatial variation of the sensitivity. Here a wire of finite radius has been used, to avoid the problem of infinite fields at the origin. The sensitivity pattern is a function only of radius; since S = 1/2πr, this clearly falls off as 1/r, a well-known feature of the so-called 'loopless catheter antenna' [118].

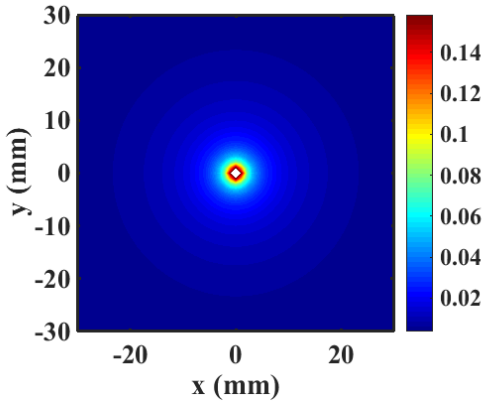

Figure 5.2 Spatial variation of sensitivity for single long wire.

5.2.2 A Single Rectangular Element

Following Atalar [138] we now extend the approach above to model the sensitivity pattern of a long, thin rectangular coil, which in a 2D approximation can be modelled as two infinitely long parallel wires. Figure 5.3 shows a cross-section. The wires are parallel and placed at y = 0, are displaced from the origin by $-x_0$ and x_0 and carry currents of -1 and 1 respectively.

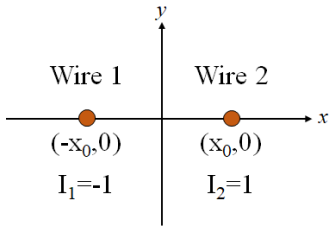

Figure 5.3 Approximation of a single element as two long wires, showing current distribution and coordinates.

Using appropriate origin shifting, the magnetic field for wires 1 and 2 alone can be obtained from the previous results for a single wire, as shown in Equ 5.15and Equ 5.16.

$$H_{x_1} = \frac{1}{2\pi}\frac{y}{((x+x_0)^2+y^2)} \qquad H_{x_2} = \frac{-1}{2\pi}\frac{y}{((x-x_0)^2+y^2)}$$

$$H_{y_1} = \frac{-1}{2\pi}\frac{x+x_0}{((x+x_0)^2+y^2)} \qquad H_{y_2} = \frac{1}{2\pi}\frac{x-x_0}{((x-x_0)^2+y^2)}$$

Equ 5.15 **Equ 5.16**

Since Maxwell's equations are linear, the total magnetic field can be found as the sum of that produced from each wire. For the x-component, we can write $H_x = H_{x_1} + H_{x_2}$, giving the total field shown in Equ 5.17:

$$H_x = \frac{-y}{2\pi}\left[\frac{-1}{((x+x_0)^2+y^2)} + \frac{1}{((x-x_0)^2+y^2)}\right]$$

Equ 5.17

In the same way, the y-component H_y can be found as:

$$H_y = \frac{-1}{2\pi}\left[\frac{x+x_0}{((x+x_0)^2+y^2)} - \frac{x-x_0}{((x-x_0)^2+y^2)}\right]$$

Equ 5.18

After some algebraic manipulation, the sensitivity variation can then be found as:

$$\sqrt{{H_x}^2 + {H_y}^2}$$

$$= \frac{1}{2\pi}\sqrt{\left[\frac{-y}{((x+x_0)^2+y^2)} + \frac{y}{((x-x_0)^2+y^2)}\right]^2 + \frac{1}{4\pi^2}\left[\frac{-(x+x_0)}{((x+x_0)^2+y^2)} + \frac{(x-x_0)}{((x-x_0)^2+y^2)}\right]^2}$$

Equ 5.19

Figure 5.4 shows a contour map of this equation, with the axes normalised by x_0. Again, we have used wires of finite radius, to avoid the problem of infinite fields at $x = \pm x_0$. Near each wire, there is a large peak in sensitivity, so the overall reception pattern is highly non-uniform. However, as r increases, the contours tend to circles, implying that radial symmetry is obtained at large distances.

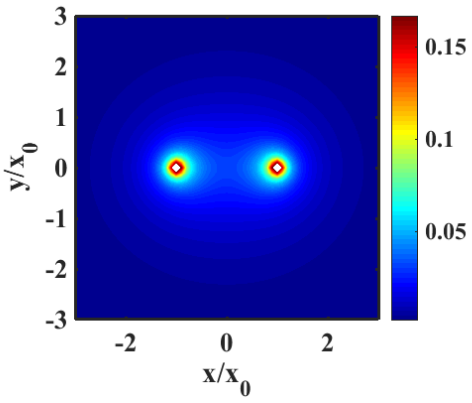

Figure 5.4 Spatial variation of sensitivity for a two-wire model of a single resonant element.

This time, in the far field when $r > x_0$, we can show that the FOV falls off as $\frac{1}{r^2}$ [138], a well known property of rectangular loop coils. We start by writing H_x and H_y as:

$$H_x = \frac{1}{2\pi}(A_{x1} - A_{x2}) \qquad H_y = \frac{1}{2\pi}(A_{y1} - A_{y2})$$

Equ 5.20

Where

$$A_{x1} = \frac{y}{(x-x_0)^2+y^2} \qquad A_{x2} = \frac{y}{(x+x_0)^2+y^2}$$

$$A_{y1} = \frac{x+x_0}{(x+x_0)^2+y^2} \qquad A_{y2} = \frac{x-x_0}{(x-x_0)^2+y^2}$$

Equ 5.21

We now evaluate A_{x1} when $r^2 >> {x_0}^2$. Firstly, the square term is expanded and since $r^2 = x^2 + y^2$, we obtain:

$$A_{x1} = \frac{y}{r^2 - 2xx_0 + {x_0}^2}$$

Equ 5.22

Since $r^2 >> {x_0}^2$, we can approximate A_{x1} as:

$$A_{x1} \approx \frac{y}{r^2 - 2xx_0}$$

We now take out a factor of r^2 from the denominator; using the binomial approximation, we then obtain:

$$A_{x1} \approx \frac{y}{r^2\left(1 - \frac{2xx_0}{r^2}\right)} \approx \frac{y\left(1 + \frac{2xx_0}{r^2}\right)}{r^2}$$

Similarly, we can approximate the rest of the terms of Equ 5.21 as follows:

$$A_{x1} \approx \frac{y\left(1 + \frac{2xx_0}{r^2}\right)}{r^2} \qquad A_{x2} \approx \frac{y\left(1 - \frac{2xx_0}{r^2}\right)}{r^2}$$

$$A_{y1} \approx \frac{(x + x_0)\left(1 - \frac{2xx_0}{r^2}\right)}{r^2} \qquad A_{y2} \approx \frac{(x - x_0)\left(1 + \frac{2xx_0}{r^2}\right)}{r^2}$$

Equ 5.23

Substituting back into H_x and H_y, we get:

$$H_x \approx \frac{1}{2\pi}\left[\frac{y\left(1 + \frac{2xx_0}{r^2}\right)}{r^2} - \frac{y\left(1 - \frac{2xx_0}{r^2}\right)}{r^2}\right] = \frac{1}{2\pi r^2}\left[\frac{4yxx_0}{r^2}\right]$$

Equ 5.24

$$H_y \approx \frac{1}{2\pi}\left[\frac{(x + x_0)\left(1 - \frac{2xx_0}{r^2}\right)}{r^2} - \frac{(x - x_0)\left(1 + \frac{2xx_0}{r^2}\right)}{r^2}\right] = \frac{2x_0}{2\pi r^2}\left[1 - \frac{2x^2}{r^2}\right]$$

Equ 5.25

If we now put $\frac{x}{r} = \cos(\theta)$, $\frac{y}{r} = \sin(\theta)$ and let $s = 2x_0$, we obtain the simplified results below:

$$H_x \approx \frac{1}{2\pi r^2}[2s\sin(\theta)\cos(\theta)]$$

Equ 5.26

$$H_y \approx \frac{1}{2\pi r^2}\left[s\left(1 - 2\cos^2(\theta)\right)\right]$$

Equ 5.27

And using the trigonometric identities $2\sin(\theta)\cos(\theta) = \sin(2\theta)$ and $1 - 2\cos^2(\theta) = -\cos(2\theta)$ we arrive at the final equations:

$$H_x \approx \frac{s}{2\pi r^2}\sin(2\theta)$$

Equ 5.28

$$H_y \approx \frac{-s}{2\pi r^2}\cos(2\theta)$$

Equ 5.29

These imply that the sensitivity in the far field can be written as:

$$S = \sqrt{{H_x}^2 + {H_y}^2} = \frac{s}{2\pi r^2}$$

Equ 5.30

Figure 5.5 shows a comparison between the exact variation in sensitivity of a parallel-wire receiver system, shown in Equ 5.19, and the far-field approximation of Equ 5.30. Here the equations are plotted along the y = 0 axis and we make use of symmetry to plot x > 0 only. The y-axis is normalised to the highest sensitivity value and the x-axis is normalised to x_0. It can be seen that in the far field – further than $3x_0$ – the two equations match and the reception sensitivity of a single rectangular loop does indeed fall off as $\frac{s}{2\pi r^2}$.

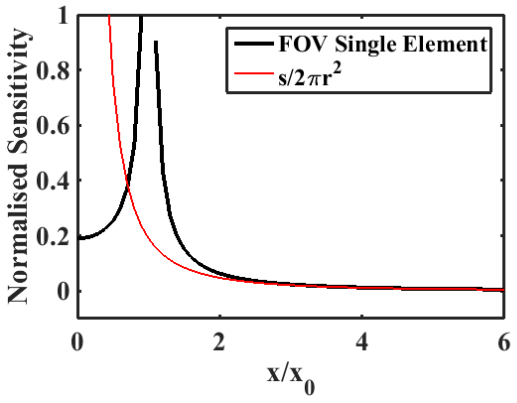

Figure 5.5 Spatial variation of sensitivity for single element compared with the far-field approximation $\frac{s}{2\pi r^2}$.

5.2.3 MI Ring Resonator

We now repeat the FOV calculations for the case of the MI ring resonator. Figure 5.6 shows a plan view of a single octagonal ring with annotated current distribution on the outside of the ring, and coordinates on the inside of the ring. For a coupled MI ring system, operating on an anti-symmetric spatial mode, the current distribution for one ring is opposite to that for the other. Consequently, the FOV will be the same as for a single MI ring resonator, with a zero where the coupled rings meet. Therefore, it is enough to calculate the FOV for a single ring, and the results will also apply to the coupled ring configuration.

In a single ring, supporting a single travelling wave, the current changes phase by a factor of $\exp(-jka)$ at every element. Thus for element, n, the current will be $I_n = I_0\exp\{-j(n-1)ka\}$, with ka = 2π/N for the primary resonance. The separate currents I_{nl} and I_{nr} can therefore be written as $I_{nl} = I_0\exp\{-j(n-1)ka\}$ and $I_{nr} = -I_0\exp\{-j(n-1)ka\}$. The coordinates ($x_n$, y_n) can of course be calculated using standard trigonometry.

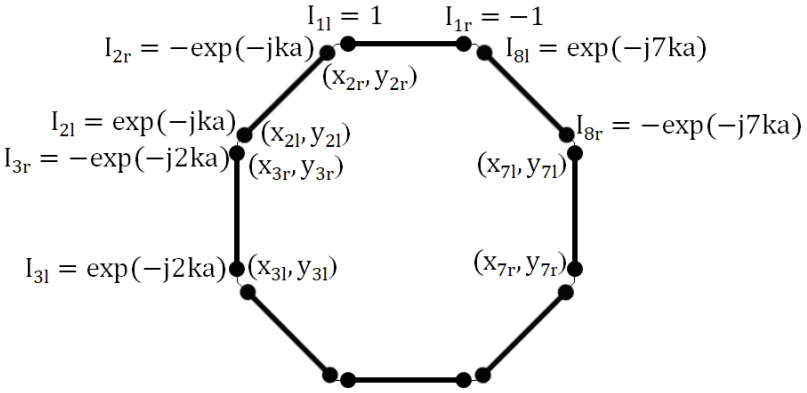

Figure 5.6 Plan view of single octagonal MI ring resonator.

In the following calculations we make use of the fact that the current magnitude is the same at every element and assume it is equal to unity. Additionally, we make the approximation that each element is made of two very long wires next to each other, each labelled 'r' or 'l' for 'right' or 'left', as shown in the coordinates of Figure 5.6. Thus the resolved magnetic field in the x-axis is the sum of the magnetic field of all the 'right' wires and the magnetic field of all the 'left' wires as shown in Equ 5.31.

$$H_x = \sum_{n=1}^{8} H_{xn,r} + H_{xn,l}$$

Equ 5.31

Here n denotes the element number and

$$H_{xn,r} = \frac{-I_{nr}}{2\pi} \frac{y - y_{nr}}{\{(x - x_{nr})^2 + (y - y_{nr})^2\}}$$ **Equ 5.32**

$$H_{xn,l} = \frac{-I_{nl}}{2\pi} \frac{y - y_{nl}}{\{(x - x_{nl})^2 + (y - y_{nl})^2\}}$$ **Equ 5.33**

Similarly, in the y-axis:

$$H_{yn,r} = \frac{I_{nr}}{2\pi} \frac{x - x_{nr}}{\{(x - x_{nr})^2 + (y - y_{nr})^2\}}$$ **Equ 5.34**

$$H_{yn,l} = \frac{I_{nl}}{2\pi} \frac{x - x_{nl}}{\{(x - x_{nl})^2 + (y - y_{nl})^2\}}$$ **Equ 5.35**

Similarly, the total y-component of the magnetic field is as shown in Equ 5.36:

$$H_y = \sum_{n=1}^{8} H_{yn,r} + H_{yn,l}$$

Equ 5.36

Note that now H_x and H_y are both complex and so the sensitivity does not simply depend on $\sqrt{{H_x}^2 + {H_y}^2}$. We must, therefore, go back to Equ 5.6, and deal with the real and imaginary parts of the magnetic field separately. Repeating the previous calculation for the signal voltage V_s, but assuming that H_x and H_y now have real and imaginary components $H_{x,re}$, $H_{x,im}$, $H_{y,re}$ and $H_{y,im}$ we obtain:

$$V_s = -j\omega_L M_0 \mu_0 \left[\left(H_{x,re} + jH_{x,im}\right) + j \left(H_{y,re} + jH_{y,im}\right)\right] dv$$

Equ 5.37

Multiplying out and separating the real and imaginary parts, we can obtain the magnitude of the induced voltage as

$$|V_s| = \omega_L M_0 \mu_0 \sqrt{(H_{x,re} - H_{y,im})^2 + (H_{x,im} + H_{y,re})^2}\, dv$$

Equ 5.38

Therefore, the spatial variation in sensitivity, is now represented as

$$S = \sqrt{(H_{x,re} - H_{y,im})^2 + (H_{x,im} + H_{y,re})^2}$$

Equ 5.39

We now present results for specific ring geometries, without and with the overlap between elements needed to control the mode spectrum. For example, Figure 5.7 (a) shows a contour map of S for an MI ring resonator with L_h = 24 mm and L_v = 4 mm, based on planar elements with no overlap, while

Figure 5.7 (b) shows that for a ring with the curved elements of the same dimensions, but with intra-ring overlap of $4L_h/9$. The overlap is simply incorporated into the calculation by changing the coordinates of the MI ring. As before, wires with finite radius have been used to avoid the problem of infinite fields at the wires themselves. The plan view of the ring itself has also been superimposed on the sensitivity plots to show where the maxima and minima are in relation to the individual elements. Additionally, the axes are normalised to, R, the equivalent ring radius.

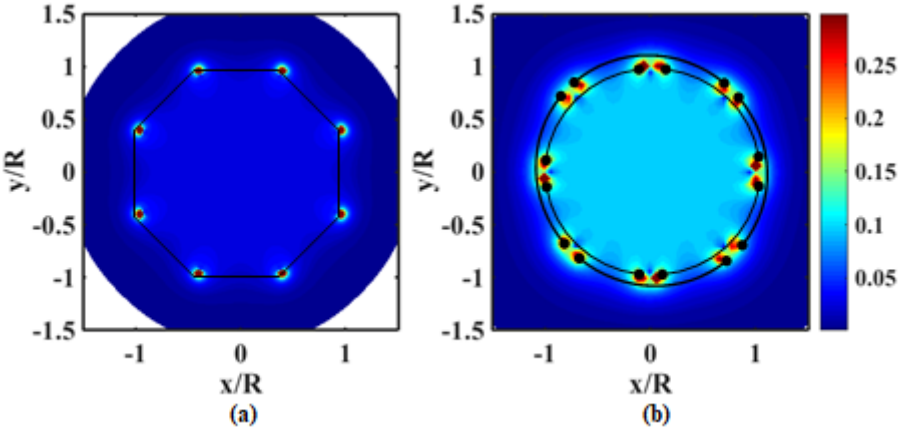

Figure 5.7 Spatial variation of sensitivity for MI ring as per Equ 5.39 (a) with no overlap, and (b) with intra-ring overlap of $4L_h/9$.

For the ring with no intra-ring overlap, there are eight bright spots, corresponding to the eight pairs of closely spaced wires. The sensitivity peaks at each such pair, and decreases as we move further away. In contrast, for the ring with intra-ring overlap, the number of bright spots has doubled, since the individual wires are now distinguishable. However, in each case, there is 8-fold symmetry in sensitivity, with the highest sensitivity in a roughly annular region near the coil itself. As with other ring-type detection coils (the body coil for example), sensitivity is broadly constant inside the ring, decreasing radially outside. It also seems that the overlapped ring has higher sensitivity inside the ring than for the no overlap case.

To quantify the variation in sensitivity of the MI ring resonator, we plot S along the diagonal formed between two pairs of closely spaced wires. For example, Figure 5.8 shows the variation in normalised sensitivity for the no overlap and overlap cases plotted along the lines $y = x/2$ and $y = 0$ respectively. Here, the y-axis has been normalised to the maximum value of S in each case and the x-axis is normalised to the device radius (which is different for each device, due to the overlap).

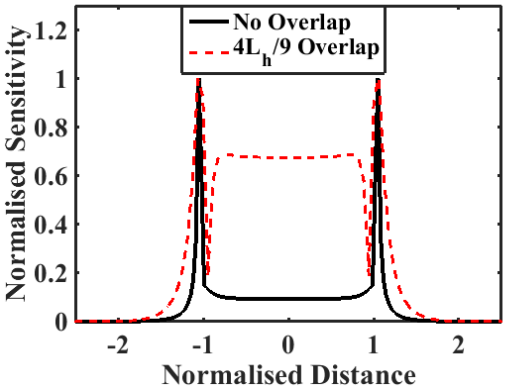

Figure 5.8 Spatial variation of sensitivity for MI ring resonator, for the two cases of i) no element overlap and ii) $4L_h/9$ element overlap.

Without overlap, there are maxima at each wire, when the normalised distance equals 1, then a decrease towards the centre of the ring and away from it. A slower decrease is seen for the case with intra-ring overlap, and we also notice minima just inside the ring due to the overlapped elements. Another difference is that inside the ring the sensitivity is relatively higher for the ring with overlapped elements.

To determine the rate of decrease of the FOV away from the ring, we first note that $I_{nl} = -I_{nr}$ and we denote this value by I_n. We will then have the x- and y-components of the magnetic field as follows.

$$H_{xn} = H_{xnl} + H_{xnr} = \frac{I_n}{2\pi}\left[\frac{(y - y_{nr})}{\{(x - x_{nr})^2 + (y - y_{nr})^2\}} - \frac{(y - y_{nl})}{\{(x - x_{nl})^2 + (y - y_{nl})^2\}}\right]$$

Equ 5.40

$$H_{yn} = H_{ynl} + H_{ynr} = \frac{I_n}{2\pi}\left[\frac{(x - x_{nl})}{\{(x - x_{nl})^2 + (y - y_{nl})^2\}} - \frac{(x - x_{nr})}{\{(x - x_{nr})^2 + (y - y_{nr})^2\}}\right]$$

Equ 5.41

As with the two wire case, we deal with each part separately, and create the A variables below to aid in manipulating the magnetic fields:

$$A_{xnl} = \frac{y - y_{nl}}{\{(x - x_{nl})^2 + (y - y_{nl})^2\}}$$ **Equ 5.42**

$$A_{xnr} = \frac{y - y_{nr}}{\{(x - x_{nr})^2 + (y - y_{nr})^2\}}$$ **Equ 5.43**

$$A_{ynl} = \frac{x - x_{nl}}{\{(x - x_{nl})^2 + (y - y_{nl})^2\}}$$ **Equ 5.44**

$$A_{ynr} = \frac{x - x_{nr}}{\{(x - x_{nr})^2 + (y - y_{nr})^2\}}$$ **Equ 5.45**

Using these, we can express the total x-component of the magnetic field as $H_{xn} = H_{xnr} + H_{xnl} = \frac{I_n}{2\pi}\left[A_{xnr} - A_{xnl}\right]$ and the total y-component magnetic field as $H_{yn} = H_{ynr} + H_{ynl} = \frac{I_n}{2\pi}\left[A_{ynl} - A_{ynr}\right]$.

We first work with A_{xnl}. Writing $r^2 = x^2 + y^2$, introducing ${r_{nl}}^2 = {x_{nl}}^2 + {y_{nl}}^2$ and noting that $r^2 >> {r_{nl}}^2$ in the far field we can write:

$$A_{xnl} = \frac{y - y_{nl}}{\{r^2 + {r_{nl}}^2 - 2(xx_{nl} + yy_{nl})\}} \approx \frac{y - y_{nl}}{\{r^2 - 2(xx_{nl} + yy_{nl})\}}$$

Equ 5.46

Using a binomial expansion, we can then approximate A_{xnl} as:

$$A_{xnl} \approx \frac{1}{r^2}(y - y_{nl})\left(1 + 2\frac{xx_{nl} + yy_{nl}}{r^2}\right)$$

Equ 5.47

Using a similar approach, we can obtain analogous expressions for the other terms, as follows:

$$A_{xnl} \approx \frac{1}{r^2}(y - y_{nl})\left(1 + 2\frac{xx_{nl} + yy_{nl}}{r^2}\right)$$ **Equ 5.48**

$$A_{xnr} \approx \frac{1}{r^2}(y - y_{nr})\left(1 + 2\frac{xx_{nr} + yy_{nr}}{r^2}\right)$$ **Equ 5.49**

$$A_{ynl} \approx \frac{1}{r^2}(x - x_{nl})\left(1 + 2\frac{xx_{nl} + yy_{nl}}{r^2}\right)$$ **Equ 5.50**

$$A_{ynr} \approx \frac{1}{r^2}(x - x_{nr})\left(1 + 2\frac{xx_{nr} + yy_{nr}}{r^2}\right)$$ **Equ 5.51**

Combining these terms, we can obtain for the magnetic fields of individual elements:

$$H_{xn} = \frac{I_n}{2\pi r^2}\left[(y - y_{nr})\left(1 + 2\frac{xx_{nr} + yy_{nr}}{r^2}\right) - (y - y_{nl})\left(1 + 2\frac{xx_{nl} + yy_{nl}}{r^2}\right)\right]$$

Equ 5.52

$$H_{yn} = \frac{I_n}{2\pi r^2}\left[(x - x_{nl})\left(1 + 2\frac{xx_{nl} + yy_{nl}}{r^2}\right) - (x - x_{nr})\left(1 + 2\frac{xx_{nr} + yy_{nr}}{r^2}\right)\right]$$

Equ 5.53

Now we make use of the symmetry of the ring to simplify the problem. Note that we have the relationships in Table 5.1 between the 'left' and 'right' coordinates and so we can represent everything in terms of the left coordinates only.

Table 5.1 Relationship between the coordinates of the 'left' and 'right' wires of each coil.

n	Relation between right and left coordinates
1, 5	$x_{nr} = x_{nl}$ $y_{nr} = -y_{nl}$
2, 6	$x_{nr} = y_{nl}$ $y_{nr} = x_{nl}$
3, 7	$x_{nr} = -x_{nl}$ $y_{nr} = y_{nl}$
4, 8	$x_{nr} = -y_{nl}$

	$y_{nr} = -x_{nl}$

Additionally, following the more detailed ring geometry shown in Figure 5.9 we have the following formulae for the 'left' ring coordinates:

$$x_{nl} = R\cos\left((n-1)\frac{\pi}{4} + \alpha\right) = R\left[\cos\left((n-1)\frac{\pi}{4}\right)\cos(\alpha) - \sin\left((n-1)\frac{\pi}{4}\right)\sin(\alpha)\right]$$

Equ 5.54

$$y_{nl} = R\sin\left((n-1)\frac{\pi}{4} + \alpha\right) = R\left[\sin\left((n-1)\frac{\pi}{4}\right)\cos(\alpha) + \cos\left((n-1)\frac{\pi}{4}\right)\sin(\alpha)\right]$$

Equ 5.55

Here R is the circumradius of the octagonal ring, L_h is the length of its side, corresponding to the horizontal length of a single element, and $\alpha = \sin^{-1}\left(\frac{L_h/2}{R}\right)$ is the half-angle subtended by each element.

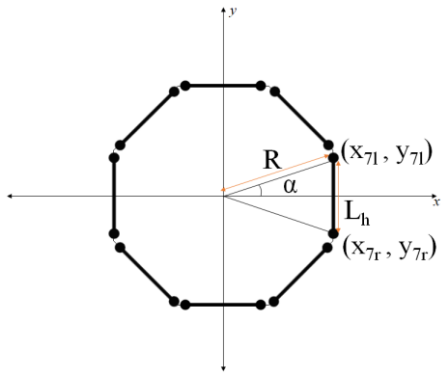

Figure 5.9 Plan view of single MI ring resonator, showing R, L_h and α dimensions.

Using Equ 5.54 and Equ 5.55, we come to the relationships in Equ 5.56 between the coordinates.

$$x_{1l} = -x_{5l} = y_{3l} = -y_{7l}$$

$$x_{2l} = -x_{6l} = y_{4l} = -y_{8l}$$

$$x_{3l} = -x_{7l} = -y_{1l} = y_{5l}$$

$$x_{4l} = -y_{2l} = y_{6l} = -x_{8l}$$

Equ 5.56

Assuming the magnitude of the current is equal to unity, $I_n = \exp\{-j(n-1)ka\}$. For the first mode of an 8-element ring, $ka = \frac{\pi}{4}$ and the current can be represented as in Equ 5.57:

$$I_n = \exp\left\{-j(n-1)\frac{\pi}{4}\right\} = \cos\left\{(n-1)\frac{\pi}{4}\right\} - j\sin\left\{(n-1)\frac{\pi}{4}\right\}$$

Equ 5.57

These results can be used to calculate $H_{x,re}$, $H_{x,im}$, $H_{y,re}$ and $H_{y,im}$ separately, and Equ 5.38 can then be used to calculate the final variation in sensitivity. Using the simplifications of Equ 5.56 and Table 5.1 $H_{x,re}$ becomes

$$H_{x,re} = \frac{1}{2\pi r^2}\left\{\left[-x_{2l}2\sqrt{2} - 4x_{3l} - x_{4l}2\sqrt{2}\right] + \frac{2y^2}{r^2}\left[x_{2l}2\sqrt{2} + 3x_{3l} + x_{4l}2\sqrt{2}\right]\right\}$$

Equ 5.58

And using Equ 5.54 it becomes

$$H_{x,re} = \frac{1}{2\pi r^2}\left\{8R\sin(\alpha) + \frac{2y^2}{r^2}[-7R\sin(\alpha)]\right\}$$

Equ 5.59

We can now make the substitution $\cos\theta = x/r$ and $\sin\theta = y/r$ to get:

$$H_{x,re} = \frac{1}{2\pi r^2}\{8R\sin(\alpha) + 2\sin^2(\theta)[-7R\sin(\alpha)]\}$$

Equ 5.60

And putting $2\sin^2(\theta) = 1 - \cos(2\theta)$ we finally get:

$$H_{x,re} = \frac{1}{2\pi r^2}\{8R\sin(\alpha) + (1 - \cos(2\theta))[-7R\sin(\alpha)]\}$$

Equ 5.61

Carrying out similar manipulations for $H_{x,im}$, $H_{y,re}$ and $H_{y,im}$, we obtain:

$$H_{x,im} = \frac{-1}{2\pi r^2}\{\sin(2\theta)[8R\sin(\alpha)]\}$$

$$H_{y,re} = \frac{1}{2\pi r^2}\{\sin(2\theta)[8R\sin(\alpha)]\}$$

$$H_{y,im} = \frac{-1}{2\pi r^2}\{[8R\sin(\alpha)] + (1 + \cos(2\theta))[-7R\sin(\alpha)]\}$$

Equ 5.62

Finally, noting that $H_{x,im} = -H_{y,re}$ we can obtain the sensitivity variation as:

$$S = \sqrt{\left(H_{x,re} - H_{y,im}\right)^2 + \left(H_{x,im} + H_{y,re}\right)^2} = \sqrt{\left(H_{x,re} - H_{y,im}\right)^2} = H_{x,re} - H_{y,im}$$

Equ 5.63

Making the necessary substitutions, we obtain the result $S = \frac{R \sin(\alpha)}{\pi r^2}$ which after substituting $\sin(\alpha)$ with $\frac{0.5 \times L_h}{R}$ becomes:

$$S = \frac{L_h}{2\pi r^2}$$

Equ 5.64

Equ 5.64 indicates that in the far field, the sensitivity of an MI ring also decreases with radial distance as $1/r^2$, a not unexpected result, since this must be a property of all quasi two-dimensional coils. Figure 5.10 shows a comparison between the exact sensitivity variation found by numerical simulation along the x-axis of the overlapped ring, and the far-field approximation of $\frac{L_h}{2\pi r^2}$ found above. Here it is seen that this approximation holds well for distances over 3R. The rate of decrease of the sensitivity is, therefore, sufficient to reduce detected body noise, hence increasing the SNR.

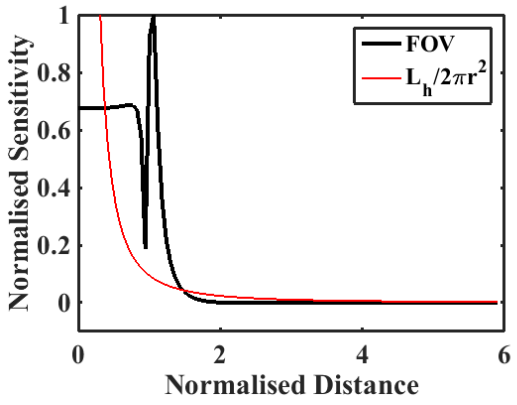

Figure 5.10 Spatial variation of sensitivity for single MI ring resonator with intra-ring element overlap of $4L_h/9$ compared with $\frac{L_h}{2\pi r^2}$ in the far field.

5.3 Effect of MRI Receiver

There are two ways to extract the output from an implanted MRI coil: via an external reading coil to which the internal coil is magnetically coupled, or via a cable that connects the coil directly to the MRI scanner. Obviously, the former is attractive since it avoids the need for any wires. However, the coupled MI ring resonator system cannot couple to the symmetric reading coil of an MRI scanner since it is operating in its anti-symmetric mode to decouple from the $\mathbf{B_1}$ field. Nevertheless, here we will explain the principles involved in mutually coupled systems, starting with a simple system based

on rectangular coils, then extending the analysis to a single MI ring resonator. Finally, we explore the option of extracting the output of the coupled MI ring resonator system using a single tap or a quadrature tap connected to the MRI scanner.

5.3.1 Rectangular coils

To find the FOV of an internal coil coupled by mutual inductance to an external read coil, we start by assuming the simple 2D geometry shown in in Figure 5.11. This shows the cross-section of the external receiver and the internal coil, labelled as coil 1 and coil 2 respectively. Both are assumed to be two-wire approximations to rectangular coils, lying in the z-direction. As is usually the case, the external read coil is larger than the internal coil. Both coils are located symmetrically about the y-axis and coil 1 is positioned above coil 2. The distance between the two coils is d_{rec}. As before, we find the FOV of the combined system by assuming unity current in the external read coil, with unity current going into the left wire and the same coming out of the right wire.

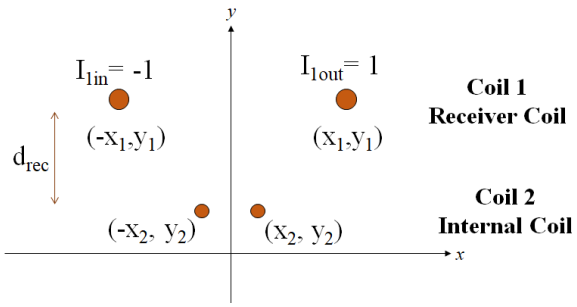

Figure 5.11 2D approximation of a readout system based on an external read coil coupled to an internal coil.

Figure 5.12 shows the equivalent circuit of the coupled coil system. Here we assume each coil has the usual parameters R_i, C_i and L_i, I_i, with i = 1 for the receiver coil and i = 2 for the internal coil, and M is the mutual inductance. The receiver coil is driven by a voltage V_1, whereas the internal coil is not driven. We also assume that both coils are tuned to the same frequency of ω_0.

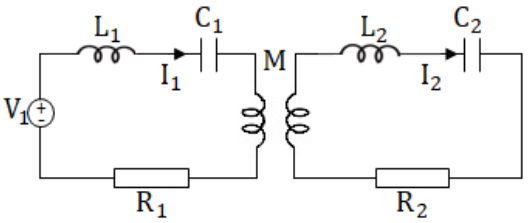

Figure 5.12 Equivalent circuit of a coupled coil system.

Using Kirchoff's voltage law, we obtain the following set of equations:

$$\left(R_1 + j\omega L_1 + \frac{1}{j\omega C_1}\right) I_1 + j\omega M I_2 = V_1$$

$$\left(R_2 + j\omega L_2 + \frac{1}{j\omega C_2}\right) I_2 + j\omega M I_1 = 0$$

Equ 5.65

At resonance, $\omega = \omega_0 = 1/\sqrt{(L_1C_1)} = 1/\sqrt{(L_2C_2)}$ and the equations above simplify to:

$$R_1 I_1 + j\omega_0 M I_2 = V_1$$

$$R_2 I_2 + j\omega_0 M I_1 = 0$$

Assuming that $I_1 = 1$, we obtain the following relationships for V_1 and I_2:

$$V_1 = R_1 + \frac{\omega_0^2 M^2}{R_2}$$

Equ 5.66

$$I_2 = -j\frac{\omega_0 M}{R_2}$$

Equ 5.67

Here M is the mutual inductance between the two coils and R_2 is the self-resistance of the internal coil. These values could be calculated or simulated. However, for now we simply introduce the normalised variable α, the ratio between the mutual impedance to and the self-resistance of the internal coil, which plays a much more significant role:

$$\alpha = \frac{\omega_0 M}{R_2}$$

Equ 5.68

As we show below, α determines the relative contribution to overall sensitivity of the internal coil and the external read coil. Using $I_1 = 1$ and the value of I_2 from Equ 5.67, we can calculate the magnetic field for each coil and sum them to obtain the total magnetic field for the coupled coil system. Since the calculations are very similar to those described above, we shall omit the details. However, in doing so, we must bear in mind that since I_2 is imaginary, the magnetic fields will be complex and therefore, S must be calculated based on Equ 5.38.

Figure 5.13 shows the spatial variation in sensitivity of the coupled coil system for α values ranging from 0.1 to 100 Here we have assumed the following parameters $x_1 = 50$ mm, $x_2 = 12$ mm and $d_{rec} = 100$ mm In each case, we see peaks in sensitivity near the conductors that form the two separate coils. However, the relative values of these peaks depends on the value of α. For low values of α, the sensitivity is dominated by the external read coil and only for α values of 10 or more do we see any

enhancement in the locality of the internal coil. Large values of α are therefore required to obtain any significant benefit. It is therefore worthwhile investigating how the value may be achieved.

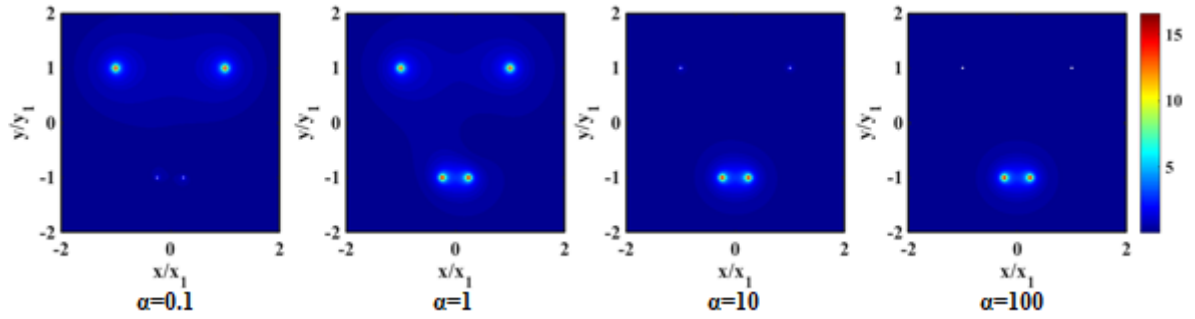

Figure 5.13 Spatial variation of sensitivity for the coupled coil system for different α values.

For the simplified system considered above, it is possible to calculate the mutual inductance and the self-resistance of the internal coil analytically and obtain an exact value for α for any particular geometry. To find the mutual inductance, we start by obtaining the linked magnetic flux, Φ, generated by coil 1 and passing through coil 2. We can then use the equation $M = \Phi/I_1$ to calculate the mutual inductance between the two coils. To calculate Φ, we start with the y-component of the magnetic field due to coil 1:

$$H_{y1} = \frac{I_1}{2\pi}\left[\frac{x - x_1}{((x - x_1)^2 + (y + y_1)^2)} - \frac{x + x_1}{((x + x_1)^2 + (y + y_1)^2)}\right]$$

Equ 5.69

Knowing that the magnetic flux density, $\mathbf{B_{y1}} = \mu_0 H_{y1}$, we can then calculate the per-unit-length Φ as shown in Equ 5.70. Here r_2 is the radius of the wire of the internal coil, and so the integration limits lie inside the physical extent of the two wires.

$$\Phi = \int_{-x_2+r_2}^{x_2-r_2} \mathbf{B_{y_1}}\, dx$$

Equ 5.70

Substituting the magnetic flux density, we obtain the following expression for the per-unit-length linked flux:

$$\Phi = \frac{\mu_0 I_1}{2\pi}\int_{-x_2+r_2}^{x_2-r_2}\left[\frac{x - x_1}{((x - x_1)^2 + (y + y_1)^2)} - \frac{x + x_1}{((x + x_1)^2 + (y + y_1)^2)}\right] dx$$

Equ 5.71

Performing the integral then yields:

$$\Phi = \frac{\mu_0 I_1}{2\pi}[\ln((x_2 - r_2 - x_1)^2 + (y + y_1)^2) - \ln((r_2 - x_2 - x_1)^2 + (y + y_1)^2) - \ln((x_2 - r_2 + x_1)^2 + (y + y_1)^2) + \ln\big((r_2 - x_2 + x_1)^2 + (y + y_1)^2\big)]$$

Equ 5.72

Re-arranging, we can then obtain:

$$\Phi = \frac{\mu_0 I_1}{2\pi} \ln\left[\frac{((x_2 - r_2 - x_1)^2 + (y + y_1)^2)}{(x_2 - r_2 + x_1)^2 + (y + y_1)^2}\right]$$

Equ 5.73

The per-unit-length mutual inductance is $M = \Phi/I_1$. To obtain the actual mutual inductance, we simply multiply this value by the actual lengths of the coils, *l*:

$$M = \frac{\mu_0}{2\pi} \ln\left[\frac{((x_2 - r_2 - x_1)^2 + (y_2 + y_1)^2)}{(x_2 - r_2 + x_1)^2 + (y_2 + y_1)^2}\right] l$$

Equ 5.74

If we assume that the position of the coils is $(x_1, y_1) = (50, 50)$ mm and $(x_2, y_2) = (12, -50)$ mm with a length of 50 mm and that the wire radius of the internal coil is 0.25 mm, the mutual inductance comes to 9.58nH.

A similar estimate can be made for the self-resistance of the internal coil. The resistance of any coil can be calculated as:

$$R = \frac{l}{2\pi r \delta \sigma}$$

Equ 5.75

Where l is the length of the coil, r is the radius of the wire, σ is the conductivity of copper (5.96×10^7 Sm^{-1}) and δ is the skin depth. The skin depth itself is also calculated as:

$$\delta = \sqrt{\frac{1}{\pi f \mu_0 \sigma}}$$

Equ 5.76

Here μ_0 is the free-space permeability ($4\pi\times10^{-7}$ Hm^{-1}) and f is the operating frequency (63.85 MHz for 1.5 T MRI or 127.74 MHz for 3.0 T).

For the 1.5 T MRI scanner, we get $R_2 = 0.0655$ Ω. This yields α = 59. Similarly, for the 3.0 T scanner, R_2 increases slightly to 0.0926 Ω and α increases to 83. This indicates that we will indeed get the

required SNR enhancement near the internal coil and that a 3.0 T MRI scanner offers an improvement to the 1.5 T one.

5.3.2 Single MI Ring Resonator

We now attempt to replicate the FOV calculations for the case of a single internal MI ring resonator coupled to an external read coil. Again we assume a 2D parallel wire model. The geometry now becomes a little more complicated, but the principles remain the same. Figure 5.14 shows the new arrangement. Here, coil 1 is still the external read coil, approximated as two wires, but coil 2 is now the MI ring resonator, approximated as eight two-wire elements. d_{rec} is the distance between the edge of the MI ring resonator and the external receiver.

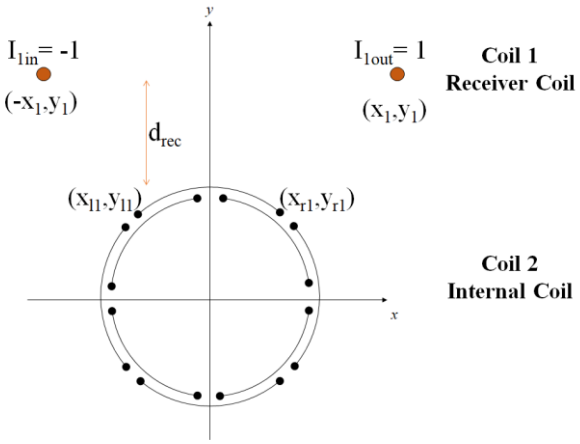

Figure 5.14 Cross section of coupled coil geometry with MI ring as internal coil.

We have previously found the x- and y-components of the magnetic field generated by each of the coils in the ring, in Equ 5.31and Equ 5.36 respectively. For clarity, we reproduce these here:

$$H_{x_{ring}} = \sum_{n=1}^{8} \frac{-I_{ring,n}}{2\pi}\left[\frac{y - y_{nr}}{\{(x - x_{nr})^2 + (y - y_{nr})^2\}} - \frac{y - y_{nl}}{\{(x - x_{nl})^2 + (y - y_{nl})^2\}}\right]$$

$$H_{y_{ring}} = \sum_{n=1}^{8} \frac{I_{ring,n}}{2\pi}\left[\frac{x - x_{nr}}{\{(x - x_{nr})^2 + (y - y_{nr})^2\}} - \frac{x - x_{nl}}{\{(x - x_{nl})^2 + (y - y_{nl})^2\}}\right]$$

Equ 5.77

Where $I_{ring,n}$ is the current in the n^{th} coil of the MI ring resonator. Similarly, the magnetic field for the receiver, has also previously been derived; again for clarity, we reproduce the necessary results here:

$$H_{x_1} = \frac{I_1}{2\pi}\left[\frac{(y-y_1)}{\{(x+x_1)^2+(y-y_1)^2\}} - \frac{(y-y_1)}{\{(x-x_1)^2+(y-y_1)^2\}}\right]$$

$$H_{y_1} = -\frac{I_1}{2\pi}\left[\frac{(x+x_1)}{\{(x+x_1)^2+(y-y_1)^2\}} - \frac{(x-x_1)}{\{(x+x_1)^2+(y-y_1)^2\}}\right]$$

Equ 5.78

Using these results, the total x- and y-components of magnetic field will be $H_{xring} + H_{x1}$ and $H_{yring} + H_{y1}$, and the sensitivity can be found as $\sqrt{\left(H_{x,re} - H_{y,im}\right)^2 + \left(H_{x,im} + H_{y,re}\right)^2}$, assuming the current patterns are complex. However, to perform the calculation, we must first calculate $I_{ring,n}$, assuming that $I_1 = 1$. This can be done using standard equivalent circuit models.

For example, for this configuration, there are eight 'external' mutual inductances, between the external read coil coil and each separate coil of the MI ring resonator as shown in Figure 5.15. If the ring is positioned symmetrically with respect to the receiver coil, the total number of different external mutual inductances can be reduced to five, denoted by M_{01}, M_{02}, … M_{05}. We also have the usual internal mutual inductances, M_{s1},…, M_{s4} between the individual coils of the ring.

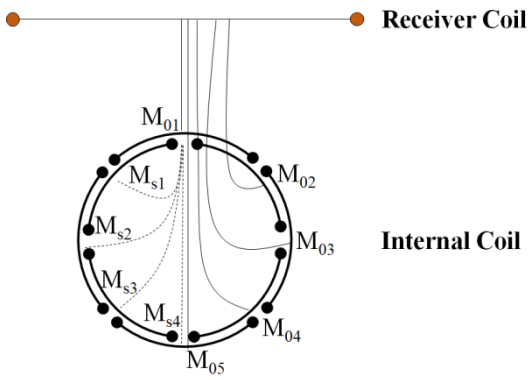

Figure 5.15 Definition of mutual inductances between an external read coil and an MI ring resonator, M_{0n}, and between the separate coils of the ring, M_{sn}.

Using KVL, these terms may be combined with other impedances in an equivalent circuit model of the complete system. The result is a set of nine simultaneous equations, which can be represented in matrix form as:

$$\bar{\mathbf{Z}}\mathbf{I} = \mathbf{V}$$

Equ 5.79

where $\bar{\mathbf{Z}}$ is the 9 × 9 impedance matrix shown in Equ 5.80. Here, $Z_{ring} = R + R_B + j\omega L + 1/j\omega C$ is the self-impedance of an individual coil of the MI ring, with R_B being the loading from the body (here, assumed to be equal to 5R). $Z_{rec} = R_{rec} + j\omega L_{rec} + 1/j\omega C_{rec}$ is the self-impedance of the external read

coil, $Z_{M0n} = j\omega M_{0n}$ is the n^{th} mutual impedance between the read coil and the ring and $Z_{MSn} = j\omega M_{sn}$ is the n^{th} mutual impedance between the individual coils of the ring.

$$\bar{\mathbf{Z}} = \begin{pmatrix} Z_{rec} & Z_{M01} & Z_{M02} & Z_{M03} & Z_{M04} & Z_{M05} & Z_{M04} & Z_{M03} & Z_{M02} \\ Z_{M01} & Z_{ring} & Z_{Ms1} & Z_{Ms2} & Z_{Ms3} & Z_{Ms4} & Z_{Ms3} & Z_{Ms2} & Z_{Ms1} \\ Z_{M02} & Z_{Ms1} & Z_{ring} & Z_{Ms1} & Z_{Ms2} & Z_{Ms3} & Z_{Ms4} & Z_{Ms3} & Z_{Ms2} \\ Z_{M03} & Z_{Ms2} & Z_{Ms1} & Z_{ring} & Z_{Ms1} & Z_{Ms2} & Z_{Ms3} & Z_{Ms4} & Z_{Ms3} \\ Z_{M04} & Z_{Ms3} & Z_{Ms2} & Z_{Ms1} & Z_{ring} & Z_{Ms1} & Z_{Ms2} & Z_{Ms3} & Z_{Ms4} \\ Z_{M05} & Z_{Ms4} & Z_{Ms3} & Z_{Ms2} & Z_{Ms1} & Z_{ring} & Z_{Ms1} & Z_{Ms2} & Z_{Ms3} \\ Z_{M04} & Z_{Ms3} & Z_{Ms4} & Z_{Ms3} & Z_{Ms2} & Z_{Ms1} & Z_{ring} & Z_{Ms1} & Z_{Ms2} \\ Z_{M03} & Z_{Ms2} & Z_{Ms3} & Z_{Ms4} & Z_{Ms3} & Z_{Ms2} & Z_{Ms1} & Z_{ring} & Z_{Ms1} \\ Z_{M02} & Z_{Ms1} & Z_{Ms2} & Z_{Ms3} & Z_{Ms4} & Z_{Ms3} & Z_{Ms2} & Z_{Ms1} & Z_{ring} \end{pmatrix}$$

Equ 5.80

I and **V** are the 9 – element current and voltage column vectors shown in Equ 5.81 and Equ 5.82 respectively. Here I_1 is the current in the external read coil (here assumed equal to 1), and $I_{ring,n}$ is the current in each of the ring coils. V_1 is the non-zero voltage driving the read coil, with zero volts across all the ring coils.

$$\mathbf{I} = \begin{pmatrix} I_1 & I_{ring,1} & I_{ring,2} & \dots & I_{ring,8} \end{pmatrix}'$$

Equ 5.81

$$\mathbf{V} = (V_1 \quad 0 \quad 0 \quad 0 \quad 0 \quad 0 \quad 0 \quad 0 \quad 0)'$$

Equ 5.82

We now have nine simultaneous equations, which can be solved to calculate the current in each coil, as shown in Equ 5.83, with the external coil and the first mode of the ring resonator tuned to the Larmor frequency.

$$\mathbf{I} = \overline{\mathbf{Z^{-1}}}\mathbf{V}$$

Equ 5.83

As before, the numerical simulator FastHenry can be used to find the values of the mutual inductances, self-inductances and self-resistances, for a full 3D geometry. Figure 5.16 shows a FastHenry model of an external read coil coupled to a ring. Here the small ring with diameter, D = 34 mm and an intra-ring overlap of $4L_h/9$ is used, and the receiver is a 50 × 100 mm rectangular coil positioned d_{rec} = 100 mm away from the internal device. In each case, the coils are assumed to be wrapped around cylindrical formers.

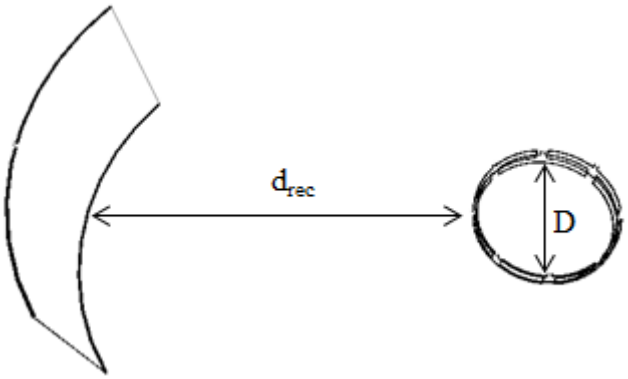

Figure 5.16 FastHenry model of coupled coil system with MI ring resonator as internal coil.

Using the extracted mutual inductances, coupling coefficients may be found, denoting $\kappa_{0i} = 2M_{0i}/L$, and so on. Table 5.2 shows the coupling coefficients and corresponding current distributions thus obtained. Here we notice that the external coupling coefficients are very small, due to the large distance between the read coil and the internal coil. It is also observed that the current distribution does not have the usual exponential pattern expected from a travelling wave on a ring resonator.

Table 5.2 Coupling coefficients and induced currents for coupled coil system with MI ring resonator as internal coil

Internal Coupling Coefficients		**External Coupling Coefficients**	
κ_{s1}	0.2878	κ_{01}	0.99×10^{-3}
κ_{s2}	-0.0182	κ_{02}	0.58×10^{-3}
κ_{s3}	-0.0041	κ_{03}	-0.13×10^{-3}
κ_{s4}	-0.0033	κ_{04}	-0.50×10^{-3}
		κ_{05}	-0.53×10^{-3}
Induced MI ring Currents			
$I_{ring,1}$		-0.0008 + 0.0114i	
$I_{ring,2}$		-0.0017 - 0.0002i	
$I_{ring,3}$		-0.0002 - 0.0126i	
$I_{ring,4}$		0.0012 - 0.0180i	
$I_{ring,5}$		-0.0002 - 0.0126i	
$I_{ring,6}$		-0.0017 - 0.0002i	
$I_{ring,7}$		-0.0008 + 0.0114i	
$I_{ring,8}$		0.0004 + 0.0159i	

To explain this, we first consider nearest neighbour coupling only between the receiver and the MI ring resonator. In this case, the receiver must induce counter-propagating current waves travelling round the ring, in the form of a pair of complex exponentials $\exp\{\pm j(n-1)ka\}$. These sum to give a cosinusoidal standing wave pattern as shown in Equ 5.84. Here I_0 is the amplitude of the wave, and we have put $ka = \pi/4$ since the ring resonator is tuned to its first mode.

$$I_{ring,n} = \frac{1}{2} I_0 [\exp\{ j(n-1)ka\} + \exp\{ -j(n-1)ka\}] = I_0 \cos\left((n-1)\frac{\pi}{4}\right)$$

Equ 5.84

This current distribution means that the ring elements now have different current magnitudes, with elements 3 and 7 having no current at all. However, if in addition we also consider the higher order coupling between the external read coil and other elements in the ring, we must obtain eight pairs of counter-propagating travelling waves. These must sum to give the overall current distribution shown in Table 5.2.

Using these values, and assuming $I_1 = 1$, we plot the sensitivity map obtained for the configuration in Figure 5.14. Figure 5.17 (a) shows the spatial variation of sensitivity for the combined system of the external read coil and the internal ring thus obtained. Here we see that the largest contribution to sensitivity is obtained from the receiver coil, and that the internal coil offers only a very small local enhancement. This is expected from the low receiver coupling observed in Table 5.2. Figure 5.17 (b) shows an enlarged view of this pattern in the vicinity of the MI ring only. Here we can see that the 8-fold symmetry previously found no longer exists, and there seems to be four 'bright spots' missing, presumably from the lack of contribution to the current from elements 3 and 7.

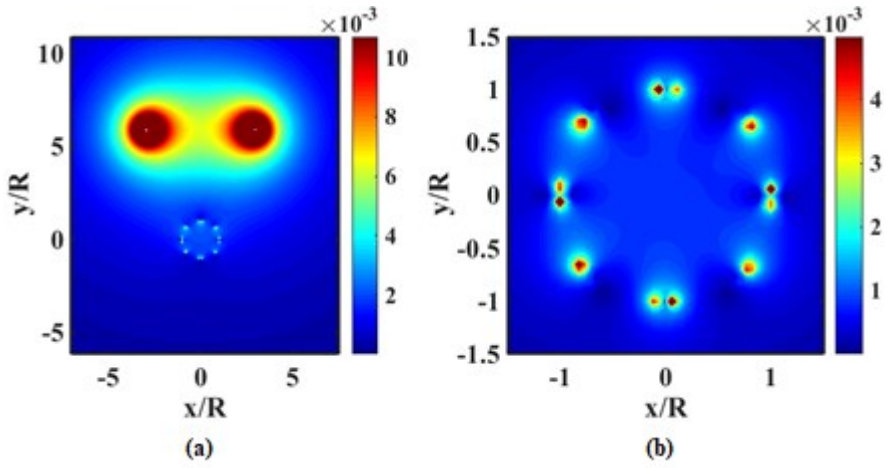

Figure 5.17 Spatial variation of sensitivity for MI ring resonator coupled to an external read coil (a) global variation, and (b) local variation near the ring.

We can compare this variation in sensitivity to that obtained using an isolated ring with a standing wave current pattern. Figure 5.18 shows the spatial variation of sensitivity of the MI ring resonator with nearest neighbour coupling only, which produces a cosinusoidal current pattern such as in Equ 5.84,with $I_0 = 1$. Firstly, we see that the sensitivity is very similar to that obtained with higher order couplings. Here we have also added the plan view of the MI ring resonator; and this confirms that when the receiver is only coupled to element 1 of the ring, there is zero current in elements 3 and 7. In practice, the coupling between these two elements and the receiver is even lower than for other

elements, due to their orientation with respect to the receiver ($\kappa_{03} < \kappa_{04}$ and κ_{05} from Table 5.2). This makes their contribution to the overall current distribution and the standing wave pattern less than for other elements, and thus their contribution to the magnetic field is also less.

There is only a 6-fold symmetry observed. If we denote the four diameters of the ring as D1 for the diameter through elements 1 and 5, D2 for that through elements 2 and 6, D3 for the diameter through elements 3 and 7 and finally D4 for the diameter through elements 4 and 8, the pattern is clearly symmetric across the diameters D1 and D3, but symmetry is lost across D2 and D4.

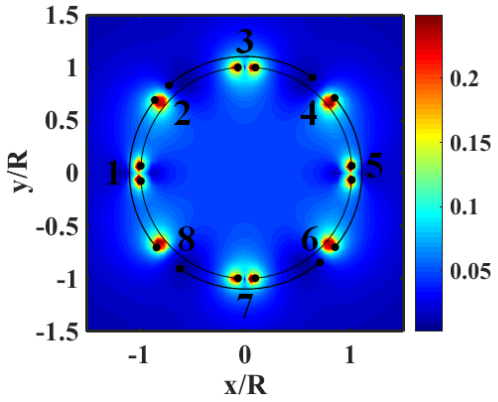

Figure 5.18 Spatial variation of sensitivity of MI ring resonator with nearest neighbour coupling to external receiver, with superimposed plan view of MI ring

Continuing with the analysis of this sensitivity pattern with reduced symmetry, we plot the sensitivity through each of the diameters. Figure 5.19 shows the variation in sensitivity across each of the four diameters. Here we have also plotted the sensitivity with the currents obtained in Table 5.2 and normalised the sensitivity to the maximum for each diameter for comparison. The two sets of data are extremely similar, with that obtained with higher order coupling only deviating slightly from the perfect symmetry round the x = 0 line. We then notice that indeed the response is different through each of D1, D2 and D3, with the sensitivity across D2 and D4 being equal.

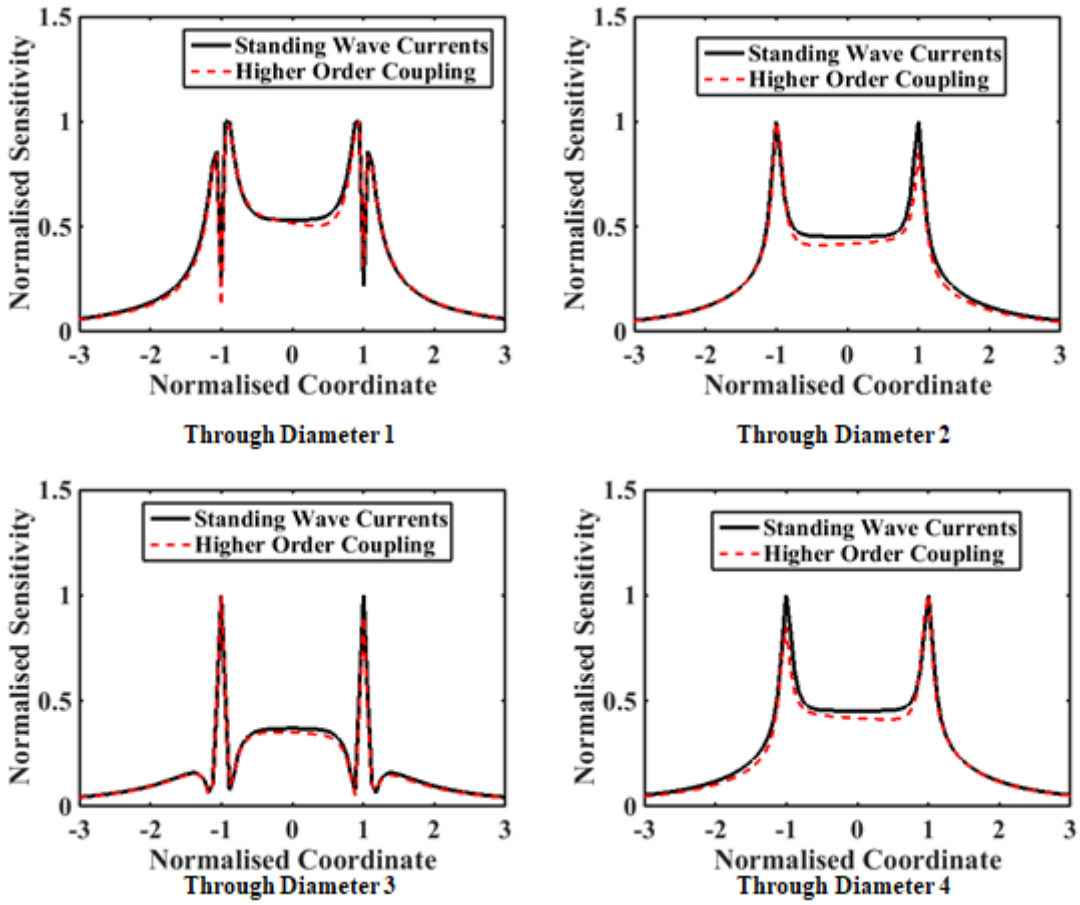

Figure 5.19 Spatial variation of sensitivity through each of the four diameters of the MI ring resonator with $4L_h/9$ intra-ring overlap.

Previously, with a single travelling wave current, we found a maximum in sensitivity at the device radius and a minimum just inside, as was shown in Figure 5.8. There was also a radial decrease outside. Here, through the first diameter, we have a zero exactly at the radius, with maxima just inside and outside. The sensitivity then falls gradually as before. Through diameters 2 and 4, at the wires of the third and seventh elements we do not find this zero in sensitivity from the elements overlapping; instead only the maximum is still there. In fact the sensitivity through D1, D2 and D4 is exactly the same, with the only difference being the zero at D1. Through D3, the variation in sensitivity is slightly different: there is a maximum at the device radius, but now there are two minima on either side, and the fall-off is very steep. There is also some sensitivity inside the device itself; however, in practice, only the annular region just outside matters since, this is where the anastomosis is located.

As we have seen in the examples above, interrogation using an external read coil may have a number of disadvantages in this application. Firstly, large separation tends to nullify the local sensitivity advantage of the internal coil, and reduce symmetry. Much more importantly, the use of a coupled ring system operating on an anti-symmetric mode to reduce $\mathbf{B_1}$ coupling will reduce the likely mutual

inductance to any form of external read coil to zero, except a closely spaced coil with a similarly anti-symmetric mode of operation. We therefore now consider the alternative of direct coupling.

5.3.3 Directly-interrogated Coupled MI Ring Device

Direct coupling requires a wired connection to at least one element of the coupled ring system. Medically, this is clearly disadvantageous. However, there is a natural body lumen down which the wire may conveniently be passed, and further protection may be provided by an additional internal sheath such as C-Seal [204].

As before, the field-of-view may be found from reciprocity, assuming that a single element in the ring is driven with unit current. Here we have a situation similar to that of the previous section: with one of the elements of the ring driven, two travelling waves propagate round the ring and sum to give the cosinusoidal wave pattern of Equ 5.84. Numerical simulation for similar parameters to those used before leads to the spatial variation in sensitivity shown in Figure 5.18. This result, with only six-fold symmetry, must also be expected for the coupled MI ring system, with the additional factor of a zero in sensitivity in the annular region between the two rings. Of course, symmetry can be restored using a quadrature taps, as is normally done for body coils [205]. All that is required are two taps, located at right angles round the ring The two taps are connected using a quadrature hybrid coupler, a well-known four-port RF component, which acts to sum their contributions appropriately.

The operation of a quadrature system can be analysed as follows [206]. Assuming the input to the coupler is unity, the output to each of the tap elements will be $\frac{1}{\sqrt{2}}$ and $\frac{1}{\sqrt{2}}\exp\left(-\mathrm{j}\frac{\pi}{2}\right)$. Thus each element will generate a standing wave pattern of the form shown in Equ 5.85.

$$\mathrm{I_{n1}} = \frac{\mathrm{I_0}}{\sqrt{2}}\cos\big((\mathrm{n}-1)\mathrm{ka}\big) \qquad \text{and} \qquad \mathrm{I_{n2}} = \frac{\mathrm{I_0}}{\sqrt{2}}\sin\big((\mathrm{n}-1)\mathrm{ka}\big)\exp\left(-\mathrm{j}\frac{\pi}{2}\right)$$

Equ 5.85

Here the sine term in the second pattern is due to the 90° rotation in the position of the element in the ring. If we now expand these terms, and put $\exp\left(-\mathrm{j}\frac{\pi}{2}\right) = -\mathrm{j}$, the current patterns can be obtained as:

$$\mathrm{I_{n1}} = \frac{\mathrm{I_0}}{\sqrt{2}}\left[\frac{\exp\{\mathrm{j}(\mathrm{n}-1)\mathrm{ka}\} + \exp\{-\mathrm{j}(\mathrm{n}-1)\mathrm{ka}\}}{2}\right]$$

$$\mathrm{I_{n2}} = \frac{-\mathrm{j}\mathrm{I_0}}{\sqrt{2}}\left[\frac{\exp\{\mathrm{j}(\mathrm{n}-1)\mathrm{ka}\} - \exp\{-\mathrm{j}(\mathrm{n}-1)\mathrm{ka}\}}{2\mathrm{j}}\right]$$

Equ 5.86

These two patterns are then effectively summed inside the ring resonator to generate the travelling wave exponential current pattern:

$$I_n = \frac{I_0}{\sqrt{2}} \exp\{j(n-1)ka\}$$

Equ 5.87

With this current pattern, we can calculate the magnetic fields as before, and must clearly obtain a symmetric sensitivity pattern as was previously shown in Figure 5.7 (b) and now reproduced below. The high degree of uniformity both inside and outside the ring suggests that a wired quadrature system will offer at least one high performance local detection system. However, we must still consider the likely effect of operation on an anti-symmetric mode, which will affect sensitivity in the perpendicular plane.

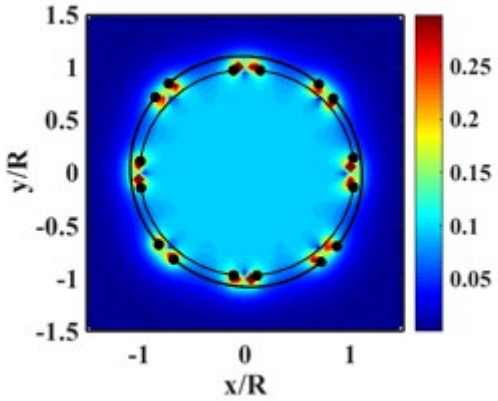

Figure 5.20 Spatial sensitivity variation of quadrature-connected MI ring resonator.

5.3.4 Perpendicular planes

We have so far concentrated on calculating the sensitivity variation of MI ring resonator systems in a plane parallel to the ring axis (likely to correspond to the plane of an axial image during MRI). We now calculate the sensitivity variation in the perpendicular plane (which might correspond to a coronal or sagittal plane during MRI) to understand the effect of detection using an anti-symmetric resonant mode. Figure 5.21 (a) shows a diagram of the coupled MI ring system, without overlapping coils for simplicity. The horizontal red dashed line shows the previously calculated 'axial' spatial variation in sensitivity, S, and the vertical red dashed line shows the corresponding 'sagittal' or 'coronal' variation calculated here.

Figure 5.21 (b) shows the geometry of the system in the x-z plane, with a description of the currents and coordinates. Here the two MI ring resonators are coupled as usual, with four wires from each MI ring shown in this cross-section. Each two wires in each quadrant are from a single coil.

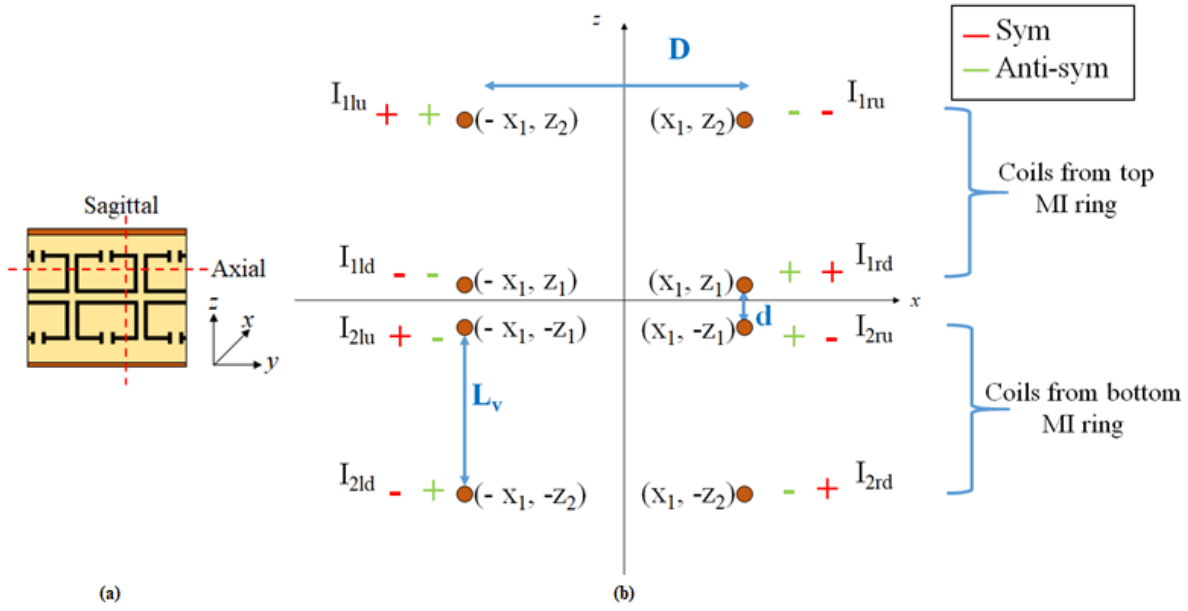

Figure 5.21 (a) Definition of axial and sagittal FOV. (b) sagittal section of a coupled MI ring resonator system.

The distance between the left and right wires is equal to the diameter of the ring, D, so that $x_1 = D/2 = R$. Furthermore, for each ring, the distance between the top and bottom wires is equal to the vertical length, L_v, while the distance between the two rings is denoted by d. We may therefore write $z_1 = d/2$ and $z_2 = d/2 + L_v$ The currents in the wires are denoted by I_1 and I_2 for the top and bottom rings respectively; with a subscript 'l' or 'r' for 'left' and 'right' elements and 'u' or 'd' for 'up' and 'down' wires. If the symmetric modes are excited, then the current in each wire will have the polarity shown in red, with the upper and lower rings having the same polarity. Conversely, when the anti-symmetric modes are excited, the polarity in each ring will be opposite, as shown in green.

To calculate the magnetic fields, we assume the wires are infinitely long as before. However, this time we may ignore H_z components, since there is no component of the transverse magnetization M_{xy} in this direction. For the x-components of the field we obtain:

$$H_{x1ld} = -\frac{I_{1ld}}{2\pi}\frac{z - z_1}{(z - z_1)^2 + (x + x_1)^2} \qquad H_{xr1d} = -\frac{I_{1rd}}{2\pi}\frac{z - z_1}{\{(z - z_1)^2 + (x - x_1)^2\}}$$

$$H_{x1lu} = -\frac{I_{1lu}}{2\pi}\frac{z - z_2}{\{(z - z_2)^2 + (x + x_1)^2\}} \qquad H_{xr1u} = -\frac{I_{1ru}}{2\pi}\frac{z - z_2}{\{(z - z_2)^2 + (x - x_1)^2\}}$$

$$H_{x2ld} = -\frac{I_{2ld}}{2\pi}\frac{z + z_2}{\{(z + z_2)^2 + (x + x_1)^2\}} \qquad H_{xr2d} = -\frac{I_{2rd}}{2\pi}\frac{z + z_2}{\{(z + z_2)^2 + (x - x_1)^2\}}$$

$$H_{x2lu} = -\frac{I_{2lu}}{2\pi}\frac{z + z_1}{\{(z + z_1)^2 + (x + x_1)^2\}} \qquad H_{xr2u} = -\frac{I_{2ru}}{2\pi}\frac{z + z_1}{\{(z + z_1)^2 + (x - x_1)^2\}}$$

Equ 5.88

The total magnetic field H_x is the sum of the magnetic field produced by each of the wires, namely $H_x = H_{x1ld} + H_{x1lu} + H_{x2ld} + H_{x2lu} + H_{x1rd} + H_{x1ru} + H_{x2rd} + H_{x2ru}$. Following similar arguments to those used before, the sensitivity variation S must be $\sqrt{H_x^2} = H_x$ since the currents are all real.

We illustrate the result using a numerical example, assuming that $I_{1lu} = 1$ and the remainder of the wires are driven accordingly. Finite wire radii are again used to avoid the problem of infinite fields at wire origins. The following dimensional parameters are assumed: D = 34 mm, d = 2 mm and L_v = 4mm. Figure 5.22 (a) and (b) shows the spatial variation of sensitivity for the symmetric and anti-symmetric modes respectively. As expected, the overall pattern is symmetric about z = 0 and x = 0. As usual, sensitivity is maximum at the wires and decreases further away. However, the anti-symmetric mode has a zero in sensitivity between the coupled rings, while the symmetric mode has no such null. Otherwise, similar sensitivity is obtained using either mode of operation.

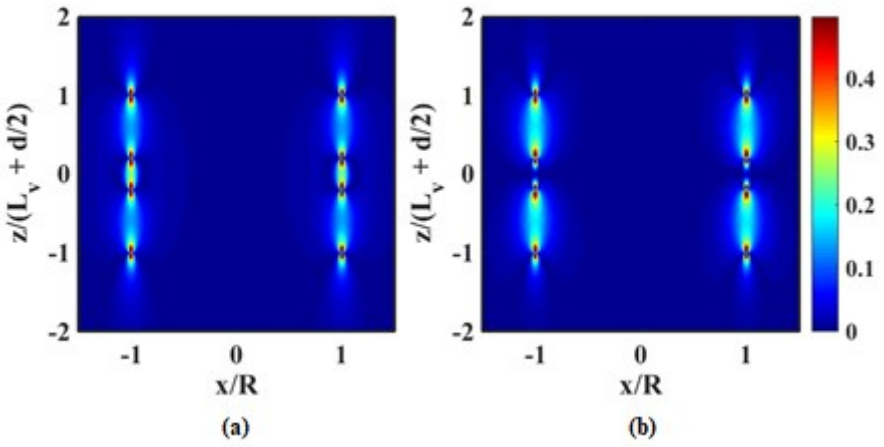

Figure 5.22 Coronal variation of sensitivity for coupled MI ring device (a) symmetric and (b) anti-symmetric mode

To confirm these observations, we plot the variation in sensitivity through the left or right wires. For example, **Figure 5.23** (a) and (b) shows S plotted along the line x = -R for the symmetric and anti-symmetric modes respectively. Clearly, there are maxima at the wires, with a decrease in sensitivity away from these points. Importantly, there is a zero in sensitivity at z = 0 for the anti-symmetric mode. Note that these results hold for either a single tap or a quadrature tap connected, since we are dealing with the elements' relative current magnitude and direction only.

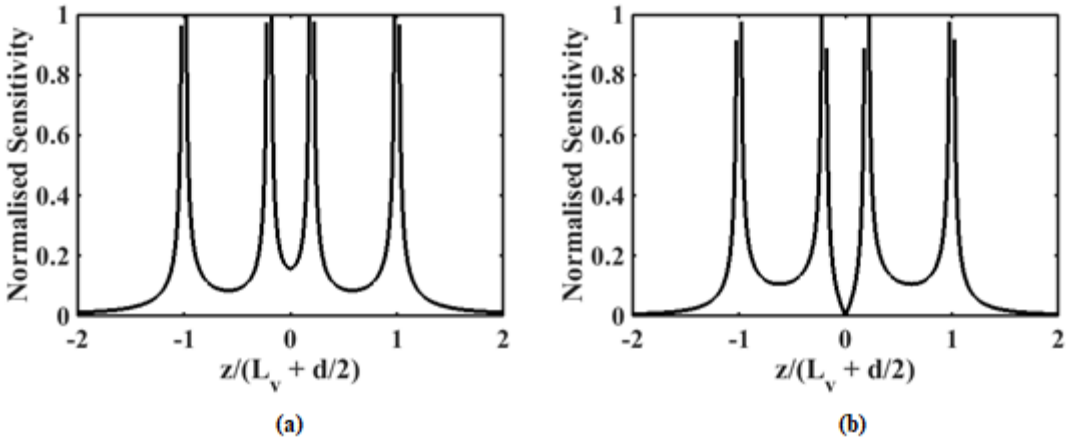

Figure 5.23 Spatial variation of sensitivity through x = -R: (a) symmetric and, (b) anti-symmetric mode

5.4 Conclusions

The general expression for the spatial variation in sensitivity, S, for an internal MRI detection coil has been derived as $\sqrt{(H_{x,re} - H_{y,im})^2 + (H_{x,im} + H_{y,re})^2}$. A number of different configurations have been considered for an internal ring resonator, and modelled in 2D. The simple (a ring operating with a travelling wave current distribution) has shown a sensitivity pattern with 8-fold symmetry in the ring plane, highest at the device radius and falling away as $1/r^2$. However, a uniform external read coil cannot be magnetically coupled to a coupled ring resonator system operating on the anti-symmetric spatial mode needed for effective decoupling. As a solution, we have proposed the less satisfactory solution of wired connection. Using a single tap, which results in a cosinusoidal current wave pattern, the sensitivity pattern is degraded to one with 6-fold symmetry. To restore symmetry, we suggest the use of quadrature taps connected to two elements at right angles. This resulted in an ideal sensitivity pattern, strongest near the anastomosis wound and falling off as $1/r^2$. However, calculation of the coronal variation in sensitivity has shown that sensitivity will be lost at the device centre.

In the next Chapter, we evaluate the experimental performance of a coupled MI ring system with a single tap in an MRI scanner, using a gel phantom. With the device aligned to the magnet bore, we would expect signal intensity variations similar to that of Figure 5.18 in axial slices. Similarly, we expect variations similar to that of Figure 5.22 (b) in coronal slices.

6 Magnetic Resonance Imaging

In Chapter 4 we considered how the resonance spectrum of a coupled MI ring resonator could be manipulated to offer an optimum mode separation, and developed a viable design for an internal sensor based on intra-ring element overlap. We then demonstrated prototype devices using flexible laminate mounted on an annular scaffold. This work yielded two devices: a first device dimensionally matched to the BAR and a second larger device with potentially improved performance. In Chapter 5 we calculated the spatial variation in sensitivity. In this Chapter, we use in vitro magnetic resonance imaging of phantoms to confirm that the device does indeed offer an SNR improvement over external coils such as the body coil and an abdominal coil array. We first describe the mounting and tuning process used to prepare the device for MRI , and then the imaging experiments and their results.

We start by considering a mutually coupled system [207], [208], using an external read coil to couple to the internal sensor. However, as discussed in Chapter 5, coupling of any symmetric reading system to the primary anti-symmetric mode of the internal device will be very low or non-existent. We therefore use these results to investigate the effectiveness or otherwise of our passive decoupling system. We then develop a directly coupled system, where the device is directly connected to the MRI scanner's auxiliary input (such as in [143], [199]) using a single tap. A significant difference in the images obtained is immediately noticed and used to quantify the local imaging advantage of the coupled MI ring resonator device.

6.1 Gel Phantom for In Vitro Evaluation

To evaluate imaging performance of the coupled MI ring device, it must be embedded in an environment that simulates both the conductive loading and the MR response of the human body. Suitable phantoms are constructed from doped Agar gel, which may conveniently be melted for casting in a suitable mould and then re-solidified at room temperature. The mould itself should provide a signal volume that matches the expected field-of-view of the device. Additional signal and loading to match a torso cross section may then be provided by standard cuboid phantoms. Figure 6.1 (a) shows a side-view of the mould used, with Figure 6.1 (b) showing a cross-section through it. From Figure 6.1 (a) we see that the mould is made up of fifteen stacked NC-machined Perspex slices, with the top and bottom slices being complete sheets to close the container. The bottom slice holds a pillar support that mounts the device at the centre of the signal-generating volume.

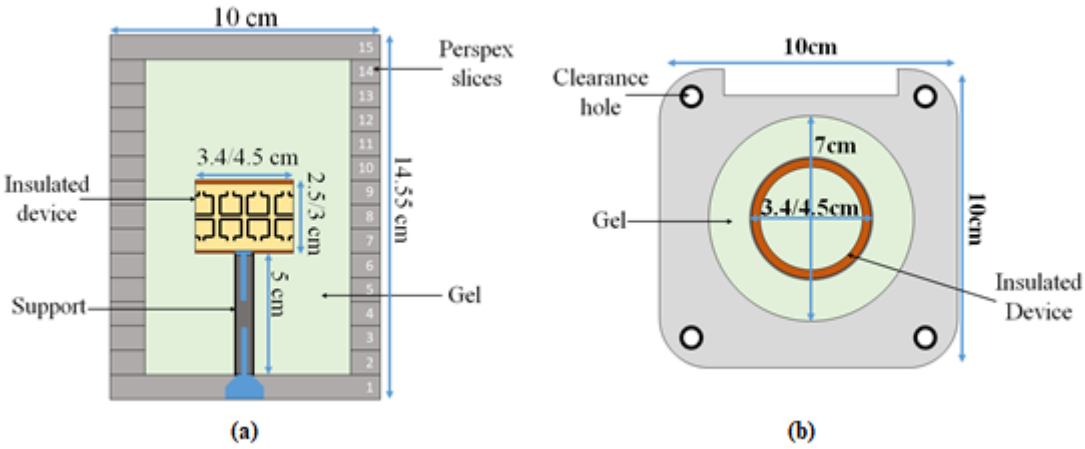

Figure 6.1 Diagram of gel phantom: (a) side-view, (b) plan view.

From Figure 6.1 (b) we see that each slice is square with dimensions 10 × 10 cm. The middle thirteen slices all have a hollow circular section, 7 cm in diameter, in which both the small and large devices fit comfortably, allowing the gel to form a cylindrical signal-generating volume round the device. Each slice also has four clearance holes at its corners to allow for plastic studding to hold the slices together, creating a gel-tight container.

Figure 6.2 (a) shows a photograph of the assembled mould and device, before gel casting. Here we see that the base of the plastic ring, on which the coupled MI ring resonator is mounted, has circular holes to allow passage of the gel. Figure 6.2 (b) shows a side view of the container being assembled.

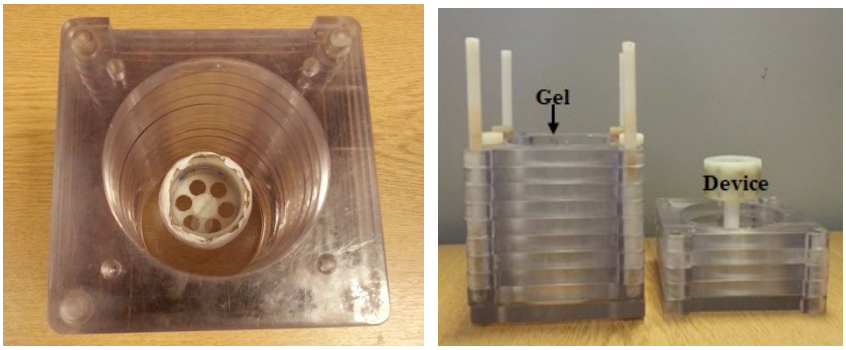

Figure 6.2 Photographs showing the gel container, (a) plan view, (b) side-view.

6.1.1 Phantom Gel

The phantom is constructed from Agar gel made from water doped with 3.37g/L $NiCl_2.6H_2O$ and 2.4g/L NaCL. Nickel chloride is used to give a relaxation time constant T2 matching that of the human body (50-60 ms), while sodium chloride is used to match the body conductivity. To make the gel, additional ingredients are needed, listed in Table 6.1. Here a glycerol concentration of 43% is used to give a relaxation time constant T1 of 300 ms, the propanol is used to keep bacteria from developing in the phantom and the agar is used to turn the phantom into a gel [209].

Table 6.1 Ingredients for agar phantom gel.

Solution	Amount
Doped Water	432ml
Glycerol	210ml
1-propanol	58ml
Agar	31.5g

Figure 6.3 shows the arrangement for making the phantom gel. Here the hot plate with an electronic stirrer is first used to mix the doped water with the glycerol and 1-propanol. Then the mixture is heated to 85°C, and the agar powder is added little by little, keeping the stirrer moving all the while. When all the agar has been added, the mixture is kept at 85° C for a further 5-10 mins. It is then poured into the mould, taking care to avoid formation of air bubbles, and allowed to cool and solidify.

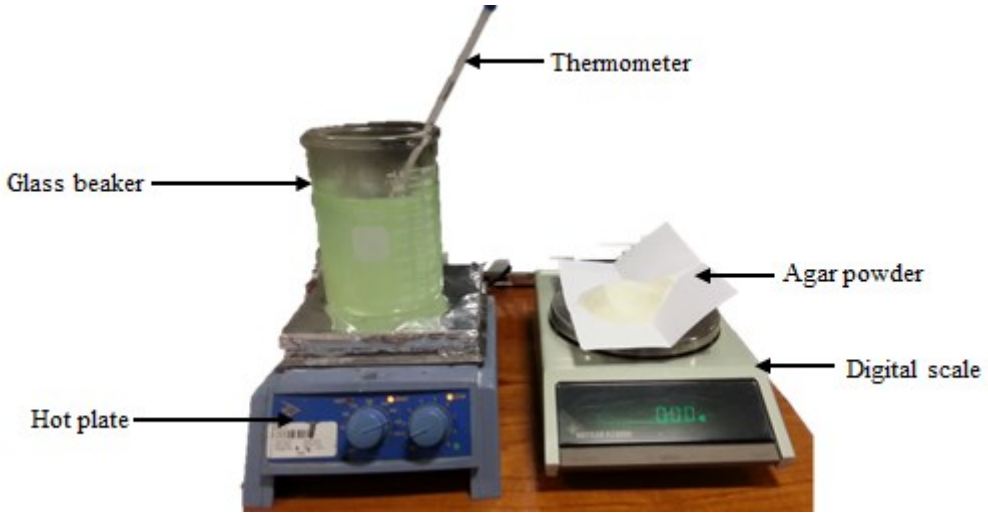

Figure 6.3 Arrangement for making agar phantom gel.

6.1.2 Gel Loading

The human body – and the phantom gel – is an electrically conductive environment, and therefore, it is necessary to insulate the device before use, either with nail varnish or with Araldite epoxy [210]. The former can easily be removed with acetone and thus allows for adjustments to be made to the device whenever necessary. The latter is permanent, but is a stronger material that will not melt when exposed to the high temperature of the liquid gel. We have used both, applying several layers of nail varnish for experimental measurements and then permanently insulating with the epoxy once the results are satisfactory.

To test the effect that the phantom gel will have on device tuning, we measure resonance spectra after immersion in the gel phantom, using a pair of inductive probes connected to the network analyser. Ideally, the probes should be positioned outside the phantom to allow several measurements to be

taken of the device in gel. However, using this configuration, we find that the distance between the probes and the device is too great and insufficient signal is received. It is, therefore, necessary to place the transducers inside the phantom itself. The disadvantage of this arrangement is that the gel must be removed and re-cast every time a new measurement is taken. However, this appears unavoidable.

Figure 6.4 shows a photograph of the transducers and the device inside the phantom, before gel casting. Here the device has been insulated with green nail varnish. The transducers are also insulated with rubber and an elastic band is used to fix them in the correct position either side of the coupled MI ring device. The resonance spectrum is then measured 'in air', then the gel is poured into the container, left to set and a second measurement 'in gel' is recorded.

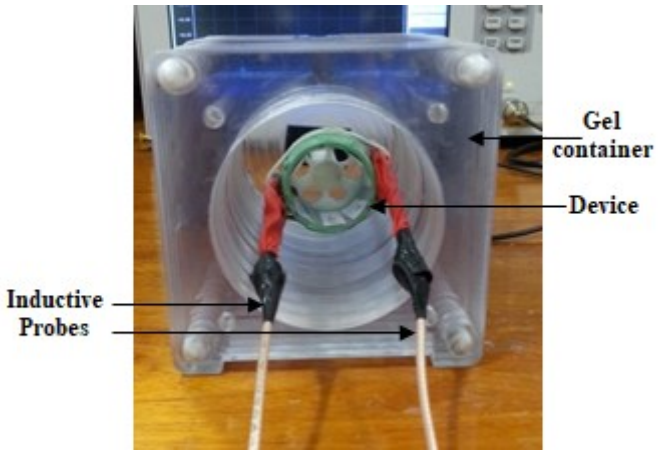

Figure 6.4 Insulated coupled MI ring device and ENA probes inside the gel container.

It is expected that the Q-factor of the resonances will decrease due to the extra loading of the gel on the device. It is also expected that there will be a downward shift in frequency due to the increased electrical conductivity of the salty gel. Figure 6.5 shows the mode spectra of the coupled MI ring resonator, i) with gel and ii) without gel. Here we see that there is a downward shift in frequency after immersion, and a reduction in the Q-factor of the resonances. The former effect may easily be compensated, by retuning to a slightly higher frequency before the insulating layer is applied. There is little that may be done to mitigate the latter, but fortunately the Q-factor is still useful despite the simulated 'body loading' effect.

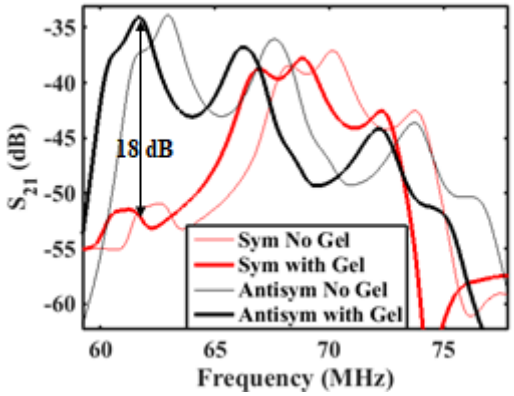

Figure 6.5 Mode spectra of the coupled MI ring resonator device with diameter = 34 mm, measured in gel and in air.

Table 6.2 summarises the changes occurring in the first anti-symmetric mode with the addition of the phantom gel. Here we see that there has been a 1.3 MHz downward shift in frequency, the Q-factor has decreased by approximately 11% and the rejection has remained approximately the same.

Table 6.2 Quantitative changes to the first anti-symmetric mode with addition of gel.

	In Air	**In Gel**
$\mathbf{f_{\mu=1anti}}$	62.97 MHz	61.67 MHz
Q-factor	43.73	39.03
Rejection	17.87 dB	17.76 dB

It is interesting to determine whether internal or external body loading most affects the results. To investigate this, an experiment is conducted where moulded gel discs are inserted into the internal volume of the sensor alone and the resonance spectrum is recorded to measure the changes, if any. Figure 6.6 shows the set-up for the experiment. Here the coupled MI ring device is seen with the insulated transducers attached. Loading is provided by four gel discs, and one is already inserted in the device. Additional discs are added one by one, until the internal volume is fully loaded.

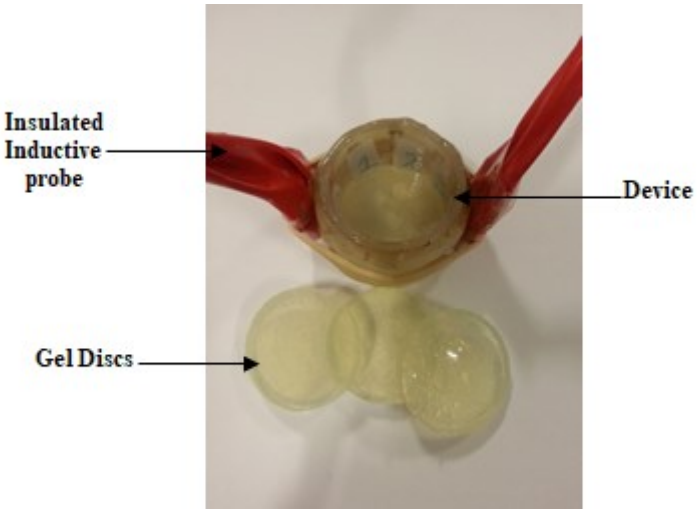

Figure 6.6 Loading the coupled MI ring device with gel discs.

Figure 6.7 shows resonance spectra obtained with gradually increasing loading of the device from the inside alone. Interestingly, the effect of loading is virtually non-existent. All resonances remain at the same frequency, with the same Q-factor, implying that external loading is primarily responsible for the observed effect. Using a multiphysics simulation package such as COMSOL, it would be simple to model the effect of external loading, and optimise the thickness of insulation used.

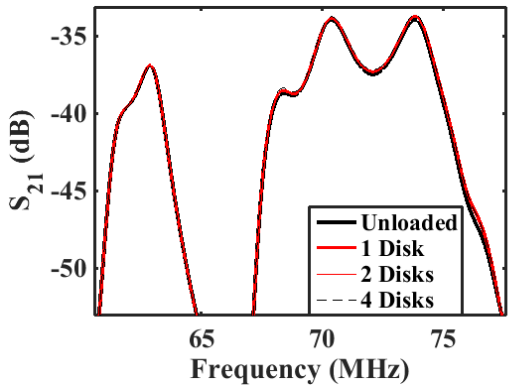

Figure 6.7 Resonance spectra of coupled MI ring device loaded with different numbers of gel discs.

Translating this result to the human body, the bowel wall and tissue outside the body will affect the resonance, but material inside the bowel – largely, faeces - will not cause any change to performance. The first anti-symmetric mode will simply have to be pre-tuned to a frequency 1.3 MHz higher than the Larmor frequency, and will automatically adjust to the correct frequency after surgical insertion.

6.2 Tuning

The instrument used for imaging experiments is a ^{1}H 3.0 T clinical scanner with a Larmor frequency of 127.74 MHz. Accounting for the frequency downshift described above, the first anti-symmetric mode must be pre-tuned to 129.04 MHz using discrete surface mount capacitors. Most capacitors are

slightly magnetic, due to the widespread use of a nickel diffusion barrier at the contacts. To avoid magnetic artefacts, non-magnetic capacitors must be used. Unfortunately, such capacitors are uncommon, and only available in certain values as shown in Table 6.3.The capacitors are labelled ASL, BSL and JSL, with the latter two types having an associated error margin of ±0.1 pF and ±5 % respectively [211].

Table 6.3 Available values of non-magnetic capacitors.

ASL (pF)	BSL (pF)	JSL (pF)
0.1	1.0	10
0.2	1.2	12
0.3	1.5	15
0.4	2.0	22
0.6	2.2	27
0.8	3.3	33
	4.7	39
	6.8	47
	36.9	68

To calculate the capacitor value required for tuning, we first require the value of $\omega_0 = 2\pi f_0$, where f_0 is the resonance of a single element of the ring. We know that the first anti-symmetric mode $f_{\mu=1anti}$ of the coupled MI ring resonator system must equal the Larmor frequency f_L. From the dispersion relationship, we can therefore find the value of $\omega_{\mu=1anti}/\omega_0$ which in turn yields ω_0. Finally, the relationship $C = 1/\omega_0^2 L$ gives the capacitor value. For the small device, at 3.0 T the required value is 35.8 pF and for the large ring it is 19.2 pF. Given the limited available capacitor values, several parallel-connected components are needed to obtain a suitable overall value.

For the small device first, the following options are possible, with the maximum and minimum value capacitance that each combination could make due to the associated error shown in brackets:

i. 33 + 2.2 = 35.2 pF (max = 36.95, min = 33.45)
ii. 33 + 2.2 + 0.6 = 35.8 pF (max = 37.55, min = 34.05)
iii. 27 + 6.8 + 2 = 35.8 pF (max = 37.35, min = 34.25)

The first option only requires two components, but does not give a close enough overall capacitance. Additionally, the first and second options both use the capacitors 33 pF and 2.2 pF. Therefore, these two capacitors are first soldered in place, and the resonance spectrum is measured. At this stage, with only two capacitors, it was found that the first anti-symmetric mode falls at 130 MHz, which is too high and suggests that a slightly larger capacitor value is needed. Thus the 0.6 pF capacitor is added and the measurement is repeated. This time, the first anti-symmetric mode fell at 129 MHz. Figure 6.8 shows the resonance spectrum of the tuned coupled MI ring device with diameter 34 mm, recorded i) without and ii) with gel. Here we see that immersion in gel downshifts the first anti-symmetric mode

to 127.8 MHz. In practise, the Larmor frequency (127.74 MHz) must fall within the 3 dB bandwidth of the resonance. Here, the 3 dB bandwidth of the first anti-symmetric mode in gel is 2.13 MHz, with a Q-factor of 60, implying that tuning is satisfactory.

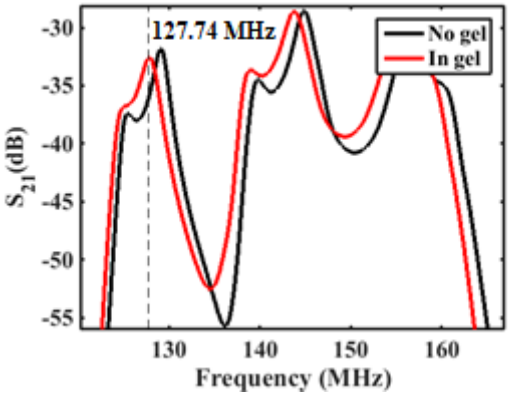

Figure 6.8 Resonance spectrum for small coupled MI ring device (i) in air and (ii) in gel.

This same procedure is repeated for the larger coupled MI ring device. This time the total capacitor value used is 18.3 pF, which makes the first anti-symmetric mode fall at 128.9 MHz without gel and downshift to 127.6 MHz in gel. With a Q-factor of 87, the 3 dB bandwidth is -1.46 MHz, implying that the Larmor frequency is within the 3 dB bandwidth of the first anti-symmetric mode.

6.3 MRI Testing

The aim of the MRI experiments is to prove that the introduction of the coupled MI ring device offers an advantage to image quality. The advantage can be verified by first observing the images obtained, and checking for decoupling artefacts. Then the local signal-to-noise ratio can be compared with results obtained using an external coil, and the SNR improvement offered by the device quantified.

An important point to consider here is the device's orientation. The best performance will be obtained with the device oriented to detect the transverse magnetization M_{xy} as dipoles precess around the z-axis, the orientation of the static magnetic field B_0. Figure 6.9 shows a diagram of a patient inside an MR scanner, with three device orientations shown. For maximum excitation, the device should be aligned with the magnet bore as seen in position A. However, if the device is in orientation B or C, excitation will be very different, since the device will couple only to M_x or M_y [199]. Therefore, throughout the following experiments, the device is oriented parallel to the z-axis, and the effect of the other orientations is briefly discussed later.

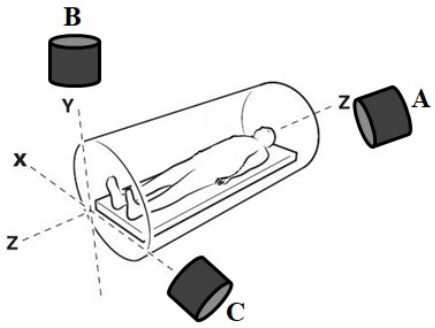

Figure 6.9 Device orientation with respect to MRI magnet bore.

To analyse the sensitivity of the device, parallel and perpendicular to its axes, axial and sagittal (or coronal) slices are taken. Axial slices produce images perpendicular to the z-axis of the scanner, in the x-y plane, while coronal and sagittal slices produce images in the x-z and y-z planes respectively. By symmetry, the last two should be the same for our device.

6.4 Mutually-Coupled System

The first experimental set-up considered has the coupled MI ring device mutually coupled to an external reading coil, either the system body coil or a surface array coil. Figure 6.10 shows the arrangement. The gel phantom is positioned between two cuboid phantoms to increase the overall loading to correspond to an entire human torso. The combination is then wrapped with the abdominal array coil, typically used for imaging the abdomen, including the bowels. Everything is placed on the patient bed, with the device parallel to the magnet bore, and loaded to the magnet isocentre.

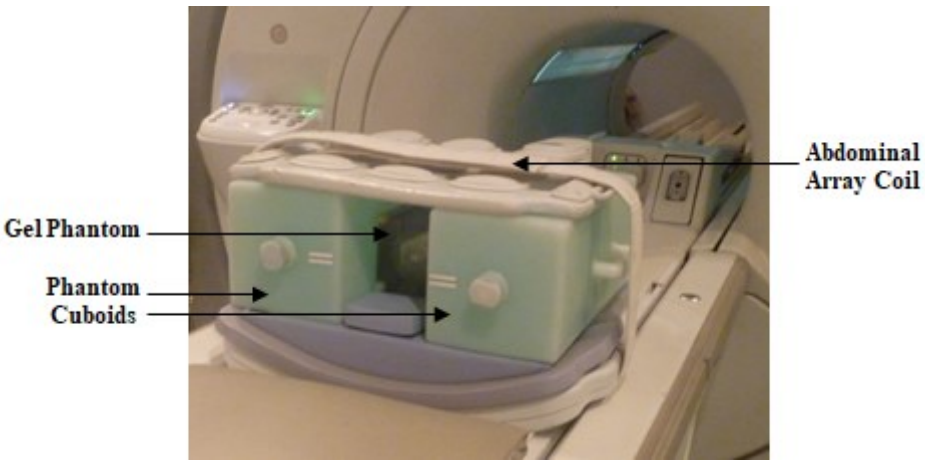

Figure 6.10 Arrangement for MRI scanning of mutually-coupled system.

The original expectation was that the device would couple to the abdominal array coil. However, it is quickly realised that if the coupled MI ring device is tuned to its first anti-symmetric mode for B_1 field decoupling, it cannot couple to the abdominal array coil. A tap was therefore added to avoid the

problem. Unfortunately, this understanding was only obtained after submission of a conference paper [212], although the presentation itself was corrected, as was a subsequent journal publication [213]. In the section below, we describe the images obtained using the mutually coupled system, which therefore mainly show decoupling artefacts. In the following section we then describe a directly-coupled system, which confirms the local SNR gain expected.

6.4.1 Experiment 1: 3.0 T MRI Scanner

^{1}H imaging was carried out at St. Mary's Hospital, Paddington, London, using a GE Discovery MR 750 working at 3.0 T. Imaging was conducted by Dr Marc Rea, a research radiologist from the Imaging Sciences Centre of the Imperial NHS Trust, who has conducted many similar experiments.

Imaging was carried out with standard spin echo (SE) sequences, which have a flip angle of 90°. The scan parameters are shown in Table 1. In designing any MRI experiment, it is crucial to choose suitable parameters, the most important of which at this stage are the slice thickness and the slice separation. The larger these parameters are the shorter the scan time, but this may not allow us to map the acquired images to the device geometry. Conversely, the thinner the slice thickness, the lower the SNR of the image, and this makes the image quality worse. The SNR can be improved by decreasing the matrix size, but this reduces image resolution. If the slice separation is made too thin, then aliasing effects can arise where a part of one slice manifests in an adjacent slice [214]. Here the slice thickness and separation are both set to 2 mm to give at least four slices through each of the devices to be tested. The default matrix size is 256 × 256; however, we decrease it to 128 × 128 to compensate for the decrease in SNR due to the thin slices. The Display FOV (DFOV) is set to 100 × 100 mm^2, the cross-section of the gel container. The pixel bandwidth has also been increased to 651 Hz, rather than the default of 130 Hz, since this eliminates chemical shift artefacts. Finally, the number of excitations (NEX) is also increased to 2 to improve the overall SNR of the images.

Table 6.4 Scanning parameters for MRI experiment 1.

Parameter	Value
Scanning Sequence	Spin Echo
MR acquisition type	2D
Repetition Time (TR)	700 ms
Echo Time (TE)	15 ms
Number of Excitations (NEX)	2
Slice Thickness	2 mm
Slice Separation	2 mm
Flip Angle	90°
Acquisition Matrix	128 × 128
Pixel Bandwidth	651.016 Hz
DFOV	100 × 100mm^2
Receiving Coil	Abdominal Array coil

At the beginning of any scanning session, a localiser scan is made in three perpendicular planes using the system body coil. This relatively crude scan helps identify the position of the subject and the optimum excitation frequency. We make use of this localiser scan to set the slice positions, thus allowing for the symmetric mapping of the device to the images obtained. Concentrating on the axial slices, Figure 6.11 (a) shows the position of the key slices required along the device. Here the shaded green represents the slice thickness, the white in between represents the slice separation and the dark green horizontal lines represent the middle of the slices. There are three highlighted slices: these are slices 10, 12 and 14, respectively along the bottom, middle and top of the device. Figure 6.11 (b) shows the position of these three slices along the coronal localiser scan. We expect to see signal enhancement in images 10 and 14, and no effect from the device in image 12. Images 11 and 13 should show decreased signal enhancement.

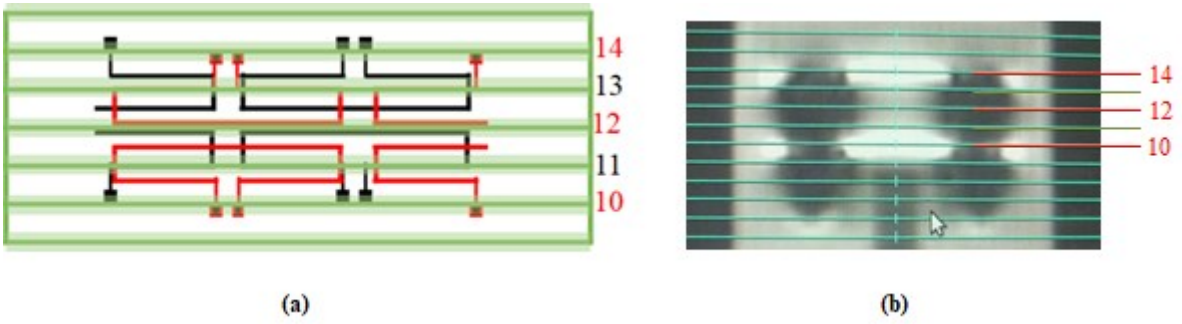

Figure 6.11 (a) Required axial slice positions, (b) slice positions on coronal localiser.

Further imaging was carried out using the array coil. Figure 6.12 shows the important axial images thus obtained. Here image 8 is some way from the device; the grey circular region therefore defines the gel signal source, while the dark regions beyond represent the Perspex mould. The small black disc is the support on which the device is held. Images before 8 and after 17 are free of any effect from the device and have been omitted.

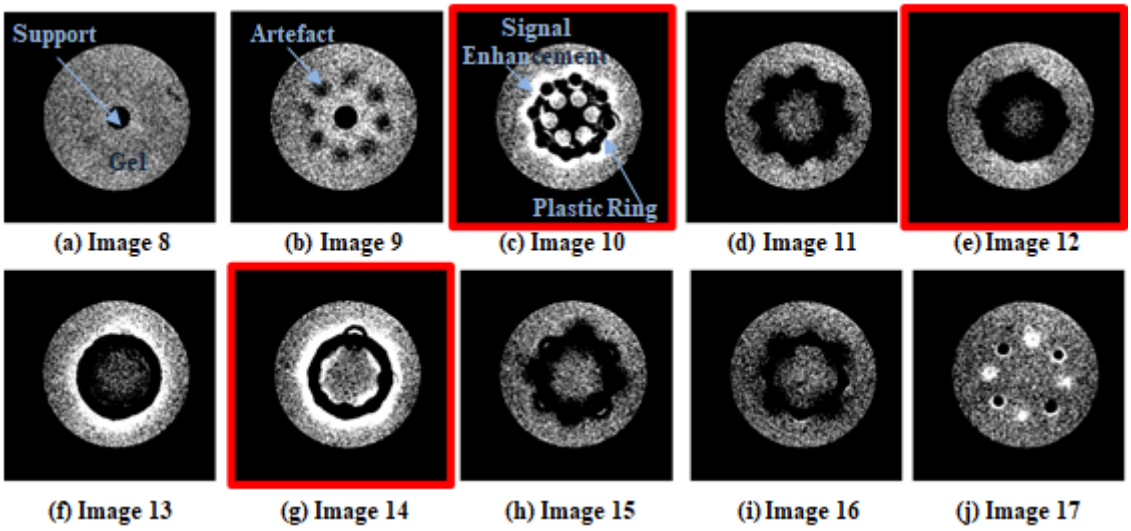

Figure 6.12 3.0 T axial images of the mutually-coupled system with the small coupled MI ring device. (a) Gel mould and plastic support, (b) dark disc artefacts, (c) dark circle and base with holes representing bottom of plastic ring, annular signal enhancement round the device, dark disc artefacts (d) no signal enhancement, dark circle representing plastic ring, dark artefacts, (e) no signal enhancement, dark circle representing plastic ring, dark artefacts, (f) dark circle representing plastic ring, annular signal enhancement round the device, dark artefacts, (g) dark circle representing plastic ring, annular signal enhancement round the device, dark artefacts, (h) dark circle representing plastic ring, dark disc artefacts, (i)) dark circle representing tip of plastic ring, dark disc artefacts, (j) light and dark disc artefacts

In image 9, we again see the small black central disc, but now there are eight more dark discs forming a ring round it. The diameter of this ring matches the device diameter, and the position of the circles corresponds to pairs of closely spaced wires from the device's second-neighbouring elements. Therefore, the dark circles are almost certainly artefacts arising from insufficient rejection of B_1 fields. Note, however, that this slice does not pass through the device itself, as confirmed by the lack of a continuous black ring representing the plastic cylindrical scaffold. By contrast, in image 10, we see this black ring, and the base of the scaffold, characterised by the holes that allow for gel filling, seen here in grey. We also see the dark artefacts again, spaced round the black ring, but now there is also a region of higher signal intensity, seen in white. This is the anticipated local signal enhancement offered by the device. Image 11 appears dark again, with only artefacts present. Image 12 contains almost no effect from the device, as expected from the localiser scan. In image 13, we see some signal enhancement again, which increases in image 14. Finally, images 15 and 16 do not pass through the coupled MI ring resonator system and show only artefacts. Image 17 lies beyond the plastic scaffold, but still has some over-excitation artefacts.

These images confirm the expected signal enhancement at the edge of each MI ring resonator, and the expected zero sensitivity where the coupled rings meet. However, knowing that there is no coupling between the anti-symmetric mode and the reading coil, we can suggest that it is the zeroth symmetric mode that has coupled to both the $\mathbf{B_1}$ field and the abdominal array coil. This is because the first anti-symmetric mode is only 5 MHz away in frequency from the zeroth symmetric mode – as seen in Figure 6.5 – and the rejection of uniform modes is only 17 dB. The coupling to the $\mathbf{B_1}$ field has of

course introduced the artefacts due to local over-excitation. However, the mutual coupling to the reading coil during the detection phase allows us to obtain the signal enhancement in images 10 and 14. Imperfections in the periodic structure of the coil will tend to confuse these two effects even further.

In Figure 6.13, which shows an axial image through one of the rings of the larger coupled MI ring device (with D = 45 mm), we see that the effect from both the $\mathbf{B_1}$ coupling and the mutual coupling to the reading coil is reduced, as seen by the decreased black artefacts and the decreased signal enhancement the device's coils. This is because the frequency separation between the first anti-symmetric and zeroth symmetric mode and the rejection of the latter are both larger for this device.

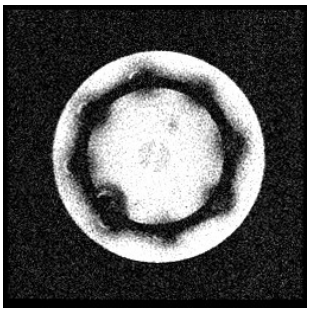

Figure 6.13 3.0 T axial image through lower ring of large coupled MI ring device using a mutually-coupled system.

6.4.2 Experiment 2: 1.5 T MRI Scanner

A second small device, tuned to 63.85 MHz, was tested in a 1.5 T scanner. The experiment was conducted in Newham University Hospital, London, using a Siemens Magnetom Symphony Syngo clinical scanner. Imaging was conducted by Tabassum Zabwala, superintendent radiographer and chief MR operator at Bart's Health NHS Trust. With this scanner, different scanning parameters were used, listed in Table 6.5. Here the pixel bandwidth is the maximum allowed in the scanner and is chosen to minimise chemical shift artefacts. Additionally, it was possible to reduce the slice separation to 0.4 mm without observing any aliasing artefacts.

Table 6.5 Scanning parameters for experiment 2.

Parameter	Value
Scanning Sequence	Spin Echo
MR acquisition type	2D
Repetition Time (TR)	700 ms
Echo Time (TE)	22 ms
Number of Excitations (NEX)	2
Slice Thickness	2 mm
Slice Separation	0.4 mm
Flip Angle	90^{o}
Acquisition Matrix	256 × 256
Pixel Bandwidth	265 Hz

DFOV	$100 \times 100 mm^2$
Receiving Coil	Abdominal Array

Figure 6.14 (a), (b) and (c) shows the three key axial images in the same positions as images 10, 12 and 14 of the previous experiment. Here there are similar black artefacts at the device conductors, with the additional signal enhancement in images (a) and (c). We thus confirm that even in the lower magnetic field strength of 1.5 T, the device still couples to both the B_1 field and the external reading coil.

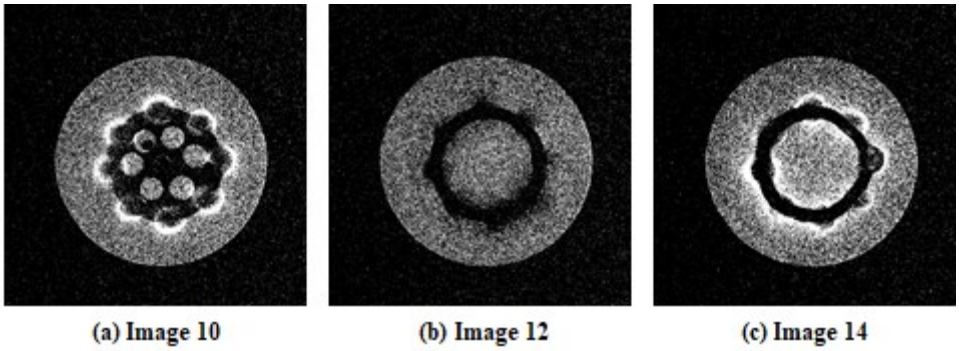

Figure 6.14 1.5 T axial images of the mutually coupled system with the small coupled MI ring device. (a) Annular signal enhancement round the device, dark circle and base with holes representing plastic ring, dark disc artefacts (b) no signal enhancement, dark circle representing plastic ring, small dark disc artefacts, (c) annular signal enhancement round the device, dark circle representing plastic ring, small dark disc artefacts.

Figure 15 shows a coronal image through the middle of the device. Here, the plastic support and screw can be seen, as well as the cylindrical scaffold. We also see the increase in SNR at the top and bottom of the device; and some artefacts manifesting as black circles just above each signal enhancement. It is interesting to note that the sensitivity pattern shown here does not resemble that calculated in Chapter 5. This further supports the unsuitability of the mutually coupled system.

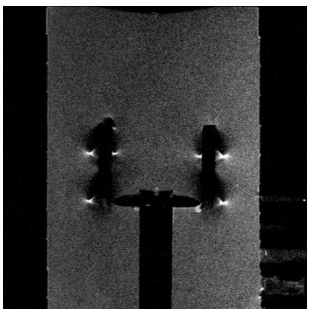

Figure 6.15 1.5T coronal image through the device centre.

6.5 Directly-Coupled System

To avoid the problems associated with mutual coupling, we now couple the device directly to the scanner using a single tap from one of the ring elements. Of course it is not ideal to have a wired

connection running through the patient; but there is a natural lumen through which the wire may be passed, and protective insulation may be provided by use of a catheter [204]. Connecting a cable to the device requires the matching of its input impedance to the self-resistance of the coil to ensure maximum power transfer. Two methods of matching are described below. The MRI experiments with the directly coupled system are then presented and a comparison is made between signal reception with this system and with the mutually coupled system.

6.5.1 Matching and Tuning: Capacitive Voltage Divider

Several matching circuits are available [134] and the exact choice normally depends on the coil impedance. We first try the most commonly used capacitive matching circuit shown in Figure 6.16 (a). Here C_T is the tuning capacitor, C_M is the matching capacitor, R is the self-resistance of the coil and L is its self-inductance. Z_0 is the system impedance, equal to 50 Ω.

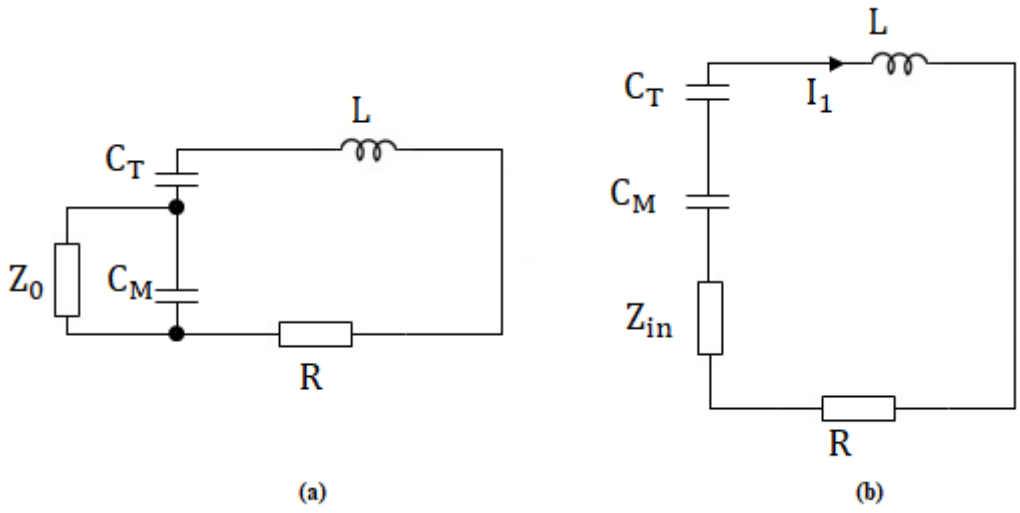

Figure 6.16 (a) Capacitive voltage divider matching circuit (b) approximation using binomial expansion.

To maximise SNR, the input impedance of the matching circuit must be matched to the output resistance of the receiving coil. To identify suitable parameters, we first transform this circuit to a simpler approximation as follows. The admittance measured between the two dots is:

$$Y_M = j\omega C_M + \frac{1}{Z_0} = j\omega C_M \left(1 + \frac{1}{j\omega C_M Z_0}\right)$$

Equ 6.1

And the matching circuit impedance, Z_M, is:

$$Z_M = \frac{1}{Y} = \frac{1}{j\omega C_M \left(1 + \frac{1}{j\omega C_M Z_0}\right)}$$

Using binomial expansion and assuming $\omega C_M Z_0 << 1$, we obtain Z_M, as:

$$Z_M = \frac{1}{j\omega C_M}\left(1 - \frac{1}{j\omega C_M Z_0}\right) = \frac{1}{j\omega C_M} + \frac{1}{\omega^2 {C_M}^2 Z_0}$$

Equ 6.2

And so the effective input 'resistance' of the matching circuit is:

$$Z_{in} = \frac{1}{\omega^2 {C_M}^2 Z_0}$$

Equ 6.3

Figure 6.16 (b) shows the equivalent circuit approximation obtained using this binomial expansion. Here we see that C_T, C_M and Z_{in} are all in series. Z_{in} should therefore equal R, for perfect matching. A suitable value can easily be achieved by adjusting the matching capacitor, C_M, and the tuning capacitor C_T can then be set to achieve resonance at the correct frequency. Generally these two components are adjusted by iteration.

We now apply this matching circuit to the coupled ring sensor. Figure 6.17 shows the ring with D = 45 mm. Here we see that an extra capacitor, C_M has been connected across one of its coils, along with the tuning capacitor, C_T. A coaxial cable output has been connected across C_M.

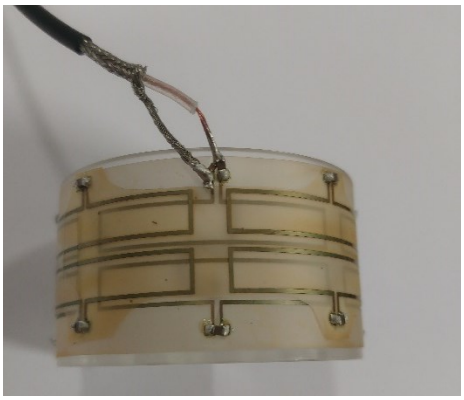

Figure 6.17 Coupled MI ring device with single tap, using capacitive voltage divider matching.

Figure 6.18 shows the tuning process in more detail. Figure 6.18 (a) shows the frequency dependence of the reflection S-parameter S_{11}, while Figure 6.18 (b) shows corresponding results for the transmission parameter S_{21}. Starting with C_T = 68 pF, the first anti-symmetric mode falls at 69.9 MHz. At this stage, we assume this is the required tuning frequency and analyse the effect of matching on the resonance spectrum. Adding $C_M = 10 \times C_T$ = 680 pF, moves $f_{\mu=1anti}$ up to 70.3 MHz. Here, the depth of the notch in S_{11} at resonance is only 1.2 dB indicating that matching has not yet been achieved. We need notch depth > 10 dB to ensure matching. Therefore, we continue the tuning and matching process, by decreasing C_M and observing the effects on the resonance spectrum. The remaining results

in Figure 6.18 (a) show that the notch depth does indeed increase as C_M is decreased. Similarly, the remaining results in Figure 6.18 (b) show that the first anti-symmetric mode is upshifted in frequency as C_M increases since the total capacitance $C_{tot} = 1/\{1/C_T + 1/C_M\}$ decreases.

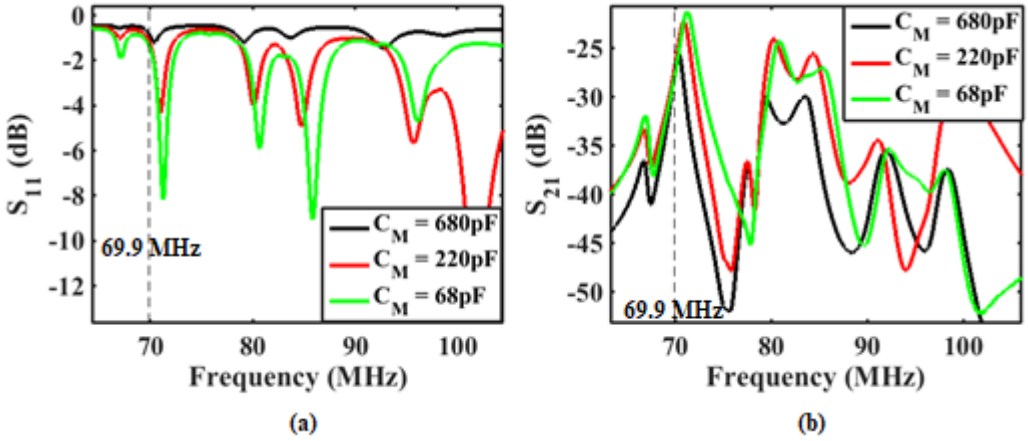

Figure 6.18 Frequency dependence of a) reflection and b) transmission S-parameters for coupled MI ring device during capacitive voltage divider matching.

Table 6.6 summarises the matching and tuning process, recording the first anti-symmetric mode resonance, its Q-factor and S_{11} depth at every capacitance change. Here it is seen that we only reach the threshold of 10 dB notch depth in S_{11} when $C_M < C_T$. However at this point, we are unable to re-tune the ring (by bringing $f_{\mu=1anti}$ back to 69.9 MHz), since C_{tot} will only be as large as the smallest of C_M and C_T. The required tuning frequency now lies outside of the 3 dB bandwidth of the first anti-symmetric mode. We thus conclude that this method of matching is not suitable for the coupled MI ring device and an alternative is needed.

Table 6.6 Tuning and matching process with capacitive voltage divider matching

C_T (pF)	C_M (pF)	C_{tot} (pF)	$f_{\mu=1anti}$ (MHz)	Q	S_{11} Depth (dB)
68	Infinite	68.0	69.9	67.8	0.47
68	680	61.8	70.3	63.2	1.21
68	470	59.4	70.5	62.3	1.89
68	220	51.9	71.0	54.6	5.54
68	150	46.8	71.1	50.7	5.39
68	68	34.0	71.2	50.5	8.17
68	56	30.7	71.3	49.9	8.68
68	47	27.8	71.3	49.3	9.26
68	33	22.2	71.5	47.5	10.12
68	22	16.6	71.6	46.2	11.04
220	22	20.0	71.7	42.2	14.87
390	22	20.8	71.7	41.7	14.29

6.5.2 Matching and Tuning: Capacitive Current Divider

We now investigate an alternative matching circuit based on a parallel rather than a series arrangement of capacitors. Figure 6.19 shows the equivalent circuit diagram, with the usual circuit parameters.

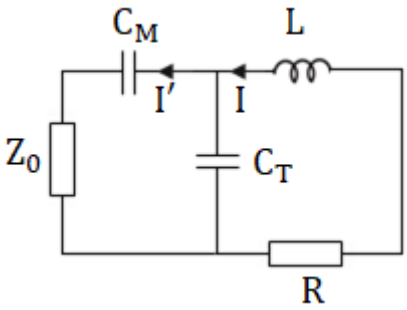

Figure 6.19 Alternative capacitive matching circuit.

This time, C_M and C_T are almost in parallel and therefore:

$$\omega_0 \cong \sqrt{\frac{1}{L(C_T + C_M)}}$$

Equ 6.4

And so we start with $C_M < C_T$ and adjust until matching is achieved. Figure 6.20 shows the same device as before, with the alternative matching applied to one of its elements. Here the tuning capacitor is attached across one of the coils and only one side of the matching capacitor is connected to it. The coaxial cable – which will connect to the scanner's auxiliary input – is then connected across both capacitors.

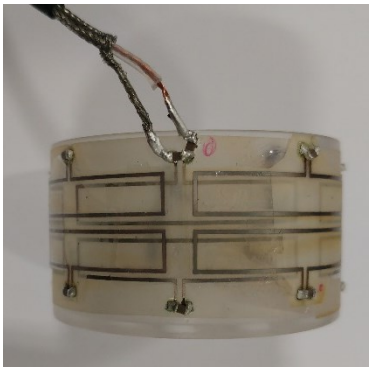

Figure 6.20 Coupled MI ring device with capacitive current divider matching circuit.

We start with C_T = 77 pF, and obtain a first anti-symmetric mode resonance at 65.25 MHz with a Q-factor of 78.5. Here we are tuning for testing at 1.5 T. We now add the matching capacitor and continue the tuning and matching process. Table 6.7 summarises this process. Starting with C_M = 15

pF, we get a notch depth in S_{11} of 17.5 dB and increasing C_M to 22 pF makes this 37.2 dB, meaning we have a very well matched system. However, the first anti-symmetric mode has now downshifted to 64.76 MHz. We, therefore, decrease the tuning capacitor to 56 pF to reduce the total capacitance C and let $f_{\mu=1anti}$ move up again to 65.58 MHz. Continuing in this manner, by adjusting C_T and C_M, we finally achieve a notch depth in S_{11} of 21.5 dB with the first anti-symmetric mode at 65.14 MHz. Thus the final capacitor values are C_T = 68 pF and C_M = 15 pF, offering a well-tuned, well-matched device. Note that the Q-factor at the first anti-symmetric mode has decreased to nearly half its starting value, which implies an almost perfectly matched system. Note also that the remaining coils for the device only have C_T = 77 pF connected.

Table 6.7 Tuning and matching process with capacitive current divider matching

C_T (pF)	C_M (pF)	C (pF)	$f_{\mu=1anti}$ (MHz)	Q factor	S11 depth (dB)
77	15	92	64.80	48.4	17.5
77	22	99	64.76	42.0	37.2
56	22	78	65.58	40.0	18.4
68	22	90	65.01	42.4	13.9
70	22	92	64.90	43.8	14.9
75	22	97	64.72	45.6	21.8
68	15	83	65.14	49.7	21.5

Figure 6.21 shows the mode spectrum for the tuned coupled MI ring device without a tap and the resonance spectrum with a tap. Here we firstly see that a rejection of 30 dB has been achieved. Comparing the response with and without a tap, we see that the spectrum has been altered by the connection of the cable; however, the same number of resonances exists, and the resonant frequencies are largely unaltered.

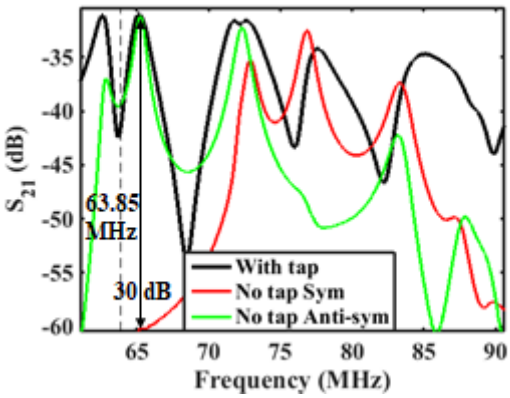

Figure 6.21 Mode spectrum for coupled MI ring device (i) with and (ii) without a tap.

To be sure, we confirm the frequency of the first anti-symmetric mode by driving the connected element with a sinusoidal source and measuring the response at different elements with an inductive probe connected to an oscilloscope, as follows. Firstly, two adjacent elements in each ring are

measured. Here, the response is a sinusoidal signal from each, with a 180° shift confirming the excitation of an anti-symmetric mode. Secondly, two elements at right angles to each other of the same ring are measured. Again, the response is a sinusoidal signal from each, but with a 90° shift, confirming that it is indeed the first mode.

Thus the coupled MI ring device with a single tap is now ready for testing in a 1.5T MR scanner. Figure 6.22 (a) shows the insulated device mounted on the support pillar and Figure 6.22 (b) shows how the Perspex slices of the gel container are utilized to allow the thin cable to pass, but are still sealed well enough to contain the liquid gel.

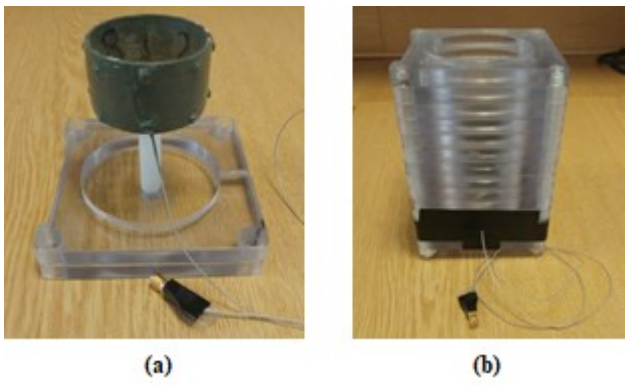

Figure 6.22 Insulated coupled MI ring device with a single tap (a) mounted on support pillar (b) inside the gel container with access to the cable maintained.

The device is tested in gel, and this time we make use of the cable already connected to the device to take the measurements. Figure 6.23 shows the resonance spectrum of the tuned and matched coupled MI ring device in air and in gel. Here we see that there has been a downshift of 1.15 MHz, making the first anti-symmetric mode fall at 64.0 MHz. The 3 dB bandwidth of the first anti-symmetric mode is 1.3 MHz (calculated from the Q-factor shown in Table 6.7); since this bandwidth includes the Larmor frequency of 63.85 MHz, the device is still well tuned.

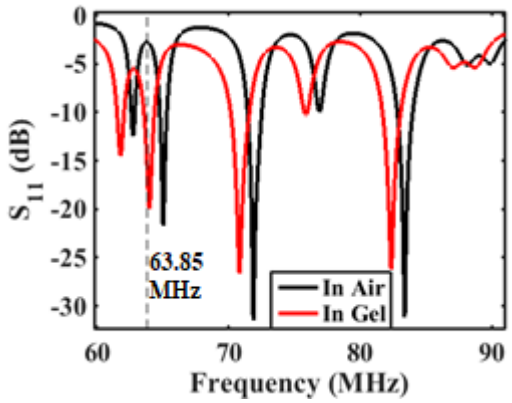

Figure 6.23 Resonance spectrum for tuned coupled MI ring device with single tap measured (i) in air and (ii) in gel.

6.5.3 Experiment 3: 1.5 T MRI Scanner

The imaging performance of the directly-connected sensor was evaluated by Dr Rebecca Quest, Head of MR Physics & MR Safety Expert at St. Mary's Hospital, Paddington, London, using a GE Signa Excite 1.5 T MRI scanner. Figure 6.24 shows the arrangement for the experiment. Here additional cuboid phantoms have again been placed either side of the gel phantom, which has its axis parallel to the scanner's magnet bore. The output from the internal coil was connected to an auxiliary coil input at the head end of the patient bed. To avoid coil clash, SNR comparisons were made with the system body coil rather than an abdominal coil array.

Figure 6.24 Arrangement for MRI scanning of directly-coupled system.

Table 6.8 shows the scan parameters for this experiment. Here it was possible to reduce the slice gap to 0.2 mm and thus obtain more slices through the device. Additionally, the pixel bandwidth is kept at 162.7 Hz to reduce chemical shift artefacts. Finally, we use a DFOV of 200 mm^2 which includes the phantoms either side of the device.

Table 6.8 Scan parameters for MR assessment of directly coupled system.

Parameter	Value
Scanning Sequence	Spin echo
MR acquisition type	2D
Repetition Time (TR)	520 ms
Echo Time (TE)	8.464 ms
Number of Excitations (NEX)	8
Slice Thickness	2 mm
Slice Separation	0.2 mm
Flip Angle	90^o
Acquisition Matrix	192 × 160
Pixel Bandwidth	162.7 Hz
DFOV	200 × 200mm^2
Receiving Coil	Body coil / Coupled MI ring device

In previous experiments, we have made use of a localiser to set the position of slices relative to the device. Here we use the coronal scan to set slice positions for the axial scan. This approach is more accurate, since the coronal scan has the internal device receiving, whereas the localiser is performed with the body coil. Figure 6.25 (a) shows how the slice positions are set on the scanner console display and Figure 6.25 (b) shows the equivalent positions with respect to the ring coils. From Figure 6.25 (a), we see that slices 7,8 and 11, 12 (with the red lines) have been positioned through the regions of signal enhancement; and slices 9, 10 (with the green lines) have been positioned in the central region of zero sensitivity. In Figure 6.25 (b) we see that this corresponds to slices 7 and 12 passing through horizontal wires of the two rings and thus we expect similar images at these positions. We expect a similar result for slices 8 and 11, and 9 and 10, with the latter two producing zero signal enhancement.

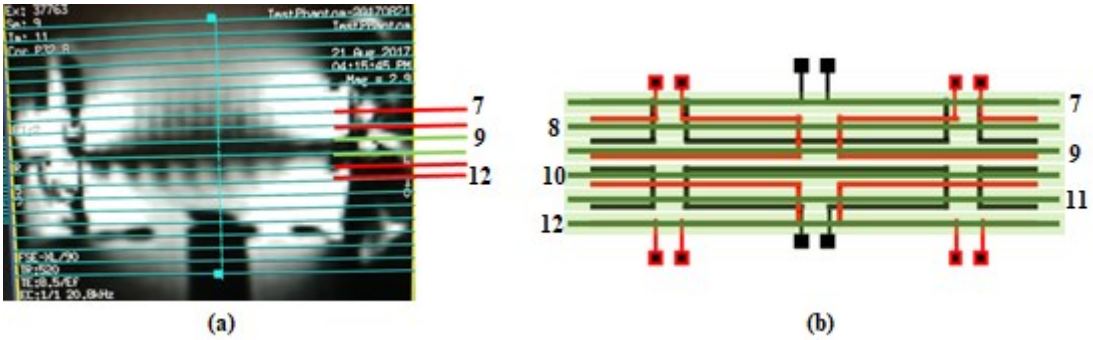

Figure 6.25 Axial slice positions (a) on the scanner console display and (b) with respect to device coils.

Figure 6.26 shows the most important axial images, with the signal received using the coupled MI ring device. Here the images intended to show signal enhancement are highlighted in red and those in a zero sensitivity area in green. Indeed, we see that the red images show increased signal intensity, with the 6-fold symmetry expected from a device with a single tap. The position of element 1 (connected to the tap) is highlighted in image 7 and we see the decreased signal intensity at elements 3 and 7. Even though there is some enhancement in the green images – due to their placement being slightly above and below the zero sensitivity line in Figure 6.25 (a) and (b) – it is clearly much lower here than through the ring coils themselves. The high signal intensity has also caused some clipping artefacts to be seen vertically above and below the phantom gel.

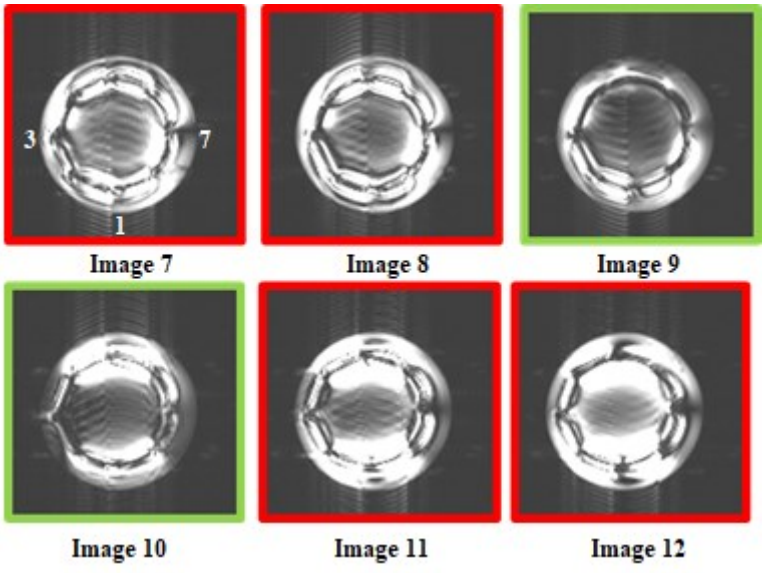

Figure 6.26 1.5 T axial images from directly coupled system, receiving with the large coupled MI ring device

To confirm any advantage of the internal coil, these images must be compared with comparable results obtained using the MRI scanner's body coil. Figure 6.27 (a) shows image 12 of the axial scan received with the body coil. Here the large uniform FOV of the body coil allows the cuboid phantoms to be seen on either side of the device. However, where there is signal present, it is largely of low and uniform intensity. Signal artefacts near the coil conductors indicate that B_1 field decoupling has only been partially achieved. The most likely explanation is the lack of symmetry – due to the offset between the two rings or during mounting of the coupled MI ring resonator system on the plastic cylindrical scaffold – which will tend to mix the symmetric and anti-symmetric modes. Figure 6.27 (b) shows the same image received with the coupled MI ring device. Here the cuboid phantoms cannot be seen, due to the limited radial FOV of the device. However, the signal intensity is locally much higher, but clearly non-uniform.

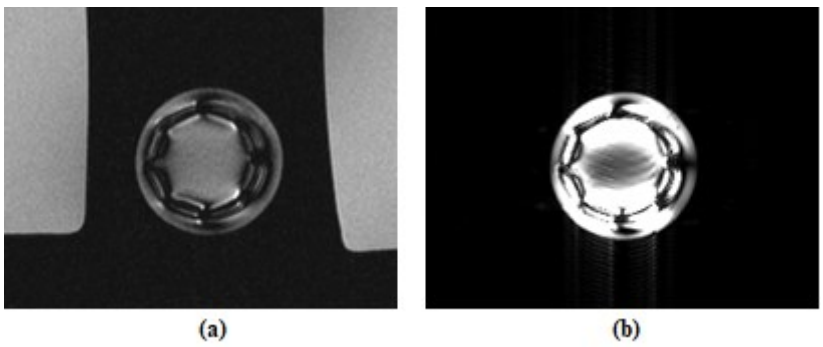

Figure 6.27 Axial image 12 obtained using (a) body coil and (b) internal coupled MI ring device.

We can calculate the SNR by taking the ratio of the signal in a region of interest (ROI) to the noise in a region devoid of signal. The noise is calculated as the standard deviation of a region devoid of signal for each image, as 8.75 and 2.7 for the body coil and the coupled MI ring coil respectively.

Figure 6.28 shows the variation in SNR plotted along a vertical line through the images taken with both coils. In the middle of the device, the SNR is 90 when receiving with the coupled MI ring but half this value using the body coil. The real SNR gain shows near the device conductors, where the SNR is more than 15 times higher when receiving with the internal device. Outside the ring, the SNR does not decay monotonically as expected; instead, there are oscillations with increasing radius, which can be ascribed to over-excitation. These would be reduced with improvements to passive decoupling, which might follow from increases in mode separation, Q-factor and symmetry.

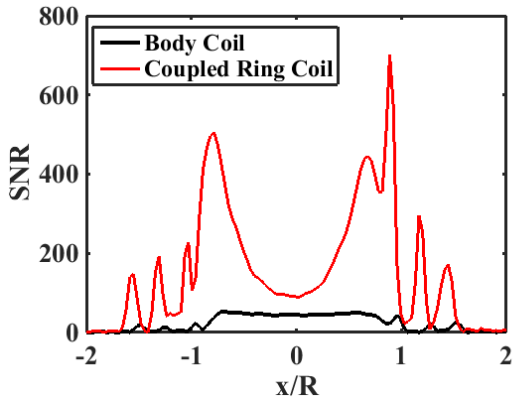

Figure 6.28 Variation of SNR with vertical position obtained using (i) the body coil and (ii) the coupled MI ring coil.

It is interesting to also compare the SNR obtained with a directly coupled system to that of experiment 1, obtained with a mutually coupled system. Figure 6.29 shows the SNR along a vertical line of the axial image of the large device in experiment 1, shown in Figure 6.13 (where the noise standard deviation is equal to 86) and along a vertical line of image 12, experiment 3. Here we see the much more significant local SNR enhancement obtained with the directly coupled system.

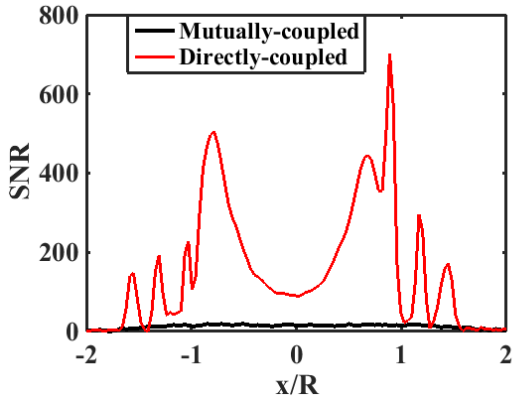

Figure 6.29 Variation of SNR with vertical position obtained using (i) mutually-coupled and (ii) directly-coupled systems.

Finally, Figure 6.30 shows a sagittal image through the middle of the device, obtained using the directly coupled ring device. Here we can see the cable – arrowed – connected to one of the elements of the lower ring; and the support pillar used to mount the device. We also see the distinctive

sensitivity pattern of the anti-symmetric mode operation, with zero sensitivity through the middle of the device, as characterised by the dark horizontal line. This pattern is exactly as calculated in Chapter 5, and was not seen in the coronal image previously obtained using the mutually coupled system (Figure 6.15).

Figure 6.30 Sagittal image through the device centre, obtained using the directly coupled system.

6.6 Conclusions

In this Chapter we have shown that mutual coupling to a uniform external read coil cannot be combined with an internal device using operation on its anti-symmetric mode to reject B_1 fields. However, we have confirmed that a directly coupled system offers a clear advantage, demonstrated by a peak SNR 15-fold enhancement in SNR. To obtain such a high enhancement by the alternative route of signal averaging would require a $15^2 = 225$ fold increase in the number of excitations, a clearly impractical requirement. The improved SNR can be directly exploited in reducing the voxel size (and hence increasing image resolution) in MRI, or in improving the resolution of peaks in MRS.

Some decoupling artefacts were seen, even when using the directly coupled system. These can be attributed to the lack of symmetry of the device coil structure, resulting in the mixing of the symmetric and anti-symmetric modes. For example, Figure 6.31 shows an X-ray scan[10] of the large coupled MI ring device before connection of the single tap. Here the lack of symmetry, evidenced by small errors in coil positions, is confirmed. It is likely that these errors could be significantly reduced by iteration of the overall design and assembly process. In the next Chapter, conclusions are summarised and original contributions are highlighted. Suggestions for future work to improve device performance and continue with this research are also presented.

[10] Thank you to Ms. Tabassum Zabwala from the Barts Health NHS Trust for taking the image.

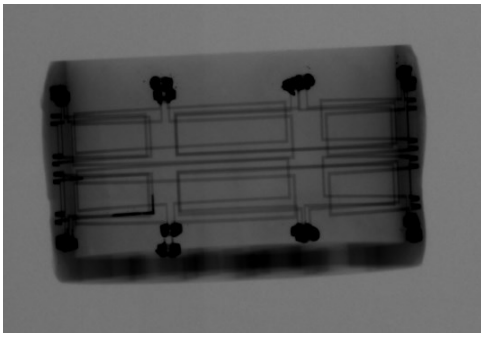

Figure 6.31 X-ray scan of large coupled MI ring device, showing misaligned coil patterns.

7 Conclusion

The aim of this research has been to design and develop an initial prototype of an internal sensor for the post-operative monitoring of colorectal anastomosis, based on magnetic resonance imaging. The overall intention is to use an implanted RF detection coil that can be mounted in a Biodegradable Anastomosis Ring (BAR) to enhance the local signal-to-noise ratio in MRI. Improved imaging may improve the diagnosis of anastomotic leak following surgical reconstruction, and potentially allow prediction of its occurrence rather than simply confirm its existence. Here we summarise the contributions made in this thesis and discuss directions for possible future work.

7.1 Contributions

The local coil was based on a magneto-inductive (MI) ring resonator; selected for its annular shape and the fact that its separate elements lack any mechanical connections. This makes it the ideal candidate to be incorporated into a BAR, a temporary mechanical scaffold that is commonly used to support an anastomosis and that is fragmented and excreted naturally after healing. The close correspondence between the surgical wound, the BAR and the field of view of the MI ring resonator implies that the latter will be in a suitable position for wound monitoring. A coupled pair of MI ring resonators was used, operating on its first anti-symmetric spatial mode to minimise coupling to the B_1 field during excitation and hence reduce RF heating and over-excitation artefacts.

Two octagonal coupled MI ring resonator systems based on planar printed circuit board (PCB) elements were compared. One was constructed using square elements, and the other using rectangular elements. The stronger inductance and intra-ring coupling of the latter resulted in a higher Q-factor and more widely separated resonances. The mode spectra for the two systems were predicted theoretically and verified experimentally, particularly noting the position of the first anti-symmetric mode and its separation in frequency from other modes. It was found that, for this configuration, this important anti-symmetric mode is too close in frequency to a symmetric mode which will certainly couple to the MRI scanner's B_1 field, allowing for RF heating and the generation of local artefacts.

Therefore, it was necessary to explore different possibilities for controlling the mode spectrum of a coupled MI ring resonator system, to increase the rejection of uniform fields. A systematic geometrical search resulted in a further octagonal configuration with a combination of axial and planar intra-ring coupling which proved effective at increasing the bandwidth occupied by the anti-symmetric modes and separating them in frequency. Additionally, it altered the ordering of the modes, allowing the first anti-symmetric mode to be separated in frequency from all symmetric modes. Using this new design, two new prototypes were constructed from flexible thin-film PCBs mounted on an annular scaffold. The first had its dimensions matched to the BAR, while the second was a larger

device potentially offering better performance. Again, the electrical response of these devices was theoretically predicted and experimentally verified.

The field-of-view (FOV) of the sensor was then estimated. Calculations were carried out using the reciprocity principle, and the FOV was first calculated for a stand-alone system. Initially a single travelling current pattern was assumed for each ring, leading to an overall pattern with 8-fold symmetry in the ring plane. However, the sensitivity was clearly non-uniform, being highest at the ring itself and decreasing radially away, and with zero sensitivity where the coupled rings meet. The FOV was then calculated for a mutually coupled system, based on a single MI ring resonator coupled to an external reading coil. The current pattern here was shown to be similar to a standing wave and resulted in the variation in sensitivity having 6-fold symmetry.

Unfortunately, there can be no mutual coupling between a uniform external read coil and a coupled MI ring resonator system, when the latter uses operation on an anti-symmetric mode to achieve B_1 decoupling. Therefore, a directly coupled system was proposed, with a single wired connection to one of the ring elements. In this case, the FOV again had 6-fold symmetry. However, a quadrature tap could be used to improve image uniformity.

^{1}H MR imaging was carried out, with the coupled MI ring device immersed in phantom gel designed to mimic the conductivity and T2 relaxation time constant of the human body. A mutually coupled system at 3 T was first used. Axial images obtained with the ring axis parallel to the B_0 field suggested a small signal enhancement at the edge of each MI ring, together with a zero in sensitivity where the two rings meet. However, since there can be no coupling between a symmetric reading coil and an anti-symmetric system, it was suggested that these effects are produced by the B_1 field and the read coil both coupling to the zeroth symmetric mode, leading to the twin effects of artefact formation and residual sensitivity. Images obtained using the larger device, which was expected to have better performance, show decreased artefact formation and decreased signal enhancement, confirming this interpretation.

Further imaging at 1.5 T was carried out with this large device, using a directly coupled system with a single wired connection. Here a local signal enhancement of double the SNR was observed at the device centre, with this value increasing to 15 fold at the coil conductors. Additionally, a significant improvement over the mutually coupled system was confirmed. However, only moderate decoupling from the B_1 field was achieved, and 6-fold symmetry in sensitivity remains a disadvantage.

7.2 Future Work

The conclusions thus far achieved in this research represent an encouraging proof of concept; however, as previously alluded, further work is required to improve device performance and move on to animal and clinical testing.

Firstly, to improve B_1 field decoupling, methods to maintain device symmetry during fabrication should be explored. Additional passive decoupling in the form of a set of diode-switched tank filters based on back-to-back diode pairs could also be considered. This approach may increase device size and complexity, but would result in significantly increased rejection. The thickness of encapsulating material, which affects the body loading on the coil, and hence the effective Q-factor, should also be investigated, since there is likely to be a thickness that yields optimum SNR. However, optimization of this parameter must be carried out in conjunction with consideration of anatomy and surgical efficacy of the BAR device itself.

Secondly, to improve image uniformity, quadrature taps should be used. These would be simple to implement; however, although there is a natural lumen provided by human anatomy down which any wired connections could be passed, it would be advantageous to eliminate these, since they present a potential pathway for infection. One approach would involve engineering an anti-symmetric external reading coil, such as a figure-of-eight coil; however, there would almost certainly be difficulties involved in placing such a coil close enough to the local sensor to achieve sufficient coupling. Another approach would be to use direct detection, frequency up-conversion and wireless transmission. A suitable power source would be required; however, due to the limited lifetime needed, it is likely that a battery would be sufficient.

Thirdly, orientation effects must be investigated, since it is expected that the field of view uniformity will reduce further in orientations parallel to the x- or y- axes, and these may be encountered depending on the location of the anastomosis within the colon. The likely effects must be modelled and confirmed experimentally in an MR scanner. Potential methods of reducing orientation dependence including the use of an array of perpendicular coils must then be explored.

Finally, since the device is intended for incorporation in a BAR, a suitable biofragmentable matrix must be developed. The effect of the matrix on the device, in terms of potentially decreasing its rejection of uniform fields or obscuring its FOV, should then be investigated as described above. Alterations to resonance tuning and FOV as the device fragments should also be considered. In the future, the availability of biodegradable conductors such as poly pyrrole may provide options for improved biofragmentation or more complete biodegradation. MRI safety should be evaluated (for example, using a fibre optical thermometer to measure RF heating of a surrounding gel phantom [215]) especially for partially fragmented devices. Lack of toxicity should then be confirmed before in

vivo testing to confirm the utility of the sensor in localised imaging or spectroscopy of annular wounds.

8 References

[1] C. C. M. Marres, A. W. H. van de Ven, L. G. J. Leijssen, P. C. M. Verbeek, W. A. Bemelman, and C. J. Buskens, "Colorectal anastomotic leak: delay in reintervention after false-negative computed tomography scan is a reason for concern," *Tech. Coloproctol.*, vol. 21, no. 9, pp. 709–714, 2017.

[2] F. Daams, M. Luyer, and J. F. Lange, "Colorectal anastomotic leakage: Aspects of prevention, detection and treatment," *World J. Gastroenterol.*, vol. 19, no. 15, pp. 2293–2297, 2013.

[3] A. N. Morks, K. Havenga, and R. J. Ploeg, "Can intraluminal devices prevent or reduce colorectal anastomotic leakage: A review," *World J. Gastroenterol.*, vol. 17, no. 40, pp. 4461–4469, 2011.

[4] M. Matthew Hoffman, "Digestive Disorders Health Centre." [Online]. Available: https://www.webmd.com/digestive-disorders/picture-of-the-colon#1. [Accessed: 21-Mar-2018].

[5] Office for National Statistics, "Cancer registration statistics, England: first release, 2016." [Online]. Available: https://www.ons.gov.uk/peoplepopulationandcommunity/healthandsocialcare/conditionsanddiseases/bulletins/cancerregistrationstatisticsengland/2016. [Accessed: 23-Mar-2018].

[6] National Cancer Institute, "Colon Cancer Treatment." [Online]. Available: https://www.cancer.gov/types/colorectal/patient/colon-treatment-pdq#section/_162. [Accessed: 23-Mar-2018].

[7] American Society of Colon and Rectal Surgeons, "Polyps of the Colon and Rectum." [Online]. Available: https://www.fascrs.org/patients/disease-condition/polyps-colon-and-rectum. [Accessed: 23-Mar-2018].

[8] NHS Choices, "Inflammatory bowel disease." [Online]. Available: https://www.nhs.uk/conditions/inflammatory-bowel-disease/#Treatment. [Accessed: 23-Mar-2018].

[9] UCSF Center for Colorectal Surgery, "Colon Cancer." [Online]. Available: https://colorectal.surgery.ucsf.edu/conditions--procedures/colon-cancer.aspx. [Accessed: 23-Mar-2018].

[10] National Institute of Diabetes and Digestive and Kidney Diseases, "Anatomic Problems of the Lower GI Tract." [Online]. Available: https://www.niddk.nih.gov/health-information/digestive-diseases/anatomic-problems-lower-gi-tract. [Accessed: 23-Mar-2018].

[11] F. Goulder, "Bowel anastomoses: The theory, the practice and the evidence base," *World J. Gastrointest. Surg.*, vol. 4, no. 9, p. 208, 2012.

[12] J. C. Slieker, F. Daams, I. M. Mulder, J. Jeekel, and J. F. Lange, "Systematic review of the technique of colorectal anastomosis," *JAMA Surg.*, vol. 148, no. 2, pp. 190–201, 2013.

[13] N. J. Mortensen and S. Ashraf, "Intestinal Anastomosis," in *ACS Surgery: Principles and Practice*, BC Decker Inc, 2008.

[14] M. M. Jawad, S. T. Abdul Qader, A. A. Zaidan, B. B. Zaidan, A. W. Naji, and I. T. Abdul Qader, "An Overview of Laser Principle, Laser-Tissue Interaction Mechanisms and Laser

Safety Precautions for Medical Laser Users," *Int. J. Pharmacol.*, vol. 7, no. 2, pp. 149–160, 2011.

[15] L. S. Bass and M. R. Treat, "Laser Tissue Welding: A Comprehensive Review of Current and Future Clinical Applications," *Lasers Surg. Med.*, vol. 17, pp. 315–349, 1995.

[16] M. Kawahara, S. Kuramoto, P. Ryan, and R. Stillwell, "First Experimental Sutureless Laser Anastomosis of the Large Bowel: Long-Term Study," *Dis. Colon Rectum*, vol. 35, no. 8, pp. 792–798, 1992.

[17] D. Spector, Y. Rabi, I. Vasserman, A. Hardy, J. Klausner, M. Rabau, and A. Katzir, "In vitro large diameter bowel anastomosis using a temperature controlled laser tissue soldering system and albumin stent," *Lasers Surg. Med.*, vol. 41, no. 7, pp. 504–508, 2009.

[18] Valleylab, "LigaSure ™ Vessel Sealing Generator Service Manual," 2009. [Online]. Available: https://cdn.shopify.com/s/files/1/1046/1086/files/ValleyLab-LigaSure-Vessel-Sealing-System-Service-Manual.pdf. [Accessed: 23-Mar-2018].

[19] K. L. Hinton, "Method of Sealing Tissue Using Radio-frequency Energy, Patent," 2010. [Online]. Available: https://patentimages.storage.googleapis.com/b7/99/e3/4d2a8d406c3fc1/US8486107.pdf. [Accessed: 23-Mar-2018].

[20] A. H. Schiphorst, B. A. Twigt, S. G. Elias, and T. Van Dalen, "Randomized clinical trial of LigaSure versus conventional suture ligation in thyroid surgery," *Head Neck Oncol.*, vol. 4, no. 2, 2012.

[21] U. Lepner and T. Vaasna, "Ligasure vessel sealing system versus conventional vessel ligation in thyroidectomy," *Scand. J. Surg.*, vol. 96, pp. 31–34, 2007.

[22] N. Sorgato, P. Bernante, and M. R. Pelizzo, "Application of the LigaSure tissue sealing system to intestinal resection. Experimental and clinical trial," *Ann. Ital. Chir.*, vol. 79, no. 5, pp. 383–388, 2008.

[23] C. A. Shields, D. A. Schechter, P. Tetzlaff, A. L. Baily, S. Dycus, and N. Cosgriff, "Method for creating ideal tissue fusion in soft-tissue structures using radio frequency (RF) energy.," *Surg Technol Int.*, vol. 13, pp. 49–55, 2004.

[24] M. Santini, A. Fiorelli, G. Messina, A. Mazzella, and M. Accardo, "The feasibility of LigaSure to create intestinal anastomosis: Results of Ex vivo study," *Surg. Innov.*, vol. 22, no. 3, pp. 266–273, 2015.

[25] T. Gehrig, A. T. Billeter, A. L. Wekerle, M. Shevchenko, K. Brand, and B. P. Müller-Stich, "Evaluation of the LigaSure™ Vessel Sealing System for bowel transection and intestinal anastomosis—an experimental study in a porcine model," *Langenbeck's Arch. Surg.*, vol. 401, no. 3, pp. 381–387, 2016.

[26] ConMed, "Altrus Thermal Tissue Fusion System," 2003. [Online]. Available: http://www.medispecperu.com/catalogos/Altrus_ENG.pdf. [Accessed: 23-Mar-2018].

[27] J. Paral, P. Lochman, S. Blazej, and M. Pavlik, "Glued versus stapled anastomosis of the colon: An experimental study to determine comparative resistance to intraluminal pressure," *Asian J. Surg.*, vol. 37, no. 3, pp. 154–161, 2014.

[28] T. Nordenroft, "Sealing of gastrointestinal anastomoses with fibrin glue coated collagen patch.," *Dan. Med. J.*, vol. 62, no. 5, 2015.

[29] Z. Wu, G. S. Boersema, L. F. Kroese, D. Taha, S. Vennix, Y. M. Bastiaansen-Jenniskens, K.

H. Lam, G. J. Kleinrensink, J. Jeekel, M. Peppelenbosch, and J. F. Lange, “Reducing colorectal anastomotic leakage with tissue adhesive in experimental inflammatory bowel disease.,” *Inflamm. Bowel Dis.*, vol. 21, no. 5, pp. 1038–1046, 2015.

[30] A. A. P. Slesser, G. Pellino, O. Shariq, D. Cocker, C. Kontovounisios, S. Rasheed, and P. P. Tekkis, “Compression versus hand-sewn and stapled anastomosis in colorectal surgery: a systematic review and meta-analysis of randomized controlled trials,” *Tech. Coloproctol.*, vol. 20, no. 10, pp. 667–676, 2016.

[31] O. Kaidar-Person, R. J. Rosenthal, S. D. Wexner, S. Szomstein, and B. Person, “Compression anastomosis: history and clinical considerations,” *Am. J. Surg.*, vol. 195, no. 6, pp. 818–826, 2008.

[32] L. Morgenstern, “John Benjamin Murphy (1857-1916): An American Surgical Phenomenon,” *Surg. Innov.*, vol. 13, no. 1, pp. 1–3, 2006.

[33] T. G. Hardy, W. G. Pace, J. W. Maney, a R. Katz, and a L. Kaganov, “A biofragmentable ring for sutureless bowel anastomosis. An experimental study.,” *Dis. Colon Rectum*, vol. 28, no. 7, pp. 484–490, 1985.

[34] K. A. Forde, K. H. Goodell, and M. DellaBadia, “A 10-year single-institutional study of the biofragmentable anastomosis ring,” *Am. J. Surg.*, vol. 191, no. 4, pp. 483–487, 2006.

[35] Medtronic, “Valtrac™ Bowel Anastomosis.” [Online]. Available: http://products.covidien.com/pages.aspx?page=ProductDetail&id=13606&cat=Devices&cat2=Model. [Accessed: 23-Mar-2018].

[36] P. Luukkonen, H. J. Jarvinen, and R. Haapiainen, “Early experience with biofragmentable anastomosis ring in colon surgery.,” *Acta Chir Scand*, vol. 156, no. 11–12, pp. 795–799, 1990.

[37] J. K. Croston, D. M. Jacobs, P. H. Kelly, D. A. Feeney, G. R. Johnston, R. L. Strom, and M. P. Bubrick, “Experience with the biofragmentable anastomotic ring (BAR) in bowel preoperatively irradiated with 6000 rad,” *Dis. Colon Rectum*, vol. 33, no. 3, pp. 222–226, 1990.

[38] F. Köckerling, I. Schneider, C. Schneider, and W. Hohenberger, “Laparoscopic intracorporeal anastomosis in the colon using the biofragmentable anastomotic ring - An animal study,” *Int. J. Colorectal Dis.*, vol. 11, no. 6, pp. 299–302, 1996.

[39] H. J. Choi, H. H. Kim, G. J. Jung, and S. S. Kim, “Intestinal anastomosis by use of the biofragmentable anastomotic ring is it safe and efficacious in emergency operations as well?,” *Dis. Colon Rectum*, vol. 41, no. 10, pp. 1281–1286, 1998.

[40] A. Thiede, D. Geiger, U. A. Dietz, E. S. Debus, R. Engemann, G. C. Lexer, B. Lünstedt, and W. Mokros, “Overview on compression anastomoses: Biofragmentable anastomosis ring multicenter prospective trial of 1666 anastomoses,” *World J. Surg.*, vol. 22, no. 1, pp. 78–87, 1998.

[41] M. L. Cossu, M. Coppola, E. Fais, M. Ruggiu, C. Sparta, S. Profili, V. Bifulco, G. B. Meloni, and G. Noya, “The use of the Valtrac ring in the upper and lower gastrointestinal tract, for single, double and triple anastomoses: a report of 50 cases.,” *Am. J. Surg.*, vol. 66, no. 8, pp. 759–762, 2000.

[42] J. Emerich, M. Liro, M. Dudziak, and J. Debniak, “New techniques with biodegradable Valtrac-Bar rings for intestinal anastomosis management of advanced cancer,” *Ginekol Pol*, vol. 73, no. 11, pp. 1034–1037, 2002.

[43] F. Ye, D. Wang, X. Xu, F. Liu, and J. Lin, “Use of intracolonic bypass secured by a

biodegradable anastomotic ring to protect the low rectal anastomosis," *Dis. Colon Rectum*, vol. 51, no. 1, pp. 109–115, 2008.

[44] B. Lunstedt and H. Sundermann, "Transanal compression anastomosis in the lower rectum with a biofragmentable anastomosis ring (Valtrac). Surgical technique and initial clinical experiences," *Chirurg*, vol. 66, no. 7, pp. 715–718, 1995.

[45] M. L. Corman, E. D. Prager, T. G. Hardy, and M. P. Bubrick, "Comparison of the Valtrac® biofragmentable anastomosis ring with conventional suture and stapled anastomosis in colon surgery; Results of a prospective, randomized clinical trial.," *Dis. Colon Rectum*, vol. 32, no. 3, pp. 183–7, Mar. 1989.

[46] C. J. Cahill, M. Betzler, J. A. Gruwez, J. Jeekel, J. C. Patel, and B. Zederfeldt, "Sutureless large cowel anastomosis: European experience with the biofragmentable anastomosis ring," *Br. J. Surg.*, vol. 76, pp. 344–347, 1989.

[47] A. Bobkiewicz, A. Studniarek, L. Krokowicz, K. Szmyt, M. Borejsza-Wysocki, J. Szmeja, R. Marciniak, M. Drews, and T. Banasiewicz, "Gastrointestinal tract anastomoses with the biofragmentable anastomosis ring: is it still a valid technique for bowel anastomosis? Analysis of 203 cases and review of the literature," *Int. J. Colorectal Dis.*, vol. 32, no. 1, pp. 107–111, 2017.

[48] L. Liu, Q. Huang, J. Wang, Q. Chen, R. Lin, and B. Ge, "Protection of low rectal anastomosis with a new tube ileostomy using a biofragmentable anastomosis ring.," *Medicine (Baltimore).*, vol. 95, no. 45, 2016.

[49] N. N. Kanshin, M. I. Lytkin, V. I. Knysh, V. I. Klur, and A. I. Khamidov, "First experience with application of compression anastomoses with the apparatus AKA-2 in operations on the large intestine.," *Vestn. Khir. Im. I. I. Grek.*, vol. 132, no. 1, pp. 52–57, 1984.

[50] I. V. Baltaĭtis, N. D. Kucher, V. A. Zhel'man, A. I. Poĭda, and M. P. Zakharash, "Compression anastomoses of the large intestine under complicated conditions.," *Vestn Khir Im I I Grek.*, vol. 150, no. 5–6, pp. 6–9, 1993.

[51] D. Matos and R. K. Phillips, "Initial experience with the AKA-2 and AKA-4 device for intestinal compression anastomosis in colorectal surgery.," *Rev Assoc Med Bras*, vol. 39, no. 1, pp. 8–11, 1993.

[52] E. Gross and H. O. Köppen, "The AKA-2 sutureless compression anastomosis of the colon and rectum," *Zentralbl Chir.*, vol. 118, no. 8, pp. 459–465, 1993.

[53] F. W. Eigler and E. Gross, "Mechanical compression anastomosis (AKA-2) of the colon and rectum. Results of a prospective clinical study.," *Chirurg.*, vol. 57, no. 4, pp. 230–235, 1986.

[54] I. I. Patiutko, V. V. Pedchenko, A. T. Lagoshnyĭ, and O. N. Efimov, "Experience in the use of the AKA-2 device in the formation of esophago-intestinal anastomosis.," *Klin Khir.*, vol. 5, pp. 31–35, 1991.

[55] A. A. Vlasov, A. V. Vazhenin, V. V. Plotnikov, and D. V. Nazarova, "Experience with using anterior resections in the surgery of the rectum.," *Vestn Khir Im I I Grek.*, vol. 168, no. 5, pp. 52–54, 2009.

[56] M. P. Zakharash, F. H. Tkachenko, O. I. Poĭda, V. O. Zhel'man, M. I. Kryvoruk, and V. A. Dubovyĭ, "Application of apparatus AKA-2 in the reconstructive-restorative surgery of the left half of colon and of rectum," *Klin Khir.*, vol. 3, pp. 31–3, 2001.

[57] C. Wullstein and E. Gross, "Compression anastomosis (AKA-2) in colorectal surgery: results in 442 consecutive patients.," *Br. J. Surg.*, vol. 87, no. 8, pp. 1071–1075, 2000.

[58] NiTi Surgical Solutions Clinical Training Team, “History of Compression Anastomosis.” [Online]. Available: https://www.slideshare.net/Iknifem/combined-14-clinical-trainingcompression-anastomosis. [Accessed: 23-Mar-2018].

[59] novogi, “ColonRing for Compression Anastomosis in Colorectal Surgery.” .

[60] A. Szold, “New concepts for a compression anastomosis: Superelastic clips and rings,” *Minim. Invasive Ther. Allied Technol.*, vol. 17, no. 3, pp. 168–171, 2008.

[61] InnoMedicus, “ColonRing for Compression Anastomosis in Colorectal Surgery,” 2012. [Online]. Available: http://www.innomedicus.com/index.asp?Language=EN&page=compression_anastomosis. [Accessed: 23-Mar-2018].

[62] D. Kopelman, S. Lelcuk, J. Sayfan, I. Matter, E. P. Willenz, L. Zaidenstein, O. A. Hatoum, B. Kimmel, and A. Szold, “End-to-end compression anastomosis of the rectum: A pig model,” *World J. Surg.*, vol. 31, no. 3, pp. 532–537, 2007.

[63] D. Stewart, S. Hunt, R. Pierce, D. Mao, M. Frisella, K. Cook, B. Starcher, and J. Fleshman, “Validation of the NITI endoluminal compression anastomosis ring (EndoCAR) device and comparison to the traditional circular stapled colorectal anastomosis in a porcine model,” *Surg. Innov.*, vol. 14, no. 4, pp. 252–260, 2007.

[64] B. S. Buchberg, H. Masoomi, H. Bergman, S. D. Mills, and M. J. Stamos, “The use of a compression device as an alternative to hand-sewn and stapled colorectal anastomoses: Is three a crowd?,” *J. Gastrointest. Surg.*, vol. 15, no. 2, pp. 304–310, 2011.

[65] H. Masoomi, R. Luo, S. Mills, J. C. Carmichael, A. J. Senagore, and M. J. Stamos, “Compression anastomosis ring device in colorectal anastomosis: A review of 1,180 patients,” *Am. J. Surg.*, vol. 205, no. 4, pp. 447–451, 2013.

[66] Z. Lu, J. Peng, C. Li, F. Wang, W. Jiang, W. Fan, J. Lin, X. Wu, D. Wan, and Z. Pan, “Efficacy and safety of a NiTi CAR 27 compression ring for end-to-end anastomosis compared with conventional staplers: A real-world analysis in Chinese colorectal cancer patients.,” *Clinics (Sao Paulo).*, vol. 71, no. 5, pp. 264–70, 2016.

[67] R. Tabola, R. Cirocchi, A. Fingerhut, A. Arezzo, J. Randolph, V. Grassi, G. A. Binda, V. D’Andrea, I. Abraha, G. Popivanov, S. Di Saverio, and A. Zbar, “A systematic analysis of controlled clinical trials using the NiTi CAR™ compression ring in colorectal anastomoses,” *Tech. Coloproctol.*, vol. 21, no. 3, pp. 177–184, 2017.

[68] N. Grassi, C. Cipolla, A. Bottino, G. Graceffa, L. Montana, C. Privitera, R. Grassi, and M. A. Latteri, “Validity of shape memory NiTi colon ring BioDynamix ColonRing™ (or NiTi CAR 27™) to prevent anastomotic colorectal strictures. Preliminary results.,” *G Chir.*, vol. 33, no. 5, pp. 194–198, 2012.

[69] Y. Khromov, I. Pliakos, M. Ibrahim, A. P. Zbar, J. Sayfan, and T. S. Papavramidis, “A prospective multi-institutional study assessing clinical outcome with the NiTi compression anastomosis ring (Biodynamix ColonRingTM) in elective colorectal anastomoses.,” *Hepatogastroenterology*, vol. 60, no. 123, pp. 522–527, 2013.

[70] I. L. Nudelman, V. V. Fuko, S. Morgenstern, S. Giler, and S. Lelcuk, “Gastrointestinal anastomosis with the nickel-titanium double ring,” *World J. Surg.*, vol. 24, no. 7, pp. 874–877, 2000.

[71] I. L. Nudelman, V. Fuko, F. Greif, and S. Lelcuk, “Colonic anastomosis with the nickel-titanium temperature-dependent memory-shape device,” *Am. J. Surg.*, vol. 183, no. 6, pp. 697–

701, 2002.

[72] I. Nudelman, V. Fuko, N. Waserberg, Y. Niv, M. Rubin, A. Szold, and S. Lelcuk, "Colonic anastomosis performed with a memory-shaped device," *Am. J. Surg.*, vol. 190, no. 3, pp. 434–438, 2005.

[73] C. Song, T. Frank, and A. Cuschieri, "Shape memory alloy clip for compression colonic anastomosis.," *J. Biomech. Eng.*, vol. 127, no. 2, pp. 351–354, 2005.

[74] I. Nudelman, V. Fuko, M. Rubin, and S. Lelcuk, "A nickel-titanium memory-shape device for colonic anastomosis in laparoscopic surgery," *Minim. Invasive Ther. Allied Technol.*, vol. 13, no. 1, pp. 36–41, 2004.

[75] T. P. Kingham and H. L. Pachter, "Colonic Anastomotic Leak: Risk Factors, Diagnosis, and Treatment," *J. Am. Coll. Surg.*, vol. 208, no. 2, pp. 269–278, 2009.

[76] N. C. Buchs, P. Gervaz, M. Secic, P. Bucher, B. Mugnier-Konrad, and P. Morel, "Incidence, consequences, and risk factors for anastomotic dehiscence after colorectal surgery: A prospective monocentric study," *Int. J. Colorectal Dis.*, vol. 23, no. 3, pp. 265–270, 2008.

[77] A. Karliczek, N. J. Harlaar, C. J. Zeebregts, T. Wiggers, P. C. Baas, and G. M. van Dam, "Surgeons lack predictive accuracy for anastomotic leakage in gastrointestinal surgery," *Int. J. Colorectal Dis.*, vol. 24, no. 5, pp. 569–576, 2009.

[78] J. Hammond, S. Lim, Y. Wan, X. Gao, and A. Patkar, "The Burden of Gastrointestinal Anastomotic Leaks: An Evaluation of Clinical and Economic Outcomes," *J. Gastrointest. Surg.*, vol. 18, no. 6, pp. 1176–1185, 2014.

[79] K. G. Walker, S. W. Bell, M. J. F. X. Rickard, D. Mehanna, O. F. Dent, P. H. Chapuis, and E. L. Bokey, "Anastomotic leakage is predictive of diminished survival after potentially curative resection for colorectal cancer," *Ann. Surg.*, vol. 240, no. 2, pp. 255–259, 2004.

[80] W. L. Law, H. K. Choi, Y. M. Lee, J. W. C. Ho, and C. L. Seto, "Anastomotic leakage is associated with poor long-term outcome in patients after curative colorectal resection for malignancy," *J. Gastrointest. Surg.*, vol. 11, no. 1, pp. 8–15, 2007.

[81] A. Mirnezami, R. Mirnezami, K. Chandrakumaran, K. Sasapu, P. Sagar, and P. Finan, "Increased local recurrence and reduced survival from colorectal cancer following anastomotic leak: Systematic review and meta-analysis," *Ann. Surg.*, vol. 253, no. 5, pp. 890–899, 2011.

[82] N. N. Haddad, B. R. Bruns, T. M. Enniss, D. Turay, J. V. Sakran, A. Fathalizadeh, K. Arnold, J. S. Murry, M. M. Carrick, M. C. Hernandez, M. H. Lauerman, A. J. Choudhry, D. S. Morris, J. J. Diaz, H. A. Phelan, and M. D. Zielinski, "Perioperative use of nonsteroidal anti-inflammatory drugs and the risk of anastomotic failure in emergency general surgery," *J. Trauma Acute Care Surg.*, vol. 83, no. 4, pp. 657–661, 2017.

[83] E. C. Z. Vasiliu, N. O. Zarnescu, R. Costea, and S. Neagu, "Review of Risk Factors for Anastomotic Leakage in Colorectal Surgery.," *Chirurgia (Bucur).*, vol. 110, no. 4, pp. 319–26, 2015.

[84] M. A. Boccola, P. G. Buettner, W. M. Rozen, S. K. Siu, A. R. L. Stevenson, R. Stitz, and Y. H. Ho, "Risk factors and outcomes for anastomotic leakage in colorectal surgery: A single-institution analysis of 1576 patients," *World J. Surg.*, vol. 35, no. 1, pp. 186–195, 2011.

[85] D. A. Telem, "Risk Factors for Anastomotic Leak Following Colorectal Surgery," *Arch. Surg.*, vol. 145, no. 4, p. 371, 2010.

[86] B. Phillips, "Reducing gastrointestinal anastomotic leak rates: review of challenges and

solutions," *Open Access Surg.*, p. 5, 2016.

[87] F. D. McDermott, A. Heeney, M. E. Kelly, R. J. Steele, G. L. Carlson, and D. C. Winter, "Systematic review of preoperative, intraoperative and postoperative risk factors for colorectal anastomotic leaks," *Br. J. Surg.*, vol. 102, no. 5, pp. 462–479, 2015.

[88] National Institute of Biomedical Imaging and Bioengineering, "Computed Tomography (CT)." [Online]. Available: https://www.nibib.nih.gov/science-education/science-topics/computed-tomography-ct. [Accessed: 23-Mar-2018].

[89] A. Doeksen, P. J. Tanis, A. F. J. Wüst, B. C. Vrouenraets, J. J. B. Lanschot, and W. F. Tets, "Radiological evaluation of colorectal anastomoses," *Int. J. Colorectal Dis.*, vol. 23, no. 9, pp. 863–868, 2008.

[90] A. Doeksen, P. J. Tanis, B. C. Vrouenraets, J. J. B. van Lanschot, and W. F. van Tets, "Factors determining delay in relaparotomy for anastomotic leakage after colorectal resection," *World J. Gastroenterol.*, vol. 13, no. 27, pp. 3721–3725, 2007.

[91] W. Khoury, A. Ben-Yehuda, M. Ben-Haim, J. M. Klausner, and O. Szold, "Abdominal Computed Tomography for Diagnosing Postoperative Lower Gastrointestinal Tract Leaks," *J. Gastrointest. Surg.*, vol. 13, no. 8, pp. 1454–1458, 2009.

[92] G. A. Nicksa, R. V. Dring, K. H. Johnson, W. V. Sardella, P. V. Vignati, and J. L. Cohen, "Anastomotic leaks: What is the best diagnostic imaging study?," *Dis. Colon Rectum*, vol. 50, no. 2, pp. 197–203, 2007.

[93] N. Hyman, T. L. Manchester, T. Osler, B. Burns, and P. A. Cataldo, "Anastomotic leaks after intestinal anastomosis: It's later than you think," *Ann. Surg.*, vol. 245, no. 2, pp. 254–258, 2007.

[94] R. Warschkow, U. Beutner, T. Steffen, S. A. Müller, B. M. Schmied, U. Güller, and I. Tarantino, "Safe and early discharge after colorectal surgery due to C-reactive protein: A diagnostic meta-analysis of 1832 patients," *Ann. Surg.*, vol. 256, no. 2, pp. 245–250, 2012.

[95] A. B. Almeida, G. Faria, H. Moreira, J. Pinto-de-Sousa, P. Correia-da-Silva, and J. C. Maia, "Elevated serum C-reactive protein as a predictive factor for anastomotic leakage in colorectal surgery," *Int. J. Surg.*, vol. 10, no. 2, pp. 87–91, 2012.

[96] A. Garcia-Granero, M. Frasson, B. Flor-Lorente, F. Blanco, R. Puga, A. Carratalá, and E. Garcia-Granero, "Procalcitonin and C-reactive protein as early predictors of anastomotic leak in colorectal surgery: A prospective observational study," *Dis. Colon Rectum*, vol. 56, no. 4, pp. 475–483, 2013.

[97] M. den Dulk, S. L. Noter, E. R. Hendriks, M. A. M. Brouwers, C. H. van der Vlies, R. J. Oostenbroek, A. G. Menon, W. H. Steup, and C. J. H. van de Velde, "Improved diagnosis and treatment of anastomotic leakage after colorectal surgery," *Eur. J. Surg. Oncol.*, vol. 35, no. 4, pp. 420–426, 2009.

[98] S. Sujatha-Bhaskar, M. D. Jafari, M. Hanna, C. Y. Koh, C. S. Inaba, S. D. Mills, J. C. Carmichael, N. T. Nguyen, M. J. Stamos, and A. Pigazzi, "An endoscopic mucosal grading system is predictive of leak in stapled rectal anastomoses," *Surg. Endosc. Other Interv. Tech.*, vol. 32, no. 4, pp. 1–7, 2017.

[99] K. L. Guyton, N. H. Hyman, and J. C. Alverdy, "Prevention of Perioperative Anastomotic Healing Complications: Anastomotic Stricture and Anastomotic Leak," *Adv Surg.*, vol. 50, no. 1, pp. 129–139, 2016.

[100] K. Vikram, "Intestinal Anastomosis," *Medscape*, 2016. [Online]. Available:

https://emedicine.medscape.com/article/1892319-overview. [Accessed: 23-Mar-2018].

[101] P. Kirchhoff, P.-A. Clavien, and D. Hahnloser, "Complications in colorectal surgery: risk factors and preventive strategies," *Patient Saf. Surg.*, vol. 4, no. 1, p. 5, 2010.

[102] P. Di Giorgio, L. De Luca, G. Rivellini, E. Sorrentino, E. D'Amore, and B. De Luca, "Endoscopic dilation of benign colorectal anastomotic stricture after low anterior resection: A prospective comparison study of two balloon types," *Gastrointest. Endosc.*, vol. 60, no. 3, pp. 347–350, 2004.

[103] G. Curcio, M. Spada, F. di Francesco, I. Tarantino, L. Barresi, G. Burgio, and M. Traina, "Completely obstructed colorectal anastomosis: A new nonelectrosurgical endoscopic approach before balloon dilatation," *World J. Gastroenterol.*, vol. 16, no. 37, pp. 4751–4754, 2010.

[104] K. Yazawa, D. Morioka, C. Matsumoto, Y. Miura, and S. Togo, "Blunt penetration technique for treatment of a completely obstructed anastomosis after rectal resection: A case report," *J. Med. Case Rep.*, vol. 8, no. 1, pp. 1–5, 2014.

[105] M. A. Amr, M. J. Alzghari, S. F. Polites, M. A. Khasawneh, D. S. Morris, T. H. Baron, and M. D. Zielinski, "Endoscopy in the Early Postoperative Setting after Primary Gastrointestinal Anastomosis," *J. Gastrointest. Surg.*, vol. 18, no. 11, pp. 1911–1916, 2014.

[106] Z. Lou, W. Zhang, E. Yu, R. Meng, and C. Fu, "Colonoscopy is the first choice for early postoperative rectal anastomotic bleeding," *World J. Surg. Oncol.*, vol. 12, no. 1, 2014.

[107] C. E. Hayes, W. A. Edelstein, J. F. Schenck, O. M. Mueller, and M. Eash, "An Efficient, Highly Homogenous Radiofrequency Coil for Whole-Body NMR Imaging at 1.5 T," *J. Magn. Reson.*, vol. 63, pp. 622–628, 1985.

[108] M. D. Harpen, "Equivalent Circuit for Birdcage Resonators," *Magn. Reson. Med.*, vol. 29, pp. 263–268, 1993.

[109] M. C. Leifer, "Resonant Modes of the Birdcage Coil," *J. Magn. Reson.*, vol. 124, no. 1, pp. 51–60, 1997.

[110] M. F. Santarelli, "Basic Physics of MR Signal and Image Generation," in *Advanced Image Processing in Magnetic Resonance Imaging*, Taylor and Francis Group, LLC, 2005, pp. 3–37.

[111] D. Weishaupt, V. D. Kochli, and B. Marincek, *How does MRI work? An Introduction to the Physics and Function of Magnetic Resonance Imaging*, Second Edi. Springer-Verlag Berlin Heidelberg.

[112] A. D. Elster, "k-space," 2017. [Online]. Available: http://mriquestions.com/what-is-k-space.html. [Accessed: 23-Mar-2017].

[113] J. M. Libove and J. R. Singer, "Resolution and signal-to-noise relationships in NMR imaging in the human body," *J. Phys. E Sci Instrum.*, vol. 13, pp. 38–44, 1980.

[114] Siemens Medical Solutions, "Siemen Healthineers Body 60/Body 30," 2018. [Online]. Available: https://usa.healthcare.siemens.com/magnetic-resonance-imaging/options-and-upgrades/coils/body-60-body-30. [Accessed: 23-Mar-2018].

[115] L. L. Arnder, M. D. Shattuck, and R. D. Black, "Signal-to-Noise Ratio Comparison Between Surface Coils and Implanted Coils," *Magn. Reson. Med.*, vol. 35, pp. 727–733, 1996.

[116] G. C. Hurst, J. Hua, J. L. Duerk, and A. M. Cohen, "Intravascular (catheter) NMR receiver probe: Preliminary design analysis and application to canine iliofemoral imaging," *Magn.*

Reson. Med., vol. 24, no. 2, pp. 343–357, 1992.

[117] J. A. Martin, D. B. Plewes, and M. Henkelman, "MR imaging of blood vessels with an intravascular coil.," *J. Magn. Reson. Imaging*, vol. 2, no. 421–429, 1992.

[118] O. Ocali and E. Atalar, "Intravascular magnetic resonance imaging using a loopless catheter antenna," *J. Magn. Reson. Med.*, vol. 37, no. 1, pp. 112–118, 1997.

[119] K. A. Shunk, J. A. Lima, A. W. Heldman, and E. Atalar, "Transesophageal magnetic resonance imaging," *J. Magn. Reson. Med.*, vol. 41, no. 4, pp. 72–726, 1999.

[120] T. Pirttimäki, R. A. Salo, A. Shatillo, M. I. Kettunen, J. Paasonen, A. Sierra, K. Jokivarsi, V. Leinonen, P. Andrade, S. Quittek, A. Pitkänen, and O. Gröhn, "Implantable RF-coil with multiple electrodes for long-term EEG-fMRI monitoring in rodents," *J. Neurosci. Methods*, vol. 274, pp. 154–163, 2016.

[121] J. C. Ginefri, A. Rubin, M. Tatoulian, M. Woytasik, F. Boumezbeur, B. Djemaï, M. Poirier-Quinot, F. Lethimonnier, L. Darrasse, and E. Dufour-Gergam, "Implanted, inductively-coupled, radiofrequency coils fabricated on flexible polymeric material: Application to in vivo rat brain MRI at 7 T," *J. Magn. Reson.*, vol. 224, pp. 61–70, 2012.

[122] M. Bilgen, "Simple, low-cost multipurpose RF coil for MR microscopy at 9.4 T," *Magn. Reson. Med.*, vol. 52, no. 4, pp. 937–940, 2004.

[123] N. K. Logothetis, H. Merkle, M. Augath, T. Trinath, and K. Uğurbil, "Ultra high-resolution fMRI in monkeys with implanted RF coils," *Neuron*, vol. 35, no. 2, pp. 227–242, 2002.

[124] H. H. Quick, J. M. Serfaty, H. K. Pannu, R. Genadry, C. J. Yeung, and E. Atalar, "Endourethral MRI," *J. Magn. Reson. Med.*, vol. 45, no. 1, pp. 138–146, 2001.

[125] M. D. Schnall, R. E. Lenkinski, H. M. Pollack, Y. Imai, and H. Y. Kressel, "Prostate: MR imaging with an endorectal surface coil.," *Radiology*, vol. 172, no. 2, pp. 570–574, 1989.

[126] Y. Eryaman, Y. Öner, and E. Atalar, "Design of internal MRI coils using ultimate intrinsic SNR," *Magn. Reson. Mater. Physics, Biol. Med.*, vol. 22, no. 4, pp. 221–228, 2009.

[127] S. Blüml, "Magnetic Resonance Spectroscopy: Basics," in *MR Spectroscopy of Pediatric Brain Disorders*, S. Blüml and A. Panigraphy, Eds. Springer, 2013, pp. 11–23.

[128] A. D. Elster, "MRS Introduction," 2017. [Online]. Available: http://mriquestions.com/mri-vs-mrs.html.

[129] H. Kashiwagi, "The lower limit of tissue blood flow for safe colonic anastomosis: an experimental study using laser Doppler velocimetry.," *Surg. Today*, vol. 23, no. 5, pp. 430–438, 1993.

[130] E. Sacristan, R. A. Baheza, A. O. Rodriguez, M. Does, B. Damon, and J. Gore, "Dual Frequency Coil and MRIS method for the Characterization of Ischemic Injury in the Intestinal Wall," in *the 25th Annual International Conference of the IEEE EMBS*, 2003, pp. 474–477.

[131] M. Millan, E. García-Granero, B. Flor, S. García-Botello, and S. Lledo, "Early prediction of anastomotic leak in colorectal cancer surgery by intramucosal pH," *Dis. Colon Rectum*, vol. 49, no. 5, pp. 595–601, 2006.

[132] V. Rieke and K. B. Pauly, "MR thermometry," *J. Magn. Reson. Imaging*, vol. 27, no. 2, pp. 376–390, 2008.

[133] P. Wang, "Evaluation of MR thermometry with proton resonance frequency method at 7T,"

Quant. Imaging Med. Surg., vol. 7, no. 2, pp. 259–266, 2017.

[134] D. D. Wheeler and M. S. Conradi, "Practical Exercises for Learning to Construct NMR/MRI Probe Circuits," *Concepts Magn. Reson. Part A*, vol. 40A, no. 12, pp. 1–13, 2012.

[135] J. B. Kneeland and J. S. Hyde, "High-resolution MR imaging with local coils.," *Radiology*, vol. 171, no. 1, pp. 1–7, 1989.

[136] G. C. Hurst and G. J. Misic, "Coils for insertion into the human body," in *Encyclopedia of nuclear magnetic resonance*, Grant D.M., Harris R.K. Eds, John Wiley and Sons, Chichester, 1996.

[137] A. Blank, G. Alexandrowicz, L. Muchnik, G. Tidhar, J. Schneiderman, R. Virmani, and E. Golan, "Miniature self-contained intravascular magnetic resonance (IVMI) probe for clinical applications," *Magn. Reson. Med.*, vol. 54, no. 1, pp. 105–112, 2005.

[138] E. Atalar, P. A. Bottomley, O. Ocali, L. C. L. Correia, M. D. Kelemen, J. A. C. Lima, and E. A. Zerhouni, "High resolution intravascular MRI and MRS by using a catheter receiver coil," *Magn. Reson. Med.*, vol. 36, no. 4, pp. 596–605, 1996.

[139] H. L. Kantor, R. W. Briggs, and R. S. Balaban, "In vivo 31P nuclear magnetic resonance measurements in canine heart using a catheter-coil.," *Circ. Res.*, vol. 55, no. 2, pp. 261–6, 1984.

[140] D. N.M., P. R., G. D.J., and B. G.M., "High resolution magnetic resonance imaging of the anal sphincter using an internal coil," *Magn. Reson. Q.*, vol. 11, no. 1, pp. 45–56, 1995.

[141] M. D. Schnall, T. Connick, C. E. Hayes, R. E. Lenkinski, and H. Y. Kressel, "MR imaging of the pelvis with an endorectal-external multicoil array," *J. Magn. Reson. Imaging*, vol. 2, no. 2, pp. 229–232, 1992.

[142] C. J. Baudouin, W. P. Soutter, D. J. Gilderdale, and G. A. Coutts, "Magnetic resonance imaging of the uterine cervix using an intravaginal coil," *Magn. Reson. Med.*, vol. 24, no. 1, pp. 196–203, 1992.

[143] M. Armenean, O. Beuf, F. Pilleul, and H. Saint-Jalmes, "Optimization of Endoluminal Loop Radiofrequency Coils For Gastrointestinal Wall MR Imaging," *IEEE Sens. J.*, vol. 4, no. 1, pp. 57–64, 2004.

[144] K. Inui, S. Nakazawa, J. Yoshino, K. Yamao, H. Yamachika, T. Wakabayashi, N. Kanemaki, and H. Hidano, "Endoscopic MRI: Preliminary Results of a New Technique for Visualization and Staging of Gastrointestinal Tumors," *Endoscopy*, vol. 27, pp. 480–485, 1995.

[145] N. M. de Souza, A. H. Gibbons, G. A. Coutts, A. S. Hall, R. Puni, J. Calam, and I. R. Young, "Magnetic resonance imaging during upper Gl endoscopy: Technical considerations and clinical feasibility," *Minim. Invasive Ther.*, vol. 4, no. 5–6, pp. 277–281, 1995.

[146] D. J. Gilderdale, A. D. Williams, U. Dave, and N. M. DeSouza, "An inductively-coupled, detachable receiver coil system for use with magnetic resonance compatible endoscopes," *J. Magn. Reson. Imaging*, vol. 18, no. 1, pp. 131–135, 2003.

[147] Y. Matsuoka, T. Ozaki, Y. Mori, K. Murakamir, and M. Matsumoto, "Development of RF coil for integration system of endoscope with MRI for esophageal examination," *Proc. 14th Sci. Meet. Int. Soc. Magn. Reson. Med.*, vol. 14, no. 3, p. 1405, 2006.

[148] U. R. Dave, A. D. Williams, J. A. Wilson, Z. Amin, D. J. Gilderdale, and D. J. Larkman, "Esophageal Cancer Staging with Endoscopic MI Imaging: Pilot Study," *Radiology*, vol. 230, no. 1, pp. 281–286, 2004.

[149] N. M. Desouza, G. A. Courts, D. J. Larkman, D. J. Gilderdale, A. D. Williams, A. Thillainagayam, and I. R. Young, "Combined MRI and fibreoptic colonoscopy: technical considerations and clinical feasibility," *Minim. Invasive Ther. Allied Technol.*, vol. 9, no. 1, pp. 25–30, 2000.

[150] C. J. Martin, A. J. Kennerley, J. Berwick, M. Port, and J. E. W. Mayhew, "Functional MRI in conscious rats using a chronically implanted surface coil," *J. Magn. Reson. Imaging*, vol. 38, no. 3, pp. 739–744, 2013.

[151] T. Janssens, B. Keil, R. Farivar, J. A. McNab, J. R. Polimeni, A. Gerits, J. T. Arsenault, L. L. Wald, and W. Vanduffel, "An implanted 8-channel array coil for high-resolution macaque MRI at 3T," *Neuroimage*, vol. 62, pp. 1529–1536, 2012.

[152] M. Bilgen, "Inductively-overcoupled coil design for high resolution magnetic resonance imaging," *Biomed. Eng. Online*, vol. 5, pp. 1–10, 2006.

[153] H. H. Quick, H. Kuehl, G. Kaiser, S. Bosk, J. F. Debatin, and M. E. Ladd, "Inductively coupled stent antennas in MRI," *Magn. Reson. Med.*, vol. 48, no. 5, pp. 781–790, 2002.

[154] M. D. Schnall, C. Barlow, V. H. Subramanian, and J. S. Leigh, "Wireless implanted magnetic resonance probes for in vivo NMR," *J. Magn. Reson.*, vol. 68, no. 1, pp. 161–167, 1986.

[155] D. J. Gilderdale, N. M. deSouza, G. A. Coutts, M. K. Chui, D. J. Larkman, A. D. Williams, and I. R. Young, "Design and use of internal receiver coils for magnetic resonance imaging.," *Br. J. Radiol.*, vol. 72, no. 864, pp. 1141–51, 1999.

[156] I. Elshafiey, "Magnetic resonance monitoring of spinal chord injury using implanted RF coil," in *Proceedings of the Twenty-First National Radio Science Conference*, 2004.

[157] Knowles Capacitors, "Non-magnetic MLC's." [Online]. Available: http://www.knowlescapacitors.com/Products/Non-magnetic-Components/Non-Magnetic.aspx. [Accessed: 23-Mar-2018].

[158] J. S. Hyde, R. J. Rilling, and A. Jesmanowicz, "Passive decoupling of surface coils by pole insertion," *J. Magn. Reson.*, vol. 89, no. 3, pp. 485–495, 1990.

[159] W. A. Edelstein, C. J. Hardy, and O. M. Mueller, "Electronic decoupling of surface-coil receivers for NMR imaging and spectroscopy," *J. Magn. Reson.*, vol. 67, no. 1, pp. 156–161, 1986.

[160] S. M. Park, R. Kamodetdacha, A. Amjad, and J. A. Nyenhuis, "MRI safety: RF-induced heating near straight wires," *IEEE Trans. Magn.*, vol. 41, pp. 4197–4199, 2005.

[161] C. J. Yeung, R. C. Susil, and E. Atalar, "RF safety of wires in interventional MRI: Using a safety index," *Magn. Reson. Med.*, vol. 47, no. 1, pp. 187–193, 2002.

[162] E. Atalar, "Safe Coaxial Cables," *Proc. 7th Annu. Meet. ISMRM, Philadelphia.*, no. c, p. 1006, 1999.

[163] P. Vernickel, V. Shulz, S. Weiss, and B. Gleich, "A safe transmission line for MRI," *IEEE Trans. Biomed. Eng.*, vol. 52, pp. 1094–1102, 2005.

[164] R. R. A. Syms, L. Solymar, and I. R. Young, "MR-Safe Cables -- an Application for Magneto-inductive Waves?," *3rd Int. Congr. Adv. Electromagn. Mater. Microwaves Opt.*, no. Mi, pp. 221–223, 2003.

[165] D. J. Gilderdale, G. A. Coutts, and N. M. deSouza, "Design and development of an endorectal array receiver coil," in *Proceedings of the International Society Magnetic Resonance in*

Medicine, 5th scientific meeting, 1997.

[166] M. Luo, A. W. Martinez, C. Song, F. Herrault, and M. G. Allen, "A microfabricated wireless RF pressure sensor made completely of biodegradable materials," *J. Microelectromechanical Syst.*, vol. 23, no. 1, pp. 4–13, 2014.

[167] P. K. Bowen, J. Drelich, and J. Goldman, "Zinc exhibits ideal physiological corrosion behavior for bioabsorbable stents," *Adv. Mater.*, vol. 25, no. 18, pp. 2577–2582, 2013.

[168] C. M. Boutry, H. Chandrahalim, P. Streit, M. Schinhammer, A. C. Hänzi, and C. Hierold, "Characterization of miniaturized RLC resonators made of biodegradable materials for wireless implant applications," *Sensors Actuators, A Phys.*, vol. 189, pp. 344–355, 2013.

[169] C. M. Boutry, W. S. W. Sun, T. Strunz, H. Chandrahalim, and C. Hierold, "Development and characterization of biodegradable conductive polymers for the next generation of RF bio-resonators," *Freq. Control Symp. (FCS), 2010 IEEE Int.*, vol. 2, no. 1, pp. 258–261, 2010.

[170] E. Shamonina and L. Solymar, "Magneto-inductive waves supported by metamaterial elements: Components for a one-dimensional waveguide," *J. Phys. D. Appl. Phys.*, vol. 37, no. 3, pp. 362–367, 2004.

[171] E. Shamonina, V. A. Kalinin, K. H. Ringhofer, and L. Solymar, "Magneto-inductive waveguide," *IEEE Electron. Lett.*, vol. 38, no. 8, pp. 37–39, 2002.

[172] E. Shamonina, V. A. Kalinin, K. H. Ringhofer, and L. Solymar, "Magnetoinductive waves in one, two, three dimensions," *J. Appl. Phys.*, vol. 92, no. 10, pp. 6252–6261, 2002.

[173] M. C. K. Wiltshire, E. Shamonina, I. R. Young, and L. Solymar, "Dispersion characteristics of magneto-inductive waves: comparison between theory and experiment," *IEEE Electron. Lett.*, vol. 39, no. 2, pp. 215–217, 2003.

[174] E. Shamonina, "Slow waves in magnetic metamaterials: history, fundamentals and applications," *Phys Stat*, vol. 245, no. (b), pp. 1471–1482, 2008.

[175] R. R. A. Syms, E. Shamonina, and L. Solymar, "Magneto-inductive waveguide devices," pp. 111–121.

[176] E. Shamonina and L. Solymar, "Properties of magnetically coupled metamaterial elements," *J. Magn. Magn. Mater.*, vol. 300, no. 1, pp. 38–43, 2006.

[177] O. Sydoruk, A. Radkovskaya, O. Zhuromskyy, E. Shamonina, and L. Solymar, "Magnetoinductive waves II: Applications," in *Chapter 36 in Theory and Phenomena of Metamaterials (Handbook of Artificial Materials), F. Capolino (Ed), CRC Press*, 2009.

[178] M. C. K. Wiltshire, J. B. Pendry, I. R. Young, D. J. Larkman, D. J. Gilderdale, and J. V. Hajnal, "Microstructured magnetic materials for RF flux guides in magnetic resonance imaging," *Science (80-.).*, vol. 291, no. 5505, pp. 849–851, 2001.

[179] M. Wiltshire, J. Hajnal, J. Pendry, D. Edwards, and C. Stevens, "Metamaterial endoscope for magnetic field transfer: near field imaging with magnetic wires.," *Opt. Express*, vol. 11, no. 7, pp. 709–715, 2003.

[180] M. C. Wiltshire, R. M. Henkelman, I. R. Young, and J. V Hajnal, "Metamaterial yoke for signal reception-an initial investigation," *Proc. 11th ISMRM*, vol. 11, p. 43, 2004.

[181] M. C. K. Wiltshire, E. Shamonina, I. R. Young, and L. Solymar, "Experimental and theoretical study of magneto-inductive waves supported by one-dimensional arrays of 'swiss rolls,'" *J. Appl. Phys.*, vol. 95, no. 8, pp. 4488–4493, 2004.

[182] M. J. Freire, R. Marques, and L. Jelinek, “Experimental demonstration of a μ=-1 metamaterial lens for magnetic resonance imaging,” *Appl. Phys. Lett.*, vol. 93, no. 23, pp. 1–4, 2008.

[183] M. J. Freire, L. Jelinek, R. Marques, and M. Lapine, “On the applications of μr= - 1 metamaterial lenses for magnetic resonance imaging,” *J. Magn. Reson.*, vol. 203, no. 1, pp. 81–90, 2010.

[184] P. A. Belov, Y. Hao, and S. Sudhakaran, “Subwavelength microwave imaging using an array of parallel conducting wires as a lens,” *Phys. Rev. B - Condens. Matter Mater. Phys.*, vol. 73, no. 3, pp. 1–4, 2006.

[185] P. A. Belov, Y. Zhao, S. Sudhakaran, and Y. Hao, “Experimental study of the subwavelength imaging by a wire medium slab,” *IEEE Antennas Propag. Soc. AP-S Int. Symp.*, vol. 262109, no. 2006, pp. 433–436, 2007.

[186] R. R. A. Syms, L. Solymar, I. R. Young, and T. Floume, “Thin-film magneto-inductive cables,” *J. Phys. D. Appl. Phys.*, vol. 43, no. 5, pp. 1–7, 2010.

[187] R. R. A. Syms, I. R. Young, M. M. Ahmad, and M. Rea, “Magnetic resonance imaging using linear magneto-inductive waveguides,” *J. Appl. Phys.*, vol. 112, no. 11, 2012.

[188] R. R. A. Syms, I. R. Young, M. M. Ahmad, S. D. Taylor-Robinson, and M. Rea, “Endoscopically compatible MR-safe magneto-inductive imaging catheter,” *2013 7th Int. Congr. Adv. Electromagn. Mater. Microwaves Opt. METAMATERIALS 2013*, no. September, pp. 25–27, 2013.

[189] K. Segkhoonthod, R. R. A. Syms, and I. R. Young, “Design of magneto-inductive magnetic resonance imaging catheters,” *IEEE Sens. J.*, vol. 14, no. 5, pp. 1505–1513, 2014.

[190] R. R. A. Syms, I. R. Young, C. A. Wadsworth, S. D. Taylor-Robinson, and M. Rea, “Magnetic Resonance Imaging Duodenoscope,” *IEEE Trans. Biomed. Eng.*, vol. 60, no. 12, pp. 3458–3467, 2013.

[191] A. Krafft, S. Müller, R. Umathum, W. Semmler, and M. Bock, “B1 field-insensitive transformers for RF-safe transmission lines,” *Magn. Reson. Mater. Physics, Biol. Med.*, vol. 19, no. 5, pp. 257–266, 2006.

[192] L. Solymar, O. Zhuromskyy, O. Sydoruk, E. Shamonina, I. R. Young, and R. R. A. Syms, “Rotational resonance of magnetoinductive waves: Basic concept and application to nuclear magnetic resonance,” *J. Appl. Phys.*, vol. 99, no. 12, 2006.

[193] R. R. A. Syms, T. Floume, I. R. Young, L. Solymar, and M. Rea, “Flexible magnetoinductive ring MRI detector: Design for invariant nearest-neighbour coupling,” *Metamaterials*, vol. 4, no. 1, pp. 1–14, 2010.

[194] O. Sydoruk, O. Zhuromskyy, A. Radkovskaya, E. Shamonina, and L. Solymar, “Magnetoinductive waves I: Theory,” in *Chapter 14 in Theory and Phenomena of Metamaterials (Handbook of Artificial Materials), F. Capolino (Ed), CRC Press*, 2009.

[195] L. Solymar and E. Shamonina, *Waves in metamaterials*. Oxford University Press, 2009.

[196] A. Radkovskaya, O. Sydoruk, M. Shamonin, E. Shamonina, C. J. Stevens, G. Faulkner, D. J. Edwards, and L. Solymar, “Experimental study of a bi-periodic magnetoinductive waveguide: comparison with theory,” *IET Microw. Antennas Propag.*, vol. 1, no. 1, pp. 80–83, 2007.

[197] A. Radkovskaya, O. Sydoruk, M. Shamonin, C. J. Stevens, G. Faulkner, D. J. Edwards, E. Shamonina, and L. Solymar, “Transmission properties of two shifted magnetoinductive waveguides,” *Microw. Opt. Technol. Lett.*, vol. 49, no. 5, pp. 1054–1058, 2007.

[198] R. R. A. Syms, O. Sydoruk, E. Shamonina, and L. Solymar, “Higher order interactions in magneto-inductive waveguides,” *Metamaterials*, vol. 1, no. 1, pp. 44–51, 2007.

[199] O. Beuf, F. Pilleul, M. Armenean, G. Hadour, and H. Saint-Jalmes, “In vivo colon wall imaging using endoluminal coils: Feasibility study on rabbits,” *J. Magn. Reson. Imaging*, vol. 20, no. 1, pp. 90–96, 2004.

[200] R. R. A. Syms and T. Floume, “Parasitic coupling in magneto-inductive cable,” *J. Phys. D. Appl. Phys.*, vol. 50, no. 22, 2017.

[201] F. E. Terman, *Radio Engineers’ Handbook*, 1st ed. McGraw-Hill.

[202] CPC and MegaElectronics, “Flexible Laminate, 305mm x 500mm - 400-105.” [Online]. Available: http://cpc.farnell.com/mega/400-105/flexible-laminate-305x500/dp/PC01694?ost=400-105&iscrfnonsku=false&ddkey=http%3Aen-CPC%2FCPC_United_Kingdom%2Fsearch. [Accessed: 23-Mar-2018].

[203] MegaElectronics, “MegaElectronics Catalogue.” [Online]. Available: https://www.megauk.com/downloads/mega_catalogue.pdf. [Accessed: 23-Mar-2018].

[204] J. L. Kolkert, K. Havenga, H. O. Ten Cate Hoedemaker, J. Zuidema, and R. J. Ploeg, “Protection of stapled colorectal anastomoses with a biodegradable device: The C-Seal feasibility study,” *Am. J. Surg.*, vol. 201, no. 6, pp. 754–758, 2011.

[205] W. A. Edelstein, C. J. Hardy, and O. M. Mueller, “Electronic Decoupling of Surface-Coil Receivers for NMR Imaging and Spectroscopy,” *J. Magn. Reson.*, vol. 67, pp. 156–161, 1986.

[206] G. Breed, “Classic Designs for Lumped Element and Transmission Line 90-Degree Couplers,” *High Freq. Electron.*, no. September, pp. 62–66, 2007.

[207] P. L. Kuhns, M. J. Lizak, S. H. Lee, and M. S. Conradi, “Inductive coupling and tuning in NMR probes; Applications,” *J. Magn. Reson.*, vol. 78, no. 1, pp. 69–76, 1988.

[208] D. I. Hoult and B. Tomanek, “Use of mutually inductive coupling in probe design,” *Concepts Magn. Reson. Part B Magn. Reson. Eng.*, vol. 15, no. 4, pp. 262–285, 2002.

[209] J. C. Blechinger, E. L. Madsen, and G. R. Frank, “Tissue-mimicking gelatin-agar gels for use in magnetic resonance imaging phantoms,” *Med. Phys.*, vol. 15, no. 4, pp. 629–636, 1988.

[210] Araldite professional adhesives, “Araldite Rapid 2 x 15ml.” [Online]. Available: http://www.go-araldite.com/products/epoxy-adhesives/araldite-rapid-2-x-15ml-tube. [Accessed: 23-Mar-2018].

[211] SRT Micro Ceramique, “NP0 Non magnetic Capacitors.” [Online]. Available: http://www.srt-microceramique.com/index.php/en/products/non-magnetic/np0-non-magnetic. [Accessed: 23-Mar-2018].

[212] H. Kamel, R. Syms, E. M. Kardoulaki, and M. Rea, “Metamaterial MRI-based Surgical Wound Monitor,” in *11th International Congress on Metamaterials*, 2017, pp. 106–108.

[213] H. Kamel, R. R. A. Syms, E. M. Kardoulaki, and M. Rea, “Surgical wound monitoring by MRI with a metamaterial-based implanted local coil,” *EPJ Appl. Metamaterials*, vol. 5, no. 5, 2018.

[214] M. Thurston and J. Yeung, “Aliasing in MRI,” *Radiopaedia*. [Online]. Available: https://radiopaedia.org/articles/aliasing-in-mri. [Accessed: 23-Mar-2018].

[215] E. M. Kardoulaki, R. R. A. Syms, I. R. Young, K. Choonee, M. Rea, and W. M. W. Gedroyc,

"Optothermal profile of an ablation catheter with integrated microcoil for MR-thermometry during Nd:YAG laser interstitial thermal therapies of the liver - An in-vitro experimental and theoretical study," *Med. Phys.*, vol. 42, no. 3, pp. 1389–1397, 2015.